Deciphering changes in photophysical properties of carbon dots and protein conformations induced by bioactive molecules

Thesis submitted for the degree of

Doctor of Philosophy

Submitted by

Ms. Mandeep Kaur

(Regn. No. 901909009)

Under the Supervision of

Dr. Banibrata Maity
Assistant Professor

Dr. Mily Bhattacharya
Associate Professor

Department of Chemistry and Biochemistry

Thapar Institute of Engineering and Technology

Patiala-147004, Punjab

Certificate

This is to certify that thesis entitled "Deciphering changes in photophysical properties of carbon dots and protein conformations induced by bioactive molecules", is being submitted by Ms. Mandeep Kaur in fulfilment of the requirement for the award of the Degree of Doctor of Philosophy in the Department of Chemistry and Biochemistry, Thapar Institute of Engineering and Technology, Patiala, is a record of candidate's own independent and original research work carried out by her under my supervision and guidance. The matter presented in the thesis has not been submitted in part or full for the award of any degree in any university or institution.

Dr. Bambrata Maity
Assistant Professor
Department of Chemistry and Biochemistry

Dr. Mily Bhattacharya
Associate Professor
Department of Chemistry and Biochemistry

(Head)
Dr. Manmohan Chhibber
Department of Chemistry and Biochemistry
TIET, Patiala-147004, Punjab, India

Candidate's Declaration

I, hereby declare that the present work in the thesis entitled "Deciphering changes in photophysical properties of carbon dots and protein conformations induced by bioactive molecules", in the fulfilment of the requirement for the award of the Degree of Doctor of Philosophy in the Department of Chemistry and Biochemistry, Thapar Institute of Engineering and Technology, Patiala is an authentic record of my work carried out under the supervision of Dr. Banibrata Maity, Assistant Professor, and Dr. Mily Bhattacharya, Associate Professor, Department of Chemistry and Biochemistry, Thapar Institute of Engineering and Technology, Patiala, India. The matter embodied in the thesis has not been submitted in part or fully to any other University or Institute for the reward of any degree in India or Abroad.

Mandeep

Mandeep Kaur

Acknowledgements

I wish to express my deep sincere gratitude to my research supervisors Dr. Banibrata Maity and Dr. Mily Bhattacharya, for giving me an opportunity to work under their guidance. I greatly appreciate their tireless support and encouragement throughout the research work. Their valuable guidance, constant encouragement, novel scientific ideas, inspiration, keep interest, and good wishes are going to be a monitoring tool throughout my life. This feat was possible only because of their unconditional support. I believe that their spacious guidance and consistent way of thinking will help me throughout my life.

I would like thank Prof. Manmohan Chhibber, Head of Department of Chemistry and Biochemistry Thapar Institute of Engineering and Technology, Patiala for his ever-helping attitude and good wishes.

I would also like to thank my doctoral committee members Dr. Manmohan Chhibber, Dr. Vijay Luxmi, and Dr. Sanjay Saxena for their valuable time, suggestion and helpful discussions. I would like to thank the former and present head of chemistry department.

I would also like to sincerely thank all faculty and staff of the Department of Chemistry and Biochemistry, Thapar institute of engineering and technology. I am thankful to my lab mates Jaspreet, Deepika, Anjali, Neeraj, Aayushi and Mallika for their timely help, cooperation, and support during my stay in the lab.

I would also like to sincerely thank Dr Samrat Mukhopadhyay lab (IISER Mohali) and his lab members for allowing me to use the lab facilities and timely help.

I would like to thank SERB for financial support and Thapar institute of engineering and technology providing fellowship as well as basic research facilities.

I would like to thank my friends Anisha Manchanda, Sunidhi Bharadwaj, Rohini Gupta, Rekha Thakur for all the good times, motivation, constant support and the unforgettable memories over the past few years.

Finally, my most sincere gratitude goes to my family for their unconditional love, continuous support, patience and encouragement which made this entire effort possible.

Table of Contents

List of Figures	i
List of Tables	x
List of Abbreviation	xii
List of Symbols	xvii
Abstract	xix
Chapter 1 Introduction and Literature review	
1.1.	Introduction
1.1.1	Bioactive compounds and pollutants
1.1.2	Proteins
1.1.3	Human serum albumin
1.1.4	Bile salts
1.1.5	Difference of aggregation phenomenon between bile salts and conventional surfactants
1.1.6	Nanomaterials
1.1.7	History and synthesis of carbon dots (CDs)
1.1.8	Hydrothermal Synthesis
1.1.9	Microwave-Assisted Synthesis
1.1.10	Optical properties and applications of CDs
1.1.11	Fluorescence quenching mechanism
1.1.12	Inner filter effect (IFE)
1.1.13	Fluorescence resonance energy transfer (FRET) mechanism
1.1.14	Waste into wealth: Biomass derived CDs

1.15	Deep eutectic solvents (DES)
1.1.16	Preparation of DES
1.1.17	Classification, properties and applications of DES
1.2	Literature review
1.3	Research gaps
1.4	Objectives
References	
Chapter 2 **Instrumentation techniques**	
2.1	High-resolution transmission electron microscopy (HRTEM)
2.2	X-ray photoelectron spectroscopy (XPS)
2.3	Grazing-incidence X-Ray diffraction (GIXRD)
2.4	Attenuated total reflectance Fourier-transform IR (ATR FT-IR) and Raman spectroscopy
2.5	Zeta Potential
2.6	Energy dispersive spectroscopy (EDS)
2.7	UV-Visible (UV-Vis) spectroscopy
2.8	Fluorescence spectroscopy
References	
Chapter 3 **Deciphering conformational changes in human serum albumin induced by bile salts using spectroscopic and molecular modeling approaches**	
3.1	Introduction

3.2	Experimental methods
3.2.1	Materials
3.2.2	Protein sample preparation
3.2.3	Preparation of bile-salt solution
3.2.4	UV-Vis absorption measurements
3.2.5	Steady-state fluorescence measurements
3.2.6	Time-resolved emission measurements
3.2.7	Molecular docking analysis
3.3	Results and discussions
3.3.1	UV-Vis absorption study
3.3.2	Steady-state fluorescence study
3.3.2.1	Steady-state Tryptophan fluorescence study
3.3.2.2	Steady-state tryptophan anisotropy study
3.3.2.3	Steady-state ANS fluorescence study
3.3.2.4	Steady state ANS anisotropy study
3.3.3	HSA-bile salt interaction using time-resolved emission study
3.3.4	Molecular docking results
3.5	Conclusions
References	

Chapter 4

Green transformation of biomass-derived Indian gooseberry into fluorescent intrinsic nitrogen-functionalized carbon quantum dots for real-time detection of vitamin B_2 in the nanomolar range

4.1	Introduction
4.2	Experimental section
4.2.1	Materials

4.2.2	Synthesis of N-CDs
4.2.3	Characterization of N-CDs
4.2.3.1	Electron microscopy
4.2.3.2	XPS and EDS analysis
4.2.3.3	GIXRD analysis
4.2.3.4	Raman spectroscopy
4.2.3.5	ATR FT-IR spectroscopy
4.2.3.6	UV-Vis spectroscopy and zeta potential measurements
4.2.3.7	Preparation of N-CDs sample for fluorescence studies
4.2.3.8	Steady state fluorescence spectroscopy
4.2.3.9	Photoluminescence quantum yield (PLQY) measurements
4.2.3.10	Time-resolved emission spectroscopy
4.3	Results and discussions
4.3.1	Morphological characterization and compositional analyses of N-CDs
4.3.2	Optical properties of N-CDs
4.3.3	Optimization of N-CDs
4.3.3.1	Reaction time and volume optimization
4.3.3.2	Storage duration optimization
4.3.4	Stability of N-CDs
4.3.5	Selectivity studies of N-CDs
4.3.6	Determination of photophysical parameters
4.3.7	Elucidation of sensing mechanism of RF (vitamin B_2) by N-CDs
4.3.8	Estimation of limit of detection

4.3.9	Method validation with real sample of vitamin B_2
4.4	Conclusions
References	
Chapter 5 **Deep eutectic solvent-assisted carbon quantum dots for nanomolar detection of 4-nitrophenol**	
5.1	Introduction
5.2	Experimental section
5.2.1	Materials
5.2.2	Synthesis of DES
5.2.3	Synthesis of S-CDs
5.2.4.	Characterization of S-CDs
5.2.4.1	Electron microscopy
5.2.4.2	XPS and EDS analysis
5.2.4.3	GIXRD analysis
5.2.4.4	ATR FT-IR spectroscopy
5.2.4.5	UV-Vis spectroscopy and zeta potential measurements
5.2.4.6	Preparation of S-CDs sample for fluorescence studies
5.2.4.7	Steady state fluorescence spectroscopy
5.2.4.8	Photoluminescence quantum yield (PLQY) measurements
5.2.4.9	Time-resolved emission spectroscopy
5.3	Results and Discussions

5.3.1	Morphological characterization and compositional analyses of S-CDs
5.3.2	Optimization of S-CDs
5.3.2.1	Reaction time and volume optimization
5.3.3	Optical properties of S-CDs
5.3.4	Stability of S-CDs
5.3.5	Selectivity studies of S-CDs
5.3.6	Plausible sensing mechanism for 4-NP detection
5.3.7	Determination of limit of detection
5.3.8	Determination of photophysical characteristics
5.3.9	Method reliability with real sample of 4-NP
5.4	Conclusions
References	
Conclusions and Future Perspective	
List of Publications	
Conferences and Workshops	
Appendix	

Table of Contents

List of Figures	i
List of Tables	x
List of Abbreviation	xii
List of Symbols	xvii
Abstract	xix
Chapter 1 Introduction and Literature review	
1.1.	Introduction
1.1.1	Bioactive compounds and pollutants
1.1.2	Proteins
1.1.3	Human serum albumin
1.1.4	Bile salts
1.1.5	Difference of aggregation phenomenon between bile salts and conventional surfactants
1.1.6	Nanomaterials
1.1.7	History and synthesis of carbon dots (CDs)
1.1.8	Hydrothermal Synthesis
1.1.9	Microwave-Assisted Synthesis
1.1.10	Optical properties and applications of CDs
1.1.11	Fluorescence quenching mechanism
1.1.12	Inner filter effect (IFE)
1.1.13	Fluorescence resonance energy transfer (FRET) mechanism
1.1.14	Waste into wealth: Biomass derived CDs

1.15	Deep eutectic solvents (DES)
1.1.16	Preparation of DES
1.1.17	Classification, properties and applications of DES
1.2	Literature review
1.3	Research gaps
1.4	Objectives
References	
Chapter 2 **Instrumentation techniques**	
2.1	High-resolution transmission electron microscopy (HRTEM)
2.2	X-ray photoelectron spectroscopy (XPS)
2.3	Grazing-incidence X-Ray diffraction (GIXRD)
2.4	Attenuated total reflectance Fourier-transform IR (ATR FT-IR) and Raman spectroscopy
2.5	Zeta Potential
2.6	Energy dispersive spectroscopy (EDS)
2.7	UV-Visible (UV-Vis) spectroscopy
2.8	Fluorescence spectroscopy
References	
Chapter 3 **Deciphering conformational changes in human serum albumin induced by bile salts using spectroscopic and molecular modeling approaches**	
3.1	Introduction

3.2	Experimental methods
3.2.1	Materials
3.2.2	Protein sample preparation
3.2.3	Preparation of bile-salt solution
3.2.4	UV-Vis absorption measurements
3.2.5	Steady-state fluorescence measurements
3.2.6	Time-resolved emission measurements
3.2.7	Molecular docking analysis
3.3	Results and discussions
3.3.1	UV-Vis absorption study
3.3.2	Steady-state fluorescence study
3.3.2.1	Steady-state Tryptophan fluorescence study
3.3.2.2	Steady-state tryptophan anisotropy study
3.3.2.3	Steady-state ANS fluorescence study
3.3.2.4	Steady state ANS anisotropy study
3.3.3	HSA-bile salt interaction using time-resolved emission study
3.3.4	Molecular docking results
3.5	Conclusions
References	

Chapter 4

Green transformation of biomass-derived Indian gooseberry into fluorescent intrinsic nitrogen-functionalized carbon quantum dots for real-time detection of vitamin B_2 in the nanomolar range

4.1	Introduction
4.2	Experimental section
4.2.1	Materials

4.2.2	Synthesis of N-CDs
4.2.3	Characterization of N-CDs
4.2.3.1	Electron microscopy
4.2.3.2	XPS and EDS analysis
4.2.3.3	GIXRD analysis
4.2.3.4	Raman spectroscopy
4.2.3.5	ATR FT-IR spectroscopy
4.2.3.6	UV-Vis spectroscopy and zeta potential measurements
4.2.3.7	Preparation of N-CDs sample for fluorescence studies
4.2.3.8	Steady state fluorescence spectroscopy
4.2.3.9	Photoluminescence quantum yield (PLQY) measurements
4.2.3.10	Time-resolved emission spectroscopy
4.3	Results and discussions
4.3.1	Morphological characterization and compositional analyses of N-CDs
4.3.2	Optical properties of N-CDs
4.3.3	Optimization of N-CDs
4.3.3.1	Reaction time and volume optimization
4.3.3.2	Storage duration optimization
4.3.4	Stability of N-CDs
4.3.5	Selectivity studies of N-CDs
4.3.6	Determination of photophysical parameters
4.3.7	Elucidation of sensing mechanism of RF (vitamin B_2) by N-CDs
4.3.8	Estimation of limit of detection

4.3.9	Method validation with real sample of vitamin B_2
4.4	Conclusions
References	
Chapter 5 **Deep eutectic solvent-assisted carbon quantum dots for nanomolar detection of 4-nitrophenol**	
5.1	Introduction
5.2	Experimental section
5.2.1	Materials
5.2.2	Synthesis of DES
5.2.3	Synthesis of S-CDs
5.2.4.	Characterization of S-CDs
5.2.4.1	Electron microscopy
5.2.4.2	XPS and EDS analysis
5.2.4.3	GIXRD analysis
5.2.4.4	ATR FT-IR spectroscopy
5.2.4.5	UV-Vis spectroscopy and zeta potential measurements
5.2.4.6	Preparation of S-CDs sample for fluorescence studies
5.2.4.7	Steady state fluorescence spectroscopy
5.2.4.8	Photoluminescence quantum yield (PLQY) measurements
5.2.4.9	Time-resolved emission spectroscopy
5.3	Results and Discussions

5.3.1	Morphological characterization and compositional analyses of S-CDs
5.3.2	Optimization of S-CDs
5.3.2.1	Reaction time and volume optimization
5.3.3	Optical properties of S-CDs
5.3.4	Stability of S-CDs
5.3.5	Selectivity studies of S-CDs
5.3.6	Plausible sensing mechanism for 4-NP detection
5.3.7	Determination of limit of detection
5.3.8	Determination of photophysical characteristics
5.3.9	Method reliability with real sample of 4-NP
5.4	Conclusions
References	
Conclusions and Future Perspective	
List of Publications	
Conferences and Workshops	
Appendix	

List of Figures

Figure No.	Title	Page No.
	Chapter 1	
Figure 1.1	The structural hierarchy of proteins	3
Figure 1.2	Ribbon diagram of Human serum albumin (PDB ID-1UOR) showing three domains (I; red, II; green, III; violet), disulfide bridges (yellow sticks), and single tryptophan (W214; hot pink), generated with PyMOL (Schrödinger Inc., New York)	5
Figure 1.3	Schematic illustration of a bile salt's steroid backbone and nomenclature along with the position and orientation of hydroxyl groups	6
Figure 1.4	Chemical structures of sodium cholate (NaC), sodium deoxycholate (NaDC) and sodium Taurocholate (NaTC)	7
Figure 1.5	Schematic representation of bile salt's primary and secondary aggregates as proposed by Small model	8
Figure 1.6	Structure of CDs, distinctive characteristics, and potential applications in numerous disciplines	11
Figure 1.7	Schematic representation of utilized CDs synthesis.	12
Figure 1.8	Schematic representation of (a) parameters used in Parker equation, (b) distance requirement for FRET, (c) spectral overlap indicating FRET	18
Figure 1.9	Schematic list of HBDs and HBAs for DESs synthesis	21
	Chapter 3	
Figure 3.1	UV-Vis absorption spectra showing binding interaction of HSA (10 μM)-bile salts at various concentrations and pH conditions, (a) HSA-NaC, (b) HSA-NaTC, (c) HSA-NaDC depicts bile salts binding at pH 7 and (d) MG HSA-CA, (e) MG HSA-TCA, (f) MG HSA-DCA shows the interaction with respective bile acids at pH 3	57

Figure 3.2	Tryptophan fluorescence emission for HSA-bile salt at pH 7 (a) HSA-NaC, (b) HSA-NaTC, (c) HSA-NaDC and HSA molten globule (MG)-bile acid at pH 3 (d) MG HSA-CA, (e) MG HSA-TCA, (f) MG HSA-DCA. (λex 295 nm, [HSA] = 10 μM)	61
Figure 3.3	Conformational changes in HSA as a function of pH and bile salts studied using steady state fluorescence spectroscopy (a) Tryptophan fluorescence emission for HSA -bile salt (NaC, NaTC, NaDC) at pH 7 (b) Tryptophan fluorescence emission at pH 3 for MG HSA-bile acids (CA, TCA, DCA), (c) Tryptophan anisotropy for HSA -bile salts at pH 7 (d) Tryptophan anisotropy for MG HSA-bile acids at pH 3. The intensity and anisotropy error bars are included in the symbols. (λex 295 nm, [HSA] = 10 μM)	62
Figure 3.4	Bile salts-induced protein conformational changes monitored using hydrophobic probe under variable bile salt concentration. Changes in ANS fluorescence spectra of (a) HSA -bile salt (NaC) at pH 7, (b) MG HSA -bile acids (CA) at pH 3, (c) MG HSA-bile acids (DCA) (10 μM) at pH 3. Changes in ANS fluorescence anisotropy of (d) HSA-bile salts (NaC, NaTC, NaDC) at pH 7, (e) MG HSA-bile salts (CA, TCA, DCA) at pH 3. The error bars are included in the symbols. (λex = 350 nm, λem = 475 nm, [HSA] = 10 μM)	64
Figure 3.5	Time-resolved fluorescence decay profiles using hydrophobic probe ANS of (a) HSA -bile salts (NaC, NaTC, NaDC) at pH 7, (b) MG HSA-bile acids (CA, TCA, DCA) at pH 3. (λex = 350 nm, [HSA] = 10 μM)	65
Figure 3.6	Scattered spectra showing dynamical insights into the HSA-biosurfactant interactions using hydrophobic probe ANS (a) Time-resolved fluorescence spectra HSA-bile salts (NaC, NaTC, NaDC) at pH 7, (b) MG HSA-bile acids (CA, TCA, DCA) at pH 3. The error bars are included in the symbols. (λex = 350 nm, [HSA] = 10 μM)	68
Figure 3.7	(a, d, h) Results obtained using molecular docking of HSA-CA, HSA-TCA and HAS-DCA (domain I - yellow, domain II - purple,	70

	domain III - cyan) where spheres (hot pink) represent the CA, TCA and DCA, respectively that are bound in subdomain II A and green color represents the only tryptophan (W214) present in HSA obtained using PyMol (Schrödinger Inc., New York). (b, e, h) All protein residues that are hydrogen bonded to ligand (CA, TCA, DCA respectively) are shown using PyMOL (Schrödinger Inc., New York). (c, f, i) All the protein residues, represented in cyan, are hydrogen bonded to the ligand whereas, the residues, represented in yellow, depict hydrophobic interaction with CA. Figures 3.7c, f, i was obtained using Ligplot+ v.2.2	
	Chapter 4	
Figure 4.1	Schematic representation of synthetic protocol of N-CDs from Indian Gooseberry	83
Figure 4.2	(a) HR-TEM image of N-CDs, inset representing particle size distribution histogram plot, (b) XRD spectrum, (c) FTIR spectrum and (d) Raman spectrum of N-CDs	87
Figure 4.3	(a) XPS survey spectrum of N-CDs, (b-d) Deconvoluted XPS spectra of N-CDs represented in an element-specific manner viz. (b) O1s, (c) N1s, and (d) C1s	90
Figure 4.4	(a) UV-Visible absorption spectrum of N-CDs with inset picture representing N-CDs under visible and UV light illumination. The other inset image depicts the magnified representation of the 355 nm band. Excitation wavelength-dependent (b) excitation wavelength dependent changes in fluorescence emission spectra of N-CDs and (c) peak position-normalized fluorescence emission of N-CDs clearly depicting the spectral shift, indicated by a dashed red arrow, from 408 nm to 518 nm in aqueous medium (λ_{ex}: 280 nm to 430 nm), (d) excitation wavelength-dependent changes in fluorescence emission spectra and (e) peak position-normalized fluorescence emission of N-CDs clearly depicting the spectral shift from 404 nm	92

	to 520 nm in pH 7.4 HEPES buffer, indicated by red dashed-arrow upon changing the excitation wavelength (λ_{ex}: 280 nm to 430 nm)	
Figure 4.5	Fluorescence emission spectra of N-CDs by optimizing the (a) reaction time, (b) volume ratio, (c) storage time, and (d) Zeta potential of N-CDs. All the experiments were performed in aqueous medium	94
Figure 4.6	(a) Fluorescence emission spectra of N-CDs at variable solution pH (b) FL intensity of N-CDs in aqueous and HEPES buffer at pH 7.4 (c) impact of ionic strength of the medium on N-CDs emission at 430 nm in the presence of variable concentrations of NaCl (0-2 M) and (d) impact of photo-irradiation by a xenon arc lamp on the emission of N-CDs at 430 nm as a function of time, (inset) photograph demonstrates practical utility of N-CDs as a fluorescent ink. (e) Selectivity studies of N-CDs with different amino acids and bioactive molecules. Error bars represent standard error of measurements obtained from three independent experiments	96
Figure 4.7	(a) Variation in fluorescence spectra of N-CDs in the presence of different concentrations of RF (0-2.2 μM) with inset image showing fluorescence quenching in aqueous medium. Black arrow depicts the progressive decrease of fl. intensity of N-CDs at shorter emission wavelength, while steady increase at longer emission wavelength is represented by red arrow, (b) spectral overlap between emission spectrum of N-CDs (red) and excitation spectrum of RF (blue) where yellow color demonstrates the overlapped region in aqueous medium, (c) Fluorescence lifetime decays of N-CDs in an aqueous medium where, the sharp, thin black line represents the instrument response function, the red and olive lines represent the actual intensity decays in the absence and presence of RF respectively. The blue and royal blue lines correspond to fits obtained in the absence and presence of RF, respectively, (d) linear relationship of	98

	fluorescence response (F_0/F) of N-CDs at $\lambda_{em.}$ = 430 nm with different concentrations of RF (0-2.2 μM; the red line indicates the linear fit of the data). Error bars represent standard error of measurements obtained from three independent experiments	
Figure 4.8	Stern-Volmer plots of N-CDs in (a) aqueous medium, (b) HEPES buffer at pH 7.4 and (c) real sample of vitamin $B_{2.}$ The parameters 'F_0' and 'F' indicate the fluorescence intensity in the absence and presence of vitamin B_2, respectively. 'K_{sv}' signifies Stern-Volmer quenching constant, which was estimated from the slope of the plots. The black line indicates the linear fit of the data using OriginPro 2021 and R^2 denotes the goodness of the fits. Error bars represent standard error of measurements obtained from three independent experiments	100
Figure 4.9	Benesi-Hildebrand plot of N-CDs in (a) aqueous medium, (b) HEPES buffer medium at pH 7.4 and (c) real sample of vitamin $B_{2.}$ The parameters 'F_0' and 'F' indicate the fluorescence intensity in the absence and presence of vitamin B_2, respectively. Q indicates the concentration of the quencher (i.e. vitamin B_2) and K_1 depicts the binding constant, which was estimated from the reciprocal of the slope of the plots. The blue line indicates the linear fit of the data using OriginPro 2021 and R^2 denotes the goodness of the fits. Error bars represent standard error of measurements obtained from three independent experiments	101
Figure 4.10	Variation in fluorescence emission of N-CDs in the presence of different concentrations of RF (0-2.2 μM) with inset image showing fluorescence quenching (a) in HEPES buffer at pH 7.4, (b) upon addition of a real sample of Vitamin $B_{2.}$ Black arrow depicts the progressive decrease of fl. intensity of N-CDs at shorter emission wavelength, while steady increase at longer emission wavelength is represented by red arrow, (c) Spectral overlap between emission spectrum of N-CDs (red) and excitation spectrum of RF (blue) where	103

	the yellow color demonstrates the overlapped region in HEPES buffer at pH 7.4, (d) Spectral overlap between emission spectrum of N-CDs (red) and excitation spectrum of RF (blue) where the yellow color demonstrates the overlapped region in real sample of Vitamin B_2, (e) Fluorescence lifetime decays of N-CDs in pH 7.4 HEPES buffer where, the sharp, thin black line represents the instrument response function, the red and olive lines represent the actual intensity decays in the absence and presence of RF respectively. The blue and royal blue lines correspond to fits obtained in the absence and presence of RF, respectively, (f) Fluorescence lifetime decays of N-CDs in the presence of a real sample of Vitamin B_2 where, the sharp, thin black line represents the instrument response function, the red and olive lines represent the actual intensity decays in the absence and presence of RF respectively. The blue and royal blue lines correspond to fits obtained in the absence and presence of RF, respectively	
Figure 4.11	Schematic representation of FRET mechanism between N-CDs and RF leading to quenching of fluorescence emission from N-CDs	106
Figure 4.12	Linear relationship of fluorescence response (F_0/F) of N-CDs with different concentrations of RF (0-2.2 μM) in (a) HEPES buffer at pH 7.4, (b) real sample of Vitamin B_2. The parameters 'F_0' and 'F' indicate the fluorescence intensity in the absence and presence of vitamin B_2, respectively. LOD signifies limit of detection. The red line indicates the linear fit of the data using OriginPro 2021 and R^2 denotes the goodness of the fits. Error bars represents standard error of measurements obtained from three independent experiments	108
	Chapter 5	
Figure 5.1	(a) Schematic representation of interactions between Choline chloride and urea to form deep eutectic solvent (DES), and (b) Schematic representation of synthetic protocol of DES from choline chloride and urea	124

Figure 5.2	Schematic representation of synthetic protocol of S-CDs from sucrose	125
Figure 5.3	(a) HR-TEM image of S-CDs, inset shows particle size distribution histogram plot, (b) XRD spectrum, (c) FTIR spectrum and (d) Energy dispersive spectroscopy (EDS) spectrum of S-CDs representing various elements presence on the S-CDs surface. The table (inset) displays the percentage composition of each element present in the S-CDs	128
Figure 5.4	Energy dispersive spectroscopy (EDS) spectrum of S-CDs demonstrating the presence of numerous elements on S-CDs surface. The table (inset) shows the percentage composition of every component found in the S-CDs	130
Figure 5.5	(a) Pie chart represents exact elemental composition of S-CDs from XPS analysis, (b) XPS survey spectrum of S-CDs, (c-f) S-CDs deconvoluted XPS spectra shown in an element-specific way i.e (c) C1s, (d) O1s, (e) N1s, and (f) Cl2p	131
Figure 5.6	S-CDs fluorescence emission spectra for optimization of the (a) reaction time, and (b) volume ratio	133
Figure 5.7	(a) S-CDs UV-visible absorption spectrum, with an inset image showing the S-CDs under visible and UV light illumination, (b) excitation and emission spectrum of S-CDs, (c) variations in fluorescence emission spectra of S-CDs and (d) peak position-normalized fluorescence emission of S-CDs plainly depicting the spectral shift, indicated by a dashed red arrow, from 443 nm to 508 nm (λ_{ex}: 310 nm to 440 nm)	134
Figure 5.8	Fluorescence emission spectra of S-CDs (a) in aqueous medium and at different solution pH (3, 5, 7, 9 12), (b) effect of medium's ionic strength on S-CDs in the presence of variable concentrations of NaCl (0-200 μM), (c) at different storage time interval, and (f) effect of photo-irradiation by a xenon arc lamp on the emission of S-CDs at	135

	as a function of time. The error bars show the standard error of measurements taken from three different experiments	
Figure 5.9	(a) Zeta potential of S-CDs, (b) impact of temperature variation on S-CDs from 10-90 °C, (c) Fl. intensity plot as function of temperature (10-90 °C). The red line shows linear fit of data using OriginPro 2023 and R^2 denotes the goodness of these fits. The error bars show standard error of measurements taken from three different experiments.	137
Figure 5.10	Selectivity studies of S-CDs with different (a) biomolecules, and (b) metal ions and pollutants	138
Figure 5.11	(a, d) Variation in fluorescence emission of S-CDs in the presence of different concentrations of 4-NP (0-3.8 μM) in standard and real samples respectively. Black arrow depicts the progressive decrease of fl. intensity of S-CDs, (b, e) The spectra depict linear correlation between F_0- F/F_0 and different concentrations of 4-NP (0 to 3.8μM), (c, f) Linear correlation between F_0- F/F_0 and some specific concentrations of 4-NP (0 to 0.56 μM). Error bars represent standard error of measurements obtained from three independent experiments	139
Figure 5.12	(a) Absorption spectrum of 4-NP with S-CDs excitation and emission spectrum, (b) Fluorescence lifetime decays of S-CDs, where the sharp, thin black line represents the instrument response function, the red and magenta lines represent the actual intensity decays in the absence and presence of RF respectively. The wine and purple lines correspond to fits obtained in the absence and presence of RF, respectively using tri-exponential function, (c) Fluorescence lifetime decays of S-CDs, where the sharp, thin black line represents the instrument response function, the red and magenta lines represent the actual intensity decays in the absence and presence of RF respectively. The wine and purple lines correspond to fits obtained in the absence and presence of RF, respectively using tri-exponential function, (d) Plot demonstrates the correction factor (CF) with	141

	various concentrations of 4-NP, (e) Suppressed efficiency (E%) of the corrected (redline, E_{cor}) and observed (blackline, E_{obsd}) fluorescence intensities	
Figure 5.13	Potential quenching mechanism of S-CDs in the presence of 4-NP through formation of the zwitterionic spirocyclic Meisenheimer complex	144
Figure 5.14	Stern-Volmer plot of S-CDs in (a) aqueous medium, and (b) real sample of 4-NP. The variables 'F_0' and 'F' indicate the fluorescence intensity in the absence and presence of 4-NP, respectively. 'K_{sv}' signifies Stern-Volmer quenching constant, calculated from the slope of the plots. Benesi-Hildebrand plot of S-CDs in (c) aqueous medium, and (d) real sample of 4-NP. The variables 'F_0' and 'F' indicate the fluorescence intensity in the absence and presence of 4-NP, respectively. Q indicates the concentration of the quencher (i.e.4-NP) and K_1 depicts the binding constant, calculated using reciprocal of the slope of the plots. The red line represents the linear fit of the data using OriginPro 2023 and R^2 denotes the goodness of the fits. The error bars show the standard error of measurements taken from three different experiments	146

List of Tables

Table No.	Title	Page No.
	Chapter 3	
Table 3.1	The binding constants (K) were determined based on changes in the absorbance using the 1:1 linear Benesi-Hildebrand method. The corresponding free energy changes (ΔG) upon binding were estimated from the binding constants using the equation $\Delta G = -RT\ln K$	59
Table 3.2	Time-resolved emission parameters of at different pH conditions (pH 3 and pH 7)	66
	Chapter 4	
Table 4.1	Photophysical parameters of N-CDs in the presence of RF	97
Table 4.2	Analytical performance data for RF (vitamin B_2) sensing by N-CDs.	102
Table 4.3	Fluorescence lifetime components of N-CDs and their respective coefficients along with the mean fluorescence lifetimes in aqueous and pH 7.4 medium	105
Table 4.4	FRET parameters of N-CDs@RF nanosensor in different systems	107
Table 4.5	A comparative analysis of LOD for the detection of RF by different nanosensors	109
Table 4.6.	Application of the developed nanosensor for detection of real sample of RF in Tablet	110
	Chapter 5	
Table 5.1	Fluorescence lifetime components of S-CDs and their respective coefficients along with the mean fluorescence lifetimes. The lifetimes were extracted by fitting the time-resolved emission decays using a tri-exponential function. χ^2 represents the goodness of the fits	142

Table 5.2	The different parameters employed to estimate IFE on the fluorescence quenching of S-CDs by 4-NP	143
Table 5.3	Analytical performance statistics for S-CDS-based 4-NP sensing.	145
Table 5.4	Comparative evaluation of LOD for 4-NP detection using different nanosensors	147
Table 5.5	Implementation of the synthesized nanosensor for detection of real sample of 4-NP in river water	148

List of abbreviations

mRNA	Messenger RNA
ATP	Adenosine triphosphate
HSA	Human serum albumin
Cys	Cysteine
CMC	Critical micellar concentration
NaDC	Sodium deoxycholate
NaC	Sodium cholate
NaTC	Sodium taurocholate
BA	Bile acids
QCE	Quantum confinement effect
CDs	Carbon dots
PL	Photoluminescence
HOMO	Highest unoccupied molecular orbital
LUMO	Lowest unoccupied molecular orbital
PET	Photoinduced electron transfer
IFE	Inner filter effect
FRET	Fluorescence resonance energy transfer
RET	Resonance energy transfer
DESs	Deep eutectic solvents
HBAs	Hydrogen bond acceptors
HBDs	Hydrogen bond donors
VOCs	volatile organic compounds
ILs	Ionic liquids
AHDMAPPC	2-amino-6-hydroxy-4-(4-N,N-dimethylaminophenyl)-pyrimidine-5-carbonitrile
FTIR	Fourier transform infrared spectroscopy
CD	Circular dichroism spectroscopy
DSP	Desipramine hydrochloride

CPZ	Chlorpromazine hydrochloride
Rh B	Rhodamine B
4-NP	4-Nitrophenol
CIP	Ciprofloxacin
QT	Quercetin
cyt-c	Cytochrome C
AGADES	Acetamide-glycolic acid deep eutectic solvent
N, Cl-CDs	N, Cl co-doped carbon dots
Trp	Tryptophan
BSA	Bovine serum albumin
SDS	Sodium dodecyl sulphate
Nano-Ber	Berberine nanoparticles
HTF	Holo-transferrin
CNTs	Carbon nanotubes
ANS	8-anilinonaphthalene-1-sulfonic acid
HCl	Hydrochloric acid
NaOH	Sodium hydroxide
TCSPC	Time-correlated single-photon counting
LGA	Lamarckian genetic algorithm
MG	Molten-globule
CA	Cholic acid
TCA	Taurocholic acid
DCA	Deoxycholic acid
UV-Vis	Ultraviolet-visible spectroscopy
Lys	Lysine
Arg	Arginine
Glu	Glutamic acid
Asn	Asparagine
Pro	Proline
Asp	Aspartic acid

Tyr	Tyrosine
RF	Riboflavin
FAD	Flavin adenine dinucleotide
FMN	Flavin mononucleotide
HPLC	High-performance liquid chromatography
DNA	Deoxyribonucleic acid
HN-CDs	Hydrophilic nitrogen-doped carbon dots
NCDs	Nitrogen-doped carbon dots
RET	Resonance energy/ electron transfer
FNCDs	Fluorescent nitrogen-doped carbon dots
N-CDs	Nitrogen-doped carbon dots
HEPES	*4-(2-hydroxyethyl)-1-piperazineethanesulfonic acid*
Ala	Alanine
Gln	Glutamine
Trp	Tryptophan
Thr	Threonine
Val	Valine
His	Histidine
Leu	Leucine
Ile	Isoleucine
Met	Methionine
AA	Ascorbic acid
PLQY	Photoluminescence quantum yield
HRTEM	High-resolution transmission electron microscopy
CCD	Charge-coupled device
XPS	X-ray photoelectron spectroscopy
EDS	Energy dispersive spectroscopy
GIXRD	Grazing-incidence X-Ray diffraction
ATR FT-IR	Attenuated total reflectance fourier-transform infrared
TCSPC	Time correlated single photon counting

IRF	Instrument response function
FWHM	Full-width at half- maximum
PL	Photoluminescence
LOD	Limit of detection
LOQ	Limit of quantification
ICHQ2	Validation of analytical procedures: text and methodology
USEPA	U.S. environmental protection agency
ChCl	Choline chloride
PEG	Polyethylene glycol
Cu-CDs	Copper doped carbon dots
$FeCl_3.6H_2O$	Ferric chloride hexahydrate
$MnCl_2.3H_2O$	Manganese (II) chloride tetrahydrate
$Pb(NO_3)_2$	Lead nitrate
KCl	Potassium chloride
$CoCl_2.6H_2O$	Cobalt chloride hexahydrate
$NiCl_2.6H_2O$	Nickel (II) chloride hexahydrate
NaCl	Sodium chloride
$MgCl_2.6H_2O$	Magnesium chloride hexahydrate
$BaCl_2.2H_2O$	Barium chloride dihydrate
NaOH	Sodium hydroxide pallets
3-NP	3-Nitrophenol
2-NP	2-Nitrophenol
$FeCl_2$	Ferrous chloride
HCl	Hydrochloric acid
$HgCl_2$	Mercuric chloride
PA	Picric acid
NH_4Cl	Ammonium chloride
$CuCl_2$	Copper chloride
$Cr(NO_3)_3$	Chromium (III) nitrate
Na_3AsO_4	Sodium arsenate

CH_4N_2S	Thiourea
CF	Correction factor
PL	Photoluminescence
Pt	Platinum
NOCDs	Nitrogen-doped oxidized carbon dots
B, N-CDs	Boron and nitrogen co-doped carbon dots
N, P-CDs	Nitrogen and phosphorus-doped carbon dots
Cu-CDs	Cu-doped carbon dots

List of symbols

mM	Millimolar
kDa	kilodalton
N	Normal
µM	Micromolar
sec	Second
ps	Picosecond
Å	Angstrom
kcal/mol	Kilocalories per mol
h	Hour
mins	Minutes
ºC	Degree Celsius
rpm	Rotations per minute
µm	Micrometer
kV	Kilo Volt
cm	Centimeter
K_{sv}	Stern-Volmer quenching constant
eV	Electron volt
ns	Nanosecond
θ	Theta
mV	Millivolt
τ_m	Mean lifetime value
ΔG	Free energy changes
T	Temperature
ϕ	Photoluminescence quantum yield
τ_f	Fluorescence lifetime
$\varepsilon_A(\lambda)$	Molar extinction coefficient of the acceptor (A) at wavelength λ
Q	Concentration of quencher

R_0	Förster distance
R^2	Regression coefficient
J(λ)	Overlap integral
$F_D(\lambda)$	Corrected fluorescence emission of the donor (D) in the wavelength range λ to λ+ Δλ
κ^2	Relative orientation factor of transition dipoles between donor and acceptor in an isotropic solution
k_{ET}	Rate of electron transfer
E	FRET efficiency
λ_{ex}	Excitation wavelength
F_0	Fluorescence intensity in the absence of quencher
F	Fluorescence intensity in the presence of quencher
ϕ_S	Sample solution fluorescence quantum yield
ϕ_R	Reference solution fluorescence quantum yield
η	Refractive index of the solvent
α	Relative amplitudes contributions of the different lifetime components
$I(t)$	Fluorescence intensity at time t
σ	Standard deviation of the intercept
K	Slope of the graph
K_1	Binding constant

Abstract

The thesis entitled “Deciphering changes in photophysical properties of carbon dots and protein conformations induced by bioactive molecules” is divided into five chapters.

Chapter-1

It describes the background information on proteins, biomolecules, bile salts, nanomaterials, nanosensor and deep eutectic solvents together with literature survey and scope of the work. This chapter provides detailed information on the significance of protein interactions with bioactive molecules (bile salts), carbon dots (CDs), its synthesis approaches, fluorescence mechanisms along with their optical properties and applications, newly emerged green deep eutectic solvents were also discussed. Are also discusses the various fluorescence quenching mechanisms of CDs in the presence of quenchers and their photophysical factors like UV-Visible absorption, steady state and time-resolved fluorescence studies, photostability, photoluminescence quantum yield, etc.

Chapter-2

Chapter 2 of the thesis includes a brief summary of the characterization techniques used in all of the experiments undertaken throughout the thesis. The widely used characterization techniques used includes UV-Visible spectroscopy, steady-state fluorescence spectroscopy, time-resolved fluorescence spectroscopy, high-resolution transmission electron microscopy (HRTEM), X-ray photoelectron spectroscopy (XPS), energy dispersive spectroscopy (EDS), attenuated total reflectance Fourier-transform infrared (ATR FT-IR) spectroscopy, Raman spectroscopy, grazing-incidence X-ray diffraction (GIXRD), and zeta potential measurements are among the most widely utilized methods for characterization. These are utilized to better understand the interactions between protein and bile salts, as well as to research the physical, chemical, and optical properties of biomass-derived carbon nanoparticles, along with their practical usefulness as a nanosensor as well as the underlying mechanism.

Chapter-3

Bile salts are physiologically-important natural amphiphilic biosurfactants synthesized in the liver and play a vital role in the solubilization and digestion of dietary lipids, cholesterol, and other fat-soluble compounds in the body. Bile salts also exhibit pharmacological and biological uses as

carriers for transporting poorly water-soluble drugs and other chemicals owing to their unique emulsifying, solubilizing capacities and micelle forming ability. In this context, we present an endeavour towards elucidating the interaction and binding between the most abundant plasma protein namely, human serum albumin (HSA) and bile salts to demonstrate an intriguing interplay of hydrophobic, electrostatic and hydrogen bonding effects using steady state absorption, fluorescence emission, anisotropy, time-resolved emission, and molecular modelling approaches. The outcome illuminates how amphiphilic interfaces of bile salts under various physico-chemical conditions trigger the conformational changes and binding affinities of native and molten-globule forms of HSA. To elucidate non-covalent interactions during HSA-bile salt supramolecular host-guest complex formation, changes in intrinsic (tryptophan) and extrinsic (ANS) fluorescence have been investigated. The results reveal upon binding of bile salts in subdomain IIA of HSA, the protein undergoes conformational changes mediated primarily by hydrophobic interactions. Furthermore, time-resolved fluorescence measurements provide important structural and dynamical insights into the protein-bile salt supramolecular complexes. Additionally, molecular docking studies on these complexes clearly reveal spontaneous binding of bile salts into subdomain IIA of HSA while suggesting that the binding affinity decreases with the decreasing order of hydrophobicity of the bile salts (NaDC>NaC>NaTC) (ΔGdock = -29.64 kJ mol^{-1}, -26.15 kJ mol^{-1}, -14.35 kJ mol^{-1}) respectively. This study exclusively highlights the molecular mechanism of conformational perturbation in native (pH 7) and molten-globule (pH 3) forms of HSA, induced by bile salts. We believe that the results reported herein will be helpful in the design and formulation of protein-bile salt-based pharmacological carriers suitable for drug delivery.

Chapter-4

Riboflavin (RF) detection is essential for controlling nutritional health due to its increasing significance in the food and pharmaceutical industries. Regular daily intake of RF (vitamin B_2) is important because it is not synthesized and stored in the human body in appreciable amounts. Therefore, an efficient and biocompatible nanosensor with good selectivity and sensitivity for RF detection is required. CDs derived from biomass have recently attracted interest in environmental science due to their simple, cost-effective methods of synthesis, as well as their sustainability advantages and practical implications. Herein, we demonstrate the utility of a ratiometric fluorescence-based CDs nanosensor for the detection of RF in its isolated, pure form as well as in

pharmaceutical tablets. We report the synthesis, characterization, and sensing potential of intrinsic nitrogen-functionalized carbon quantum dots (N-CDs) from Indian gooseberry (a renewable biomass precursor) using a microwave assisted pyrolysis method that involves a green methodology. High-resolution transmission electron microscopy (HRTEM) indicated that N-CDs are monodisperse with an average diameter of ~8.1 nm. Fourier-transform infrared (FTIR) and X-ray photoelectron spectroscopy (XPS) validated intrinsic nitrogen functionalization and the presence of amino, hydroxyl, and carboxyl groups on the surface of N-CDs. Further, X-ray diffraction (XRD), UV-Visible and fluorescence spectroscopy, and time-correlated single photon counting (TCSPC) measurements were also employed for the characterization of N-CDs. The as-prepared nanoprobe exhibits bright green emission with a remarkable fluorescence quantum yield of ~48%. Moreover, N-CDs are highly water-soluble and are extremely stable in a range of pH, ionic strength, and photoirradiation. Additionally, N-CDs selectively and specifically detect RF (vitamin B_2) in aqueous media w.r.t various bio-analytes with a limit of detection (LOD) ~35 nM. Our nanosensor can also detect vitamin B_2 present in commercially available pharmaceutical tablets with an LOD of ~61 nM. Mechanistic studies confirmed that sensing involves fluorescence resonance energy transfer (FRET) between RF and N-CDS interfaces. Overall, the present work provides a new vision for the development of an innovative and sensitive approach of a green fluorescent nanosensor for the detection of RF which may find potential applications in the pharmaceutical and food industries.

Chapter-5

The significant toxicity and environmental persistence of 4-nitrophenol (4-NP) create an urgent need for eco-friendly, effective detection methods. Due to its persistence, toxicity, and carcinogenicity, 4-NP has been classified by the U.S. Environmental Protection Agency as a primary pollutant. It commonly contaminates the environment, primarily as a byproduct of the pharmaceutical industry. In biological systems, 4-NP can cause significant damage to organs such as the liver and kidneys, impair central nervous system function, and contaminate the bloodstream. To address the challenge of 4-NP detection, the study introduces a novel and sustainable detection technique using nitrogen and chlorine co-functionalized carbon dots (abbreviated as S-CDs). The synthesis protocol was employed through hydrothermal method, using sucrose as a carbon

precursor and deep eutectic solvent (DES) composed of choline chloride and urea in a 1:2 molar ratio. The synthesized nanosensor exhibited brilliant green fluorescence under UV light, showed excellent water solubility, high photostability with a quantum yield value of ~56%. HRTEM analysis revealed that the S-CDs were spherical, monodisperse, and had an average diameter of 3.06 nm. FTIR and XPS analyses confirmed intrinsic nitrogen and chlorine functionalization, showing the presence of amino, hydroxyl, carboxyl, and chlorine groups on the surface of S-CDs. Further characterization of S-CDs included X-ray diffraction (XRD), ultraviolet-visible (UV-Vis) spectroscopy, fluorescence spectroscopy, and time-correlated single photon counting (TCSPC) studies. The nanoprobe exhibited high selectivity and sensitivity for 4-nitrophenol (4-NP), with a detection limit of 10 nM. Mechanistic studies verified an inner filter effect (IFE) mechanism between S-CDs and 4-NP, with significant spectral overlap and no change in average lifetime values, attributed to the formation of a zwitterionic spirocyclic Meisenheimer complex. Additionally, photophysical parameters, including quenching efficiency and binding constant, were also assessed to further understand the sensing mechanism. This work paves the way for developing a sensitive, green fluorescent nanosensor for rapid, cost-effective and environmentally friendly approach as well as on-site detection of 4-NP, offering a promising tool for pollution monitoring and control for environmental water samples.

Chapter 1

Introduction and Literature review

1.1 Introduction

1.1.1 Bioactive compounds and pollutants

Biologically-active compounds, also known as phytochemicals and bioactive compounds, are classified by consensus as "necessary and non-essential compounds that exist in nature, are part of the food chain, and can be seen to have an impact on human health."[1] These are derived from plants (vegetables, fruits, herbs, etc.) and are usually categorized as polyphenolics, carotenoids, glycosylates, and so on. Phenol compounds exhibit their beneficial effects through a variety of mechanisms such as free radical elimination, *etc*. Polyphenolics can be utilized for the development of natural therapeutic agents for the treatment of various diseases related to lifestyle, as they exhibit effective interactions with proteins, DNA, and numerous other biomolecules. They have been shown to improve public health and reduce disease risk.[1,2] However, using these compounds directly in food formulations or as a medication still remains a formidable task due to certain aspects such as inconsistency of environmental conditions (light and temperature), weakening formulation agents (pH, metal ions, and ionic strength), limited biostability, low solubility, etc. The encapsulation of bioactive compounds by inserting/immobilizing them into a carrier matrix is among the most efficient approaches to tackle the aforementioned issues such as targeted delivery, controlled release, and improved stability. Additionally, elucidating the molecular basis of protein-small molecule interactions (either natural or artificial) is important in the development of next generation, prevention-based targeted therapeutics.[3,4]

However, the body's capacity to absorb these bioactive compounds at a consistent pace and degree typically restricts their bioavailability. Nanoencapsulation technology enables the delivery of bioactive chemicals such as antioxidants, vitamins, and nutraceuticals into food products. Nanotechnology is a rapidly expanding and transformative field of study with unique features and a variety of uses, like in biological and biomedical fields. Significant advancements in nanotechnology over the last few decades have produced a wide range of fluorescent nanomaterials. Nano-sensors accurately identify different biomolecules as well as quantify contaminants, assuring food safety due to their unique features, including large surface-volume

ratio, superior sensitivity, selectivity, and flexible electrical as well as optical characteristics. Vitamins, being biologically active compounds, are essential for biochemistry and metabolism.[5-7] Of all the vitamins, water-soluble riboflavin (RF), sometimes referred to as vitamin B_2, is necessary for the body's cells to grow, develop, and function by converting carbohydrates, lipids, and proteins into energy. It cannot be produced in the body and has to be consumed through everyday diets. The vitamin B_2 level in the body is extremely important for human health.[8,9] It is also critical to develop sensors for the speedy and precise detection of Vitamin B_2 which have been done in chapter 4 of the thesis.

Further, anthropogenic environmental degradation poses a challenge to a clean, green, and sustainable environment. Hazardous chemical buildup pollutes the air, water, and soil, which has a major impact on all ecosystems. For the identification and cleanup of contaminants, biosensing technology has drawn a lot of interest. In addition, nanoparticles have been employed for on-site remediation and visual detection of antibiotics, organic colors, pesticides, contaminants, and heavy metals. Research is being done extensively on the specificity, sensitivity, and extremely low detection limit of nanosensors in complicated wastewater. In order to address recent water pollution issues and provide a healthy environment for both current and future generations, it is imperative that nanosensors be designed to detect developing pollutants.[10-12]

Among the quite hazardous and toxic phenols that can adversely affect human health as well as the environment, 4-nitrophenol (4-NP) stands out. Notably, 4-NP has a strong environmental impact and can reach humans via the food chain. Owing to its high toxicity, it has been added to the priority pollutants list by US Environmental Protection Agency's (USEPA) for contaminating water and the environment. In Chapter 5, we demonstrate an efficient analytical approach for rapidly detecting trace levels of 4-nitrophenol, which will eventually lead to effective pollution management and human health maintenance.[13]

1.1.2 Proteins

Proteins are the most prevalent and functional biological macromolecules, accounting for the majority of cell proportion (besides water). The polypeptides are involved in carrying out a wide range of functions e.g. enzyme catalysis, serving as structural elements, performing regulatory roles, cellular metabolism, and also as transporters carrying specific substances across a cell

membrane. These biomacromolecules are typically heteropolymers comprising various amino acids that are covalently connected to each other via amide/peptide bonds.[14] The linear polypeptide chain starts to fold into its three-dimensional form after it is synthesized by a ribosome from a sequence of mRNA. Molecular chaperones aid protein folding *in vivo* by binding and releasing the polypeptide in an ATP-dependent manner. Folding is a cooperative mechanism that happens when a high-energy, high-entropy state gives way to a low-energy, low-entropy one. According to the sequence-structure-function paradigm, a unique sequence of amino acids encrypts three-dimensional native structure regulated by a framework of structural organization created by the interaction of numerous non-covalent interactions (Figure 1.1).[14] For instance, the amino acids sequence that makes up the polypeptide chain is the primary structure while the secondary structure relates to the local/short-range, ordered spatial organization of short stretches of amino acid residues primarily mediated by hydrogen bonds. Depending on the form of hydrogen bonding, the secondary structure can be either α-helix or a β-pleated sheet. The hierarchical structural organization within the polypeptide chain leads to the formation of the globular, native, tertiary structure that entails the interaction of many non-covalent interactions, including hydrogen bonding, hydrophobic, and electrostatic interactions.

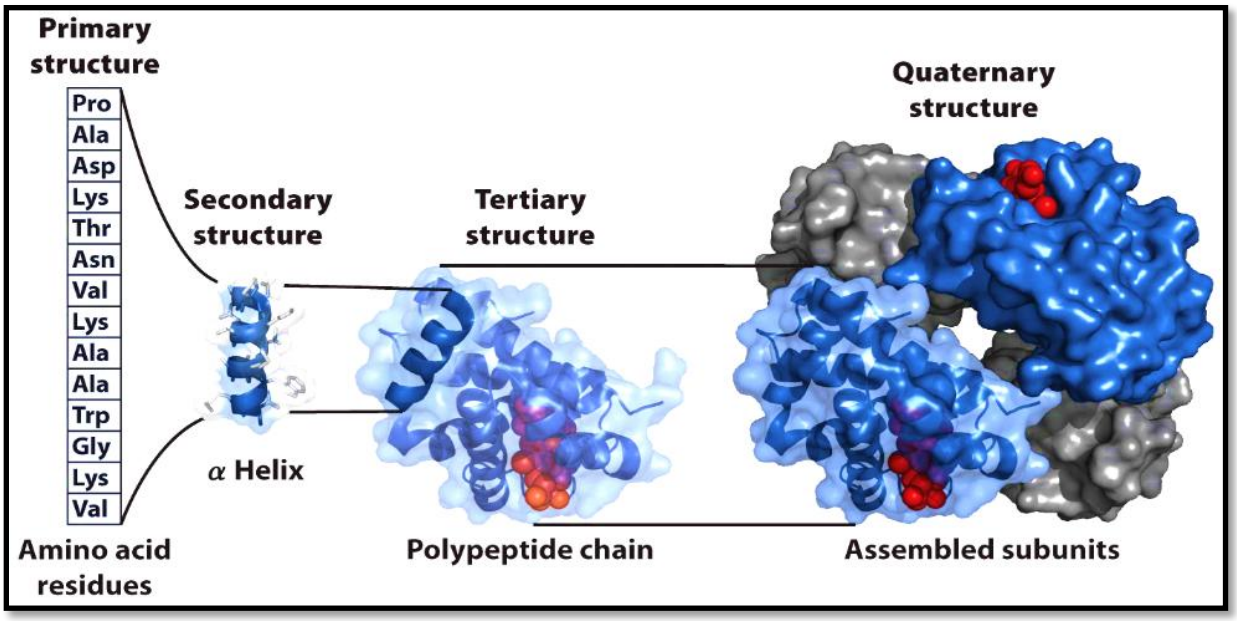

Figure 1.1. The structural hierarchy of proteins.[1]

A further arrangement of two or more polypeptide chains, in a three-dimensional array, might result in the development of a quaternary structure of a protein that is generally known as

comprising subunits. Although, all of the proteins or the polypeptide chains are composed from a basis set of same 20 amino acids, due to sequence heterogeneity, the structurally-diverse proteins exhibit strikingly different characteristics that result in their varied physico-chemical properties and functional roles. It is also well-documented that apart from these biomacromolecules, small molecules, biological metabolites such as vitamins, biosurfactants, steroid hormones, etc. play crucial roles in regulating protein functions, as ligands during allosteric binding, substrates and products during enzyme catalysis, signalling events, etc. They also act as important mediators during protein-protein interactions. Apart from these natural small molecules, another major class of these molecules are artificial, chemically-engineered drugs that are also known to modulate protein-protein interactions.[15,16]

1.1.3 Human serum albumin

Human serum albumin (HSA), often known as albumin, is a heart-shaped, globular protein that is frequently present in plants, milk, egg white, and blood plasma and is the most abundant plasma protein found in all vertebrates. The liver produces pre-pro-albumin, which develops in the endoplasmic reticulum and Golgi apparatus, and is then secreted by hepatocytes. Human serum albumin (HSA) is present in both the extravascular and intravascular compartments, with a plasma concentration that ranges from 35 - 50 mg/mL and an estimated half-life of 19 days. Three domains of about similar size make up a single polypeptide chain spanning 585 amino acids that makes up HSA. HSA has no β-sheets and is composed of 67% α-helices, 10% turns, and 23% random coils.[17,18] Three primary domains in albumin are revealed by high-resolution X-ray crystallography; commonly referred to as domain I (1–195 aa), domain II (196–383 aa), and domain III (384–585 aa) (Figure 1.2). Each domain is subsequently divided into two subdomains: A and B (Figure 1.2).[19,20] In general, serum albumins from various sources exhibits 62 percent sequence identity, with HSA and BSA showing 76% commonality at the sequence level. HSA has 17 intramolecular disulfide bridges, primarily between α-helices. The disulfide connections are essential for protein stability. Furthermore, it possesses a single free cysteine residue (Cys-34) found in domain I, that is conserved across many species.

It performs a number of essential tasks. It regulates the blood's pH levels as well as plasma oncotic pressure. Furthermore, it binds and transports a wide range of bioactive substances, including

amino acids, fatty acids, peptides, medicines, proteins, nutrients, and metal ions. These features make albumin a great option for a variety of clinical and biotechnological applications.[14-16]

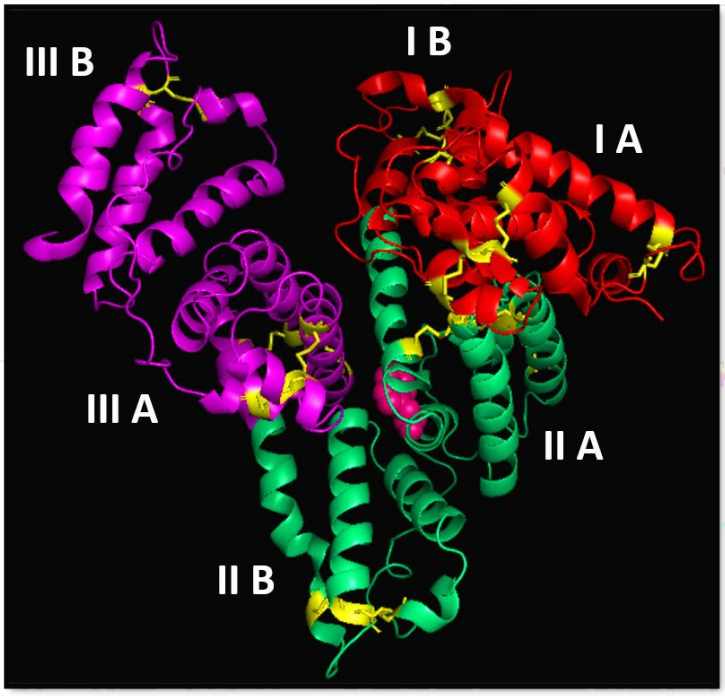

Figure 1.2. Ribbon diagram of Human serum albumin (PDB ID-1UOR) showing three domains (I; red, II; green, III; violet), disulfide bridges (yellow sticks), and single tryptophan (W214; hot pink), generated with PyMOL (Schrödinger Inc., New York).

1.1.4 Bile salts

Bile, an a yellow-greenish secretory and excretory fluid, is found in all animals, including humans. Bile salts are present in bile, which is produced in the liver via cytochrome P450-mediated oxidation of cholesterol and stored in the gall bladder.[21] A human adult secretes about 0.4 to 0.8 L of bile per day. Bile is a complex fluid comprising electrolytes, water, and phospholipids, cholesterol, and bilirubin which flow through the small intestine via the biliary tract.[22] Bile acid is comprised of cholic, deoxycholic, chenodeoxycholic, and lithocholic acids with the quantitative proportions as 12:7:13:1, respectively.[23] Bile salt corresponds to the deprotonated (-COO−) form of the molecule, whereas bile acid being the protonated (-COOH) form. Bile acids interact with taurine or glycine, producing a range of diverse bile derivatives. Although everyday significant volumes of bile salts are produced into the gut, only modest quantities are excreted from the human

body, since roughly 95% of the bile salts offered to the duodenum are absorbed back into the blood inside the ileum. According to this enterohepatic circulation mechanism, each bile salt molecule is "reused" around 20 times. They are essential for gallstone development and digestion in the physiological environment.[24]

Bile salts can be easily recognized by their hydrocarbon core, cyclopentanoperhydrophenanthrene, which has three rings with six members (A, B, and C) and one with five members (D) (Figure 1.3). Both synthetic and natural steroids are derivatives of this centre. The hydroxyl groups can be found at locations C_3, C_7, and C_{12} in either beta (β) or alpha (α) orientation. that differs based on the number, position, and stereochemistry.[25]

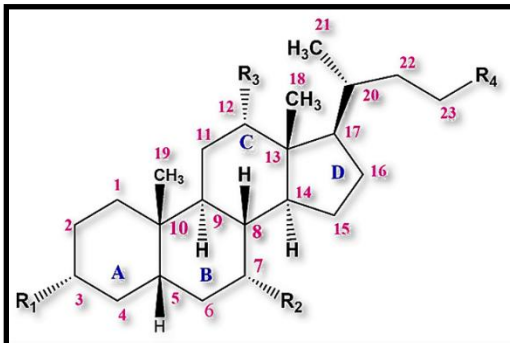

Bile-salts	R_1	R_2	R_3	R_4
Sodium cholate (NaC)	-OH	-OH	-OH	–COOH
Sodium taurocholate (NaTC)	-OH	-OH	-OH	$–CONHCH_2CH_2SO_3H$
Sodium deoxycholate (NaDC)	-OH	-H	-OH	–COOH

Figure 1.3. Schematic illustration of a bile salt's steroid backbone and nomenclature along with the position and orientation of hydroxyl groups.

Figure 1.4 displays the chemical structures of all the bile salts used in this thesis's second chapter, including sodium taurocholate (NaTC), sodium cholate (NaC), and sodium deoxycholate (NaDC).

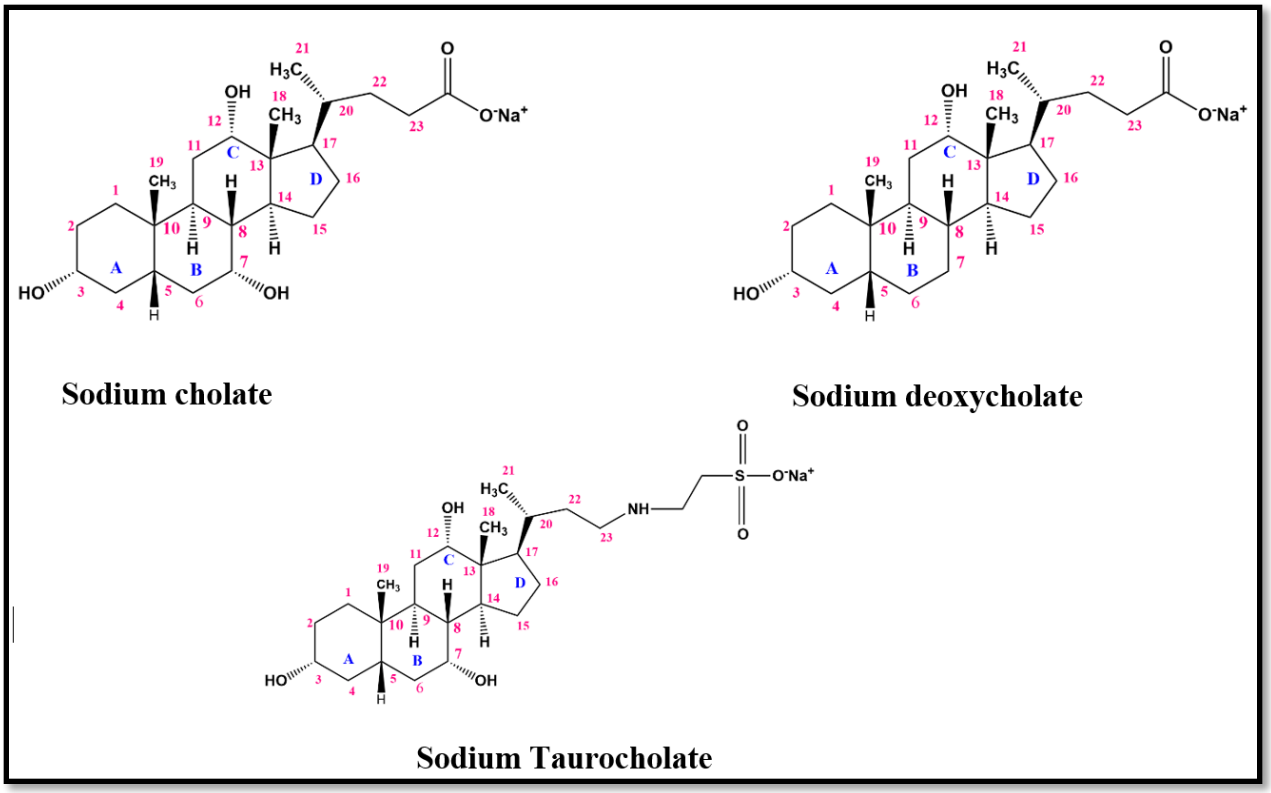

Figure 1.4. Chemical structures of sodium cholate (NaC), sodium deoxycholate (NaDC) and sodium Taurocholate (NaTC).

1.1.5 Difference of aggregation phenomenon between bile salts and conventional surfactants

Bile salt has a broad, stiff, and hydrophobic steroid nucleus with an ionic carboxyl head group and two to three hydroxyl groups which render the molecule with a dual facial polarity in both hydrophilic and hydrophobic domain compared to the conventional surfactants that contain a well-defined, distinct hydrophilic and hydrophobic region. Consequently, when distributed in an aqueous media, these amphiphilic molecules have a tendency to self-organize. The hydrophobic effect is the fundamental driving force for aggregation. They are also called bio-surfactants due to their micelle-forming ability.[23,26-28] Bile salts, like classical amphiphiles, create micelles at critical micellar concentrations. (*CMC*). Bile salt micelles are often smaller than normal surfactant micelles owing to the molecule's planar structure, which must isolate/protect the hydrophobic component from the aqueous phase.[27,28]

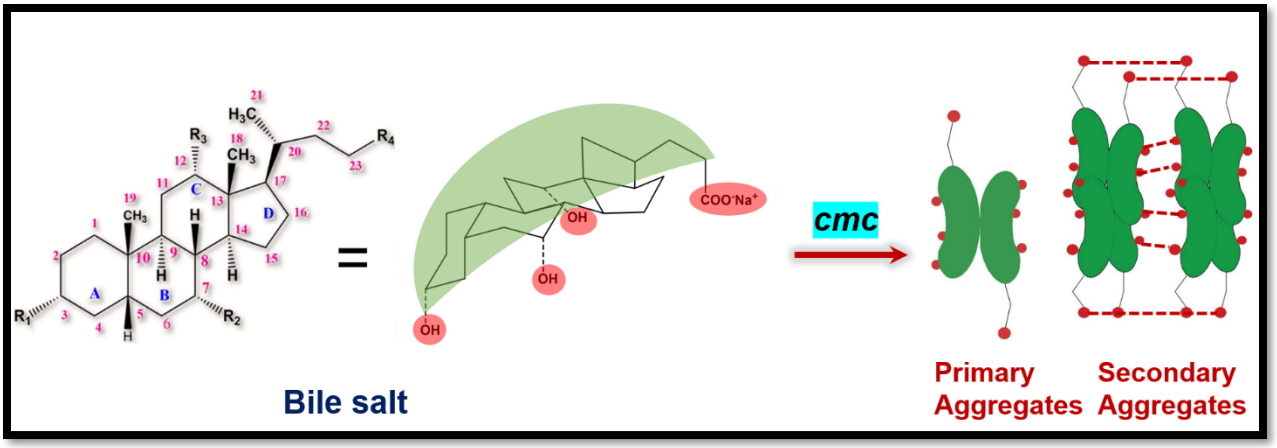

Figure 1.5. Schematic representation of bile salt's primary and secondary aggregates as proposed by Small model.

Numerous models[29-31] for the micellar structure of bile salts have been proposed by Small,[32,33] Kawamura *et al.,*[34] Giglio *et al.*[35,36] over the last five decades, the most renowned of which being the one suggested by Small (Figure 1.5). According to the Small model, primary aggregates comprising two to nine monomers form at low bile salt concentrations due to the hydrophobic convex surface of monomers.[37] These primary aggregates form secondary aggregates at higher concentrations with an extended rod-like shape and are stabilized by hydrogen bonds between the primary micelles' hydroxyl groups.[22,34]

Bile salts are essential for solubilizing and digesting dietary lipids, cholesterol, and other fat-soluble compounds in the body.[22] Their exceptional emulsifying and solubilizing properties make them valuable in cosmetics and various chemical formulations. Additionally, they have significant applications in biochemical and pharmaceutical fields.[23] More than half of all drugs exhibit poor water solubility.[26]The enterohepatic circulation of bile salts converts them into drug delivery systems, enhancing drug bioavailability by improving intestinal absorption and metabolic stability. These drugs dissolve well in bile salts, facilitating their transfer to targeted organs. The facial amphiphilicity of bile salts grants them unique binding specificity with various molecules, a property that is effectively utilized in the medicinal field.[27]

1.1.6 Nanomaterials

The term "Nano" originates from the Greek word "Nanos," meaning dwarf or extremely small. Nano means one billionth, or 10^{-9}. Nanomaterials range in size from 1 to 100 nm. Research on nanomaterials is a fascinating field with diverse biotechnological applications, from sensing to drug delivery. Their unique physical and chemical properties, attributed to a high surface-to-volume ratio and nanoscale size, make them highly valuable. The physicochemical characteristics of nanomaterials are influenced by their size, shape, and composition. As a result, nanomaterials exhibit variations in surface area, magnetism, quantum effects, thermal and electrical conductivity, and optical characteristics upon changing their size, shape and compositions. The size-dependent effect in nanomaterials is known as the quantum confinement effect (QCE), which occurs due to electronic transitions from the valence band to the conduction band. As a result, the optical properties of different sized nanomaterials impart variations in the colors due to difference of absorption in the visible regions.[38,39] Nanomaterials of carbon are comprised of nanotubes, carbon dots, fullerenes, carbon polymer dots[40] and others, which are relatively abundant in nature. Nanomaterials find applications across nearly every field of life, including diagnostics and drug delivery in the medical area, catalysts in chemical reactions (metal-based nano catalysts, quantum dots), fuels, optoelectronic devices, and also find its usage even in waste-water and dyeing industries.[41,42]

Nanomaterials are classified into four main categories based on the degree of spatial confinement, zero-dimensional (0D) nanomaterials where all dimensions are at the nanometre scale (e.g., carbon dots), one-dimensional (1D) nanomaterials where one dimension is at the nanometre scale (e.g., nanorods, nanowires), two-dimensional (2D) nanomaterials where two dimensions are at the nanometre scale (e.g., nanosheets, nanoplates, nano-coatings), three-dimensional (3D) nanomaterials where all three dimensions exceed 100 nm, with no electron confinement in any direction (e.g., nanoflowers, nanotubes).[43,44]

1.1.7 History and synthesis of carbon dots (CDs)

The most prevalent element in the universe is carbon. Its propensity for catenation and hybridization (sp^3, sp^2, sp) enables it to exist in a variety of allotropic forms, including graphite, amorphous carbon, graphene, diamond, and fullerenes. Each of these allotropes displays a wide

range of characteristics, some of which are completely opposite. For instance, diamond is an insulator in nature, but graphite conducts electricity. Owing to their unique and intriguing features, all of these materials has drawn a lot of attention. Carbon-based materials will play an increasingly essential role in future renewable energy conversion, storage, biofuel, and sensing applications.[45]

The current study is concentrated on the synthesis of diverse carbon-based materials, their characterization, and the development of applications in the domains of fluorescence sensing.[46-48] The potential of semiconductor quantum dots has been the subject of much research throughout the years.[49-51] However, the environment is seriously threatened by the heavy metals included in these quantum dots. Therefore, it is crucial to investigate alternative synthesis methods that may resolve these concerns, ensuring the safe and effective use of CDs in clinical studies, bioimaging, drug delivery, and similar applications. Fluorescent carbon nanoparticles have piqued researchers' interest due to their unique tunable properties, thermal stability, minimal cytotoxicity, good biocompatibility, low cost, ease of synthesis, chemical inertness, high solubility, relatively non-toxic nature, and ease of functionalization, along with their excellent fluorescence qualities to semiconductor quantum dots. Applications for CDs are growing in practically every scientific and technological domain, including cell imaging, organophosphate pesticide metal detection, sensor technology, and light-emitting devices, etc.[49,52]

Carbon dots (CDs) were discovered by chance in 2004 during the purification process of single-walled carbon nanotubes (SWCNTs). Two years later, in 2006, researchers successfully synthesized stable, photoluminescent carbon nanoparticles of varying sizes, naming them "carbon dots" or "CDs." As the latest addition to the nanomaterial's family, CDs are generally spherical, with an average diameter of less than 10 nm. They consist of both sp^2 and sp^3 hybridized carbon networks. Additionally, CDs can be easily functionalized with hydroxyl, carboxyl, carbonyl, amino, and epoxy groups on their surfaces, enabling interactions with both organic and inorganic substances (Figure 1.6). These functional groups allow CDs to exhibit either hydrophilic or hydrophobic properties, ensuring their stability in different solvents.[52]

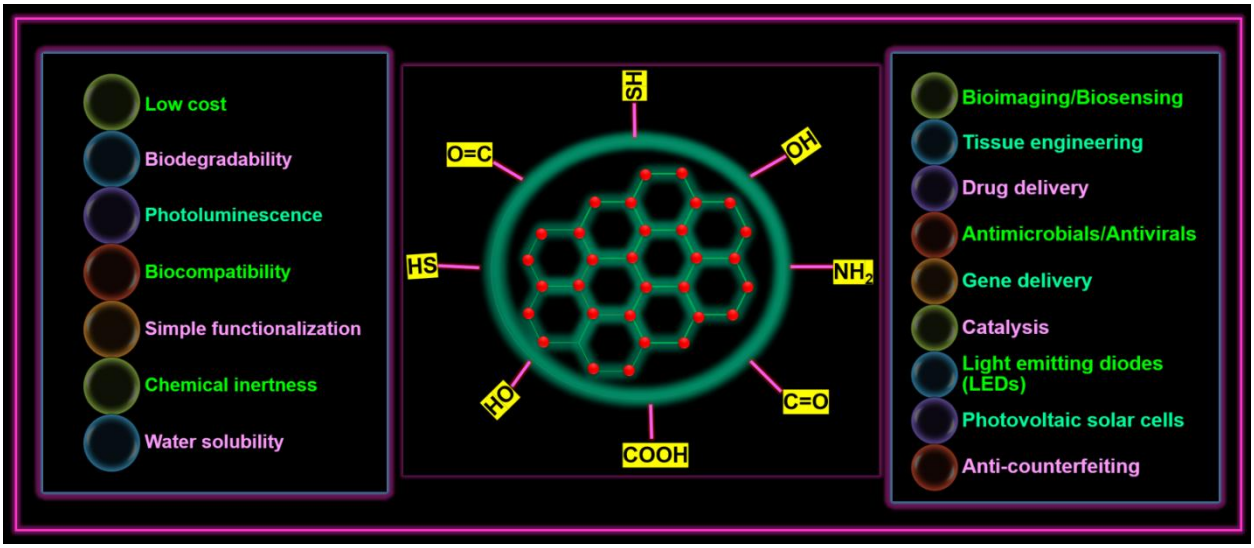

Figure 1.6. Structure of CDs, distinctive characteristics, and potential applications in numerous disciplines.

Since the development of CDs, many approaches for preparing CDs have been developed. In general, the synthesis of carbon dots (CDs) can be classified into two main categories: top-down and bottom-up methods (Figure 1.7).[53-55] Top-down processes involve the dispersion of macromolecules into small-sized CDs using physical, chemical, or electrochemical means. Typical top-down methods include electrochemical oxidation (electrolysis), laser ablation, sono-chemical synthesis, and arc discharge techniques. CDs produced via the bottom-up approach are created by carbonizing or pyrolyzing small organic precursors, nanosized particles are produced. As CDs grow, these organic molecules generally undergo four distinct stages: condensation, polymerization, carbonization, and passivation. In contrast, bottom-up methods typically use microwave irradiation and hydrothermal, or solvothermal treatment, etc.[53,56]

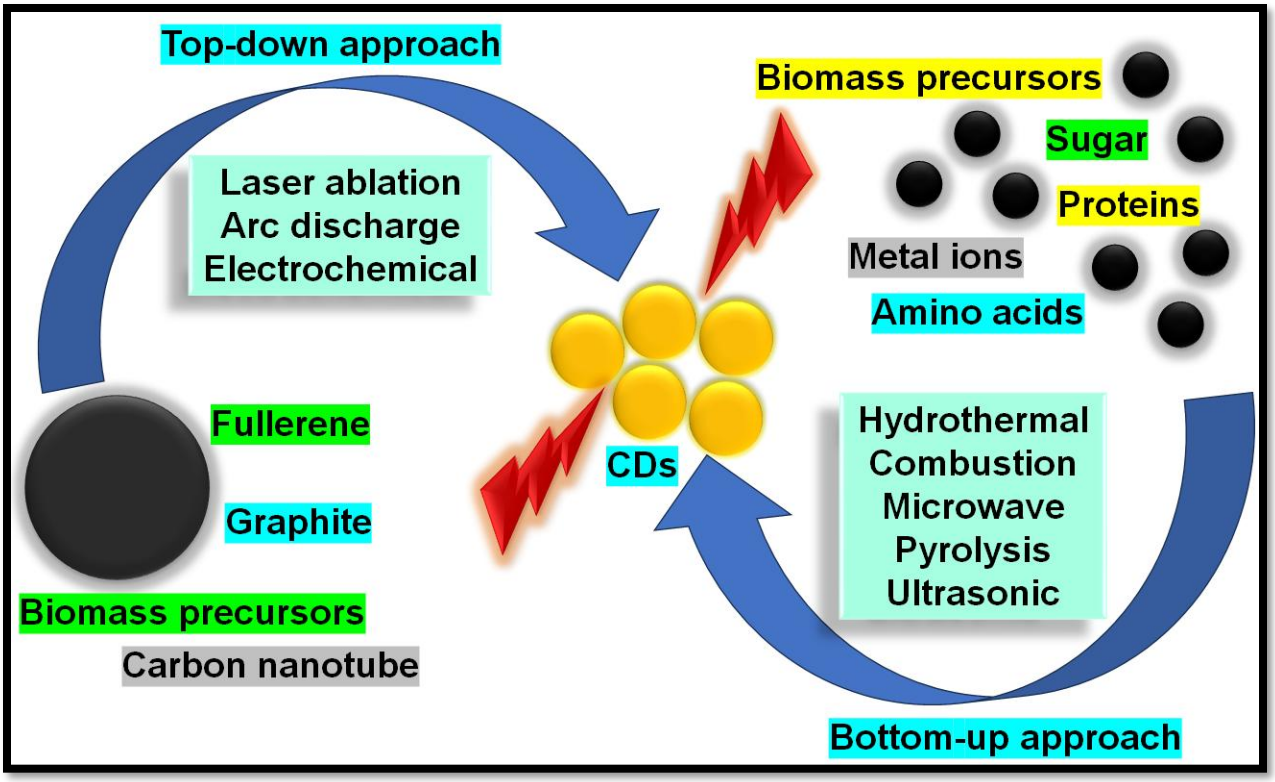

Figure 1.7. Schematic representation of utilized CDs synthesis.

Top-down approaches generally yield smaller flakes or particles with a broad size distribution, limited spectral efficiency, low product yield, and often require toxic chemicals or high temperatures. In contrast, bottom-up approaches produce uniformly sized particles, making them more suitable for biomedical applications. Although precise nanoparticle synthesis can be achieved using a focused ion beam or lithography, these techniques demand expensive equipment. Consequently, the bottom-up method is considered a simpler and more precise approach for synthesizing nanoparticles smaller than 100 nm, while the top-down method is preferred for producing thin films and nanoparticles exceeding 100 nm.[38,56,57]

1.1.8 Hydrothermal Synthesis

Hydrothermal/solvothermal synthesis is a commonly used method because it can generate large amounts of CDs with a high quantum yield while maintaining a simple experimental setup. This technique also allows for a broad temperature range, from room temperature to extremely high temperatures. Moreover, hydrothermal/solvothermal synthesis facilitates the production of nanomaterials under high vapor pressure conditions, enhancing yield. The morphology and

composition of the synthesized nanosensor can be regulated by adjusting the reaction's vapor pressure and utilizing liquid-phase or multiphase reactions. Generally, small organic precursors are either dissolved or dispersed (for polymers) in water, and the mixture is then placed in a Teflon-lined stainless-steel autoclave. Following this, the mixture undergoes high-temperature exposure to synthesize CDs.[53,58,59]

1.1.9 Microwave-Assisted Synthesis

The microwave-assisted technique is recognized as a rapid, eco-friendly, and cost-efficient synthesis method that adheres to green chemistry principles, making it a sustainable option. It has been extensively utilized for producing carbon-based nanomaterials, as microwave radiation facilitates uniform and rapid heating while exhibiting strong interactions with carbon materials.[58] An additional benefit of microwave-assisted methods is their ability to regulate internal and volumetric heating of materials. These techniques function by generating molecular-level heating through the interaction of alternating electric and magnetic fields with the dipole moment of polar molecules in a solvent. This process, known as dielectric heating, is responsible for the heat absorbed by the carbon precursors. Unlike conventional heating methods, microwave radiation directly penetrates target materials, generating thermal energy at the atomic and molecular levels, which ensures uniform and consistent volumetric heating. Microwave-assisted techniques are widely employed in green synthesis due to their efficiency in producing carbon-based nanomaterials within short reaction times, while also minimizing energy consumption and allowing precise control over reaction temperature.[58,60,61]

1.1.10 Optical properties and applications of carbon dots (CDs)

CDs synthesized from diverse carbon sources or through different methods consistently exhibit differing absorption properties. However, they often exhibit strong absorption in the ultraviolet (UV) region (200–400 nm), with a tail that extends into the visible region due to the presence of aromatic ring structures. The optical absorption peaks of CDs in the UV-visible region are typically attributed to the π-π* transitions of sp^2-conjugated carbon and the n-π* transitions arising from hybridization with heteroatoms such as N, S, P and others. Specifically, certain CDs with red or near-infrared (NIR) emission usually contain π-conjugated electrons within sp^2 domains and/or

attached surface groups or polymer chains, resulting in long-wavelength absorption in the 500−800 nm range. CDs absorption characteristics are principally determined by the types and amounts of surface groups, the size of π-conjugated domains, and changes in the oxygen/nitrogen concentration of the carbon cores. The characteristics can be altered through surface passivation or modification.[53,62]

Photoluminescence (PL) is one of the fascinating properties of CDs, making them valuable for both fundamental research and practical applications. Compared to other fluorescent materials-such as conventional quantum dots containing lead and cadmium, rare-earth nanomaterials, and organic dyes-CDs demonstrate superior light stability, higher quantum yields, lower toxicity, readily available low-cost sources, and outstanding biocompatibility.[53,63] A key characteristic of PL in CDs is its strong dependence on both emission wavelength and intensity. The precise origins of their fluorescence emissions remain a subject of debate, requiring further research for a clearer understanding. However, three primary mechanisms have been proposed: the quantum confinement effect, surface defect states, and the integration of fluorophores. The quantum confinement effect (QCE) occurs when CDs are smaller than the exciton Bohr radius. As the size of CDs decreases, the band gap energy between the conduction and valence bands increases, resulting in a blue shift in their photoluminescence. This shift leads to a band gap transition within the ultraviolet-visible region. Since the optical properties of CDs are closely linked to the π-electron state of sp^2 carbons, modifying the size of conjugated π-domains can either enhance or suppress the direct transition of conduction band electrons to the valence band, thereby influencing band gap fluorescence. In addition to the quantum confinement effect, surface defect states have also been identified as a possible fluorescence mechanism.[58,64]

Surface defects refer to a spheroidal region distinct from the carbon core of CDs, primarily formed as a result of surface oxidation. Surface defects typically function as capture centres for excitons, resulting in multicolour light emission and contributing to excitation-dependent behaviour. An increase in surface defects, which correlates with a higher level of surface oxidation, causes a red-shift in the emission wavelength. Additionally, the presence of surface functionalities another common factor contributing to CDs fluorescence, particularly when smaller molecules are used as starting materials in synthesis. These low molecular weight molecules readily form connections

during the synthesis process, potentially leading to the formation of fluorophores with aromatic structures.[58,64,65]

Additionally, various other luminescent properties of CDs—such as phosphorescence, two-/multiphoton fluorescence, electrochemiluminescence, photoinduced electron transfer (PET), and chemiluminescence-have been progressively discovered and explored. The diverse optical characteristics of CDs enable their wide range of applications, including sensors, information encryption, drug delivery, photocatalysis, and bioimaging. Due to their numerous advantages, such as low dosage requirements, low detection limits, broad linear range, ease of use, affordability, rapid response, simple preparation methods, and high accuracy, CDs have been extensively applied in environmental, pharmaceutical, clinical, and food analysis. Their small size, large specific surface area, and abundance of surface functional groups make them highly reactive and sensitive to environmental factors like temperature, ionic strength, and solvent composition. This sensitivity influences their optical properties, often resulting in fluorescence enhancement/activation (turn-on) or quenching (turn-off). To date, CDs have been utilized for detecting metal ions, anions, drug molecules, biomolecules, bacteria, pH levels, fingerprints, and more. Theoretically, their detection mechanisms primarily involve static and dynamic quenching, fluorescence resonance energy transfer (FRET), and the inner filter effect (IFE), which are further discussed below.[66]

1.1.11 Fluorescence quenching mechanism

The alteration in the fluorescence properties of CDs is driven by various molecular mechanisms.[67,68] The quenching of fluorescence in CDs is due to the interaction of biomolecules or metal ions with their surface functional groups. With the assistance of the energy-transfer pathway, this interaction leads to the development of new electron–hole recombination, which alters the carbon dot's fluorescence behaviour. Some of the mechanisms influencing fluorescence properties includes charge transfer, photoinduced electron transfer (PET), inner-filter effect (IFE), Förster (fluorescence) resonance energy transfer (FRET), static quenching, and dynamic quenching.[68]

Static quenching happens when a non-fluorescent ground-state complex forms through the interaction between CDs and a quencher. Upon absorbing light, the complex instantly returns to the ground state without emitting a photon. The formation of a ground-state complex alters the CDs absorption spectrum. Additionally, rise in temperature lessens the stability of the ground-state

complex, consequently reducing the static quenching effect. Dynamic quenching occurs when the excited state of CDs returns to the ground state as a result of collisions between the quencher and CDs, following either an energy transfer mechanism or a charge transfer mechanism.[69] Dynamic quenching differs from static quenching in multiple ways. The lifetime of CDs is altered in the presence of a quencher, whereas dynamic quenching only affects the excited states of the CDs, maintaining their absorption spectra unchanged. Additionally, a rise in temperature may boost the impact of dynamic quenching.[70]

1.1.12 Inner filter effect (IFE)

Inner filter effect (IFE) occurs when the absorption spectrum of a quencher in the detection system overlaps with the excitation or emission spectra of CDs. While IFE is often described as apparent quenching, it is not a true quenching phenomenon. Instead, it arises from the attenuation of the excitation beam or the absorption of emitted radiation due to either an excessive concentration of CDs or the presence of a quencher in the solution. This effect leads to a reduction in fluorescence intensity without affecting decay time. However, it should not be classified as quenching, as a secondary absorber is merely filtering the emission of a particle. IFE can also occur when the distance between the emitter and the re-absorber exceeds 10 nm. Since IFE is neither a static nor a dynamic quenching mechanism, the absorption peaks of CDs remain unchanged, indicating that no new substances are formed. As a result, the fluorescence lifetime of CDs remains unaffected.[70,71]

Furthermore, the Parker equation can be used to examine the IFE process as demonstrated below:[72]

$$\frac{F_{cor}}{F_{obsd}} = \frac{2.3dA_{ex}}{1-10^{-dA_{ex}}}\, 10^{gA_{em}}\, \frac{2.3sA_{em}}{1-10^{-sA_{em}}} \qquad (1)$$

where F_{obsd} is the observed fluorescence intensity and F_{cor} is the corrected fluorescence intensity after subtracting IFE from F_{obsd}. The absorbances at maximal excitation and emission wavelengths are denoted as A_{em} and A_{ex}, respectively. Further as shown in Figure 1.8a is the cuvette's width (d =1.00 cm), g indicates the distance between the edge of the excitation beam to the edge of the cuvette (g = 0.40 cm) and s indicates the thickness of the excitation beam (s = 0.10 cm). So, the effect of IFE increases as F_{cor}/F_{obsd} value rises.

1.1.13 Fluorescence resonance energy transfer (FRET) mechanism

The electrodynamic phenomenon known as FRET can be explained by classical physics. It takes place between a ground-state acceptor (A) molecule and an excited donor (D) molecule. Typically, donor molecules emit across shorter wavelengths that coincide with the absorption spectrum of the acceptor. Long-range dipole-dipole interactions among the donor and acceptor leads to energy transfer, which occurs in the absence of a photon. (Figure 1.8b, c).[70] Resonance energy transfer (RET) term is preferred since no photons are involved in the process. The quantum yield of the donor, the relative orientation of the donor and acceptor transition dipoles, the distance between the donor and acceptor molecules, and the degree of spectral overlap between the emission and absorption spectra of the donor and the acceptor all affect the rate of energy transfer. The Förster distance, typically between 20 and 60 Å, is the distance where RET is 50% efficient.[69,73] The donor-acceptor energy transfer rate (k_{ET}) is determined by:

$$k_{ET} = \frac{1}{\tau_{DA}} - \frac{1}{\tau_D} \qquad (2)$$

The average lifetime values for CDs with and without quencher are shown by τ_{DA} and τ_D, respectively. This occurs only when the emission spectrum of donor in the excited state overlaps with the absorption spectrum of acceptor in the ground state. For the FRET mechanism to take place, the distance between the donor and acceptor must be between 1-10 nm. In the FRET process, the average lifetime of donor decreases as the concentration of the quencher increases.[74,75]
Resonance energy transfer provides molecular information that is distinct from that disclosed by solvent relaxation, excited-state processes, fluorescence quenching, or fluorescence anisotropy.[69]

$$J(\lambda) = \frac{\int_0^\infty F_D(\lambda)\, \varepsilon_A(\lambda) \lambda^4 D\lambda}{\int_0^\infty F_D(\lambda)\, d\lambda} \qquad (3)$$

'$F_D(\lambda)$' is the corrected fluorescence emission of the donor (D) in the wavelength range λ to λ+ Δλ with the total fluorescence intensity (area under the curve), and '$\varepsilon_A(\lambda)$' is the molar extinction coefficient of the acceptor (A) at wavelength λ. Furthermore, the Förster distance (R_0) for the carbon dot and quencher pair is computed using the following equation:[69]

$$R_0 = 0.211[\kappa^2 \eta^{-4} \Phi_D J(\lambda)]^{1/6} \qquad (4)$$

The term 'κ^2' denotes the relative orientation factor of transition dipoles between the donor and acceptor in an isotropic solution. The κ^2 for an isotropic solution is assumed as 2/3, 'η'specifies the relative viscosity of the medium, 'ϕ_D' signifies the fluorescence quantum yield of the donor and 'J(λ)' is the overlap integral in a region of acceptor absorbance and donor emission spectra. Furthermore, to understand the nature of the electron transfer process, FRET efficiency (E) was computed using the following equation.[69]

$$E = \frac{k_{ET}}{k_r + k_{ET} + k_{nr}} \qquad (5)$$

Whereby 'k_{nr}' and 'k_r' are the non-radiative and radiative rate constants. Furthermore, the separation distance (r) between the carbon dot and the quencher is calculated from the respective FRET efficiency (E) values using the following formula:[69]

$$E = \frac{1}{1 + (\frac{r}{R_0})^6} \qquad (6)$$

We inferred that both FRET and IFE are involved in the quenching mechanisms of fluorescent CDs employed in the detection of analytes in this thesis.[69]

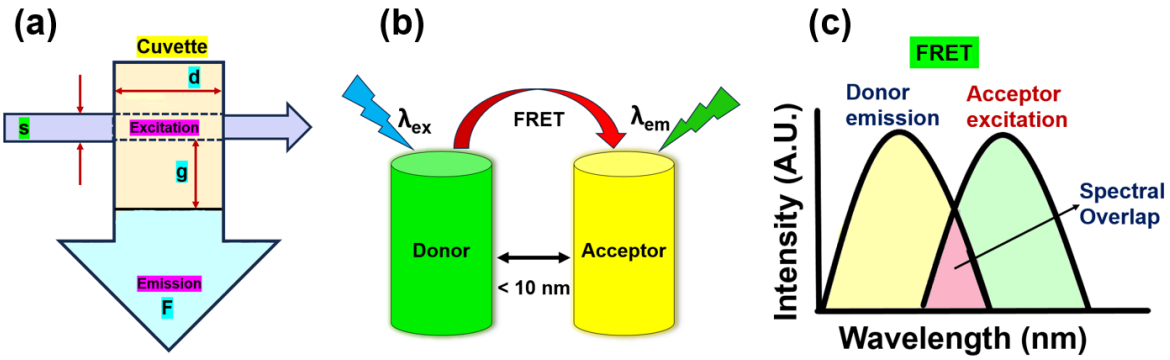

Figure 1.8. Schematic representation of (a) parameters used in Parker equation, (b) distance requirement for FRET, (c) spectral overlap indicating FRET.

1.1.14 Waste into wealth: Biomass derived CDs

Most researchers tend to focus on the utility of the resource, often overlooking the high costs and environmental impact of the precursors. The green chemistry approach aims to achieve sustainability at the molecular level. Given this objective, it is no surprise that it has been implemented across various industry sectors. From aerospace, automotive, cosmetics, electronics, energy, and household products to pharmaceuticals and agriculture, there are countless examples of successful, award-winning, and commercially viable inventions.[76] The 12 green chemistry principles were introduced in 1998 by Paul Anastas and John Warner, and serves as "design rules" to help chemists in achieving sustainability.[77,78]

Biomass-waste-derived CDs are a promising substitute to traditional CDs, which often call for expensive and toxic precursors. These biomass-derived CDs offer several advantages, such as eco-friendly synthesis, use of renewable sources, cost-effective production, and environmentally benign characteristics. As a green and sustainable precursor material, they facilitate the large-scale production of green CDs. Transforming biomass into value-added CDs is beneficial for solid waste management and aids in fostering the development of environmentally friendly initiatives for greener economy.[79]

Examples of biomass for CD synthesis includes animal products (including silkworm and chicken eggs), herbs and spices, vegetables, fruits, juice, fruit peels, residual kitchen trash (such as plant leaves and waste piece of paper and its derivatives.[80-82]

These carbon-based nanomaterials have been intensively researched in a variety of domains, including cancer treatment, regenerative therapy, drug/gene delivery, photocatalysis, tissue engineering, optoelectronics and sensing/imaging. Additionally, creating multipurpose CDs from biowaste that have a high efficacy-toxicity ratio for targeted and long-term drug administration and imaging capabilities opens up new opportunities for theranostic applications.[83]

1.1.15 Deep eutectic solvents (DES)

Sustainable and eco-friendly solvents have shaped recent advancements in the chemical industry, with deep eutectic solvents (DES) emerging potentially a viable sustainable platform. These DES offer a more viable and refined alternative to previous attempts, delivering an entirely new kind of

substance with excellent environmental and health qualities, low costs of production, minimal toxicity, and increased biodegradability.[84]

DES are a first kind of green solvent which are generally made of non-toxic substances and natural goods and are renewable. DES is a low-melting (eutectic) mixture comprising a hydrogen bond acceptor (HBA) and a hydrogen bond donor (HBD). Several HBAs and HBDs are represented in Figure 1.9. The compound's charge is delocalized and the lattice energy is reduced due to interactions between the donor and acceptor of the hydrogen bond; therefore, the melting point drops, which is why the combination is regarded as a deep eutectic solvent.[85]

DESs has great solubility and can dissolve a range of organic and inorganic substances to provide a stable dispersion system that guarantees flawless complex synthesis without any trouble. Further DES can be employed in the wide range of reaction circumstances, thus enabling their usage for the reaction at a low temperature and low pressure, so minimizing the risk of the operation. Last but not least, the components of DES can be modified to meet the needs of the synthesis, implying that the use of DES can provide more options for synthesizing functional materials. Thus, significant progress has been made in the design and implementation of DES.[86-88]

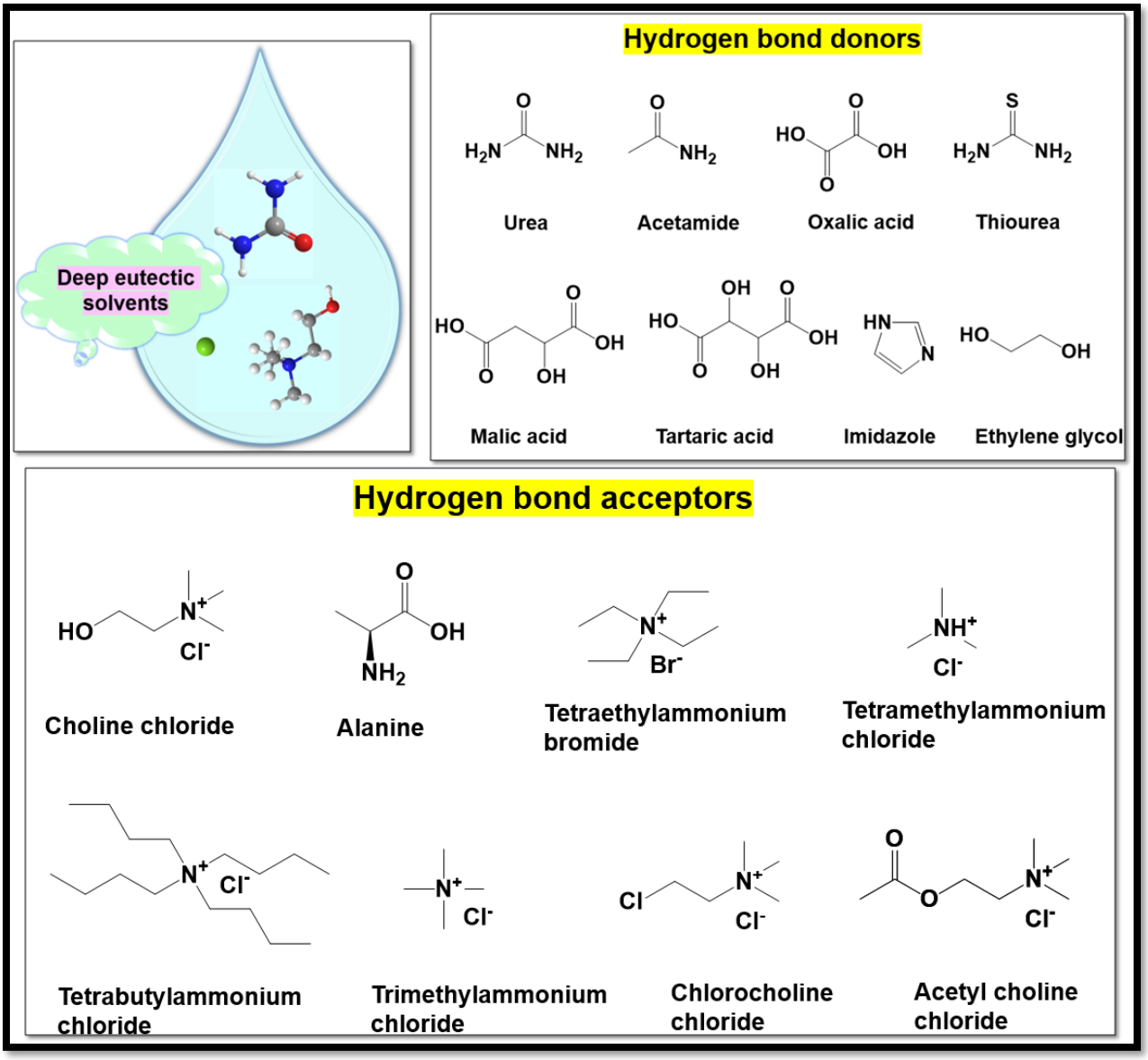

Figure 1.9. Schematic list of HBDs and HBAs for DESs synthesis.

The generic formula to describe deep eutectic solvents is $Cat^{+}X^{-}zY$, where X is a Lewis base, often a halide anion, and Cat+ is an, phosphonium, ammonium or sulfonium cation. X- and a Brønsted or Lewis acid Y produce complex anionic species, with z being the number of Y molecules engaging with the anion. The majority of research has focused on imidazolium and quaternary ammonium cations, with a special focus on more useful systems, especially those that use choline chloride [ChCl, $HOC_2H_4N^{+}(CH_3)_3Cl^{-}$] (Figure 1.9). [89]

1.1.16 Preparation of DES

The development of DES has been tightly linked to component interactions, yet the exact mechanism is still unknown. Most views suggest that the main mechanism causing the production of DES is hydrogen bonding among the halide salt anion and HBD. Because hydrogen bonding lower the constituent molecules' lattice energy, the combination has a lower point of melting and liquid phase.[79] Dai et al. used nuclear magnetic resonance spectroscopy to discover hydrogen bonds in DES and found that water plays an integral role in their creation. The influence of compound structure on the formation and stability of DES was studied, and it was revealed that the number of HBD or HBA, along with the location of the bonds all had important impacts.[91]

DES are produced via vacuum evaporation, freeze drying, and heating. Heating can be used to create DES whose components are dry chemicals with high thermal stability. The HBD and HBA are mixed in an ideal molar ratio at a particular temperature (50-100°C) and spun until a homogenous clear liquid appears. Evaporation can be used to produce DES if its individual components are heat-sensitive. The DES elements are allowed to dissolve in water and then evaporated under vacuum. The freeze-drying technique dissolves individual thermally unstable compounds at proper molar ratios in aqueous solutions. After that, the mixture is freeze-dried for a minimum of twenty-four hours to ensure that the weight stays constant.[92]

1.1.17 Classification, properties and applications of DES

DES are primarily classified based on the basis of complexing agent employed. Most DES prepared and studied till date fall into the following categories: Type I involves the combination of a metal chloride and a quaternary ammonium salt, type II involves the combination of a metal chloride hydrate and a quaternary ammonium salt; type III is composed of a HBD and a quaternary ammonium salt as HBA, usually an organic molecule like an amide, carboxylic acid, or polyol, type IV is composed of a metal chloride hydrate and an HBD, and type V is a relatively new class that only includes non-ionic, molecular HBAs and HBDs. Type III of DES is extensively studied throughout this thesis. These DES primarily consist of choline chloride combined with HBDs such as carboxylic acids, carbohydrates, amides, and others. Owing to their ability to solvate an array of transition metal species, these DES types are very significant. They are inexpensive, mostly biodegrade, simple to make, and reasonably stable in water. For the preparation of this class of DES, an enormous amount of HBDs is available (Figure 1.9). The physical properties of this type

of DES depend on the nature of the hydrogen bond donor and can be easily tailored for specific applications.[89,93]

The fundamental physicochemical properties of a material are paramount in all research fields and more so in the development of relatively new field of DES. DES are frequently employed as potential solvents in industries due to their diverse properties, including, freezing temperature, viscosity, miscibility, conductivity, surface tension density and polarity. Furthermore, a large variety of DES can be created using various combinations of HBA and HBD, making DES more designable, hence the term designer solvents. In addition to the variety of HBA to HBD, the molar ratio, purity, temperature, water content, and preparation method of HBA and HBD all have an impact on the physical and chemical characteristics of DES. The investigation of DES' physiochemical characteristics is related to their utilization as solvents for chemical operations.[86,94]

DES have been extensively employed in extracting flavonoids, saponins, polysaccharides, alkaloids, phenolic acids, quinones, essential oils, and other bioactive compounds from natural sources. It is evident that optimized DES outperform traditional methods in extracting these active ingredients.[95]

Deep eutectic solvents (DES) can dissolve a range of bioactive compounds that are otherwise insoluble, while also enhancing their chemical stability. Additionally, DES enhance oral absorption and increase the solubility of phytonutrients through hydrogen bonding, thereby improving oral bioavailability.[84,96] The development of bioactive eutectic systems including active principles expands the potential of these systems and offers up new avenues for future development in pharmaceutical and biological applications.[97]

It is also worth noting that DES can be utilized in a variety of other applications, demonstrating the mixture's incredible adaptability. DES have been effectively utilized to stabilize many types of samples prior to analysis while avoiding interference with the procedures. Furthermore, several studies have proved the utility of DES as antibacterial agents in the development of various candidate materials for medicinal applications. More recently, DES have been created for usage as nanocarriers for the encapsulation of anticancer medicines in order to prevent and treat breast cancer. In addition, DES can function as therapeutic agents on their own.[96,98]

1.2. Literature review

Mukherjee and coworkers in 2015[99] examined the interaction between HSA-bile salt (NaC, NaTC, NaDC) with the help of UV-Vis spectroscopy, isothermal titration calorimetry (ITC) along with circular dichroism, steady-state and time-resolved fluorescence, and molecular docking studies. Results obtained from the steady-state fluorescence experiments revealed that the interaction of bile salts with HSA can be characterized by three distinct regions in a sequential manner. The time-resolved fluorescence characteristics of the HSA Trp residue were also investigated to validate steady-state findings. Using circular dichroism, the effect of interaction with the bile salts on the protein native conformation was explored, which demonstrated a rise in the hydrophobicity around the sole tryptophan residue, with a concomitant decrease in the α-helical content of HSA induced by bile salts. The molecular docking studies indicated that bile salts bind in the HSA subdomain IIA, and coupled with the ITC data, it was inferred that the binding event is entropically-driven and hence, spontaneous. All of the findings, including esterase activity assays and acrylamide quenching experiments, suggested that the degree of HSA-bile salt interaction is directly proportional to the hydrophobic nature of bile salt.

The interactions between β-casein micelles (β-CMs) and biosurfactants i.e. bile salts (NaDC and NaC) in terms of self-assembling and structural behaviour have been studied using steady-state and time-resolved fluorescence spectroscopy, fluorescence correlation spectroscopy (FCS), and dynamic light scattering (DLS) at a physiological pH (pH 7.4). The change in critical micellar concentration (*CMC*) of β-CMs in the presence of NaDC and NaC was determined by taking pyrene as a fluorescent probe. FCS studies also suggested structural dynamics by measuring the translation diffusion of R6G in β-CMs in the presence of NaDC and NaC. The main driving force for the mixed self-assembly formation is the hydrophobic interactions and hydrogen bonding between bile salts and β-CMs. Overall, these results suggest that NaDC, upon complexation with β-CMs, forms larger aggregates than NaC due to its enhanced hydrophobic nature than that of NaC.[100]

In 2018, Selvam and coworkers[101] investigated whether bile salts could be utilized as protein stabilizers. BSA was used as a model protein, and bile salts namely, NaC and NaDC were used, which differ in their hydrophobicity. The changes in the absorption as well as intrinsic tryptophan fluorescence of BSA was monitored using both steady-state and time-resolved fluorescence

measurements. Analysis of both absorption and fluorescence spectral signature revealed that the BSA-bile salt interaction is hydrophobic in nature, and follows a three-step model of BSA-bile salt association. The pre-formed BSA-bile salt systems were subjected to both urea (a chemical denaturant) and various temperature (a physical denaturant). The hydrophobic nature of the BSA-bile salt complex was suggested to play a key role in stabilizing the conformation of BSA which prevents a greater degree of conformational unfolding in the presence of urea and during thermal denaturation.

Xu and coworkers in 2015[102] studied the interaction between sodium deoxycholate (NaDC) and bovine serum albumin (BSA) and gelatin using surface tension, fluorescence, and circular dichroism (CD) techniques. At a low concentration of surfactant, both NaDC/BSA and NaDC/gelatin systems shows the lowering of surface tension of water. However, a comparison between these two systems indicated that the potential of NaDC/BSA to lower surface tension is greater than that of NaDC/gelatin. NaDC, being a facial amphiphile with both polar and nonpolar faces, can interact with gelatin and BSA primarily through hydrophobic interactions, hydrogen bonding, and steric effect. The formation of complexes affects the polarity of the systems microenvironment which is manifested in the changes of their fluorescence spectra. The changes in far-UV CD spectra indicated that upon increasing the concentration of NaDC, the α-helical content of BSA increases followed by a decrease, whereas, the random coil content of gelatin keeps on increasing. Furthermore, comparisons of the properties of NaDC/BSA and NaDC/gelatin systems show that the influence of NaDC on the protein properties is strongly dependent on the intrinsic structures of proteins.

Zhao *et al.*[103] developed a simple and environmentally-friendly method for synthesizing CDs from mussels. The developed CDs were examined for their chemical makeup and optical characteristics at different reaction temperatures (140, 160, and 180 °C). As the reaction temperature rose, it was found that the luminous CDs' average size shrunk from 2.06 to 1.30 nm with a fluorescence quantum yield ~15%. These CDs possess extensive number of functional groups including -OH, $-NH_2$, and -COOH on their surface, resulting in good water solubility and biocompatibility. Moreover, the zebrafish, $HepG_2$ cells, and onion endothelium cells were successfully imaged using the mussel-derived CDs in bio-imaging applications. CDs could be used as a biosensor to detect

riboflavin. Consequently, mussels offer a viable carbon source for making N-doped CDs that can be used for riboflavin monitoring and bioimaging.

Joh and colleagues[104] established a straightforward and environmentally-friendly hydrothermal approach for producing CDs from the rhizomes of Acorus calamus. The designed CDs were utilized in four distinct applications including the catalytic reduction of rhodamine B (Rh B) and sunset yellow (SY), the fluorescence detection of morin, the use of fluorescent ink for writing and drawing, and research on apoptosis and anticancer employing SKMEL-28 human skin cancer cell lines. Various characterization techniques were used to investigate optical, structural, and morphological features. The CDs had an average particle size of 6 nm and emitted blue fluorescence when exposed to UV radiation. Based on static and inner filter effects (IFE), the developed nanosensor demonstrated good selectivity for morin, with a detection limit of 96 nM. Using a $NaBH_4$-carbon dots mixture, the ionic dyes Rh B and SY were catalytically reduced in seconds. The process followed pseudo-first-order kinetics and had a rate constant of 0.0116 min^{-1}. CDs demonstrated anticancer activity in SKMEL 28 cell lines, with a low LD50 value of 102 µg/mL. Thus, this study highlights the many practical applications of CDs and highlights their versatility.

Kundu *et al.*[105] illustrated the synthesis of green-emissive and intrinsically nitrogen doped CDs with exclusive chemosensing properties using orange pomace as a precursor based on biomass utilizing a simple microwave-assisted approach with no chemicals. The synthesized CDs' average size was found to be 7.5 nm. The manufactured CDs demonstrated luminous quantum yield of approximately 54%, aqueous solubility, and high photostability. The produced CDs showed encouraging results for the detection of 4-nitrophenol (4-NP) and Cr^{6+} ions having detection limits of 14 nM and 59.6 nM, respectively. The synthesized CDs showed fluorescence quenching with increasing concentration of quencher, which is explained via inner filter effect. Real sample analysis was also conducted to evaluate the effectiveness of the detection strategy. The study paves the way for utilizing orange pomace, a biowaste precursor, to produce CDs with improved properties.

The study by Fu and colleagues[106] described a novel method for developing a sensitive and effective ratio fluorescent probe for ciprofloxacin (CIP) detection. The technique employed a hydrothermal approach to manufacture blue fluorescent carbon quantum dots (b-carbon dots) with

an average size of 3.29 nm and a quantum yield of ~20% using the biomass materials passionfruit shell and diethylenetriamine as carbon and nitrogen sources, respectively. The newly constructed b-carbon dots/riboflavin ratio fluorescent probe offers an advantage for CIP monitoring, with a low detection limit of 0.86 μM. The b-Carbon dots' excellent selectivity, broad detection range, low detection limits, and high quantum yield highlight their significant potential in the development of more sophisticated sensing probes for efficient ciprofloxacin detection, providing promising insights for future sensor technology advancements.

Raveendran and colleagues[107] reported CDs synthesis from mint leaf extract (M-CDs) using a green process and used them for an array of applications. M-CDs were employed for sensing of physiologically significant folic acid via a quenching reaction triggered by inner filter effect, having a lowest detection limit around 280 nM. The CDs demonstrated high selectivity for folic acid among a group of 16 biomolecules. In addition to sensing, M-CDs has been proposed as an environmentally friendly reducing agent by showcasing their ability to reduce Fe (III) and synthesize noble metal nanoparticles from their salt solutions. The 3-(4,5-dimethylthiazol-2-yl)-2,5-diphenyltetrazolium bromide (MTT) test, carried out on primary H8 cells, revealed that the particles were notably non-cytotoxic. Additionally, HeLa cells were employed to illustrate the utility of M-CDs for multicolour imaging.

Xin *et al.*[108] created nitrogen-doped carbon quantum dots (N-Carbon dots), a novel green fluorescent probe material, by employing acetamide-glycolic acid DES (AGADES) as a modifier and walnut green skin as a carbon source. The resulting N-Carbon dots show a uniform distribution of particle sizes and a quantum efficiency of fluorescence that has increased from around 12% to 32%. The linear detection limit for Pb^{2+} is 1.55 nM within the concentration range of 0.01 to 1000 μM. This study successfully detects and recovers Pb^{2+} in real water bodies, introducing novel strategies to identify the presence of heavy metal ions.

In a recent study, Yin and colleagues designed[106] DES assisted N, Cl co-doped carbon dots (N, Cl-CDs) via hydrothermal procedure. This fluorescent probe was employed for selective and sensitive morphine measurement in food, and it had an outstanding quantum yield of about 14%. Additionally, the impact of analogues, interfering substances, system temperature, solution pH, on the morphine detection was investigated. When morphine was added, the CDs luminescence intensity grew linearly under optimal conditions, within concentration range of 0.15–280.25 μg

mL^{-1} the detection limit was 46.5 ng mL^{-1}. These results suggest that N, Cl-CDs is a suitable fluorescent probe for the sensitive and selective assessment of morphine.

1.3. Research gaps

According to the literature review, a few research gaps were recognized:

(1) In-depth understanding of the molecular level interaction of the protein–biosurfactant system under diverse solution conditions is scarce and needs to be explored further.

(2) The changes in free concentration, metabolism, distribution, and many other characteristics of biologically active compounds when they bind to proteins remain restricted under various circumstances.

(3) The structural changes in proteins in the presence of a variety of bioactive chemicals under various pH, temperature, and other environments were seldom reported and poorly understood.

(4) There are very few reports available on the synthesis of fully biomass derived carbon dots without addition of any chemical reagent.

(5) Limited literature reports are available on the deep eutectic solvent assisted caron dots.

(6) Very few reports were present on nanosensor that are cost effective, simple and sustainable indulging green chemistry principles with limit of detection for the detection of biomolecules and pollutants in the nanomolar range.

(6) There are only a few studies found that explains all the photophysical parameters of carbon dots.

(7) Nanosensor for the selective and sensitive detection of RF (Vitamin B_2) in aqueous as well as at physiological pH at nanomolar range.

1.4. Objectives

Based on the above research gaps, the following are the thesis's precise objectives:

1) To investigate the effects of biosurfactants on protein conformations under various solution conditions.

2) To elucidate the interactions between various biologically-active molecules (bile salts, flavonoids, etc.) and structurally-diverse proteins.

3) To gain molecular insights into interactions between biomolecule/bioactive molecule/pollutants and fluorescent nanomaterials.

References

1) Zlabur, J. S.; Voca, S.; Brncic, M.; Brncic, S. R. New trends in food technology for green recovery of bioactive compounds from plant materials. *Role of Materials Science in Food Bioengineering.* **2018**, 1-36. https://doi.org/10.1016/B978-0-12-811448-3.00001-2
2) Khashayar, Sarbandi K.; Gharehbeglou, P.; Jafari, S. M. Chapter Three-Scanning electron microscopy (SEM) of nanoencapsulated food ingredients. *Characterization of Nanoencapsulated Food Ingredients* **2020***, 4,* 83-130. https://doi.org/10.1016/B978-0-12-815667-4.00003-1
3) Kumar K. Nutraceutical potential and utilization aspects of food industry by-products and wastes. *Food Industry Wastes* **2020**, 89-111. https://doi.org/10.1016/B978-0-12-817121-9.00005-X
4) Chatterjee, S.; Mukherjee, T. K. Insights into the morphology of human serum albumin and sodium dodecyl sulfate complex: A spectroscopic and microscopic approach. *J Colloid Interface Sci.* **2016**, *478*, 29-35. https://doi.org/10.1016/j.jcis.2016.05.055
5) Pugazhendhi, A.; Alshehri, M. A.; Kandasamy, S.; Sarangi, P. K.; Sharma, A. Deciphering the importance of nanoencapsulation to improve the availability of bioactive molecules in food sources to the human body. *Food Chem.* **2025**, *464*, 141762. https://doi.org/10.1016/j.foodchem.2024.141762
6) Ji, A.; Hamid, A.; Andrabi, S. A. H.; Haq, E. Tombuloglu, H. Chapter eight - Interaction of nanoparticles with biomolecules. *Molecular Impacts of Nanoparticles on Plants and Algae* **2024**, 143-157. https://doi.org/10.1016/B978-0-323-95721-2.00008-7
7) Sargazi, S.; Fatima, I.; Kiani, M. H.; Mohammadzadeh, V.; Arshad, R.; Bilal, M.; Rahdar, A.; Díez-Pascual. A. M; Behzadmehr, R. Fluorescent-based nanosensors for selective detection of a wide range of biological macromolecules: A comprehensive review. *Int. J. Biol. Macromol.* **2022**, *206*, 115-147. https://doi.org/10.1016/j.ijbiomac.2022.02.137

8) Luo, Y.; Guo, Y. Nanomaterials for fluorescent detection of vitamin B_2: A review. *Anal. Biochem.* **2023**, *683*, 115351. https://doi.org/10.1016/j.ab.2023.115351

9) Kalaivani, A.; Babu, R. S.; Narayanan, S. S. Highly Sensitive Sensor for the Determination of Riboflavin Using Thionine Coated Cadmium Selenide Quantum Dots Modified Graphite Electrode. *Micro.* **2023**, *3*, 686-698. https://doi.org/10.3390/micro3030048

10) Yadav, N.; Grag, V. K.; Chhillar, A, K. Rana, J. S. Detection and remediation of pollutants to maintain ecosustainability employing nanotechnology: A review. *Chemosphere* **2021**, *280*, 130792-130815. https://doi.org/10.1016/j.chemosphere.2021.130792

11) Mehta, J.; Dilbaghi, N.; A.; Hai, F. I.; Hassan, A. A.; Kaushik, A.; Kumar, S. Plastic waste upcycling into carbon nanomaterials in circular economy: Synthesis, applications, and environmental aspects. *Carbon* **2025**, *234*, 119969. https://doi.org/10.1016/j.carbon.2024.119969

12) Singh, H.; Kumar, D.; A.; Puri, S.; Khatri, M.; Bhardwaj, N. Fluorescent nanosensors for detection of microbial toxins in food matrices: a review. *Food Measure.* **2024**, *18*, 7669–7699. https://doi.org/10.1007/s11694-024-02757-7

13) Khan, K. O.; Assiri, M. A.; Irshad, H.; Rafique, S.; Khan, A. M.; Khan, A. K.; Imran, M.; Shahzad, S. A. Fluorescence based detection of industrially important and hazardous 4-Nitrophenol in real Samples: A combination of Extensive optical and theoretical studies. *J. Photochem. Photobiol. A Chem.* **2023**, *442*, 114805. https://doi.org/10.1016/j.jphotochem.2023.114805

14) Cox, M.; Nelson, D. L. *Lehninger Principles of Biochemistry*; 5th Ed., WH Freeman, **2008**.

15) Voet, D.; Voet, J. G.; Pratt, C. W. *Principles of Biochemistry*, 4th Ed., John Wiley & Sons, Inc. **2013**.

16) Chiti, F.; Dobson, C. M. Protein misfolding, amyloid formation, and human disease: A summary of progress over the last decade. *Annu. Rev. Biochem.* **2017**, *86,* 27–68. https://doi.org/10.1146/annurev-biochem-061516-045115

17) Mishra, V.; Heath, R. J. Structural and biochemical features of human serum albumin essential for eukaryotic cell culture. *Int. J. Mol. Sci.* **2021**, *22*, 8411. https://doi.org/10.3390/ijms22168411

18) Bhattacharya, A.; Bhowmik, S.; Singh, A. K.; Kodgire, P.; Das, A. K.; Mukherjee, T. K. Direct Evidence of Intrinsic Blue Fluorescence from Oligomeric Interfaces of Human Serum Albumin. *Langmuir* **2017**, *33*, 10606–10615. https://doi.org/10.1021/acs.langmuir.7b02463

19) He, X. M.; Carter, D. C. Atomic structure and chemistry of human serum albumin. *Nature.* **1992**, *358*, 209-215. https://doi.org/10.1038/358209a0

20) Sugio, S.; Kashima, A.; Mochizuki, S.; Noda, M.; Kobayashi, K. Crystal structure of human serum albumin at 2.5 A^0 resolution. *Protein Eng.* **1999**, *12*, 439-446. https://doi.org/10.1093/protein/12.6.439

21) Garidel, P, Hildebrand, A.; Knauf K.; Blume, A. Membranolytic Activity of Bile Salts: Influence of Biological Membrane Properties and Composition. *Molecules* **2007**, *12,* 2292-2326. https://doi.org/10.3390/12102292

22) Vlahcevic, Z. R.; Schwartz, C. C.; Gustafsson, J.; Halloran, L. G.; Danielsson, H.; Swell, L. Biosynthesis of bile acids in man. *J. Biol. Chem.* **1980**, *255,* 2925-2933. https://doi.org/10.1016/S0021-9258(19)85829-5

23) Menzies, J. A. Observation on the secretion and composition of human bile. *Biochem. J.* **1912**, *6,* 210-218. https://doi.org/10.1042/bj0060210

24) Heinze, W. L. Organized Assemblies in Chemical Analysis. *JAI Press*, **1996**, *2,* 87-99.

25) Sharma, P.; Sohal, N.; Maity, B. Encapsulation and release of non-fluorescent crystal violet confined in bile-salt aggregates. *RSC Adv*. **2021**, *11,* 10912–10921. https://doi.org/10.1039/d0ra06599d

26) Moroi, Y. Micelles. Theoretical and Applied Aspects. *Springer-Verlag.* **1992**, *49,* 492–497.

27) Funasaki, N.; Fukuba, M.; Kitagawa, T.; Nomura, M.; Ishikawa, S.; Hirota, S.; Neya, S. Two dimensional NMR study on the structures of micelles of sodium taurocholate. *J. Phys. Chem. B* **2005**, *109,* 9851-9852. https://doi.org/10.1021/jp0455374

28) Funasaki, N.; Fukuba, M.; Hattori, T.; Ishikawa, S.; Okuno, T.; Hirota, S. Micelle formation of bile salts and zwitter ionic derivative as studied by two-dimensional NMR spectroscopy. *Chem. Phys. Lipids* **2006**, *142,* 43-57. https://doi.org/10.1001/archinte.1972.03650040040005

29) Mukherjee, P.; Mysels, K. J. Critical micelle concenteration of aqueous surfactant systems Natl. Stand. Ref. Data Ser. (US. Natl. Bur. Stand.) NSRDS-NBS 36, Washington, D.C. 1971. https://doi.org/10.6028/NBS.NSRDS.36

30) Roda, A.; Hofmann, A. F.; Mysels, K. J. The influence of bile salt structure on self-association in aqueous solutions. J Biol. Chem. 1983, 25, 258, 6362-70. https://doi.org/10.1016/S0021-9258(18)32418-9

31) Malliaris, A.; Lang, J.; Zana, R. Micellar aggregation numbers at high surfactant concentration, J. Colloid Interface Sci. 1986, 110, 237-242. https://doi.org/10.1016/0021-9797(86)90372-3

32) Small, D. M. Size and structure of bile salt micelles: influence of structure, concentration, counterion concentration, pH, and temperature. *Adv. Chem. Ser. B* **1968**, *84*, 31-52. https://doi.org/10.1021/ba-1968-0084.ch004

33) Small, D. M.; Penkett, S. A.; Chapman, D. Studies on simple and mixed bile salt micelles by nuclear magnetic resonance spectroscopy. *Biochim. Biophys. Acta*. **1969**, *176*, 178-189. https://doi.org/10.1016/0005-2760(69)90086-1

34) Kawamura, H.; Murata, Y.; Yamaguchi, T.; Igimi, H., Tanaka, M.; Sugihara, G.; Kratohvil, J. P. Spin label studies of bile salt micelles. *J. Phys. Chem.* **1989**, *93*, 3321-3326. https://doi.org/10.1021/j100345a087

35) Coello, A.; Meijide, F.; Nunez, E. R.; Tato, J. V. Aggregation behaviour of bile salts in aqueous solution. *J. Pharm. Sci.* **1996**, *85*, 9-15. https://doi.org/10.1021/js950326j

36) Galantini, L.; Giglio, E.; Pavel, N. V.; Punzo, F. QELS and X-ray of two dihydroxy bile salt aqueous solutions. *Colloid Surf. A* **2004**, *248*, 79-84. https://doi.org/10.1016/j.colsurfa.2004.06.044

37) Carey, M. C.; Small, D. M. Micelle formation by bile salts. Physical-chemical and thermodynamic considerations. *Arch. Intern. Med.* **1972**, *130*, 506-527. https://doi.org/10.1001/archinte.1972.03650040040005

38) Kolahalam, L. A; Viswanath, I. V. K.; Diwakar, B. S.; Govindh, B.; Reddy, V.; Murthy, Y.L.N. Review on nanomaterials: Synthesis and applications. *Mater. Today: Proc.* **2019**, *18,* 2182–2190. https://doi.org/10.1016/j.matpr.2019.07.371

39) Baig, N.; Kammakakam, I.; Falath, W. Nanomaterials: a review of synthesis methods, properties, recent progress, and challenges. *Mater. Adv.* **2021**, *2,* 1821–1871. https://doi.org/10.1039/d0ma00807a

40) Nayak, S.; Guleria, k.; Sen, A.; Banerjee, S.; Subramanian, R.; Das, P. Chemically induced crosslinked enhanced emission of carbon polymer dots discerning healthy and cancer cells

through pH-dependent tunable photoluminescence. *J. Mater. Chem. B* **2023**,*11*, 594-605. https://doi.org/10.1039/D2TB01836E

41) Singh, S.; Vaishnav, J. K.; Mukherjee, T. K. Quantum Dot-Based Hybrid Coacervate Nanodroplets for Ultrasensitive Detection of Hg^{2+}. *ACS Appl. Nano Mater.* **2020**, *3*, 3604–3612. https://doi.org/10.1021/acsanm.0c00317

42) Parveen, R.; Shamsi, T. N.; Fatima, S. Nanoparticles-protein interaction: Role in protein aggregation and clinical implications. *Int. J. Biol. Macromol.* **2017**, *94,* 386–395. http://doi.org/10.1016/j.ijbiomac.2016.10.024

43) Paras, Yadav, K.; Kumar, P.; Teja, D. R.; Chakraborty S.; Chakraborty M.; Mohapatra, S. S.; Sahoo, A.; Chou, ,. M. C.; Liang, C.-T.; Hang, D.-R. A review on low-dimensional nanomaterials: nanofabrication, characterization and applications. *Nanomaterials* **2023**, *13*,160. https://doi.org/10.3390/nano13010160

44) Bayda, S.; Adeel, M.; Tuccinardi, T.; Cordani, M.; Rizzolio, F. The history of nanoscience and nanotechnology: From chemical-physical applications to nanomedicine. *Molecules* **2020**, *25*, 112-120. https://doi.org/10.3390/molecules25010112

45) Kumar, V. B.; Porat Z.; Gedanken A. Synthesis of doped/hybrid carbon dots and their biomedical applications. *Nanomaterials* **2022**, *12*, 898-924. https://doi.org/10.3390/nano12060898

46) Aggarwal, M.; Sahoo, P.; Saha, S.; Das, P. Machine Learning-Mediated Ultrasensitive Detection of Citrinin and Associated Mycotoxins in Real Food Samples Discerned from a Photoluminescent Carbon Dot Barcode Array. *J. Agric. Food Chem.* **2023**, *71*, 34, 12849–12858. https://doi.org/10.1021/acs.jafc.3c04846

47) Singh, R.; Praneeth, NVS; Biswas, S.; Palabathuni, M.; Muralidharan, A.; Mishra, N.; Khatua, S. Understanding the Size-Dependent Photostability and Photoluminescence Intermittency of Blue-Emitting Core/Graded Alloy/Shell “giant”-Quantum Dots. *Adv. Opt. Mater.* **2024**, *12*, 2401132. https://doi.org/10.1002/adom.202401132

48) Chatterjee, S.; Biswas, S.; Sourav, S.; Rath, J.; Akhil, S.; Mishra, N. Strategies To Achieve Long-Term Stability in Lead Halide Perovskite Nanocrystals and Its Optoelectronic Applications. *J. Phys. Chem. Lett.* **2024**, *15*, 40, 10118–10137. https://doi.org/10.1021/acs.jpclett.4c02240

49) Abu, N.; Chinnathambi, S.; Kumar, M.; Etezadi, F.; Bakhori, N. M.; Zubir, Z. A.; Salleh, S. N. M.; Shueb, R. H.; Karthikeyan, S.; Thangavel, V.; Abdullah, J.; Pandian, G. N. Development of biomass waste-based carbon quantum dots and their potential application as non-toxic bioimaging agents. *RSC Adv.* **2023**, *13*, 28230-28249. https://doi.org/10.1039/D3RA05840A

50) Chinnathambi, S.; Shirahata, N.; Kumar, M.; Karthikeyan, S.; Abe, K.; Thangavel, V.; Pandian, G. N. Nano-bio interaction between human immunoglobulin G and nontoxic, near-infrared emitting water-borne silicon quantum dot micelles. *RSC Adv.* **2023**, *13*, 6051-6064. https://doi.org/10.1039/D3RA00552F

51) Chinnathambi, S.; Shirahata, N. Recent advances on fluorescent biomarkers of near-infrared quantum dots for in vitro and in vivo imaging. *Sci. Technol. Adv. Mater.* **2019**, *20*, 337-355. https://doi.org/10.1080/14686996.2019.1590731

52) Kumar, M.; Chinnathambi, S.; Bakhori, N.; Abu, N.; Etezadi, F.; Thangavel, V.; Packwood, D.; Sivaniah, E.; Pandian, G. N. Biomass-derived carbon dots as fluorescent quantum probes to visualize and modulate inflammation. *Sci. Rep.* **2024**, *14*, 12665-12676. https://doi.org/10.1038/s41598-024-62901-7

53) Wang, X. Feng, Y.; Dong, P.; Huang, J. A mini review on carbon quantum dots: preparation, properties and electrocatalytic application. *Front. Chem.* **2019**, *7*, 671- 677. https://doi.org/10.3389/fchem.2019.00671

54) Anwar, S.; Ding, H.; Xu, M.; Hu, X.; Li, Z.; Wang, J.; Liu, L.; Jiang, L.; Wang, D.; Dong, C.; Yan, M.; Wang, Q.; Bi, H. Recent advances in synthesis, optical properties, and biomedical applications of carbon dots. *ACS Appl. Bio Mater.* **2019**, *2*, 2317–2338. https://doi.org/10.1021/acsabm.9b00112

55) Naik, V.; Zantye, P.; Gunjal, D.; Gore, A.; Anbhule, P.; Kowshik, M**.;** Bhosale, S. V.; Kolekar, G. Nitrogen-doped carbon dots via hydrothermal synthesis: naked eye fluorescent sensor for dopamine and used for multicolor cell imaging. *ACS Appl. Bio Mater.* **2019**, *2*, 2069–2077. https://doi.org/10.1021/acsabm.9b00101

56) Barman, M. K.; Patra, A. Current status and prospects on chemical structure driven photoluminescence behaviour of carbon dots. *J. Photochem. Photobiol. C: Photochem Rev.* **2018**, *37*, 1-12. https://doi.org/10.1016/j.jphotochemrev.2018.08.001

57) Namakka, M.; Rahman, M. R.; Mohamad, K. A.; Said, B.; Mannan, M. A.; Patwary, A. M. A review of nanoparticle synthesis methods, classification, applications, and characterization. *Environ. Nanotechnol. Monit. Manag.* **2023**, *20*, 100900. https://doi.org/10.1016/j.enmm.2023.100900

58) Sousa, H. B. A.; Martins, C. S. M.; Prior, J. A. V. You don't learn that in school: An updated practical guide to carbon quantum dots. *Nanomaterials* **2021**, *11*, 611-681. https://doi.org/10.3390/nano11030611

59) Gan, Y.X.; Jayatissa, A.H.; Yu, Z.; Chen, X.; Li, M. Hydrothermal Synthesis of Nanomaterials. *J. Nanomater.* **2020**, 1–3. https://doi.org/10.1155/2020/8917013

60) Singh, R.K.; Kumar, R.; Singh, D.P.; Savu, R.; Moshkalev, S.A. Progress in microwave-assisted synthesis of quantum dots (graphene/carbon/semiconducting) for bioapplications: A review. *Mater. Today Chem.* **2019**, *12*, 282–314. https://doi.org/10.1016/j.mtchem.2019.03.001

61) Gawande, M.B.; Shelke, S.N.; Zboril, R.; Varma, R.S. Microwave-assisted chemistry: Synthetic applications for rapid assembly of nanomaterials and organics. *Acc. Chem. Res.* **2014**, *47*, 1338–1348. https://doi.org/10.1021/ar400309b

62) Li, W.; Liu, Y.; Wu, M.; Feng, X., Redfern, S. A. T., Shang, Y.; Yong, X.; Feng, T.; Wu, K.; Liu, Z.; Li, B.; Chen, Z.; Tse, J. S. Lu, S.; Yang, B. Carbon-quantum-dots-loaded ruthenium nanoparticles as an efficient electrocatalyst for hydrogen production in alkaline media. *Adv. Mater.* **2018**, *30*, 1800676-1800683. https://doi.org/10.1002/adma.201800676

63) Yuan, J.-M.; Zhao, R.; Wu, Z.-J.; Li, W.; Yang, X.-G. Graphene oxide quantum dots exfoliated from carbon fibers by microwave irradiation: two photoluminescence centers and self-assembly behavior. *Small* **2018**, *14*, 1703714. https://doi.org/10.1002/smll.201703714

64) Yan, F.; Sun, Z.; Zhang, H.; Sun, X.; Jiang, Y.; Bai, Z. The fluorescence mechanism of carbon dots, and methods for tuning their emission color: A review. *Mikrochim. Acta* **2019**, *186*, 583. https://doi.org/10.1007/s00604-019-3688-y

65) Wu, Y.F.; Wu, H.C.; Kuan, C.H.; Lin, C.J.; Wang, L.W.; Chang, C.W.; Wang, T.W. Multi-functionalized carbon dots as theranostic nanoagent for gene delivery in lung cancer therapy. *Sci. Rep.* **2016**, *6*, 2117. https://doi.org/10.1038/srep21170

66) Yang, H.-L.; Bai, L.-F.; Geng, Z.-R.; Chen, H.; Xu, L.-T.; Xie, Y.-C.; Wang, D.-J.; Gu, H.-W.; Wang, X.-M. Carbon quantum dots: preparation, optical properties, and biomedical applications. *Mater. Today. Adv.* **2023**, *18*, 100376-100399. https://doi.org/10.1016/j.mtadv.2023.100376

67) Singh, P.; Arpita; Kumar, S.; Kumar, P.; Kataria, N.; Bhankar, V.; Kumar, K.; Kumar, R.; Hsieh, C.-T.; Khoo, K. S. Assessment of biomass-derived carbon dots as highly sensitive and selective templates for the sensing of hazardous ions. *Nanoscale* **2023**, *15*, 16241-16267. https://doi.org/10.1039/d3nr01966g

68) Arpita; Kumar, P.; Kataria, N.; Narwal, N.; Kumar, S.; Kumar, R.; Khoo, K. S.; Show, P. L. Plastic Waste-Derived Carbon Dots: Insights of Recycling Valuable Materials Towards Environmental Sustainability. *Curr. Pollut. Rep.* **2023**, 433-453. https://doi.org/10.1007/s40726-023-00268-5

69) Lakowicz, J. R. Principles of Fluorescence Spectroscopy; Lakowicz, J. R., Ed.; Springer US: Boston, MA, **2006**. https://doi.org/10.1007/978-0-387-46312-4.

70) Zu, F.; Yan, F.; Bai, Z.; Xu, J.; Wang, Y.; Huang, Y.; Zhou, X. The Quenching of the 20 Fluorescence of Carbon Dots: A Review on Mechanisms and Applications. *Microchim. Acta* **2017**, *184*, 1899–1914. https://doi.org/10.1007/s00604-017-2318-9

71) Yang, B.; Li, X.; Wang, L.; An, J.; Wang, T.; Zhang, F.; Ding, B.; Li, Y. A Water-Stable MOF-$AgClO_4$-Abtz as Fluorescent Sensor for Detection of Folic Acid Based on Inner Filter Effect. *Talanta*. **2020**, *217*, 121019. https://doi.org/10.1016/j.talanta.2020.121019

72) Liu, J.; Chen, Y.; Wang, W.; Feng, J.; Liang, M.; Ma, S.; Chen, X. "Switch-on" fluorescent sensing of ascorbic acid in food samples based on carbon quantum dots-MnO_2 probe. *J. Agric. Food chem.* **2016**, *64*, 371-380. https://doi.org/10.1021/acs.jafc.5b05726

73) Vaishnav, J. K.; Mukherjee, T. K. Selective uptake and modulation of nanometal surface energy transfer from quantum dot to Au nanoparticle across lipid bilayer of liposomes. *J. Photochem. Photobiol. A: Chem*. **2020**, *401*, 112773-112784. https://doi.org/10.1016/j.jphotochem.2020.112773

74) Sun, X.; Lei, Y. Fluorescent Carbon Dots and Their Sensing Applications. *Trends Anal. Chem.* **2017**, *89*, 163–180. https://doi.org/10.1016/j.trac.2017.02.001

75) Nayak, S.; Banerjee, S.; Kamra, A.; Das, P.; Rana, S. Carbon-Nanodot-Based Bicontinuous Particles for FRET-Based pH Sensing. *ACS Appl. Nano Mater.* **2024**, *7*, 25261–25269. https://doi.org/10.1021/acsanm.4c04310

76) Anastas, P.; Eghbali, N. Green chemistry: Principle and practices. *Chem. Soc. Rev.* **2010**, *39*, 301–312. https://doi.org/10.1039/b918763b

77) Anastas, P. T.; Warner, J. C. in Green Chemistry: Theory and Practice, Oxford University Press, New York, 1998; I. Horvath and P. T. Anastas, *Chem. Rev.* **2007**, *107*, 2167.

78) Anastas, P. T.; Williamson, T. C. in Green Chemistry: Designing Chemistry for the Environment, American Chemical Series Books, Washington, DC, **1996**, 1–20.

79) Dong, Z.; Qi, J.; Yue, L.; Zhou, H.; Chen, L.; Gu, J.; He, Y.; Wu, H. Biomass-based carbon quantum dots and their agricultural applications. *Plant Stress* **2024**, *11*, 100411-100422. https://doi.org/10.1016/j.stress.2024.100411

80) Rani, N.; Singh, P.; Kumar, S.; Kumar, P.; Bhankar, V.; Kumar, K. Plant-mediated synthesis of nanoparticles and their applications: A review. *Mater. Res. Bull.* **2023**, *163*, 112233. https://doi.org/10.1016/j.materresbull.2023.112233

81) Kang, C.; Huang, Y.; Yang, H.; Yan, X. F.; Chen, Z. P. *Nanomaterials* **2020**, *10*, 1–24, https://doi.org/10.3390/ nano10112316.

82) Zhang, C.; Xiao, Y.; Ma, Y.; Li, B.; Liu, Z.; Lu, C.; Liu, X.; Wei, Y.; Zhu, Z.; Zhang, Y. J. *Photochem. Photobiol. B* **2017**, *174*, 315–322. https://doi.org/10.1016/j. jphotobiol.2017.06.024.

83) Rabiee, N.; Iravani, S.; Varma, R. S. Biowaste-derived carbon dots: A perspective on biomedical potentials. *Molecules* **2022**, *27*, 6186-6223. https://doi.org/10.3390/molecules27196186

84) Lomba, L.; García, C. B.; Ribate, M. P.; Giner, B.; Zuriaga, E. Applications of deep eutectic solvents related to health, synthesis, and extraction of natural based chemicals. *Appl. Sci.* **2021**, *11*, 10156-10173. https://doi.org/10.3390/app112110156

85) Yi, L.; Wu, X.; Guo, L.; Chen, J.; Gauthier, M.; Li, W.-Y. Applications of ionic liquids and deep eutectic solvents for the extraction of phenolic compounds from coal-based crude oils. *Sep. Purif. Technol*. **2024**, *337*, 126383. https://doi.org/10.1016/j.seppur.2024.126383

86) Hansen, B. B.; Spittle, S.; Chen, B.; Poe, D.; Zhang, Y.; Klein, J. M.; Horton, A.; Adhikari, L.; Zelovich, Y.; Doherty, B. W.; Gurkan, B.; Maginn, E. J.; Ragauskas, A.; Dadmun, M.;

Zawodzinski, T. A.; Baker, G. A.; Tuckerman, M. E.; Savinell, R. F.; Sangoro, J. R. Deep eutectic solvents: a review of fundamentals and applications. *Chem. Rev*. **2021**, *121*, 1232–1285. https://doi.org/10.1021/acs.chemrev.0c00385

87) Singh, S.K.; Savoy, A.W. Ionic liquids synthesis and applications: An overview. *J. Mol. Liq.* **2020**, *297*, 112038. https://doi.org/10.1016/j.molliq.2019.112038

88) Welton, T. Ionic liquids: A brief history. *Biophys. Rev.* **2018**, *10*, 691–706. https://doi.org/10.1007/s12551-018-0419-2

89) Smith, E. L.; Abbott, A. P.; Ryder, K. S. Deep eutectic solvents (DES) and their applications. *Chem. Rev*. **2014**, *114*, 10697-11130. https://doi.org/10.1021/cr300162p

90) Li, D. Natural deep eutectic solvents in phytonutrient extraction and other applications. *Front. Plant Sci*. **2022**, *13*, 1004332-1004342. https://doi.org/10.3389/fpls.2022.1004332

91) Dai, Y.; Spronsen, J. V.; Witkamp, G.-J.; Verpoorte, R.; Choi, Y. H. Ionic liquids and deep eutectic solvents in natural products research: mixtures of solids as extraction solvents. *J. Nat. Prod.* **2013**, *76*, 2162–2173. https://doi.org/10.1021/np400051w

92) Negi, T.; Kumar, A.; Sharma, S. K.; Rawat, N.; Saini, D.; Sirohi, R.; Prakash, O.; Dubey, A.; Dutta, A.; Shahi, N. C. Deep eutectic solvents: preparation, properties, and food applications. *Heliyon* **2024**, *10*, 28784-28803. https://doi.org/10.1016/j.heliyon.2024.e28784

93) Rozas, S.; Zamora, L.; Benito, C.; Atilhan, M.; Aparicio, S. A study on monoterpenoid-based natural deep eutectic solvents. *Green Chem. Eng*. **2023**, *4*, 99-114. https://doi.org/10.1016/j.gce.2022.05.005

94) Ijardar, S. P.; Singh, V.; Gardas, R. L. Revisiting the physicochemical properties and applications of deep eutectic solvents. *Molecules* **2022**, *27*, 1368-1405. https://doi.org/10.3390/molecules27041368

95) Kalyniukova, A.; Holuša, J.; Musiolek, D.; Sedlakova-Kadukova, J.; Płotka-Wasylka, J.; Andruch, V. Application of deep eutectic solvents for separation and determination of bioactive compounds in medicinal plants. *Ind. Crop. Prod*. **2021**, *172*, 114047-114056. https://doi.org/10.1016/j.indcrop.2021.114047

96) Javed, S.; Mangla, B.; Sultan, M. H.; Almoshari, Y.; Sivadasan. D.; Alqahtani, S. S.; Madkhali, O. A.; Ahsan, W. Pharmaceutical applications of therapeutic deep eutectic systems (THEDES) in maximizing drug delivery. *Heliyon* **2024**, *10*, 29783-29802. https://doi.org/10.1016/j.heliyon.2024.e29783

97) Stott, P.W.; Williams, A.C.; Barry, B.W. Transdermal delivery from eutectic systems: Enhanced permeation of a model drug, ibuprofen. *J. Control. Release* **1998**, *50*, 297–308. https://doi.org/10.1016/S0168-3659(97)00153-3

98) Sun, X.; Kumar, P. P.; Rajendran, N. K.; Shakila, H.; Houreld, N. N.; Farraj, D. A. A.; Elnahas, Y. M.; Elumalai, N.; Rajan, M. Natural deep eutectic solvents supported targeted solid-liquid polymer carrier for breast cancer therapy. *RSC Adv*. **2020**, *10*, 36989–37004. https://doi.org/10.1039/d0ra03790g

99) Ghosh, N.; Mondal, R.; Mukherjee, S. Hydrophobicity Is the Governing Factor in the Interaction of Human Serum Albumin with Bile Salts. *Langmuir* **2015**, *31*, 1095−1104. https://doi.org/10.1021/la504270a

100) Khalid, I. M.; Sharkh, S. E. A.; Samamarh, H.; Alfaqeeh, R.; Abuteir, M. M.; Darwish, S. M. Spectroscopic Characterization of the Interaction between Dopamine and Human Serum Albumin. *Biophys. J*. **2019**, *9*, 110-130. https://doi.org/10.4236/ojbiphy.2019.92009

101) Malarkani, K.; Sarkar, I.; Selvam, S. Denaturation studies on bovine serum albumin–bile salt system: Bile salt stabilizes bovine serum albumin through hydrophobicity. *J. Pharm. Anal.* **2018**, *8*, 27–36. https://doi.org/10.1016/j.jpha.2017.06.007

102) Ren, H.; Xin, X.; Wang, L.; Ju, H.; Zhamanding, A.; Xu, G. A direct comparison of the interaction of bovine serum albumin and gelatin with sodium deoxycholate in aqueous solutions. *J. Mol. Liq.* **2015**, *207*, 164–170. http://dx.doi.org/10.1016/j.molliq.2015.03.017

103) Zhao, W.; Zheng, Y.; Cao, B.; Li, Z.; Sun, C.; Cao, X.; Cong, S. Characteristics of mussels-derived carbon dots and their applications in bio-imaging and detection of riboflavin. *Foods* **2022**, *11*, 2451-2460. https://doi.org/10.3390/foods11162451

104) Joh, B. K.; Mathew, J.; K. S.; K. R. E.; Mathew, B. Biomass derived carbon quantum dots as a versatile platform for fluorescent sensing, catalytic reduction, fluorescent ink and anticancer agents. *Mater. Today. Sustain*. **2024**, *6*, 100715. https://doi.org/10.1016/j.mtsust.2024.100715

105) Kundu, A.; Basu, S.; Maity, B. Orange pomace-derived fluorescent carbon quantum dots: detection of dual analytes in the nanomolar range. *ACS Omega* **2023**, *8*, 22178–22189. https://doi.org/10.1021/acsomega.3c02474

106) Fu, M.; lan, Y.; Bao, W.; Li, G.; Lu, H.; Zhou, L.; Lan, H.; Mo, X. Construction of carbon quantum dots/riboflavin fluorescent probe and its application in the detection of ciprofloxacin. *Luminescence*. **2024**, *39*, 4858-4867. https://doi.org/10.1002/bio.4858

107) Raveendran, V.; Kizhakayil, R. N. Fluorescent carbon dots as biosensor, green reductant, and biomarker. *ACS Omega* **2021**, *6*, 23475-23484. https://doi.org/10.1021/acsomega.1c03481

108) Xing, S.; Zheng, K.; Shi, L.; Kang, K.; Peng, Z.; Zhang, X.; Liu, B.; Yang, H.; Yue, G. Fluorescence detection of Pb^{2+} in environmental water using biomass carbon quantum dots modified with acetamide-glycolic acid deep eutectic solvents. *Molecules* **2024**, *29*,1662-1679. https://doi.org/10.3390/molecules29071662

109) Yin, Q.; Wang, M.; Fang, D.; Zhu, Y.; Yang, L. Novel N, Cl-doped deep eutectic solvents-based carbon dots as a selective fluorescent probe for determination of morphine in food. *RSC Adv.* **2021**, *11*, 16805-16813. https://doi.org/10.1039/D1RA00886B

Chapter 2

Instrumentation techniques

This chapter describes the experimental methodologies employed in the work to understand the physical, chemical and optical characteristics of the nanoparticles and study the interactions possible between the protein and bile salt complex linked to this thesis. The widely used characterization techniques involved are UV-Visible spectroscopy, steady-state fluorescence spectroscopy, time-resolved fluorescence spectroscopy, high-resolution transmission electron microscopy (HRTEM), X-ray photoelectron spectroscopy (XPS), energy dispersive spectroscopy (EDS), attenuated total reflectance Fourier-transform IR (ATR FT-IR) spectroscopy, Raman spectroscopy, grazing-incidence X-ray diffraction (GIXRD), and zeta potential (ζ) measurements.

2.1 High-resolution transmission electron microscopy (HRTEM)

High-resolution techniques like HR-TEM are valuable for gaining insights into the structural patterns and size distribution of carbon dots, which are particles smaller than 10 nm. By using high-resolution transmission electron microscopy (HR-TEM) analysis, one can easily determine whether the synthesized carbon dots are crystalline or amorphous. HR-TEM images are generated by directing a high-energy electron beam onto a very thin sample, which is then transmitted through the sample surface, revealing its internal structure.[7] In this thesis work, high-resolution transmission electron microscopy (HRTEM) was performed using a JEM 2100 plus (JEOL) equipped with a charge-coupled device (CCD) camera at an acceleration voltage of 80-200 kV in chapter 4 and chapter 5. Size distribution studies of HR-TEM images were carried out using ImageJ software, and the size distribution curve was plotted using the Gaussian distribution available in OriginPro 2023.

2.2 X-ray photoelectron spectroscopy (XPS)

X-ray photoelectron spectroscopy (XPS) is a highly utilized analytical method for surface chemical analysis and is also used to characterize nanoscale materials. It operates based on the photoelectric effect. XPS is a robust quantitative method that helps reveal the electronic structure,

elemental composition, and oxidation states of elements in a material. The specimen for analysis is maintained in an ultra-high vacuum state and scanned with X-rays on its top surface, resulting in the emission of excited electrons known as photoelectrons. These excited electrons are likely from the top surface of the specimen, with a detectable penetration depth of around 1-10 nm. The energy of the core level electrons is particularly specific for a given element, thus providing data on the elemental composition of the specimen's thin surface region Additionally, shifts in the binding energy position can indicate the corresponding oxidation states of the elements.[4-6]

In this study, XPS measurements were conducted using the Physical Electronics (PHI 5000 Versa Probe III) with monochromatized Al Kα X-rays (Japan) (Chapter 4) and the ESCALAB QXi X-ray photoelectron spectrometer microprobe from ThermoFisher Scientific (USA) (Chapter 5). The spectra were first baseline corrected, followed by peak identification using the peak analyzer option and deconvolution through multiple peak-fitting involving the Gaussian function both available in the OriginPro 2023 software.

2.3 Grazing-incidence X-Ray diffraction (GIXRD)

X-ray diffraction is a non-destructive technique used to investigate the crystal structure of materials. The analysis is done on the diffraction pattern's intensity and the observed theta position. The X-ray diffraction pattern works as a fingerprint tool with unique crystallographic phases, making it significant for comparison with standard databases like the Joint Committee on Powder Diffraction Standards (JCPDS). Using this method, one comprehends the surface characteristics of the carbon dots and concluded that carbon dots exhibiting an amorphous carbon phase, owing to the variations of the crystalline peak of chitosan at 2θ = 20° to 23°. The broad peak observed in the XRD study reflects a high degree of disorder among the carbon atoms on the carbon dots surface.[7, 8]

The interlayer distance (d-spacing) was calculated using Bragg's equation:

$$n\lambda = 2\mathrm{d}\sin\theta \qquad (1)$$

where 'λ' represents the wavelength of the incident X-ray (λ = 1.5406 Å), 'n' is a positive integer that represents the "order" of reflection, variable 'd' indicates the spacing between the diffracting planes.

The diffraction pattern of carbon dots was captured on Rigaku SmartLab within the angular range (2θ) of 10-90°, and OriginPro 2023 was utilized to plot the spectral data, as illustrated in chapters 4 and 5.

2.4 Attenuated total reflectance Fourier-transform Infrared (ATR FT-IR) and Raman spectroscopy

The research thesis entailed vibrational spectroscopic analyses, specifically involving Raman and Infrared spectroscopy in chapter 4 and 5. FT-IR is a highly advanced spectroscopic method employed to study the varied functionalities present on the synthesized nanomaterial surface. Carbon dots primarily consist of oxygen, carbon, and hydrogen. Since carbon dots are produced through the partial oxidation of a carbon precursor, their surfaces are rich in carboxyl or carboxylic acid groups, hydroxyl groups, and ether/epoxy groups. Therefore, FTIR is a valuable tool for examining these oxygen-containing groups.[7,11,12] In this study, the ATR-FTIR spectra of the carbon dots were obtained using an IRTracer-100 spectrophotometer (Shimadzu). The spectral data were then re-plotted using OriginPro 2023 software.

Raman scattering reveals structural features in carbon dots. It is a non-destructive, non-coercive spectroscopic method. Raman spectroscopy was employed to gain a better understanding of the surface structure of carbon dots by monitoring several vibrational modes. It also addresses the crystalline and amorphous characteristics of the developed carbon dots. Typically, carbon dots display two types of bands in Raman spectroscopy. The D band (1350 cm^{-1}) relates to the vibrations of disordered carbon atoms having the presence of dangling bonds in the ending plane of graphitic carbon linked with D-band, which implies the presence of defects with orbital alloying predominantly of sp^3 nature. The G band (1600 cm^{-1}) correlates to the in-plane stretching vibration mode E_{2g} of crystalline graphite carbon atoms, that is linked to the two-dimensional (2D) hexagonal lattice vibration of sp^2-bonded carbon atoms. The I_D/I_G ratio of Raman band intensities is used to examine the carbon framework, specifically the degree of crystallinity and relative abundance of carbon atoms as compared to surface atoms.[13,14] The Raman measurements were

taken using a LabRAM HR Confocal Micro-Raman Spectrometer (HORIBA, France). The data were collected with the LabSpec 6 software included with the Raman spectrometer and re-plotted using OriginPro 2023.

2.5 Zeta Potential

The zeta-potential of the specimen determines the stability of colloidal dispersions. The zeta potential represents the net electrical charge on the surface of carbon dots. Highly positively or negatively charged particles repel each other, resulting in stable colloidal solutions with only slight agglomeration. Such highly charged particles are linked with pH levels that are far from the so-called 'isoelectric point' of a solution, which is the pH value at which the zeta potential is zero. On the contrary, a low value for the zeta-potential leads the flocculation of the colloids and it corresponds to values closer to the isoelectric point of the system. This technique has proven to be a valuable tool for studying the behavior of nanoparticles in biological environments. It offers the advantage that the nanoparticles are not at risk of clustering during sample preparation.[5,9,10] In our study, as illustrated in chapters 4 and 5, carbon dots exhibit a negative surface charge. This charge originates from the presence of functional groups or chemical species on the carbon dots surface that ionize in solution, leading to the accumulation of negatively charged particles around the carbon dots, such as carboxyl (–COOH), hydroxyl (-OH), and amino ($–NH_2$) groups. The surface functional groups on carbon dots are responsible for their negative charge, causing them to migrate towards the positive electrode in an electric field and resulting in negative zeta potential values. The zeta potential experiments were carried out on Zetasizer 2000, nano series-ZS (Malvern Instruments Ltd, UK) in chapter 4 whereas Brookhaven 90 Plus zeta potential analyzer was used in Chapter 5 of this thesis. All the data is plotted using OriginPro 2023.

2.6 Energy dispersive spectroscopy (EDS)

The energy dispersive spectroscopy (EDS) method is primarily employed for the qualitative analysis of nanomaterials. Energy-Dispersive Spectroscopy (EDS) is a method used to analyze the elemental composition of materials when a high-intensity X-ray beam is directed onto the sample.[15] The EDS of N-CDs was recorded using Talos F200S (Thermo Fisher Scientific) in chapter 4 and using the Bruker QUANTAX 200 from ZEISS Sigma in chapter 5 in this thesis.

2.7 UV-Visible (UV-Vis) spectroscopy

UV-Visible absorption spectroscopy is a method used for quantification characterization. It operates on the principle that molecules can absorb ultraviolet and visible light. The molecules absorb energy as the outer electrons are excited from the highest occupied molecular orbital (HOMO) to the lowest unoccupied molecular orbital (LUMO). The resulting absorption spectra are valuable for estimating the energy levels of the molecules.[1] The UV-Vis spectra were obtained using a Shimadzu UV-2600 UV-Vis spectrophotometer with freshly prepared solutions, as described in the respective chapters.

In our case, it assists in determining the concentration of the protein stock solution and gives an initial indication of the complex formation between HSA and bile salts/acids. The Beer-Lambert law, which assists in finding concentration, is expressed by the following equation:[2]

$$A = \epsilon c l \qquad (2)$$

Where 'A' represents absorbance, 'ϵ' denotes molar absorptivity with units L mol^{-1} cm^{-1}, 'c' is the concentration of the specimen expressed in mol L^{-1}, and 'l' is the cell length measured in cm.

The quantitative estimation of the binding of bile salts to the protein and the interaction strength, based on changes in absorbance, is done using the 1:1 linear Benesi-Hildebrand method.[3] The equation for this method is provided below:

$$\frac{1}{A_0 - A} = \frac{1}{A_0 - A_1} + \frac{1}{K[Q](A_0 - A)} \qquad (3)$$

In this context, 'A_0' and 'A' are the absorbances in the absence and presence of bile salts/acids, respectively. 'Q' denotes the concentration of bile salts/acids, and 'A_1' represents the absorbance of the HSA-bile salts/acids complex at a 1:1 stoichiometry. The parameter 'K' indicates the binding constants of various bile salts/acids. The plot of $(1/(A - A_0))$ versus 1/[Q] results in a straight line, from which the binding constants (K) are determined using the slope and intercept.

2.8 Fluorescence spectroscopy

Fluorescence measurements are broadly categorized into two types: steady-state and time-resolved. In steady-state measurements, the sample is irradiated with a constant beam of light, and its emission spectrum is recorded. Because of the ns timescale of fluorescence, the majority of

measurements are steady-state. When the sample is first exposed to light, it achieves steady state almost instantly. The second form of measurement is time-resolved, which is used to assess intensity or anisotropy decays. For these measurements, the sample is subjected to a light pulse with a width that is typically shorter than the sample's decay time frame. This intensity decay is recorded using a high-speed detection device, allowing the intensity or anisotropy to be monitored on a ns timeline.[16]

Most modern research involving the sensing of biomolecules, inorganic analytes, or other significant species requires a quenching process, which can be either static or dynamic. The creation of a non-fluorescent ground state complex between the quencher and the carbon dots causes static quenching. It will be clear from the difference between the UV-Vis spectra of alone and in the presence of interacting species. It has no effect on the life time of in the presence or absence of interacting species. Dynamic quenching is an excited-state phenomena. The collision between the excited state of the carbon dots and the quencher results in the transfer of energy or charge. If the following conditions are met, we may confidently classify the process as dynamic quenching. First and foremost, dynamic quenching occurs in the excited state of carbon dots, hence the UV-Vis spectra of the carbon dots remain unchanged. Second, the lifetime of the carbon dots would vary depending on whether the quencher was present or not. Third, increasing the temperature enhances the quenching process by increasing the number of collisions between the excited state of the carbon dots and the quencher.

Anisotropy measurements are frequently employed in fluorescence's biological applications. Anisotropy analyses provide insights into protein size and shape, as well as the rigidity of different molecular environments. Anisotropy measurements have been used to evaluate protein-protein interactions, membrane fluidity, and immunoassays of various chemicals. Anisotropy measurements are based on the photo selective excitation of fluorophores with polarized light. Fluorophores preferentially absorb photons with electric vectors oriented parallel to their transition moment.[16]

As detailed in detail in Chapter 3 of the thesis, fluorescence intensity and anisotropy were evaluated to investigate the conformational and size changes in pH-induced conformational isomers of monomeric protein in the absence and presence of bile salts/ acids.

The steady-state Trp fluorescence (intensity and anisotropy) measurements were carried out using the Fluoromax-4, Jobin Yvon (Horiba Scientific), and the resulting spectrum was smoothed using the Savitzky-Golay method available in the Origin Pro Version 2021 software.

The steady-state fluorescence anisotropy (r_{ss}) is given by the following relation:

$$r_{SS} = \frac{I_{\parallel} - GI_{\perp}}{I + 2GI_{\perp}} \qquad (4)$$

where 'I_{II}' and '$I_{\perp}$' are the fluorescence intensities collected when emission polarizer is oriented parallel and perpendicular to polarized excitation, respectively, and the measured intensities were corrected using the corresponding G-factor. A time-correlated single-photon counting (TCSPC) setup (Fluorocube, Horiba Jobin Yvon, NJ) was used for assessing the time-resolved fluorescence measurements. All of the decays were acquired and replotted using OriginPro 2021.

Additionally, time correlated single photon counting spectroscopy (TCSPC) and steady state spectroscopy are employed in chapters 4 and 5 as very useful tools to comprehend both the mechanism of sensing as well as the optical characteristics of the carbon dots themselves.

These spectroscopic methods are used to comprehend the fluorescent carbon dots surface energy states.

The fluorescence spectra of carbon dots were obtained using a Shimadzu RF-6000 spectrofluorometer. All of the data collected is plotted using OriginPro 2021. Using steady state fluorescence spectroscopy, we determined the exact mechanism of fluorescence quenching as well as numerous photophysical characteristics of the carbon dot-biomolecule interaction, as reported in further chapters. The Stern-Volmer quenching constants were determined using the following formula in order to better comprehend the degree of carbon dot quenching efficiency:[3]

$$\frac{F_0}{F} = 1 + K_{SV}[Q] \qquad (5)$$

The parameters 'F' and 'F_0' denotes the fluorescence intensity in the presence and absence of RF, respectively, Q denotes quencher's concentration, 'K_{sv}' is the Stern-Volmer quenching constant, which was computed from the slope of the plots.

Furthermore, by taking into account the corresponding fluorescence intensity and implementing the 1:1 linear Benesi-Hildebrand equation, the excited-state binding constant was determined in order to estimate the carbon dots-quencher stoichiometry and comprehend the degree of interaction and binding between carbon dots and quencher.[3]

$$\frac{1}{F_0-F} = \frac{1}{F_0-F_1} + \frac{1}{K_1[Q](F_0-F)} \qquad (6)$$

'F_1' denotes the fluorescence intensity of carbon dot-quencher complex. The plot of ($1/F_0$-F) against 1/[Q] yields a straight line. Carbon dot-quencher complex binding constants (K_1) are obtained from the reciprocal of the corresponding slope values.

Time-resolved fluorescence emission decays were recorded using a time-correlated single photon counting (TCSPC) fluorometer using the modular fluorescence lifetime device (DeltaFlex, HORIBA Scientific). OriginPro 2021 was used to replot all of the acquired decays. The fluorescence emission decays were further deconvoluted in relation to the instrument response function and further evaluated and fitted.[16]

References

1) Rooj, B.; Mandal, U. A review on characterization of carbon quantum dots. *Vietnam J. Chem*. **2023**, *61*, 693-718. https://doi.org/10.1002/vjch.202300022
2) Noble, J. E. Chapter two- Quantification of Protein concentration using UV absorbance and Coomassie dyes. *Methods Enzymol.* **2014**, *536*, 17-26. https://doi.org/10.1016/B978-0-12-420070-8.00002-7
3) N. Sohal, B. Maity, S. Basu, Carbon dot–MnO2 nanosphere composite sensors for selective detection of glutathione. *ACS Appl. Nano Mater.* **2020**, *3*, 5955–5964, https://doi.org/10.1021/acsanm.0c01088
4) Sarma, D. D.; Santra, P. K.; Mukherjee, S.; Nag, A. X-ray Photoelectron Spectroscopy: A unique tool to determine the internal heterostructure of nanoparticles. *Chem. Mater.* **2013**, *25*, 1222−1232. dx.doi.org/10.1021/cm303567d
5) Mourdikoudis, S.; Pallares, R. M.; Thanh, N. T. K. Characterization techniques for nanoparticles: comparison and complementarity upon studying nanoparticle properties. *Nanoscale* **2018**, *10*, 12871-12934. DOI: 10.1039/c8nr02278j
6) Lu, L. T. Ph.D. thesis, water-dispersible magnetic NPs for biomedical applications: Synthesis and characterisation, University of Liverpool, **2011**.
7) Rooj, B.; Mandal, U. A review on characterization of carbon quantum dots. *Vietnam J. Chem*. **2023**, *61*, 693-718. https://doi.org/10.1002/vjch.202300022

8) Majithia, M. Barretto, D. A. Chapter 12 - Biocompatible green-synthesized nanomaterials for therapeutic applications. Advances in Nano and Biochemistry. Academic; **2023**. pp. 285–367. https://doi.org/10.1016/B978-0-323-95253-8.00012-7

9) Samadiana, S.; Karbalaei, A.; Pourmadadia, M.; Yazdian F.; Rashedia H.; Omidic, M.; Malmir, S. A novel alginate-gelatin microcapsule to enhance bone differentiation of mesenchymal stem cells. *Int. J. Polym. Mater. Polym. Biomater.* **2022**, *71*, 395-402. https://doi.org/10.1080/00914037.2020.1848828

10) Setianto, S.; Men, L. K.; Bahtiar, A.; Panatarani, C.; Joni, I. M. Carbon quantum dots with honeycomb structure: a novel synthesis approach utilizing cigarette smoke precursors. *Sci Rep.* **2024**, *14*, 1996-2003. https://doi.org/10.1038/s41598-024-52106-3

11) Singh, I.; Arora, R.; Dhiman, H.; Pahwa, R. Carbon quantum dots: synthesis, characterization and biomedical applications. *Turk. J. Pharm. Sci.* **2018**, *15*, 219-230. https://doi.org/10.4274/tjps.63497

12) Azam, N.; Ali, M. N.; Khan, T. J. Carbon Quantum Dots for Biomedical Applications: Review and Analysis. *Front. Mater.* **2021**, *8*, 700403-700423. https://doi.org/10.3389/fmats.2021.700403

13) Ateia, E. E.; Rabie, O.; Mohamed, A. T. Assessment of the correlation between optical properties and CDS preparation approaches. *Eur. Phys. J. Plus*. **2024**, *139*, 1-12. https://doi.org/10.1140/epjp/s13360-023-04811-7.

14) Das, P.; Bhattacharya, S. K.; Banerji, P.; Das, N. C. Acoustic cavitation assisted synthesis and characterization of photoluminescent carbon quantum dots for biological applications and their future perspective. *Nano-Struct. Nano-Objects* **2021**, *25*, 100641-100660. https://doi.org/10.1016/j.nanoso.2020.100641

15) Nasrazadani, S.; Hassani, S. Chapter 2- Modern analytical techniques in failure analysis of aerospace, chemical, and oil and gas industries. Handbook of Materials Failure Analysis with Case Studies from the Oil and Gas Industry. **2016**, pp-39-54. https://doi.org/10.1016/B978-0-08-100117-2.00010-8

16) Lakowicz, J. R. Principles of Fluorescence Spectroscopy, 3rd edition, Springer, New York, **2006**, 1–95 and 529–575

Chapter 3

Deciphering conformational changes in human serum albumin induced by bile salts using spectroscopic and molecular modeling approaches

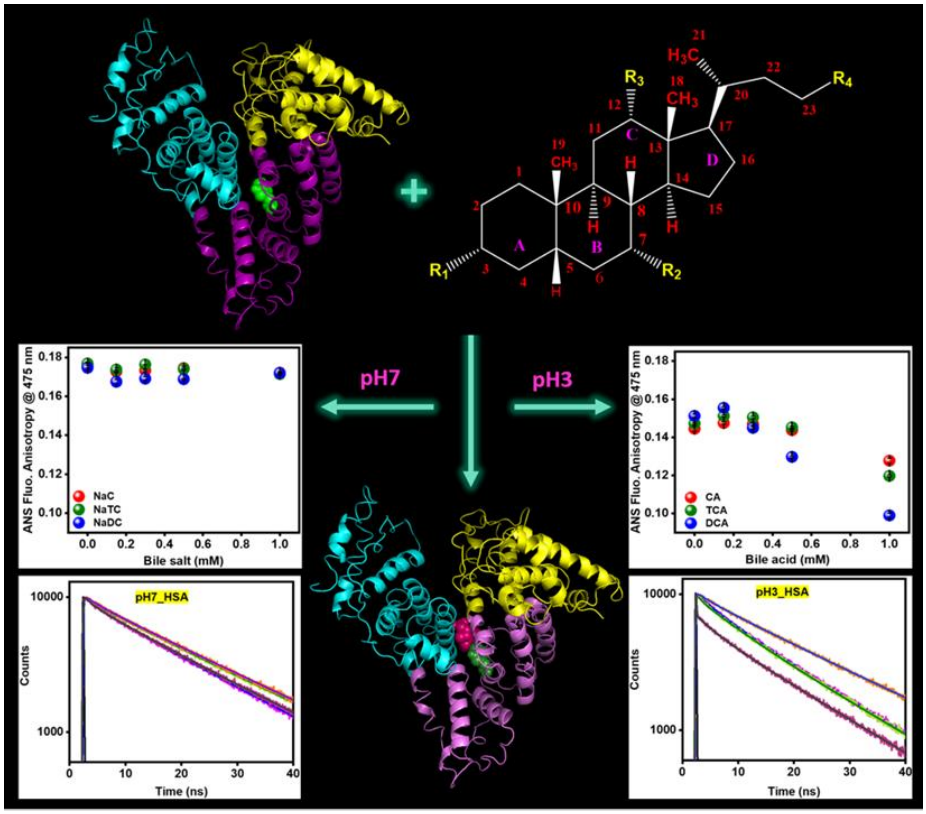

3.1 Introduction

Proteins are the molecular workhorses accounting for the majority of cell proportions and participate in practically all aspects of life. On the other hand, bile salt aggregates may encapsulate a variety of guest molecules owing to the presence of tunable binding sites on these aggregates. This, in turn, leads to a broad implementation of such supramolecular assemblies across various biological and biotechnological fields.[1]Binding surfactant molecules to proteins is widely agreed to disrupt the native structure of the majority of globular proteins. Bile salts and serum proteins form reversible complexes on the interaction that aid in transferring ligands from the plasma to the liver. Protein-biosurfactant complexes play an essential role in biochemical processes and can be employed in cosmetics, enzymatic or regulatory action, detergency, targeting specific tissues or organs for medication administration, and protein-based vaccinations since proteins have a specific and complex range of roles that are helpful and nearly impossible to replicate with simple drug molecules. However, difficulties such as protein solubility and stability in their native condition, along with their ways of administration and distribution, need to be considered, especially during the formulation of proteins as therapeutic candidates, which would be greatly facilitated by their interaction with bile salts.[2,3-6] Bile salts are frequently used to purify proteins, such as during chromatographic protein separation and protein reconstitution. In biological processes, protein-biosurfactant complexes play a crucial role. For instance, albumin-bile salt complexes are involved in entero-hepatic circulation as well as in pulmonary expansion and contraction.[7] The interaction of surfactants and proteins is a subject of great interest since it can revolutionize the functional properties of proteins.[8] Bile acids (BA) have been known to interact with plasma proteins since 1957 when Rudman and Kendall discovered that HSA protein have the highest binding affinity towards bile acids, and the affinity reduces upon introducing polar groups to the steroid moiety of Bile acids (BA).[9] In 2018, Malarkani et al. suggested that hydrophobic nature of the BSA-bile salt complex plays a key role in stabilizing the conformation of BSA, which prevents a greater degree of conformational unfolding in the presence of urea and during thermal denaturation.[10] Ghosh et al. reported the interaction between HSA-bile salts (NaC, NaTC, NaDC) at physiological conditions and revealed that the degree of interaction is directly proportional to the hydrophobic nature of bile salt.[1] Schweitzer et al. investigated the effect of BSA on sodium cholate cooperative binding induced by SDS.[6] Scagnolari et al. examined the thermodynamic

features of bile salt-human serum albumin interaction.[11] Farruggia et al. reported that binding of 3,6-disubstituted bile salts to human serum albumin induces conformational changes in the protein.[12] Rohacova et al. employed the singlet excited state properties of NBD fluorescent derivatives of cholic acid to investigate certain interesting attributes of HSA-bile acid interactions.[13] De et al. studied how cooperatively bovine serum albumin binds to bile salts. Furthermore, this study shows that covalent labelling is not always a non-perturbing approach of analysis. In some cases, using an indirect non-covalent labelling method may be more favourable.[2] To better understand pharmacokinetics and pharmacodynamics sciences as well as the role of cyanidin in the food and pharmaceutical industries in the future, Moghadam et al. investigated the binding of cyanidin with HSA and HTF, which act in the form of binary and ternary systems.[14] Rad et al. developed a method for the synthesis of Berberine nanoparticles (Nano-Ber) in order to enhance its aqueous-phase solubility and its complex formation with holo-transferrin (HTF) and human serum albumin (HSA). This study offers important details on the distribution and transportation of Nano-Ber in living things.[15] Esfandiari et al. explored how Rebeccamycin interacted with calf thymus (ctDNA) both with and without H_1. The assessment gave important information for better understanding pharmacokinetics and action mechanisms in the development of anti-cancer medicines.[16] Hosseinzadeh et al. examined the interaction between carbon nanotubes (CNTs) and human Serum Albumin (HSA) using spectroscopy and molecular modelling. These analyses are critical in drug delivery and pharmacodynamics research to have a better knowledge at nanoscale levels.[17] Taheri et al. investigated the subtle yet profoundly complex features and aspects of the interaction between SN, HSA, and calf thymus DNA (ctDNA). These findings suggest that SN binds with HSA, which reduces the proliferation of lung cancer cells mediated by apoptosis through the down regulation of PI3K/AKT/m TOR signaling pathway.[18] Chamani et al. looked at how CMCyDs affect the structure of lactoglobulin. According to the findings, hydrophobic forces play a crucial role in the stabilisation and shielding of LG-CMCyD conjugates.[19] Darban et al. investigated the physiological binding of inhibitory peptides (P4 and P6) to human serum albumin (HSA). The binding study is clearly significant in pharmacy, pharmacology, and biochemistry for understanding chemical distribution, storage, and disease therapy. These discoveries should aid in determining the appropriate chemical doses and preventing protein molecules from undergoing permanent structural changes that might jeopardise

their biological functioning.[20] To the best of our knowledge, no study has been reported till date about protein-bile salt interaction under diverse solution conditions in the literature and unexplored. As a result, this essential topic of study remains an open question. A piece of more in-depth knowledge about protein-bile salt interactions varying with pH of the medium must be investigated to decipher the interaction mechanism in terms of molecular-level analysis. The study will arise several open questions only hydrophobicity is the main responsible factor or some other specific interaction also accountable for HSA-bile salt confined complexes (as shown by autodocking hydrogen bonding is also involved but major driving factor is hydrophobicity).

In this work, we have elucidated protein structural changes during binding of bile salts of varying polarity (NaC, NaTC, and NaDC) with human serum albumin (HSA) as a model protein utilizing several spectroscopic tools under variable solution pH. Utilizing the exceptional sensitivity of fluorescence spectroscopy, we monitored the changes in the fluorescence properties of both intrinsic (tryptophan) and extrinsic fluorophores (ANS) to examine conformational variations in HSA as a consequence of complex formation with bile salts. Additionally, time-resolved fluorescence measurements provided unique structural and dynamical insights into protein-bile salt complexes. Further, we performed simulations to validate our experimental results which are described below in the following sections.

3.2. Experimental methods

3.2.1 Materials

Human Serum albumin (HSA), 8-anilinonaphthalene-1-sulfonic acid (ANS) ammonium salt, sodium citrate tribasic dihydrate, sodium phosphate monobasic dihydrate were purchased from Sigma Aldrich, India and used as such. Sodium taurocholate, sodium cholate, sodium deoxycholate were procured from Loba Chemie and used without further purification. Sodium citrate (pH 3-6) and sodium phosphate monobasic dihydrate (pH 6-7) were used for the buffer preparation. Before each pH titration experiment, all buffers were freshly prepared with double distilled water and pH was adjusted with 4N HCl or NaOH. A pH meter (EUTECH pH/Ion510) was used to check the pH of the buffers. The final pH was in the range of ± 0.02 at ~24-25 ºC. All studies were performed at least three times for reproducibility of the experiments.

3.2.2. Protein sample preparation

To conduct pH titration, the requisite HSA protein was mixed in phosphate buffer at pH 7, 5 mM to yield a stock solution of 1 mM and kept at 4°C. A UV-Visible Spectrophotometer (UV-2600 SHIMADZU) was used to estimate the precise protein concentration by measuring the tryptophan absorbance at 280 nm.[21-24] HSA protein has molar extinction coefficients of 35219 M^{-1} cm^{-1} at 280 nm. Generally, 1 mM of HSA protein in phosphate buffer (pH 7, 5 mM) medium was diluted 100-fold in respective pH buffer (pH 3, pH 7) to make the desired protein concentration of 10 μM. All measurements were carried out at room temperature (~24-25 ºC).

3.2.3 Preparation of bile-salt solution

The requisite amount of bile salts (NaC, NaTC and NaDC) was mixed in milli-Q water to yield a stock solution of 100 mM and kept at 4 °C. Working solutions of all bile salts were made fresh in the milli-Q water at a concentration of 50 mM by dilution from their respective stock solutions.

3.2.4 UV-Visible absorption measurements

The UV-Vis spectra were recorded on Shimadzu UV- 2600 UV-VIS spectrophotometer using freshly prepared HSA protein in buffer solutions over a scan range of 260-450 nm in the absence and presence of bile salts using quartz cuvette of pathlength 10 mm. The final protein concentration was kept 10 μM, and bile salt concentration was varied from 100 μM - 1 mM in a total 3 mL solution. All the samples (required buffer and HSA (10 μM) at pH 3 and 7 were incubated at room temperature (~24-25 ºC) overnight for~12-16 hours.

3.2.5 Steady-state fluorescence measurements

The fluorescence intensity and anisotropy of tryptophan and ANS were measured to probe the conformational and size changes in the pH-induced conformational isomers of monomeric HSA in the absence and presence of bile salts/ acids. The steady-state Trp fluorescence (intensity and anisotropy) measurements were performed on Fluoromax-4, Jobin Yvon (Horiba Scientific) at room temperature (~24-25 ºC), and the final protein concentration was kept at 10 μM. All the samples at pH 3 (required buffer and HSA (10 μM)) were incubated at room temperature (~24-25 ºC) overnight before measuring the Trp fluorescence. The intrinsic fluorescence was recorded by exciting the protein samples at 295 nm with scan range 330-450 nm and the excitation and emission band were fixed at 2 nm and 2 nm respectively. All the Trp fluorescence emission spectra were

scanned with integration time of 0.5 seconds and averaged over 2 scans. The final spectrum was smoothened using Savitzky-Golay algorithm available in the Origin Pro Version 2021 software.

For ANS fluorescence experiments, 10 μM of ANS was used which was obtained by suitable dilution of a stock solution (1 mM) of ANS (prepared in Milli-Q water and stored at 4°C) into protein solution (kept constant at 10 μM) prior to the ANS intensity and anisotropy measurements. Fluoromax-4, Jobin Yvon (Horiba Scientific) was used for recording ANS fluorescence intensity; the parameters were kept as follow: λ_{ex} = 350 nm, λ_{em} = 475 nm, scan range: 450-600 nm, excitation and emission bandpass 1 nm and 1.5 nm respectively. The final spectrum was an averaged over 2 scans, integration time is 0.5 sec.

The steady-state fluorescence anisotropy (r_{ss}) is given by the following relation:

$$r_{ss} = \frac{I_{\parallel} - GI_{\perp}}{I_{\parallel} + 2GI_{\perp}} \text{----------(1)}$$

where 'I_{II}' and '$I_{\perp}$' are the fluorescence intensities collected when emission polarizer is oriented parallel and perpendicular to polarized excitation, respectively, and the measured intensities were corrected using the corresponding G-factor.

For measuring tryptophan fluorescence anisotropy throughout experiments, the following parameters were adjusted: excitation wavelength (λ_{ex} = 295 nm), emission wavelength (λ_{em} = 350 nm), excitation band pass 3.5 nm, emission band pass 5.0 nm. Integration time was kept 1 sec.

For monitoring ANS fluorescence anisotropy, the following parameters were adjusted: λ_{ex} = 350 nm, λ_{em} = 475 nm, excitation band pass = 2 nm, emission band pass = 3 nm, integration time is 1 second.

3.2.6 Time-resolved emission measurements

The time-resolved fluorescence measurements were made using a time-correlated single-photon counting (TCSPC) setup (Fluorocube, Horiba Jobin Yvon, NJ). The samples were excited using a 375 nm NanoLED picosecond diode laser. The instrument response function was recorded using a diluted colloidal suspension of silica, and the full-width at half-maxima was estimated to be ~270 ps. For fluorescence lifetime measurements, the emission polarizer was set at the magic angle (54.7°) orientation with respect to the excitation polarization. An emission monochromator

was fixed at 475 nm with a band pass of 10 nm. A long-pass filter was placed just after the sample to block any scattering from the sample. All the data were acquired at 25 °C.

3.2.7 Molecular docking analysis

HSA native structure, with the PDB ID 1UOR, was obtained from the Protein Data Bank. The 3D structures of bile acid were downloaded as a 3D SDF file from PubChem and then converted to PDB format using PyMOL. The docking analysis was carried out using the AutoDock 1.5.6 software, which employs Lamarckian genetic algorithm (LGA). Additionally, a semi-flexible model for molecular docking was used, which calls for the elimination of all water molecules from the acceptor and the addition of hydrogen atoms while distributing Gasteiger charges. The docking was performed in a grid box (97 Å×105 Å×99 Å for CA), (TCA 95 Å ×87 Å ×81 Å for TCA) and (101 Å ×95 Å ×119 Å for DCA) which covered the whole protein. GA population size = 150, maximum number of energy assessments = 250 000, and GA crossover mode two points have been the autodocking specifications for choosing the optimum docking conformation. Typically, a more stable conformation is referred to as the optimum docking conformation. The Lamarck genetic algorithm (LGA) defines the docking energy as docking energy = receptor energy + ligand energy - complex energy.[25,26] The most suitable conformation with the highest binding energy (kcal/mol) was found among 20 possible conformations and selected for further investigation. The PyMOL and Ligplot^{+} v.2.2 software has been used to produce 2D figures and for in-depth analysis the varieties of interaction forces between amino acids' functional groups and ligands, and to visualize the docked conformations.

3.3 Results and discussions

Using various spectroscopic tools, we thoroughly investigated and characterized the binding patterns between pH-induced conformational isomers of HSA viz. in its native state at pH 7 and partially-unfolded, molten-globule (MG) form at pH 3 and several bile salts viz. NaC, NaTC, and NaDC. It must be noted that the apparent pK_a value of the carboxylic acid present in the bile acids vary due to structural differences. For instance, the apparent pK_a of cholic acid (CA) is 4.98, taurocholic acid (TCA) is 1.4, and deoxycholic acid (DCA) is 6.58.[27,28-33] Therefore, it implies that at pH 7, all of these bile acids will be ionized and deprotonated to form the respective bile salts whereas, under acidic conditions (at pH 3), they will exist in the protonated forms as bile acids.

3.3.1 UV-Vis absorption study

UV-Vis absorption spectroscopic tool provides primary idea about the interaction between protein-bile salt complexes. The central absorption zone of HSA protein lies in between 260-300 nm region, which depicts the absorption of aromatic amino acid residues (phenylalanine, tyrosine, and tryptophan) present in the polypeptide chain. Typically, HSA shows a prominent absorption band at ~280 nm owing to the presence of a tryptophan residue (W214).[21-24] We observed that upon addition of an increasing amount of bile salts (at pH 7) and bile acids (at pH 3) to the native and molten-globule form of HSA, respectively, the absorbance at ~280 nm increased steadily without any measurable shift in the absorption maximum (Figure 3.1a-f). This could be possibly attributed to the formation of a complex between HSA and bile salts/acids.

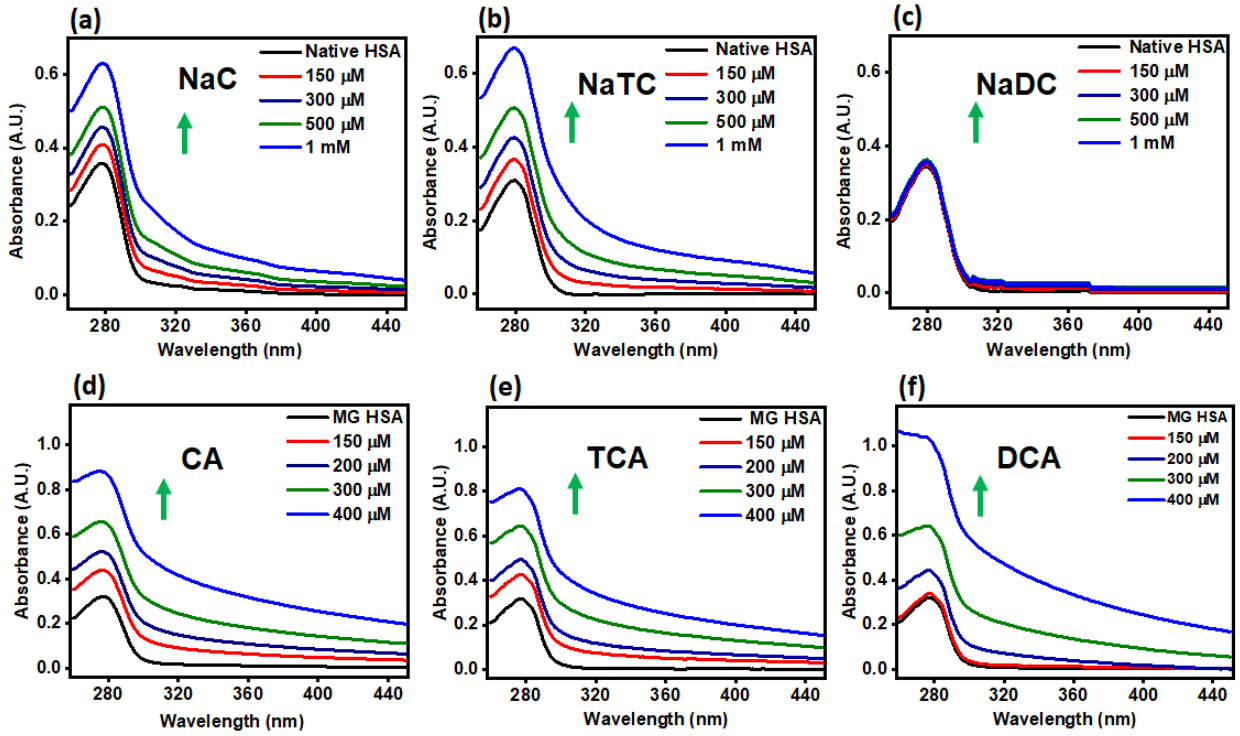

Figure 3.1. UV-Vis absorption spectra showing binding interaction of HSA (10 µM)-bile salts at various concentrations and pH conditions, (a) HSA-NaC, (b) HSA-NaTC, (c) HSA-NaDC depicts bile salts binding at pH 7 and (d) MG HSA-CA, (e) MG HSA-TCA, (f) MG HSA-DCA shows the interaction with respective bile acids at pH 3.

Furthermore, we determined the binding constants based on the changes in absorbance using the 1:1 linear Benesi-Hildebrand method to obtain the stoichiometry of the protein-bile salt/acid complex and interaction strength[34] according to the following equation:

$$\frac{1}{A_0 - A} = \frac{1}{A_0 - A_1} + \frac{1}{K[Q](A_0 - A)} \quad \text{----------(2)}$$

where, 'A_0' and 'A' are the absorbances in the absence and presence of bile salts/acids, respectively. Q denotes the concentration of bile salts/acids; 'A_1' depicts the absorbance of the respective concentrations of HSA-bile salts/acids complex at 1:1 stoichiometry. The parameter 'K' represents the values of the binding constants of various bile salts/acids. The plot ($1/A-A_0$) vs. 1/[Q] yields a straight line. The binding constants (K) were calculated from the slope and the intercept (Table 1). As expected, the binding constants of native HSA-bile salt complexes (formed at pH 7) were found to be higher than that of the partially-expanded, molten-globule HSA-bile acids-based complexes (formed at pH 3) since the molten-globule form involves a tertiary structural loss that may impede the binding efficiency of the bile acids to HSA. A careful look and comparison between the binding constants revealed that at pH 7, the binding constant varied amongst the bile salts whereas, at pH 3, the binding constants remained almost similar irrespective of the type of bile acids. Additionally, as the change in the absorbance is dependent on the modulation in the micro-environment of the chromophore (W214), we presumed that the HSA-bile salt/acid interaction possibly leads to alterations in the HSA conformation during the binding event. This prompted us to investigate the effect of bile salts/acids on the local (or short-range) protein structural changes under different solution conditions.

Bile Salt/Bile Acid	**Binding Constant (K) pH = 7**	**ΔG (kJ mol^{-1})**	**Binding Constant (K) pH = 3**	**ΔG (kJ mol^{-1})**
NaC / CA	3.87×10^2 M^{-1}	-14.77	2.34×10^2 M^{-1}	**-13.53**
NaTC / TCA	2.50×10^2 M^{-1}	-13.68	2.04×10^2 M^{-1}	**-13.13**
NaDC / DCA	6.18×10^2 M^{-1}	-15.90	3.56×10^2 M^{-1}	**-14.54**

Error limit: ±5%

Table 3.1. The binding constants (K) were determined based on changes in the absorbance using the 1:1 linear Benesi-Hildebrand method. The corresponding free energy changes (ΔG) upon binding were estimated from the binding constants using the equation ΔG = -RTlnK

3.3.2 Steady-state fluorescence study

Next, in order to gain structural insights into the short-range protein conformational changes as a consequence of binding of bile salt/acid to various pH-induced conformational isomers of HSA, we utilized multiparametric fluorescence spectroscopy. It is well-known that the emission intensity of a fluorophore is sensitive to its local environment whereas steady-state fluorescence anisotropy measurements provide information on the probe's overall flexibility when bound to macromolecules.[13,35-37] This allowed us to probe the conformational and overall size variations of monomeric HSA as a function of bile salts/acids at pH 7 and pH 3, respectively. In our studies, we monitored the changes in fluorescence intensities and anisotropies of intrinsic tryptophan and non-covalently bound ANS (at various concentrations of bile salts/acids) in order to obtain information regarding protein structural changes upon binding of bile salts/acids.

3.3.2.1 Steady-state tryptophan fluorescence study

According to the crystal structure of HSA, the protein comprises a single tryptophan residue in sub-domain IIA (W214) which is slightly exposed to the solvent, whereas ligand binding occurs primarily in sub-domains II A and III A.[1,2,38] Due to the hydrophobic nature of bile salts, they bind to sub-domain IIA and hence, interact with the lone tryptophan residing therein. It is well-known

that tryptophan is an environment-sensitive fluorophore which implies that any variation in the microenvironment of intrinsic tryptophan residue, as a consequence of changes in the protein conformation, will lead to alterations in the tryptophan fluorescence intensity. Additionally, such intensity changes may be accompanied by a spectral shift viz. a red shift is observed if the tryptophan is exposed to an aqueous environment whereas, a blue shift indicates that the tryptophan residue is buried deep inside the protein core.[36]

At neutral pH (pH 7), the tryptophan (Trp-214) of the native monomeric protein fluoresced intensely at ~350 nm. We observed that upon addition of an increasing amount of bile salts (NaC, NaTC, and NaDC) to HSA, the tryptophan fluorescence intensity decreased significantly accompanied by a blue shift (~14 nm for NaC, ~13 nm for NaTC, and ~18 nm for NaDC) in the emission maxima. (Figures 3.2a, b, c) This blue shift can be ascribed to the formation of a bile salt-protein complex accompanied by a conformational change in HSA, and indicates that Trp-214 experiences more hydrophobic environment and is buried inside the protein scaffold as bile salt concentrations are increased progressively. Moreover, the reduction in tryptophan emission may be due to the presence of certain amino acid residues viz. lysine, glutamate, arginine, phenylalanine, etc. present in its immediate vicinity.[36,39] Under acidic solution condition (pH 3), addition of bile acids to the partially-expanded, molten-globule state of HSA also showed a variation in tryptophan emission. Addition of cholic acid (CA) and taurocholic acid (TCA) to HSA resulted in a gradual drop in Trp-214 emission although the extent of decrease was significantly lesser than that observed at pH 7 without any measurable blue shift (Figures 3.2d, e, f) suggesting that these bile acids were unable to perturb the protein structure to the same extent at pH 3 compared to that at pH 7. This is expected as the molten globule form of HSA at pH 3 exists as a partially-unfolded conformer and the binding of bile acids to HSA might be non-specific whereby the partially-expanded protein conformation remains largely unaffected. On the contrary, a gradual addition of deoxycholic acid (DCA) to HSA resulted in a substantial increase in tryptophan emission along with a blue shift of ~14 nm. This indicated that addition of DCA might influence protein conformational changes whereby tryptophan gets buried into a more hydrophobic environment. However, non-specific interactions between the hydrophobic surface of DCA and tryptophan cannot be ruled out. From these observations, we inferred that hydrophobic interactions are the major driving forces during HSA-bile salts/acids binding events.

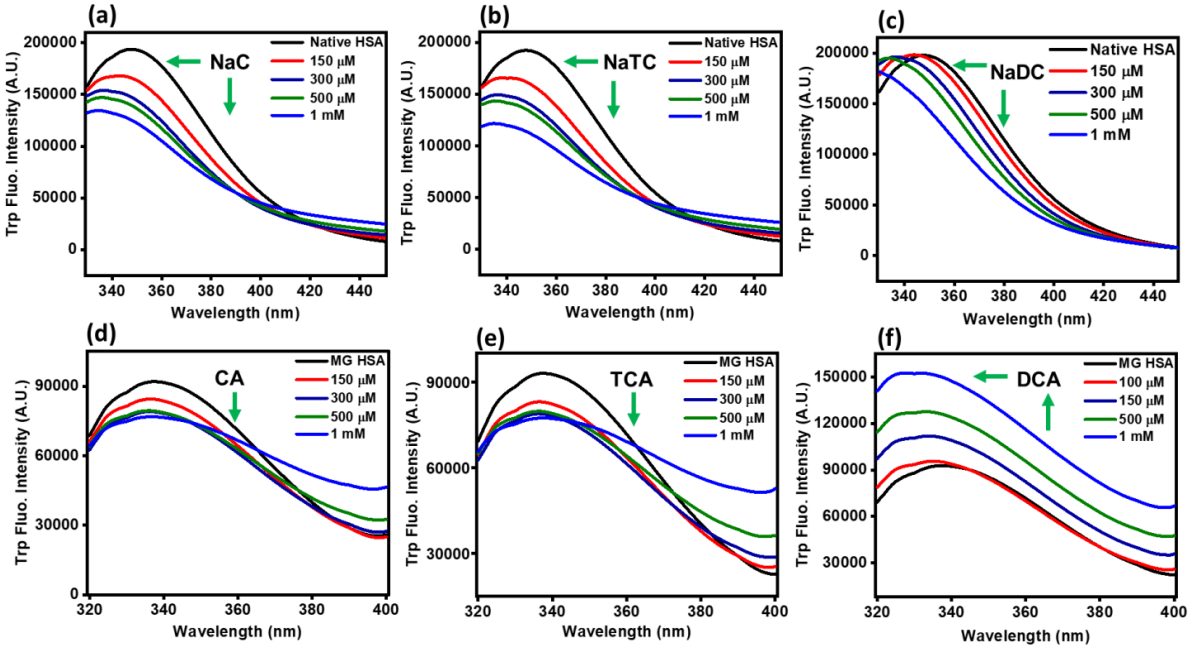

Figure 3.2. Tryptophan fluorescence emission spectra for HSA-bile salt at pH 7 (a) HSA-NaC, (b) HSA-NaTC, (c) HSA-NaDC and HSA molten globule (MG) -bile acid at pH 3 (d) MG HSA-CA, (e) MG HSA-TCA, (f) MG HSA-DCA. (λ_{ex} 295 nm, [HSA] = 10 μM)

3.3.2.2 Steady-state tryptophan anisotropy study

As we mentioned earlier, the protein structural changes upon bile salts/acids binding were also monitored using steady-state fluorescence anisotropy of the intrinsic tryptophan (W214). The steady-state anisotropy values indicate a fluorophore's rotational flexibility. Greater the flexibility, lower is the anisotropy and vice-versa.[35] Based on our aforementioned spectroscopic findings, we expected that at pH 7, we would observe an increase in the W214 anisotropy with an increasing concentration of bile salts due to HSA-bile salt complexation. Nevertheless, no significant changes in the tryptophan anisotropy were observed compared to that of the native HSA in the absence of bile salt (Figure 3.3a). This was quite surprising given the fact that our tryptophan emission data suggested that HSA-bile salt complex formation involved conformational changes in the protein leading to the sequestration of tryptophan into the hydrophobic interior. In contrast, upon addition of bile acids to HSA at pH 3, the tryptophan anisotropy remained almost constant at lower concentrations of bile acids (up to 300 μM) which was found to be similar to that of the MG-HSA in the absence of bile acid. However, at higher bile acid concentrations, binding of both cholic acid

and taurocholic acid led to a significant increase in the tryptophan anisotropy indicating a dampening in the rotational flexibility of tryptophan. This could be due to non-specific binding of bile acids to HSA in the vicinity of tryptophan in addition to the formation of a loosely-bound HSA-bile acid complex. On the other hand, at a higher concentration of deoxycholic acid, a sharp decrease in the tryptophan anisotropy was observed (Figure 3.3b) which suggested that DCA resulted in a significant structural loss of the partially-unfolded, molten globule protein conformer to a greater extent leading to an enhancement in the rotational flexibility and hence, a drop in the fluorescence anisotropy was observed.

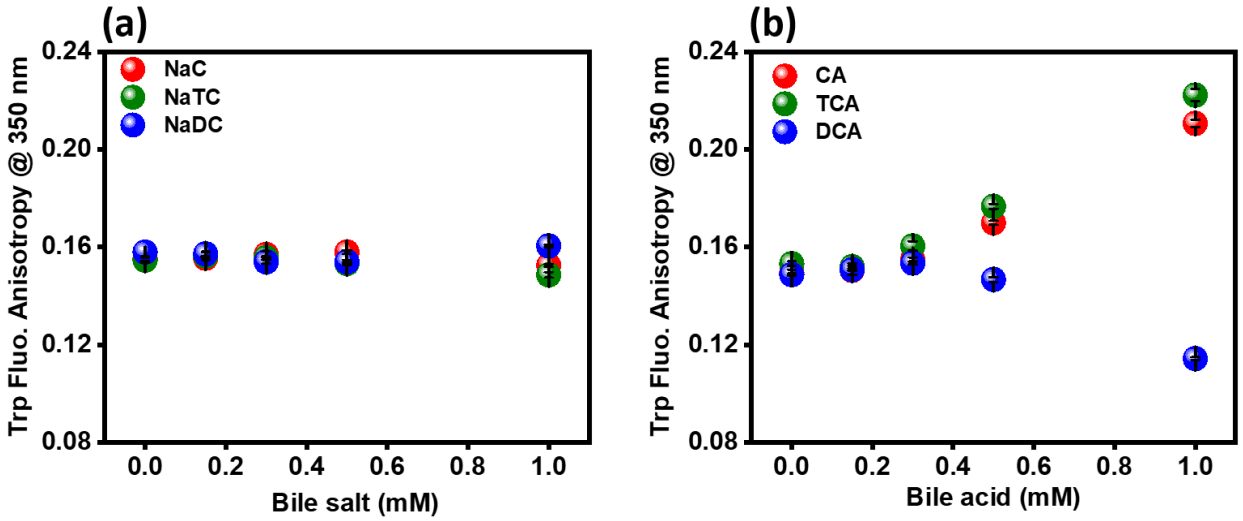

Figure 3.3. Conformational changes in HSA as a function of pH and bile salts studied using steady-state fluorescence spectroscopy (a) Tryptophan fluorescence emission for HSA -bile salt (NaC, NaTC, NaDC) at pH 7 (b) Tryptophan fluorescence emission at pH 3 for MG HSA-bile acids (CA, TCA, DCA), (c) Tryptophan anisotropy for HSA -bile salts at pH 7 (d) Tryptophan anisotropy for MG HSA-bile acids at pH 3. The intensity and anisotropy error bars are included in the symbols. (λ_{ex} 295 nm, [HSA] = 10 μM)

3.3.2.3 Steady-state ANS fluorescence study

Next, in order to investigate the changes in hydrophobicity in HSA as a function of bile salts/acids concentrations at both pH 7 and pH 3, we utilized an extrinsic fluorophore namely, 8-anilinonaphthalene-1-sulfonic acid (ANS) which binds non-covalently to the protein. ANS is weakly fluorescent in an aqueous medium but fluoresces strongly when it is attached to a

hydrophobic site (with a corresponding blue shift in its emission maxima from ~515 nm to ~475 nm).[13,35,37] It has been reported earlier that at low ANS concentrations, ANS binds to the hydrophobic regions present within domains II and III of HSA but it exhibits a preferential binding towards the sub-domain III A. It has also been suggested that the binding domains II A and III A of HSA share a common interface; thus, binding in domain III impacts protein conformational changes and binding affinities in domain II.[38,40,41] In our studies, we observed that in the absence of any bile salt, ANS showed an intense emission at ~465 nm upon binding to the hydrophobic sites of the native HSA at pH 7 which corroborates with the earlier reports.[34] As incremental amounts of bile salt NaC (150-500 μM) were added to the native HSA, the intensity of ANS fluorescence at ~465 nm dropped progressively with a red shift (~465 to ~470) (~5 nm) then blue shift with NaC (500 μM-1 mM) (Figure 3.4a). This might be attributed to the fact that since the amphiphilic bile salt was preferentially bound to the hydrophobic pockets of HSA, it interfered and plausibly inhibited the binding of ANS to the same hydrophobic regions that led to a drop in the ANS emission intensity. However, a slight blue shift at a higher bile salt concentration suggested that there could be non-specific binding of ANS to HSA and/or ANS was bound at the interface of HSA and bile salts. On the other hand, upon increasing the bile acid (CA) concentration at pH 3 in the presence of MG-HSA, we observed an increase in ANS emission without any spectral shift implying that ANS could efficiently bind to the molten globule form as it comprised more exposed hydrophobic sites compared to that of the native protein. Nevertheless, ANS emission was the highest when DCA was added to MG-HSA (Figure 3.4c) which reaffirmed that DCA induced a significant conformational change within MG-HSA due to stronger binding as compared to other bile acids implying that hydrophobicity is the primary driving force during HSA-bile salt/acid binding.

3.3.2.4 Steady state ANS anisotropy study

Next, we monitored the changes in ANS fluorescence anisotropy as a function of addition of various bile salt/acid concentrations to pH-induced conformational isomers of HSA at pH 7 (Figure 3.4d) and pH 3 (Figure 3.4e), respectively. In the absence of bile salt, a significantly higher value of ANS anisotropy compared to free ANS was observed. This suggested that ANS was non-covalently bound to the hydrophobic pockets of HSA and consequently, the rotational mobility of ANS was restricted that resulted in a higher anisotropy value. Upon the addition of bile salts (NaC,

NaTC, NaDC) to native HSA at pH 7, we hypothesized that the bile salts would also bind to the hydrophobic pockets of HSA following the displacement of bound ANS. As a consequence, ANS would be released into the aqueous environment, its rotational flexibility would increase which would result in a substantial drop in its fluorescence anisotropy. On the contrary, we observed a small but measurable reduction in the ANS anisotropy, indicating that upon binding of the bile salt, ANS was either bound to the bile salt-HSA hydrophobic interface or bound non-specifically to other sites of HSA and/or to bile salts as well. Therefore, the rotational flexibility of ANS remained restricted. Nevertheless, we observed a lower anisotropy of ANS bound to the MG-HSA at pH 3 in the absence of bile acid compared to that at pH 7. Upon addition of bile acids (CA, TCA, DCA) to MG-HSA at pH 3, the ANS anisotropy remained almost similar till 500 µM of CA and TCA whereas it demonstrated a larger variability and reduction in anisotropy as a function of DCA concentration. Also, at higher concentrations of bile acids, a significant drop in ANS anisotropy was observed irrespective of the nature of the bile acid, however, the extent of reduction was found to be the largest in the presence of DCA than that in the presence of other two bile acids. These findings reaffirmed that DCA exhibited stronger binding in the hydrophobic subdomain II A of HSA which resulted in extensive protein conformational changes that also supported our previous results.

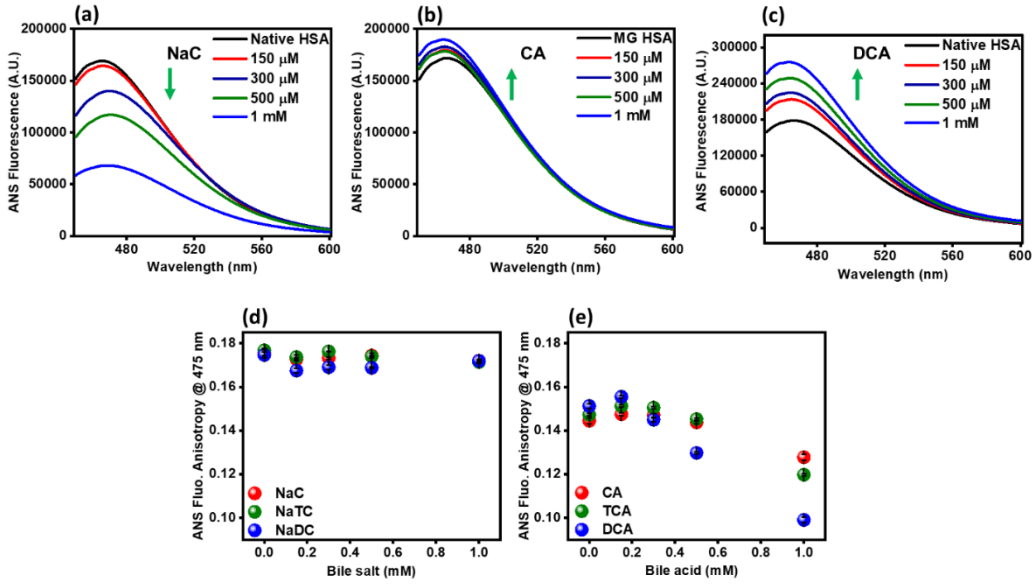

Figure 3.4. Bile salts-induced protein conformational changes monitored using hydrophobic probe under variable bile salt concentration. Changes in ANS fluorescence spectra of (a) HSA -bile salt

(NaC) at pH 7, (b) MG HSA -bile acids (CA) at pH 3, (c) MG HSA-bile acids (DCA) (10 µM) at pH 3. Changes in ANS fluorescence anisotropy of (d) HSA-bile salts (NaC, NaTC, NaDC) at pH 7, (e) MG HSA-bile salts (CA, TCA, DCA) at pH 3. The error bars are included in the symbols. (λ_{ex} = 350 nm, λ_{em} = 475 nm, [HSA] = 10 µM)

3.3.3 HSA-bile salt interaction using time-resolved emission study

While local and global dynamics are averaged out, steady-state anisotropy does not always offer evident local flexibility and size assignments.[21,42] We used time-resolved fluorescence emission spectroscopy to separate variation from local flexibility variations Figure 3.5 shows the typical time-resolved fluorescence decay patterns of ANS bound to HSA in the presence of different bile salt concentrations at pH 7 (Figures 3.5a, b, c) and different bile acid concentrations at pH 3 (Figures 3.5d, e, f) and the decay parameters are compiled in Table 2.

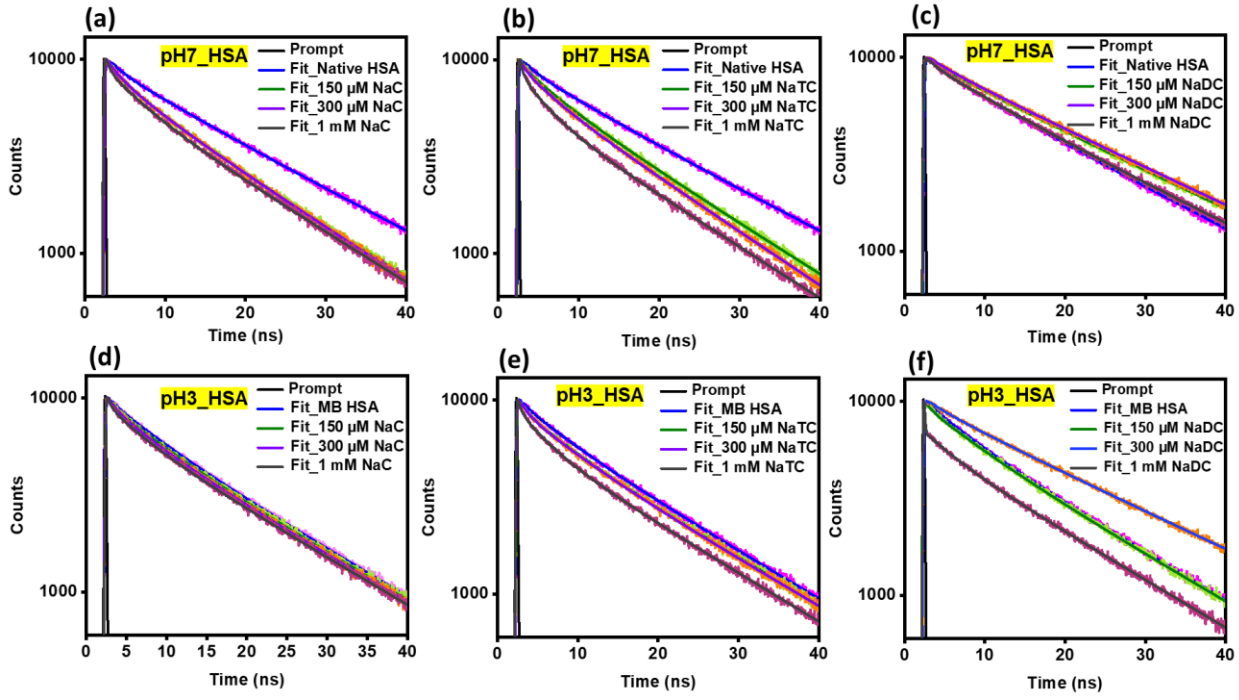

Figure 3.5. Time-resolved fluorescence decay profiles using hydrophobic probe ANS of (a) HSA -bile salts (NaC, NaTC, NaDC) at pH 7, (b) MG HSA-bile acids (CA, TCA, DCA) at pH 3. (λ_{ex} = 350 nm, [HSA] = 10 µM)

	Fluorescence lifetime in ns (amplitude)			Mean lifetime in ns	
System	τ_1 (α_1)	τ_2 (α_2)	τ_3 (α_3)	τ_m	χ^2
HSA_ANS_pH7	7.66 (0.16)	0.63 (0.11)	20.52 (0.73)	16.27	1.10
HSA_ANS_pH7_NaC_150 µM	0.96 (0.18)	6.699 (0.21)	16.94 (0.61)	11.92	1.12
HSA_ANS_pH7_NaC_300 µM	0.95 (0.08)	3.93 (0.18)	15.66 (0.74)	12.34	1.08
HSA_ANS_pH7_NaC_1 mM	0.45 (0.24)	4.72 (0.21)	16.77 (0.55)	10.29	1.09
HSA_ANS_pH7_NaTC_150 µM	0.65 (0.13)	4.81 (0.18)	16.29 (0.69)	12.27	1.01
HSA_ANS_pH7_NaTC_300 µM	0.50 (0.14)	3.61 (0.18)	15.39 (0.68)	11.18	1.04
HSA_ANS_pH7_NaTC_1mM	0.37 (0.32)	3.44 (0.23)	16.13 (0.46)	8.25	1.10
HSA_ANS_pH7_NaDC_150 µM	1.63 (0.07)	9.79 (0.11)	22.46 (0.82)	19.63	1.04
HSA_ANS_pH7_NaDC_300 µM	2.54 (0.06)	10.08 (0.09)	22.68 (0.86)	20.44	1.07
HSA_ANS_pH7 _NaDC_1mM	1.12 (0.12)	10.46 (0.21)	22.13 (0.68)	17.30	1.01
HSA_ANS_pH3	0.58 (0.09)	5.71 (0.19)	17.46 (0.72)	13.76	1.06
HSA_ANS_pH3_NaC_150 µM	0.69 (0.13)	5.55 (0.19)	17.50 (0.68)	13.10	1.07
HSA_ANS_pH3_NaC_300 µM	0.65 (0.14)	4.89 (0.19)	17.33 (0.67)	12.63	1.07
HSA_ANS_pH3_NaC_1 mM	0.45 (0.22)	4.63 (0.18)	17.50 (0.60)	11.48	1.07
HSA_ANS_pH3_NaTC_150 µM	0.76 (0.16)	6.05 (0.20)	17.81 (0.64)	12.79	1.08
HSA_ANS_pH3_NaTC_300 µM	0.87 (0.17)	6.15 (0.20)	17.82 (0.63)	12.62	1.09
HSA_ANS_pH3_NaTC_1 mM	0.35 (0.26)	3.56 (0.22)	16.87 (0.52)	9.72	1.15
HSA_ANS_pH3_NaDC_150 µM	0.53 (0.16)	6.95 (0.20)	18.15 (0.64)	13.01	1.13

HSA_ANS_pH3_NaDC_300 µM	0.13 (0.32)	4.97 (0.14)	17.47 (0.54)	10.22	1.06
HSA_ANS_pH3_NaDC_1 mM	0.05 (0.90)	4.14 (0.02)	17.33 (0.08)	1.48	1.09

Table 3.2. Time-resolved emission parameters of at different pH conditions (pH 3 and pH 7).

It is clearly evident that the addition of the bile salts gradually reduces the average fluorescence lifetime of ANS in HSA Similar to the steady-state measurements, the pattern of fluctuation in the average lifetimes of ANS upon interaction with the various bile salts can be seen here as well. A substantially higher value of ANS lifetime was discovered when bile salt was not present. This indicated that the hydrophobic pockets of HSA were non-covalently bonded to ANS. When bile salts (NaC, NaTC, and NaDC) were added to native HSA at pH 7, we predicted that the bile salts would likewise attach to the hydrophobic spots of HSA after displacing bound ANS. As a result, ANS would be released into the aquatic environment, where it would experience an increase in rotational flexibility and a significant decrease in lifespan value. Instead, we noticed a little but discernible decline, indicating that ANS was either linked to the hydrophobic interface between the bile salt and HSA or non-specifically to other regions of HSA and/or bile salts following binding of the bile salt. As a result, ANS's rotational flexibility was still limited. Despite this, we found that ANS bound to MG-HSA decayed more slowly at pH 3 in the absence of bile acid than it did at pH 7. When bile acids (CA, TCA, and DCA) were added to MG-HSA at pH 3, it was discovered that the extent of reduction was greater in the presence of DCA than it was in the presence of the other two bile acids. These results confirmed that DCA showed increased binding in the HSA hydrophobic subdomain II A, leading to significant protein conformational changes, and also highlights the fact that hydrophobicity underlines this binding interaction. Scattered plots for ANS lifetime decay for HSA at pH 7 (Figure 3.6a) and pH 3 (Figure 3.6b) are further complementing the above explanation very well.

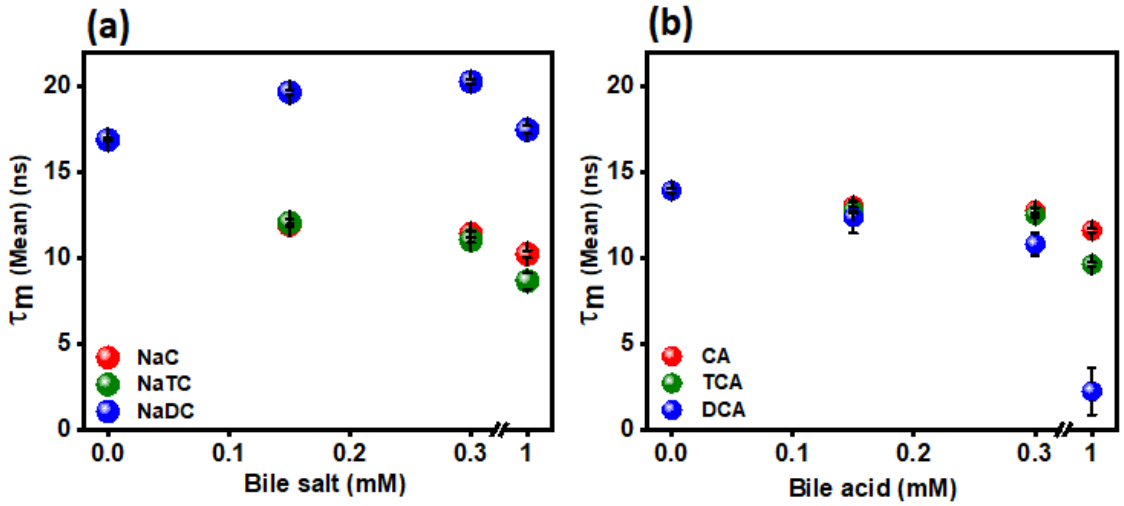

Figure 3.6. Scattered spectra showing dynamical insights into the HSA-biosurfactant interactions using hydrophobic probe ANS (a) Time-resolved fluorescence spectra HSA-bile salts (NaC, NaTC, NaDC) at pH 7, (b) MG HSA-bile acids (CA, TCA, DCA) at pH 3. The error bars are included in the symbols. (λ_{ex} = 350 nm, [HSA] = 10 μM)

3.3.4 Molecular docking results

Next, we directed our efforts in gaining molecular insights into the HSA-bile acid binding using molecular docking which also shed light into the average binding energy of various bile acid used in this study. Results obtained from our molecular docking studies revealed that the hydrophobic sub-domain IIA of HSA is an excellent binding site for all the three bile salts. Figure 3.7a depicts the binding of cholic acid in the subdomain IIA of HSA. We also observed variations in the free energy changes, pertaining to the bile acid docking onto HSA varies amongst different bile acids viz. for DCA (ΔG_{dock} = -29.64 kJ mol^{-1}), for CA (ΔG_{dock} = -26.15 kJ mol^{-1}), and for TCA (ΔG_{dock} = -14.35 kJ mol^{-1}), which depicts that DCA exhibits the highest binding energy among all the three owing to its hydrophobicity and satisfactorily supports our spectroscopic data that corroborates with the reported literature.[1] Trp-214 experiences more hydrophobic environment and is buried inside the protein scaffold as bile salt concentrations are increased progressively. Moreover, the drop in the tryptophan emission intensity could be due to quenching by nearby residues such as tyrosinate ion (from tyrosine residues), deprotonated carboxyl (from aspartic and glutamic acid residues), protonated amino groups (from lysine residues), protonated imidazole (from histidine residues), phenylalanine, arginine, and nearby disulfide bridges.[36,38] Additionally, we visualize

information on the residue-specific interactions with the bile acids. For instance, amino acid residues which are involved in the formation of hydrogen bonds with cholic acid are Lys 195, Arg 222, Glu 292, and Lys 436 as seen with the help of PyMOL (Figure 3.7b). Moreover, the Ligplot software further allowed us to visualize residue-specific hydrophobic interactions which further corroborated our PyMol depiction of hydrogen bonded residues and further revealed that the residues Arg 218, Glu 294, Asn 295, Lys 444, Pro 447, Cys 448, Asp 451, and Tyr 452 are involved in the hydrophobic interactions (Figure 3.7c). Similarly, details of amino acids residues of HSA participating in such kinds of non-covalent interactions with other bile acids are also shown. (Figures 3.7d, e, f, g, h, i) Taken together, it is reasonable to assume that the extent of binding is maximum for DCA and occurs in the following order: DCA > CA > TCA, which is a clear indication that the hydrophobicity plays a predominant role during the binding event with HSA. Furthermore, we also inferred that in addition to the hydrophobic interactions, electrostatic interactions also play a substantial role.

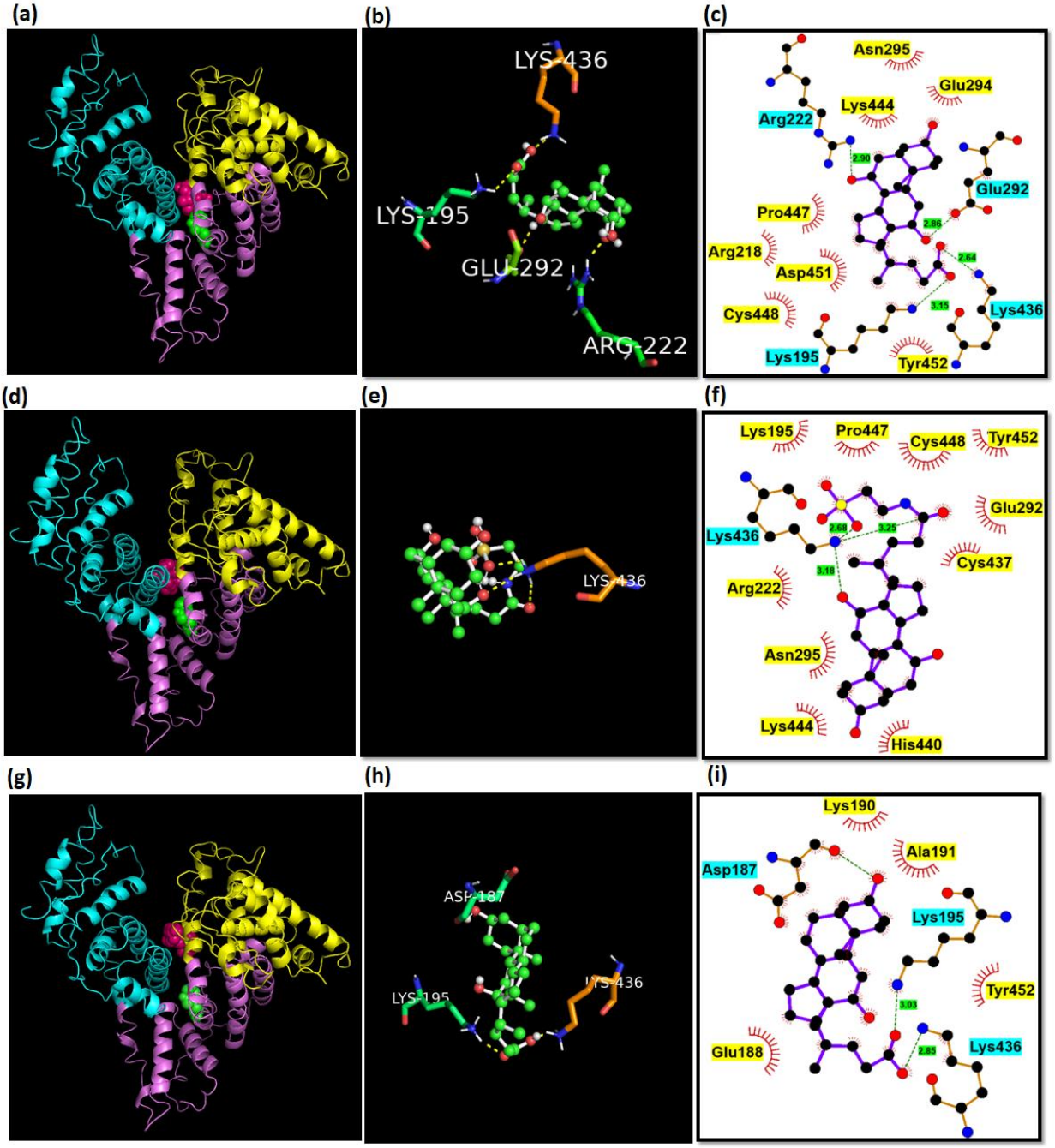

Figure 3.7. (a, d, h) Results obtained using molecular docking of HSA-CA, HSA-TCA and HSA-DCA (domain I - yellow, domain II - purple, domain III - cyan) where spheres (hot pink) represent the CA, TCA and DCA, respectively that are bound in subdomain II A and green color represents the only tryptophan (W214) present in HSA obtained using PyMol (Schrödinger Inc., New York). (b, e, h) All protein residues that are hydrogen bonded to ligand (CA, TCA, DCA respectively) are

shown using PyMOL (Schrödinger Inc., New York). (c, f, i) All the protein residues, represented in cyan, are hydrogen bonded to the ligand whereas, the residues, represented in yellow, depict hydrophobic interaction with CA. Figures 3.7c, f, i was obtained using Ligplot^{+} v.2.2.

3.5 Conclusions

According to various spectroscopic methods employed here, the hydrophobicity of the bile salts appears to be the primary factor governing the interaction between bile salts and HSA. While NaDC is the most hydrophobic among the bile salts reported in this study, molecular docking results on HSA-bile salt supramolecular complexes indicate spontaneous binding of bile salts into subdomain IIA of HSA while suggesting that the binding affinity decreases with the decreasing order of hydrophobicity of the bile salts (NaDC>NaC>NaTC). Additionally, our experimental findings involving steady-state and time-resolved spectroscopic approaches shed light into the extent of structural perturbation in the pH-induced conformational isomers of HSA in the presence of bile salts. We observed that upon addition of bile salts, the well-folded, globular native structure of HSA is significantly perturbed compared to that in the partially-unfolded, molten-globule-like conformer as expected. We believe that the structural and dynamical insights described herein will be helpful in the design and formulation of protein-bile salt-based pharmacological carriers suitable for drug delivery.

References

1. Ghosh, N.; Mondal, R.; Mukherjee, S. Hydrophobicity Is the Governing Factor in the Interaction of Human Serum Albumin with Bile Salts. *Langmuir* **2015**, *31*, 1095−1104. https://doi.org/10.1021/la504270a
2. De, S.; Das, S.; Girigoswami, A. Spectroscopic probing of bile salt–albumin interaction. *Colloids Surf. B* **2007**, *54*, 74–81. https://doi.org/10.1016/j.colsurfb.2006.09.015
3. Vasilescu, M.; Angelescu, D. Interactions of Globular Proteins with Surfactants Studied with Fluorescence Probe Methods. *Langmuir* **1999**, *15*, 2635-2643. https://doi.org/10.1021/la981424y
4. Palacios, A. C.; Antonelli, M. L.; Mesa, C. L. Interactions between bovine serum albumin and sodium taurodeoxycholate: thermodynamic properties. *Thermochim. Acta*. **2004**, *418*, 69-77. https://doi.org/10.1016/j.tca.2003.11.043

5. Malarkani, K.; Sarkar, I.; Selvam, S. Denaturation studies on bovine serum albumin–bile salt system: Bile salt stabilizes bovine serum albumin through hydrophobicity. *J. Pharm. Anal.* **2018**, *8*, 27–36. https://doi.org/10.1016/j.jpha.2017.06.007
6. Schweitzer, B.; Felippe, A. C.; Bó, A. D.; Minatti, E.; Zanette, D.; Lopes, A. Sodium dodecyl sulfate promoting a cooperative association process of sodium cholate with bovine serum albumin. *J. Colloid Interface Sci.* **2006**, *298*, 457–466. https://doi.org/10.1016/j.jcis.2005.12.025
7. Antonelli, M. L.; Capalbi, A.; Gente, G.; Palacios, A.C.; Sallustio, S.; Mesa C. L. Thermodynamic properties of the bovine serum albumin–sodium taurodeoxycholate system. *Colloids Surf, A Physicochem Eng Asp.* **2004**, *246*, 127–134. https://doi.org/10.1021/j150660a057
8. Ren, H.; Xin, X.; Wang L.; Ju, H.; Zhamanding, A.; Xu, G. A direct comparison of the interaction of bovine serum albumin and gelatin with sodium deoxycholate in aqueous solutions. *J. Mol. Liq.* **2015**, *207*, 164–170. https://dx.doi.org/10.1016/j.molliq.2015.03.017
9. Rudman, D.; Kendall, F. E.; Bile Acid Content of Human Serum. I. Serum Bile Acids in Patients with Hepatic Disease. *J. Clin. Invest.* **1957**, *36*, 530-537. https://doi.org/10.1172/JCI103450
10. Malarkani, K.; Sarkar, I.; Selvam, S. Denaturation studies on bovine serum albumin–bile salt system: Bile salt stabilizes bovine serum albumin through hydrophobicity. *J. Pharm. Anal.* **2018**, *8*, 27–36. https://doi.org/10.1016/j.jpha.2017.06.007
11. Scagnolari, F.; Roda, A.; Fini, A.; Grigolo, B. Thermodynamic features of bile salt-human serum albumin interaction. *Biochim. Biophys. Acta* **1984**, *791*, 274-277. https://doi.org/10.1016/0167-4838(84)90019-0
12. Farruggia, B.; Picó G. A. The binding of 3,6-disubstituted bile salts to human serum albumin induces conformational change on the molecule of this protein. *Biochim. Biophys. Acta* **1999**, *1429*, 299-306. https://doi.org/10.1016/S0167-4838(98)00192-7
13. Rohacova, J.; Marin, M. L.; Miranda, M. A.; Complexes between Fluorescent Cholic Acid Derivatives and Human Serum Albumin. A Photophysical Approach to Investigate the Binding Behavior. *J. Phys. Chem. B* **2010**, *114*, 4710–4716. https://doi.org/10.1021/jp911114n

14. Moghadam, S.K.; Toroghi, S. E.; Vatanparast, M. K.; Jouyaeian, P.; Mokaberi, P.; YazdyaH.; Tehranizadeh, N. Z. A.; Saberi, M. R.; Chamani, J. Novel perspective into the interaction behavior study of the cyanidin with human serum albumin-holo transferrin complex: Spectroscopic, calorimetric and molecular modeling approaches. *J. Mol. Liq.* **2022**, *356*, 119042-119061. https://doi.org/10.1016/j.molliq.2022.119042
15. Rad, A. S.; Mehrzad, J.; Darroudi, M.; Saberi, M. R.; Chamani, J. Oil-in-water nanoemulsions comprising Berberine in olive oil: Biological activities, binding mechanisms to human serum albumin or holotransferrin, and QMMD simulation. *J. Biomol. Struct.* **2021**, *39*, 1029-1043. https://doi.org/10.1080/07391102.2020.1724568
16. Esfandiari, Z. M.; Noghani, A. R.; Sohrabi, T.; Mokaberi, P.; Tehranizadeh, Z. A.; Chamani, J. Molecular Dynamics and Multi-Spectroscopic of the Interaction Behavior between Bladder Cancer Cells and Calf Thymus DNA with Rebeccamycin: Apoptosis through the Down Regulation of PI3K/ AKT Signaling Pathway. *J. Fluoresc.* **2023**, *33*, 1537-1557. https://doi.org/10.1007/s10895-023-03169-4
17. Hosseinzadeh, M.; Nikjoo, S.; Zare, N.; Delavar, D.; Beigoli, S.; Chamani, J. Characterization of the structural changes of human serum albumin upon interaction with single-walled and multi-walled carbon nanotubes: spectroscopic and molecular modeling approaches. *Res. Chem. Intermed.* **2019**, *45*, 401-423. https://doi.org/10.1007/s11164-018-3608-5.
18. Taheri, R.; Hamzkanlu, N; Rezvani, Y.; Niroumand, S.; Samandar, F.; Tehranizadeh, Z. A.; Saberi, M. R.; Chamani, J. Exploring the HSA/DNA/lung cancer cells binding behavior of p-Synephrine, a naturally occurring phenyl ethanol amine with anti-adipogenic activity: multi spectroscopic, molecular dynamic and cellular approaches. *J. Mol. Liq.* **2022**, *368*, 120826-120844. https://doi.org/10.1016/j.molliq.2022.120826
19. Chamani, J.; Movahedi, A. A. M.; Hakimelahi, G. H. Structural changes in β-lactoglobulin by conjugation with three different kinds of carboxymethyl cyclodextrins. *Thermochim. Acta* **2005**, *432*, 106-111. https://doi.org/10.1016/j.tca.2005.04.014
20. Darban, R. A.; Shareghi, B.; Asoodeh, A.; Chamani, J. Multi-spectroscopic and molecular modeling studies of interaction between two different angiotensin I converting enzyme inhibitory peptides from gluten hydrolysate and human serum albumin. *J. Biomol. Struct.* **2017**, *35*, 3648-3662. https://doi.org/10.1080/07391102.2016.1264892

21. Alsamamra, H.; Khalid, I.; Alfaqeh, R.; Farroun, M.; Abuteir, M.; Darwish, M. Spectroscopic Investigation of Procaine interaction with Human Serum Albumin. *J. Biomed. Sci.* **2018**, *7,* 3-8. https://doi.org/10.4172/2254-609X.100087
22. Rub, M. A.; Khan, J. M.; Azum, N.; Asiri, A. M. Influence of antidepressant clomipramine hydrochloride drug on human serum albumin: Spectroscopic study. *J. Mol. Liq.* **2017**, *241*, 91-98. https://doi.org/10.1016/j.molliq.2017.05.143
23. Li, M.; Zhou, D.; Wu, D.; Hu, X.; Hu, J.; Geng, F.; Cheng, L. Comparative analysis of the interaction between alpha-lactalbumin and two edible azo colorants equipped with different sulfonyl group numbers. *Food Chem.* **2023**, *416*, 135826-135836. https://doi.org/10.1016/j.foodchem.2023.135826
24. Arya, S.; Kumari, A.; Dalal, V.; Bhattacharya M.; Mukhopadhyay, S. Appearance of annular ring-like intermediates during amyloid fibril formation from human serum albumin. *Phys. Chem. Chem. Phys.* **2015**, *17*, 22862-22871. https://doi.org/10.1039/C5CP03782D
25. Wu, W.; Hu, X.; Zeng, Z.; Wu, D.; Li, H.; Li, Hui. Characterization of the Binding Properties of Sorafenib to c-MYC G-Quadruplexes: Evidence for Screening Potential Ligands. J. Phys. Chem. B **2023**, 127, 4, 874–883. https://doi.org/10.1021/acs.jpcb.2c06488
26. Li, M.; Zhou, D.; Wu, D.; Hu, X.; Hu, J.; Geng, F.; Cheng, L. Comparative analysis of the interaction between alpha-lactalbumin and two edible azo colorants equipped with different sulfonyl group numbers. *Food Chem.* **2023**, *416*, 135826-135836. https://doi.org/10.1016/j.foodchem.2023.135826
27. Maity, B.; Ahmed, S. A.; Seth, D. Interaction of Biologically Active Flavin inside Bile Salt Aggregates: Molecular Level Investigation. J. Phys. Chem. B **2016**, 120, 9854–9866. https://doi.org/10.1021/acs.jpcb.6b04870
28. Garidel, P, Hildebrand, A.; Knauf K.; Blume, A. Membranolytic Activity of Bile Salts: Influence of Biological Membrane Properties and Composition. *Molecules* **2007**, *12*, 2292-2326. https://doi.org/10.3390/12102292
29. Vlahcevic, Z. R.; Schwartz, C. C.; Gustafsson, J.; Halloran, L. G.; Danielsson, H.; Swell, L. Biosynthesis of bile acids in man. *J. Biol. Chem.* **1980**, *255*, 2925-2933. https://doi.org/10.1016/S0021-9258(19)85829-5

30. Menzies, J. A. Observation on the secretion and composition of human bile. *Biochem. J.* **1912**, *6*, 210-218. https://doi.org/10.1042/bj0060210
31. Heinze, W. L. Organized Assemblies in Chemical Analysis. *JAI Press*. 1996, 2, 87-99.
32. Sharma, P.; Sohal, N.; Maity, B. Encapsulation and release of non-fluorescent crystal violet confined in bile-salt aggregates. *RSC Adv.* **2021**, *11*, 10912–10921. https://doi.org/10.1039/d0ra06599d
33. Moroi, Y. Micelles. Theoretical and Applied Aspects. *Springer-Verlag*. **1992**, *49*, 492– 497
34. Sohal, N.; Maity B.; Basu, S. Carbon Dot–MnO_2 Nanosphere Composite Sensors for Selective Detection of Glutathione. *A*CS Appl. Nano Mater. **2020**, 3, 5955–5964. https://doi.org/10.1021/acsanm.0c01088
35. Bhattacharya, M.; Mukhopadhyay, S. Structural and Dynamical Insights into the Molten-Globule Form of Ovalbumin. *J. Phys. Chem. B* **2012**, *116*, 520–531. https://doi.org/10.1021/jp208416d
36. Lakowicz, J. R. Principles of Fluorescence Spectroscopy, 3rd edition; Springer: New York, 2006, 1-95 and 529-575.
37. Daniel E, Weber G. Cooperative effects in binding by bovine serum albumin I: the binding of 1-anilino-8-naphthalenesulfonate fluorometric titrations. *Biochem.* **1966**, 5, 1893–1900. https://doi.org/10.1021/bi00870a016
38. He, X. M.; Carter, D. C. Atomic structure and chemistry of human serum albumin. *Nature* **1992**, *358*, 209-215. https://doi.org/10.1038/358209a0
39. Shaw, A. K.; Pal, S. K. Spectroscopic studies on the effect of temperature on pH-induced folded states of human serum albumin. *J. Photochem. Photobiol. B, Biol.* **2008**, *90*, 69-77. https://doi.org/10.1074/jbc.274.41.29303
40. Takehara, K.; Yuki, K.; Shirasawa, M.; Yamasaki, S.; Yamada, S. Binding Properties of Hydrophobic Molecules to Human Serum Albumin Studied by Fluorescence Titration. *Anal Sci.* **2009**, *25*, 1115-120. https://doi.org/10.2116/analsci.25.115
41. Ranjbar, S.; Shokoohinia, S.; Ghobadi, S.; Bijari, N.; Gholamzadeh, S.; Moradi, N.; Ashrafi-Kooshk, M. R.; Aghaei A.; Khodarahmi, R. *Sci. World J.* **2013,** 1-13. https://doi.org/10.1155/2013/305081

42. Majumdar, A.; Mukhopadhyay, S. Chapter Twelve - Fluorescence Depolarization Kinetics to Study the Conformational Preference, Structural Plasticity, Binding, and Assembly of Intrinsically Disordered Proteins. *Methods Enzymol.* **2018**, *611*, 347-381. https://doi.org/10.1016/bs.mie.2018.09.031

Chapter 4

Green transformation of biomass-derived Indian gooseberry into fluorescent intrinsic nitrogen-functionalized carbon quantum dots for real-time detection of vitamin B_2 in the nanomolar range

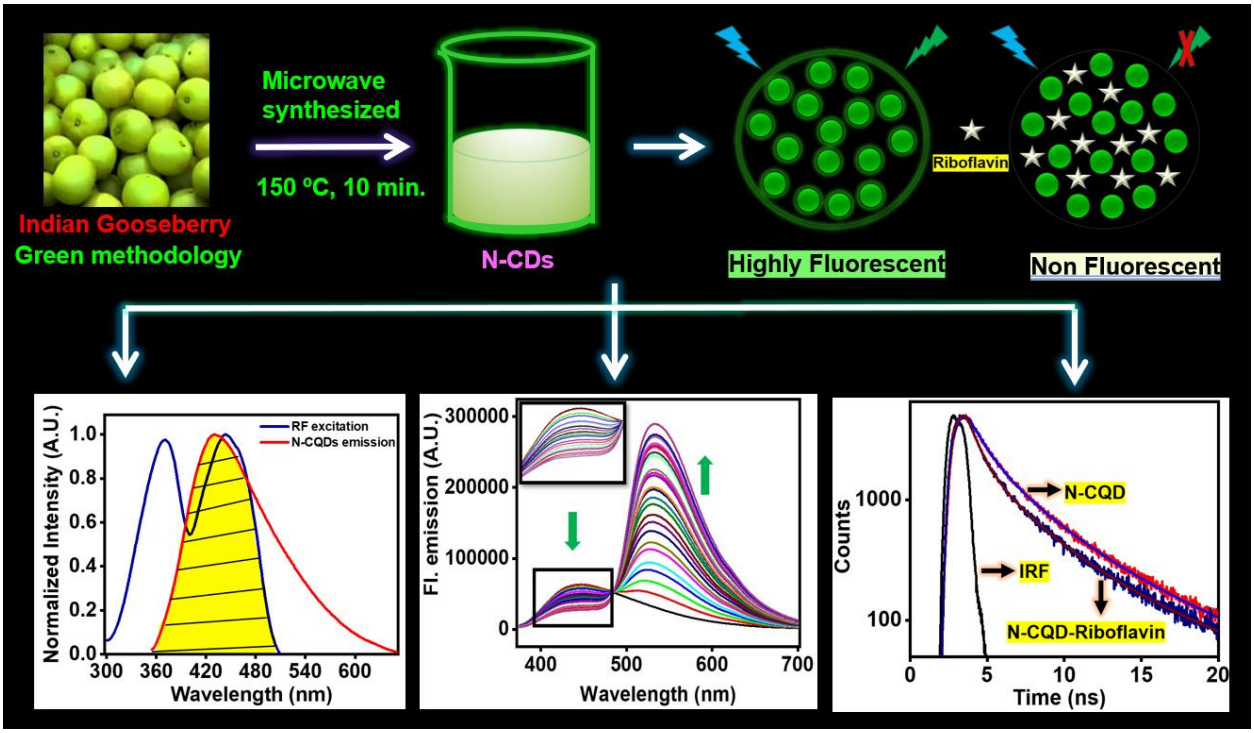

4.1 Introduction

Riboflavin (RF), commonly known as vitamin B_2, is an essential water-soluble vitamin for human health. All the flavoproteins need RF as most of it is converted to its cofactor forms, flavin mononucleotide (FMN) and flavin adenine dinucleotide (FAD). Additionally, RF is a requisite during protein, lipid, carbohydrate, and ketone metabolism, as well as during electron transport processes in the respiratory chain. In human beings, RF serves as an antioxidant, combating free radicals and protects against cancer. Since vitamin B_2 is neither generated nor stored in significant amounts in the human body, a regular consumption of the vitamin through various RF-rich food items such as milk, yogurt, cereals, pork, eggs, almonds, fresh green vegetables, and dairy products, is considered to be essential. Deficiency of RF causes mucocutaneous infections, anemia, fatigue, acute photophobia, delayed growth, angular cheilitis, cardiovascular and digestive issues, seborrheic dermatitis, scrotal cheilosis, vulvar skin abnormalities, and many more. Therefore, it is essential to develop a simple and reliable method to determine the concentration of RF in various food, vitamin B_2 supplements, human blood, and in metabolic processes.[1-5] The conventional methods for detecting riboflavin in foods, pharmaceuticals, and supplements include high-performance liquid chromatography (HPLC), ultraviolet-visible spectroscopy (UV-Vis), capillary electrophoresis, electrochemical approaches, immunoassay colorimetric approach, molecular imprinting etc. Most of these methods have a variety of shortcomings, including lack of selectivity, slow response time, expensive equipment, require substantial amount of solvents, limited stability/selectivity, and time-consuming sample preparations. In contrast, among all the different types of analytical techniques, the fluorescence method is considered to be one of the most effective analytical techniques due to its rapid detection, ease of use, simplicity, low cost, and high sensitivity compared to all of the aforementioned processes, which enables a broader application such as role in disease diagnosis as well as in biological research.[6,7] Hu *et al.* reported a diagnostic method to determine riboflavin in urine and beverages using capillary electrophoresis with the help of in-column optical fiber laser-induced fluorescence.[8] Zandomeneghi *et al.* demonstrated direct fluorometric determination of vitamin B_2 levels in low riboflavin-containing powders such as wheat flours.[9] Primarily RF is electron carrier group and has tendency to interact with electron donor moiety and FRET is the primary mechanism for sensing. The current method for RF

detection is based on FRET and is shown to be superior to the methods stated above, such as a quicker response time, increased simplicity, reduced cost, and enhanced selectivity along with sensitivity.[1] The majority of the biological processes occur via fluorescence resonance energy transfer (FRET) mechanism, which is a non-radiative photophysical phenomenon comprising a donor and acceptor fluorophore separated by around 1-10 nm.[10] The donor molecule emits energy in its excited state which is further transferred to the ground state of acceptor molecule. This results in dipole-dipole interactions between the donor and acceptor fluorophores causing an overlap between the emission and absorption spectra of the donor and acceptor fluorophores, respectively. These unique attributes of the FRET principles promote their widespread use in a wide range of fields, such as analytical science, biophysical studies, and the study of conformational arrangement and dynamics of biomolecules like DNA, protein, etc.[10] However, FRET reports on CDs are scarce in nature. Now-a-days, CDs are used as fluorescent biosensor materials for recognizing targeted analytes and for specifically detecting biologically-active molecules *via* FRET mechanism.[11,12] In modern era, CDs have emerged as a promising star in the category of zero-dimensional nanomaterials because of their outstanding sensitivity, rapid response time, relatively non-toxic nature, simple synthesis method, low cost, chemical inertness, ease of functionalization, and many other advantages.[13,14] CDs have superior properties compared to other semiconductor quantum dots, including low toxicity, high photostability against photobleaching and blinking and biocompatibility.[15,16] CDs exhibit intrinsic fluorescence properties due to their small size (1-10 nm), monodispersed nature, presence of hetero-atom-based functional groups on the surface, quantum confinement effect, etc.[17,18] Microwave-assisted synthesis of CDs is significantly simpler, has a shorter reaction time, and avoids typical harsh reaction conditions involving the usage of strong acids/bases, high temperature, and prolonged reaction times. Recently, cutting-edge research has focused on the utilization of a simple and fast microwave treatment technique to produce CDs from a variety of chemical and biomass precursors.[19] Biomass-derived CDs have recently become a new frontier in the field of environmental science because of their high carbon content, eco-friendly, straightforward methodology, cost-effectiveness, high quantum yield (QY), self-passivation, abundance, practicability, non-toxicity, sustainable, and recyclable nature. However, getting a suitable green resource to produce CDs remains a challenging task.[20] The numerous precursors of biomass include plant leaves, fruit peels and juice, kitchen waste,

agricultural waste, etc. The quantum yield of CDs derived from biomass waste precursors was found to be higher than chemical precursors.[21,22] Kundu *et al.* synthesized fluorescent CDs with the help of biomass precursor rice husk for selective and sensitive detection of Fe^{3+} and fluoroquinolones.[23] Monte-Filho *et al.* reported the synthesis of highly fluorescent CDs using lemon and onion juices in order to determine riboflavin in multivitamin/mineral supplements.[3] Lee and coworkers successfully transformed kiwi fruit peels into valuable kiwi fruit peel carbon dots (KFP-CDs) using a simple hydrothermal carbonization process. These KFP-CDs were employed for variety of purposes such as they were used as fluorescent ink for writing and drawing and interestingly, i was immediately visible when exposed to UV light. They suggested that KFP-CDs can be used as an agent to label cells, specifically for mesenchymal stem cells, thyroid cancer cells and breast cancer cells for *in vitro* imaging.[24] Atchudan et al. used an easy hydrothermal approach to manufacture hydrophilic nitrogen-doped carbon dots (HN-CDs) from dwarf banana peel biowaste that selectively and sensitively detect Fe^{3+} ions by the FL quenching of HN-CDs.[25] Atchudan et al. employed one-pot hydrothermal carbonization method to synthesize nitrogen-doped carbon dots (NCDs) using Piper betel (Betel) leaf which were brightly fluorescent. The fluorometric method was used to determine Fe^{3+} ion with a detection limit of 0.43 mM as a result of resonance energy/electron transfer (RET) mechanism.[26] A one-step hydrothermal approach is employed by Atchudan et al. to produce extremely durable fluorescent nitrogen-doped carbon dots (FNCDs) using *Phyllanthus acidus* and aqueous ammonia. These FNCDs are utilized here for the sensitive, selective and label-free detection of Fe^{3+} with a detection limit of 0.9 μM.[27] Atchudan et al. reported synthesis of N-CDs using an effective hydrothermal method that utilized aqueous ammonia as nitrogen source and unripen peach fruit. The synthesised N-CDs exhibited an enhancement in its catalytic activity in an alkaline solution and are extremely biocompatible, and hence they can be employed as fluorescent imaging probes.[28]

Medicinal plants are a unique gift to humanity that promote a disease-free and healthy existence. *Phyllanthus emblica*, often known as the Indian Gooseberry, has great significance in Ayurveda and commonly used as medicine in liver tonic, antipyretic, ulcer preventive, common cold, hair tonic etc. It contains a lot of minerals including sodium, calcium, iron, phosphorus, and plenty of polyphenols, tannins, alkaloids, cholesterol, carotene and amino acids. It is a good source of

vitamin C (200-900 mg per 100 g of consumable component) and has various chemical elements with biological action.[29,30] Arul *et al.* synthesized CDs from Indian Gooseberry with the help of hydrothermal method involving ammonia as a doping agent and investigated their catalytic role to detoxify of effluents from textile industry.[31] Atchudan *et al.* demonstrated hydrothermal synthesis of N-CDs with the help of ammonium hydroxide been used as a doping agent and was further recognized as a promising staining agent since they were used to stain human colon cancer cells for cellular imaging.[32] All the synthetic protocols have certain limitations as it involves high temperature (200 ºC), use of chemical reagents for doping and long reaction time (12 h).[31,32]

Herein, we report a simple, rapid, low-cost, one step microwave-assisted carbonization technique to synthesize highly fluorescent N-CDs from *Phyllanthus emblica* (Indian Gooseberry) as the biomass precursor. To the best of our knowledge, this is the first report in which without using any harsh chemicals, intrinsic nitrogen containing N-CDs were developed. The synthetic protocol involved purely green methodology. Presence of ascorbic acid, citric acid, polyphenols, amino acids are responsible for nitrogen source in Indian Gooseberry, which results in surface passivation by bottom-up methodology in the presence of microwave irradiation (10 mins) to form N-CDs. The synthesized N-CDs showed high selectivity in order to detect of riboflavin. In addition, their interaction was confirmed by FRET mechanism. The limit of detection was found in nanomolar range. Moreover, the as-prepared nanoprobe was validated in real samples (vitamin B_2 supplements).

4.2 Experimental section

4.2.1 Materials

For the preparation of fluorescent N-CDs, fresh Indian Gooseberries were bought from the local market of Patiala, Punjab. Sodium phosphate monobasic, sodium citrate, trizma base, *4-(2-hydroxyethyl)-1-piperazineethanesulfonic acid* (HEPES), sodium chloride, riboflavin, alanine (Ala), arginine (Arg), asparagine (Asn), aspartic acid (Asp), cysteine (Cys), glutamic acid (Glu), glutamine (Gln), histidine (His), isoleucine (Ile), leucine (Leu), lysine (Lys), methionine (Met), threonine (Thr), tryptophan (Trp), tyrosine (Tyr), valine (Val), N-acetyl-L-cysteine methyl ester were purchased from Sigma Aldrich, India and were used as such without any further purification.

Ascorbic acid (AA), glucose, and dopamine were purchased from HiMedia and used as obtained. Quinine sulfate was purchased from Loba Chemie and was used as a standard for photoluminescence quantum yield (PLQY) measurements. Double-distilled water has been used throughout this investigation. The pH of the buffers was set to a final value (± 0.02) using EUTECH pH / Ion 510 pH meter at ~24-25 ºC. The 0.22 µM and 0.02 µM membrane filters were obtained from Merck Millipore and Whatman (GE Healthcare Life Sciences), respectively. The dialysis membrane (Dialysis membrane-110 LA395-1MT) having molecular weight cut off between 12 to 14 kDa was obtained from HiMedia Laboratories, India. For real sample testing, commercially available multivitamin/multimineral (vitamin B_2) supplement was purchased from medical stores in Patiala, Punjab.

4.2.2 Synthesis of N-CDs

A microwave-assisted synthesis approach was used in order to synthesize N-CDs. The gooseberries were washed in double-distilled water, cut into small pieces, and were transferred into a mixer grinder followed by grinding for ~10 minutes till they were fully crushed. The resulting juice was extracted using a sieve and filtered with Whatman® filter paper. The filtrate (juice) was transferred into a microwave vial and the reaction was set up in a microwave synthesizer (Anton Parr) at 150 °C for 10 minutes. Carbonization caused a change in the juice color from pale green to dark brown indicating the formation of N-CDs. After cooling down the solution to room temperature, it was centrifuged at 7000 rpm for 20 minutes, and the solution was decanted. The decanted solution was transferred into a dialysis bag whereby it was dialyzed against double-distilled water for three days (at ~24-25 ºC without stirring). The clear light brown color solution was filtered further through a 0.22 µm syringe filter followed by 0.02 µm membrane filter, respectively to remove the larger particles. The schematic representation of the protocol involving synthesis of N-CDs is shown here (Figure 4.1). Finally, the clear light brown solution of N-CDs was collected, and stored in a refrigerator at 4 °C for further experimental studies.

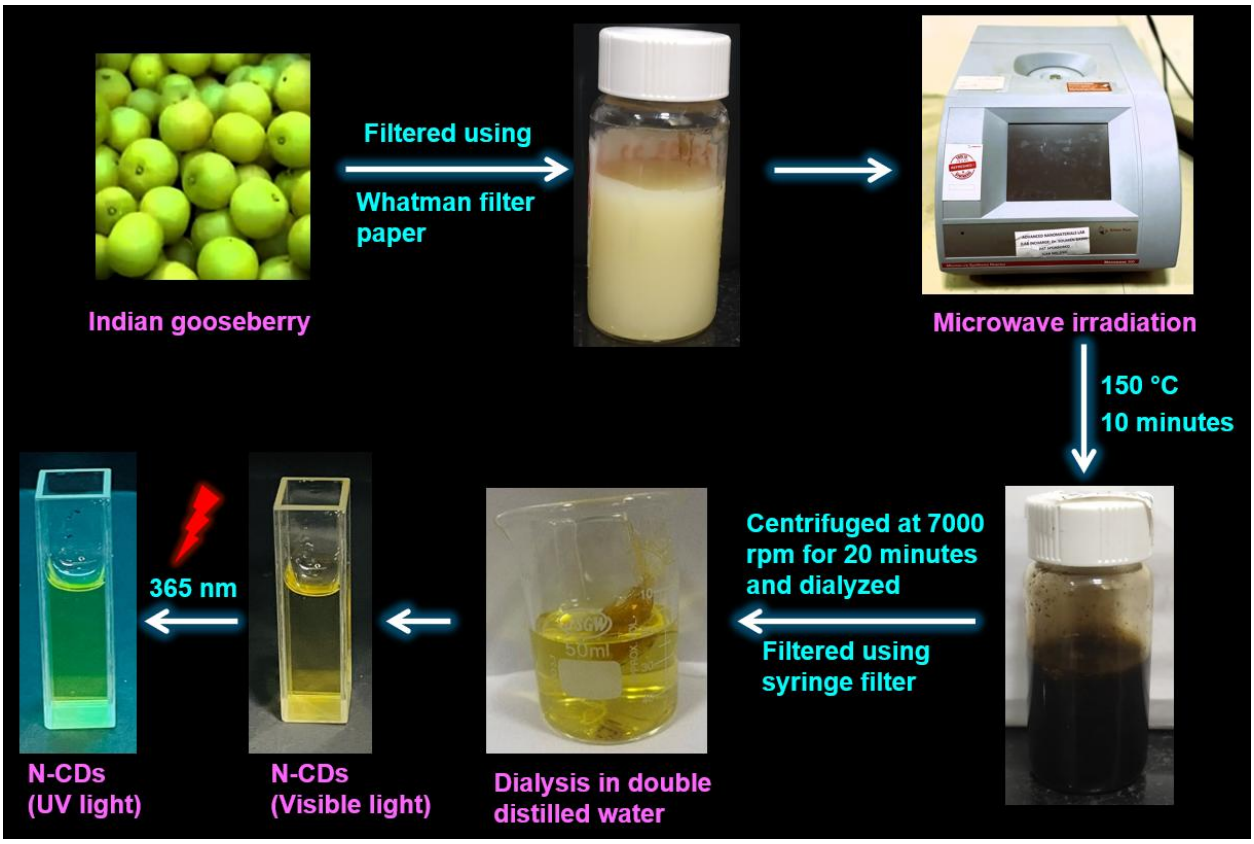

Figure 4.1. Schematic representation of synthetic protocol of N-CDs from Indian Gooseberry.

4.2.3 Characterization of N-CDs

4.2.3.1 Electron microscopy

The synthesized N-CDs were characterized by high-resolution transmission electron microscopy (HRTEM) on JEM 2100 plus (JEOL) fitted with a charge-coupled device (CCD) camera at an acceleration voltage of 80-200 kV. The samples were prepared by spreading a small droplet of diluted N-CDs solution (1:1 (v/v) of N-CDs and water on a copper grid and allowed to dry at room temperature (~24-25 ºC) overnight for ~12-16 hours.

4.2.3.2 XPS and EDS analysis

The XPS of N-CDs was performed on Physical electronics (PHI 5000 Versa Probe III). The spectra were first baseline corrected and then the peaks were identified by the peak analyzer option and

deconvoluted using multiple peak-fitting involving Gaussian function available in the OriginPro 2021 software. The EDS of N-CDs was recorded using Talos F200S (Thermo Fisher Scientific).

4.2.3.3 GIXRD analysis

The diffraction pattern of N-CDs was recorded on Rigaku SmartLab in the angular range (2θ) of 10-90°. The scan resolution was 0.0001 degree with a scan speed of 3.02 deg/min.

4.2.3.4 Raman Spectroscopy

The purity and structural defects of the N-CDs were evaluated using LabRAM HR Confocal Micro-Raman Spectrometer, (HORIBA, France) using a 532 nm laser as an excitation source that was focused onto the sample spot using a 50X objective lens. A charge-coupled device (CCD) multichannel array detector was used to detect the signal. The Rayleigh scattering was eliminated by collecting the scattered light via the same objective and allowing it to pass through a 532 nm edge filter. All the spectra were collected in the range of 1200-1800 cm^{-1} and the final spectrum was averaged over 2 scans with a resolution of ~1 cm^{-1}. The data were acquired using LabSpec 6 software provided with the Raman spectrometer and replotted using OriginPro 2021. For XPS, EDS, XRD, and laser Raman spectroscopy, samples of N-CDs (without any dilution) were drop cast on a glass coverslip to form a thin film and allowed to dry at room temperature (~24-25 ºC) overnight for ~12-16 hours.

4.2.3.5 ATR FT-IR Spectroscopy

IRTracer-100 spectrophotometer (Shimadzu), comprising the QATR™ single-reflection integration-type ATR accessory involving a diamond crystal and an air-cooled DLATGS detector, was used to obtain the ATR-FTIR spectra of the N-CDs. A sample drop of 10 µL was used for recording the spectra in the range of 400-4000 cm^{-1}. All the spectra were recorded at a resolution of 2 cm^{-1} in the transmittance mode. The final spectrum was an average of 100 scans. The crystal surface was cleaned with methanol before putting a sample drop and background scan was run with 100 accumulations prior to recording spectrum. OriginPro 2021 was used for replotting the spectral data.

4.2.3.6 UV-Vis spectroscopy and zeta potential measurements

The UV-Vis absorption spectra of aqueous solutions of N-CDs were recorded on a UV-Vis spectrophotometer (Shimadzu, RF-2600) using a quartz cuvette of 1 cm path length. 100 µL of the N-CDs solution was added into double-distilled water to a total volume of 3 mL for recording the absorbance. The zeta potential experiments of N-CDs were carried out on Zetasizer 2000, nano series-ZS (Malvern Instruments Ltd, UK).

4.2.3.7 Preparation of N-CDs sample for fluorescence studies

50 µL of the synthesized N-CDs was added to 2.45 mL of double-distilled water to make a total volume of 2.5 mL. The volume of N-CDs was kept constant while the concentration of riboflavin (RF) was varied (0-2.2 µM) during the fluorescence emission measurements with an excitation wavelength of 340 nm.

4.2.3.8 Steady state fluorescence spectroscopy

The fluorescence spectra of N-CDs were collected using the Shimadzu RF-6000 spectrofluorometer. The following parameters were used for collecting the fluorescence spectra of N-CDs: λ_{ex} = 340 nm with a scan range of 350-650 nm (in aqueous medium) and λ_{ex} = 360 nm with a scan range of 370-700 nm (at pH 7.4). The excitation and emission bandwidths were varied for different sets of fluorescence studies involving N-CDs. For collection of the excitation wavelength-dependent emission spectra and for volume optimization studies in aqueous medium and pH 7.4, both excitation and emission bandwidths were set at 10 nm. Similarly, for N-CDs optimization studies (i.e. for optimizing N-CDs storage duration, and optimal fluorescence emission as a function of pH), both the bandwidths were fixed at 5 nm whereas for optimizing the reaction duration in microwave synthesizer and for biomolecule sensing studies, the excitation and emission bandwidths were set at 5 and 10 nm, respectively. Further to estimate the limit of detection, binding constant, and Stern-Volmer quenching constant (K_{sv}), the emission intensities were fit using a linear equation available in the OriginPro 2021 as shown below:

$$y = a + bx \qquad (1)$$

y is the ratio of fluorescence intensities i.e. F_0/F where parameters 'F_0' and 'F' indicate the fluorescence intensity in the absence and presence of RF, respectively. 'a' is the intercept, 'b' is the slope, and 'x' represents quencher concentration (vitamin B_2). All of the steady state fluorescence experiments were performed at least three times.

4.2.3.9 Photoluminescence quantum yield (PLQY) measurements

The photoluminescence quantum yield (PLQY) of N-CDs was measured using quinine sulfate in 0.1 M H_2SO_4 as a standard reference solution (quantum yield ~0.546).[10] The PLQY values were calculated using the following equation[34]:

$$\phi_S = \phi_R \times \frac{A_S}{A_R} \times \frac{(Abs)_R}{(Abs)_S} \times \frac{\eta_S^2}{\eta_R^2} \qquad (2)$$

The parameters 'ϕ_S' and 'ϕ_R' represent the fluorescence quantum yield of the sample (N-CDs) and the reference solution (quinine sulfate), respectively. '*Abs*' denotes absorbance, '*A*' represents the area under the fluorescence emission, and 'η' is the refractive index of the solvent (1.333 for water). The subscripts '*S*' and '*R*' denote the corresponding parameters for the N-CDs (sample) and quinine sulfate (reference), respectively.

4.2.3.10 Time-resolved emission spectroscopy

Time-resolved fluorescence emission decays were recorded using time correlated single photon counting (TCSPC) fluorometer instrument using the modular fluorescence lifetime system (DeltaFlex, HORIBA Scientific) with an excitation source of 340 nm (nano-LED pulse diode). The instrument response function (IRF) was recorded using a LUDOX®TMA colloidal silica, 34 wt.% suspension in distilled water (Sigma-Aldrich), and the full-width at half- maximum (FWHM) was estimated to be ~200 ps. For fluorescence lifetime measurements, the emission polarizer was set at the magic angle (54.7°) with respect to the excitation polarization. An emission monochromator was fixed at 430 nm with a bandpass of 16 nm. The time-resolved lifetime measurements were carried out w.r.t. 100 ns decay range and time per channel is 0.055 ns. A long-pass filter was placed just after the sample to block any scattering from the sample. All of the decays were acquired at 25 °C and replotted using OriginPro 2021. The fluorescence emission

decays were further deconvoluted with respect to the instrument response function and were analyzed and fitted using the following equation[10]:

$$I(t) = \sum_i \alpha_i e^{-\frac{t}{\tau_i}} \qquad (3)$$

where α_i and τ_i represent the contributions and lifetimes, respectively, of the different lifetime components, *I(t)* represent the fluorescence intensity at time t. All the data were acquired at 25 °C.

4.3 Results and discussions

4.3.1 Morphological Characterization and Compositional Analyses of N-CDs

The size and morphological characteristics of N-CDs were confirmed by HR-TEM. Figures 4.2a show that the N-CDs are spherical particles which are also monodisperse. The histogram plot (Figure 4.2a inset) depicted that the average diameter of N-CDs was 8.1 nm with the particle size ranging from 2 to 16 nm, which closely resembles the Gaussian distribution. Figure 4.2b shows the X-ray diffraction pattern of synthesized N-CDs. An intense broad diffraction peak was observed around 2θ = 24.5° of (002) lattice plane, and a weak spike appeared at 2θ = 42.9° (100) lattice plane, demonstrating an amorphous carbon phase and a partial graphitization of the N-CDs, respectively which is in good accord with other literature reports.[33,34] The partial graphitization is due to the presence of nitrogen and oxygen-containing moieties on the surface of N-CDs.[30,31]

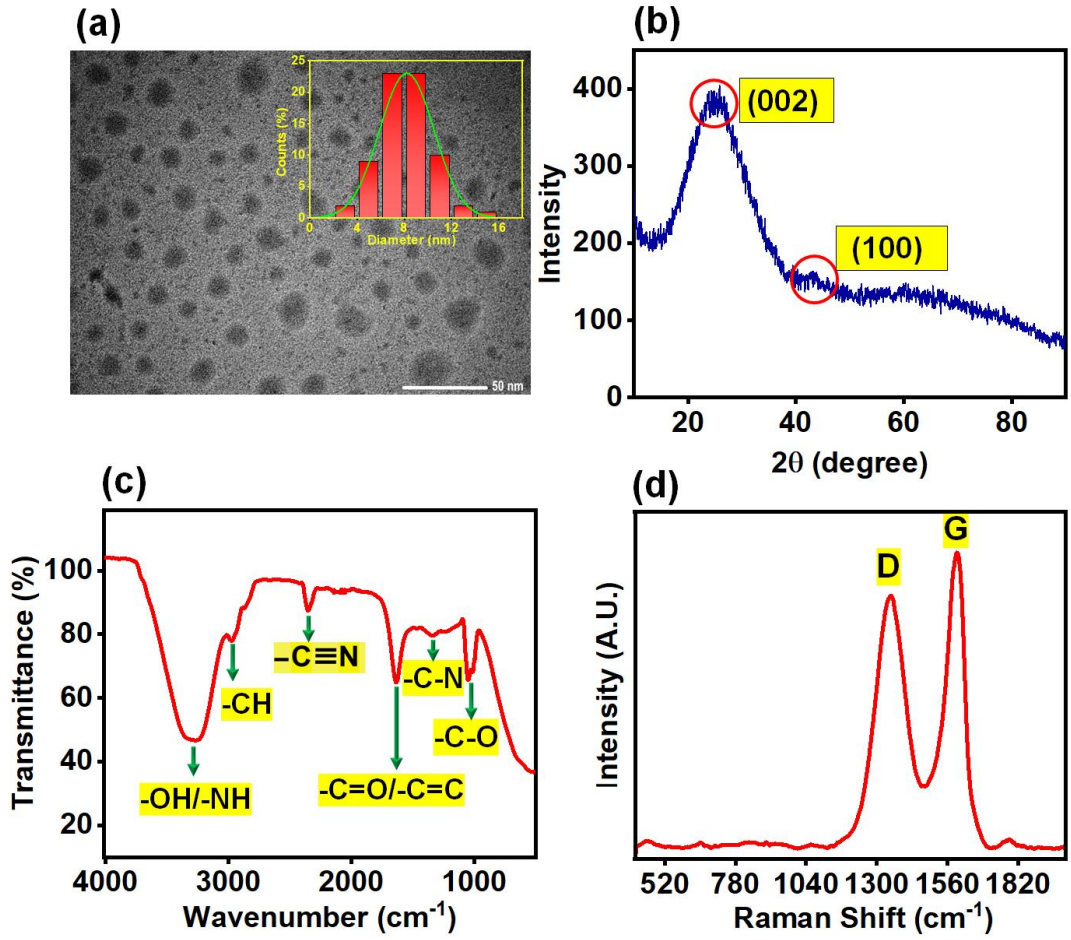

Figure 4.2. (a) HR-TEM image of N-CDs, inset representing particle size distribution histogram plot, (b) XRD spectrum, (c) FTIR spectrum and (d) Raman spectrum of N-CDs.

The interlayer distance (d-spacing) was determined using Bragg's equation:

$$n\lambda = 2d\sin\theta \qquad (4)$$

where 'λ' denotes the wavelength of the incident X-ray (λ = 1.5406 Å), 'n' is a positive integer that signifies the "order" of reflection, 'd' is the variable that indicates the spacing between the diffracting planes. The estimated d-spacing values of N-CDs were 0.36 and 0.21 nm, which correspond to (002) and (100) lattice planes, respectively. The different interlayer distance of N-CDs, compared to bulk graphite (0.34 nm), suggest that nitrogen and oxygen-containing functional groups are well decorated on the surface of N-CDs.[32,35,36] FTIR spectral analysis of as prepared N-CDs (Figure 4.2c) aided in identifying the functional groups attached to the surface. The broad

peak at 3364-3224 cm^{-1} was recognized as the stretching vibration of the O-H/N-H band, whereby hydrogen bonding is responsible for its broadening[37], the weak band found at 2970 cm^{-1} was attributed to stretching vibrations of the C-H band, and the signal at 2355 cm^{-1} was ascribed to -C≡N stretching vibration.[38] The signal at 1633 cm^{-1} was assigned to stretching vibrations of alkenyl C=C/carbonyl C=O[39] groups present in N-CDs. The peaks cantered at 1366 cm^{-1} and 1028 cm^{-1} were ascribed to -C-N stretching[40], and -C-O stretching[41] respectively. Thus, the FTIR spectra corroborated successful incorporation of the amino, hydroxyl, and carboxyl groups on the surface, conferring high polarity and water solubility of the N-CDs. Figure 4.2d shows Raman spectrum of N-CDs, comprising two peaks at 1378 cm^{-1} and 1598 cm^{-1}, which are attributed to D-band and G-band, respectively.[42,43] The D-band appears due to the breathing motion of κ-point phonons with the A_{1g} symmetry, which is induced by defects in the sp^3 carbons, whereas the G-band occurs due to the first-order scattering of E_{2g} phonons in sp^2 hybridized carbon atoms.[42,43] Therefore, overall, the Raman data demonstrated that sp^3 (D-band) and sp^2 (G-band) hybridized carbon defects were present in N-CDs. Furthermore, the intensity ratio of D to G band (I_D/ I_G) is 0.85 demonstrating that N-CDs possess a moderate degree of graphitization.[44]

X-ray photoelectron spectroscopy (XPS) is the most useful tool for elemental identification as well as to determine the surface oxidation state and the exact quantity (percentage) of the elements present. The deconvoluted XPS spectra for the C1s, N1s, and O1s elements are shown in Figure 4.3, together with the survey spectrum of the synthesized N-CDs. The elemental carbon (64.9%), nitrogen (4.1%), and oxygen (31.1%) peaks emerged at 283.1, 397.8, and 531.3 eV, respectively (Fig 4.3a).[33,45,46] The deconvolution spectrum of O1s showed one binding energy peak at 531.8 eV, corresponding to the -C=O/-C-O-C groups (Figure 4.3b).[47] The deconvolution spectrum of N1s displayed two peaks at 399.3 and 401.1 eV, owing to amide -C_3N (Pyridine N) and -C-N-C (Pyrrolic N) groups on the N-CDs surface, respectively (Figure 4.3c).[39] The C1s deconvolution spectrum exhibits characteristic peaks at 283.8, 285.3 and 287.2 which are attributed to transitions involving the -C=C/-C-C, -C=N/-C=O, -O-C=O, respectively (Figure 4.3d).[48,49]The primary peak around 284.5 eV corresponds to the carbon atoms in the graphitic structure. This peak clearly shows that the carbon dots synthesized have mostly sp^2 carbons.[50, 51]The XPS results corroborated well with the previous findings of FTIR analysis.

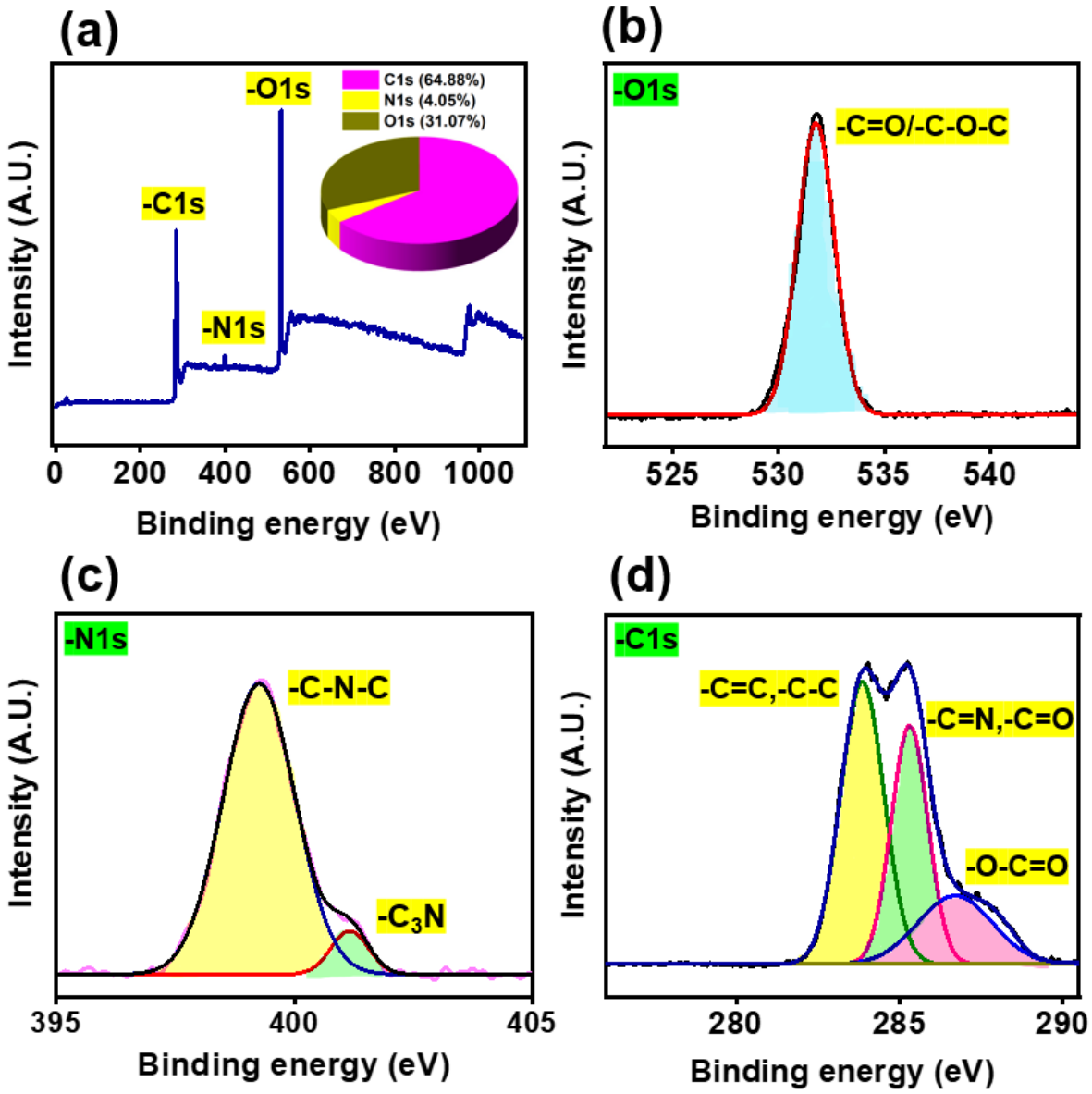

Figure 4.3. (a) XPS survey spectrum of N-CDs, (b-d) Deconvoluted XPS spectra of N-CDs represented in an element-specific manner viz. (b) O1s, (c) N1s, and (d) C1s.

4.3.2 Optical properties of N-CDs

The absorption spectrum of N-CDs showed a peak at 280 nm along with a long tail at approx. 355 nm (Figure 4.4a). The absorption maximum at 280 nm was attributed to the π-π* transition of the conjugated C=C (sp^2) bonds[54] whereas the band at 355 nm corresponded to n-π* transition of the C=N/C=O/N=O groups (containing heteroatoms of nitrogen and oxygen) present on the surface of

N-CDs.[55] The presence of heteroatom containing functional groups was also confirmed by XPS, EDS, and FTIR analysis as already mentioned previously (Section 3.1). The inset of Figure 4.4a shows that N-CDs exhibit light brown color as observed by naked eye and green fluorescence emission under UV light illumination at 365 nm. The fluorescence emission of N-CDs is due to photoinduced charge separation along with entrapment at the surface, which causes radiative recombination between hole and electron pairs.[56] In aqueous medium, N-CDs showed a maximum emission intensity at 430 nm upon excitation at 340 nm (Figure 4.4b); while in HEPES buffer (pH 7.4), the emission maximum appeared at 450 nm upon excitation at 360 nm (Figure 4.4d). In both aqueous and buffer media, excitation wavelength-dependent emission spectral shifts were observed. The excitation-dependent emission property of N-CDs is due to the quantum confinement effect, surface defects, zigzag sites, formation of aromatic structure on its surface, non-uniform particle distribution, etc.[57] Figure 4.4c, 4.4e display normalized fluorescence emission of N-CDs in aqueous and buffer media, respectively. In aqueous medium, N-CDs showed a significant bathochromic shift (~110 nm) in the fluorescence emission when the excitation wavelength was varied from 280 to 430 nm (Figures 4.4c). Similarly, in HEPES buffer, a bathochromic shift of ~116 nm was observed upon varying the excitation wavelengths in the similar range (Figures 4.4e). This experimental study reveals that N-CDs showed similar kinds of excitation-dependent emission properties irrespective of the dispersant medium. Moreover, these photophysical studies of the as-prepared nanoprobe in buffer medium reaffirm that N-CDs can be used as an effective nanosensor under physiological conditions.

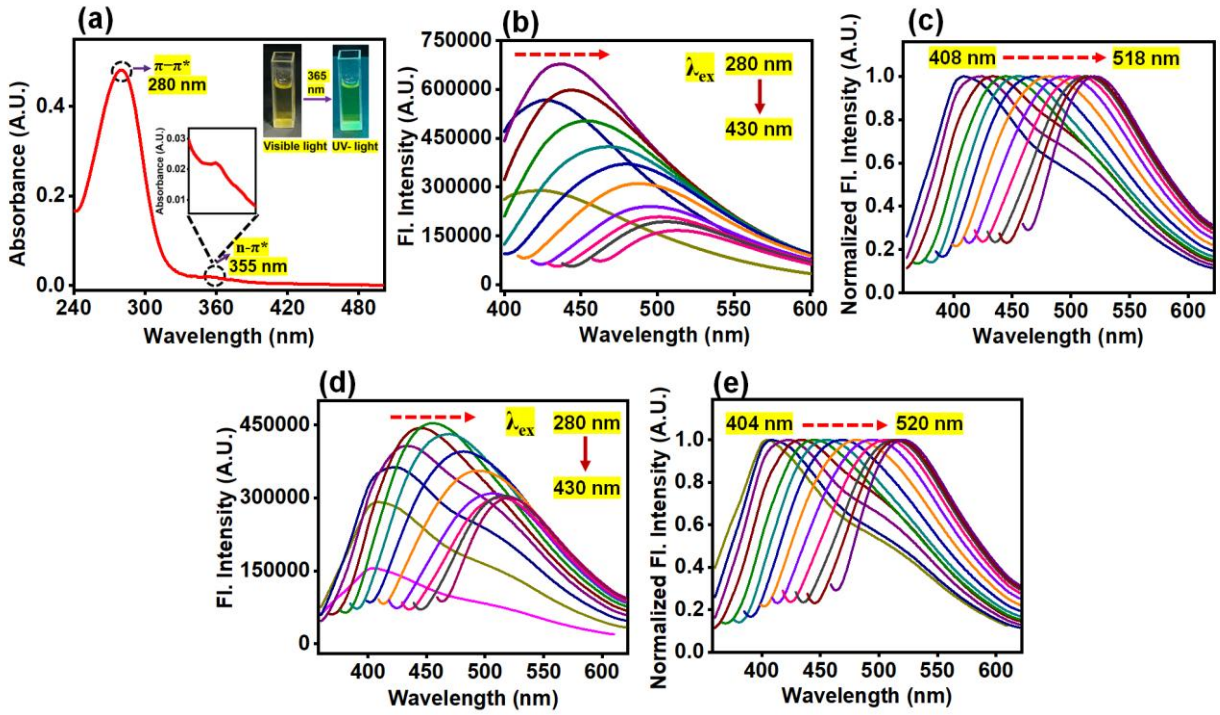

Figure 4.4. (a) UV-Visible absorption spectrum of N-CDs with inset picture representing N-CDs under visible and UV light illumination. The other inset image depicts the magnified representation of the 355 nm band. Excitation wavelength-dependent (b) excitation wavelength dependent changes in fluorescence emission spectra of N-CDs and (c) peak position-normalized fluorescence emission of N-CDs clearly depicting the spectral shift, indicated by a dashed red arrow, from 408 nm to 518 nm in aqueous medium (λ_{ex}: 280 nm to 430 nm), (d) excitation wavelength-dependent changes in fluorescence emission spectra and (e) peak position-normalized fluorescence emission of N-CDs clearly depicting the spectral shift from 404 nm to 520 nm in pH 7.4 HEPES buffer, indicated by red dashed-arrow upon changing the excitation wavelength (λ_{ex}: 280 nm to 430 nm).

4.3.3 Optimization of N-CDs

As aforementioned (Section 3.2), the synthesized N-CDs exhibited photoluminescence (PL) upon irradiation with UV light. In order to develop an effective optical nanosensor with strong PL properties, it is essential to optimize the reaction time, volume, and time-duration of storage of the as-prepared N-CDs.

4.3.3.1 Reaction time and volume optimization

It is well known that the reaction time affects the photoluminescence characteristics of N-CDs. To figure out optimum reaction condition, N-CDs were synthesized by varying the reaction times ranging from 5 minutes to 20 minutes. We observed that our microwave pyrolysis method, involving a reaction time of 10 minutes at 150 °C, yields the desired N-CDs with the highest PL intensity (Figure 4.5a).

After three days of dialysis, the synthesized N-CDs were dispersed in aqueous solution using double-distilled water followed by centrifugation and filtration. We noticed that N-CDs were highly water soluble. Further, for the sensing efficiency as well as to achieve the maximum fluorescence intensity of the synthesized nanoprobe, volume optimization is required. So next for volume optimization, we monitored the changes in the N-CDs emission intensity by adding varying amounts of aliquots (10-100 µL), from the respective stock solution of N-CDs, into double-distilled water. It was found that 50 µL of N-CDs and 2.45 mL of double-distilled water exhibited the maximum PL intensity (Figure 4.5b).

4.3.3.2 Storage duration optimization

The emission spectra of N-CDs were recorded at various time intervals for up to 60 days (i.e. ~2 months). Figure 4.5c shows the emission spectra of N-CDs at different storage durations, which clearly depicted no appreciable changes in the fluorescence intensity. Therefore, the findings clearly indicated that the synthesized nanoprobe was highly stable in an aqueous medium for prolonged time and hence, could be useful for diverse analytical applications

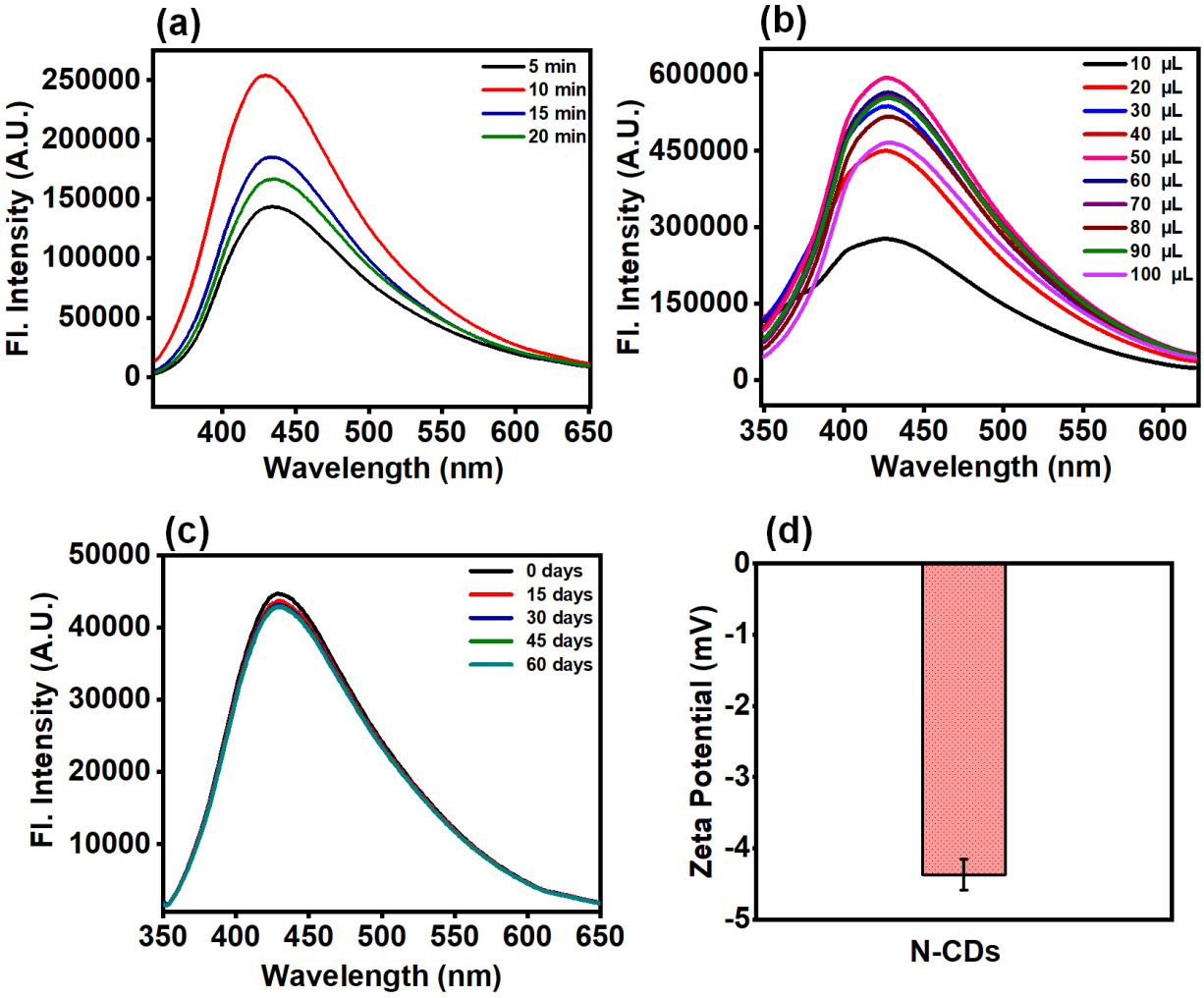

Figure 4.5. Fluorescence emission spectra of N-CDs (λ_{ex}: 340 nm to 430 nm) by optimizing the (a) reaction time, (b) volume ratio, (c) storage time, and (d) Zeta potential of N-CDs. All the experiments were performed in aqueous medium.

4.3.4 Stability of N-CDs

The photostability and chemical stability of an ideal nanosensor are essential for its practical applications. Therefore, to examine the stability of N-CDs, effect of photo-irradiation, ionic strengths, and pH were investigated. The inherent pH value of N-CDs was found to be ~3.2, implying its acidic nature, presumably due to the presence of carboxylates. Furthermore, zeta potential value (-4.37 mV) of N-CDs confirmed the presence of negatively charged moieties on

N-CDs surface (Figure 4.5d), which corroborated with the inherent pH value of the as-prepared nanoprobe (due to the presence of carboxylates). Additionally, N-CDs showed remarkable stability in a pH range of 3 to 7 with minute changes in fluorescence emission intensity as well as their emission maxima (Figure 4.6a). Moreover, the fluorescence intensity of N-CDs was also recorded in HEPES buffer at pH 7.4, which also confirmed that the synthesized nanoprobe was significantly stable and can be effectively used in physiological pH (Figure 4.6b). Thus, the synthesized N-CDs can be efficiently applied as versatile pH sensor in the pH range of pH 3 to 7.4. In acidic to neutral pH range, several functional groups present on the surface of the N-CDs leads to higher net surface charge (negative), which in turn leads to electrostatic repulsion and enhances the PL emission.[41] Nevertheless, as the alkalinity of the solution was increased, a drop in the PL intensity was observed. This is most likely to be caused by deprotonated carboxylates present on the surface. Additionally, at higher alkaline pH, the charged polyphenols get deprotonated coupled with deprotonation of ammonium ions. These deprotonated species may further trigger negative charge accumulation. Consequently, energy levels are being occupied, the electronic transitions of different emissive traps are being hindered which leads to a drop in PL emission along with bathochromic shift in the emission spectra. Thus, there is a positive correlation between acidic and basic ranges implying the practical usability of N-CDS as a pH sensor.[52,53] Furthermore, the influence of ionic strength on N-CDs emission was evaluated in the presence of 0-2 M NaCl solution. No appreciable changes in the PL intensity along with the emission maxima of N-CDs were observed by varying the ionic strength of the medium, clearly suggesting high stability of the nanoprobe in the presence of a salt (Figure 4.6c). Additionally, the PL intensity of N-CDs remained stable upon continuous photo-irradiation by a xenon-arc lamp of 150 W as shown in Figure 4.6d. Moreover, we found that our N-CDs can be used as fluorescent ink which shows green emission (Figure 4.6d inset) upon irradiation with UV light (365 nm), indicating its potential utility in practical applications.

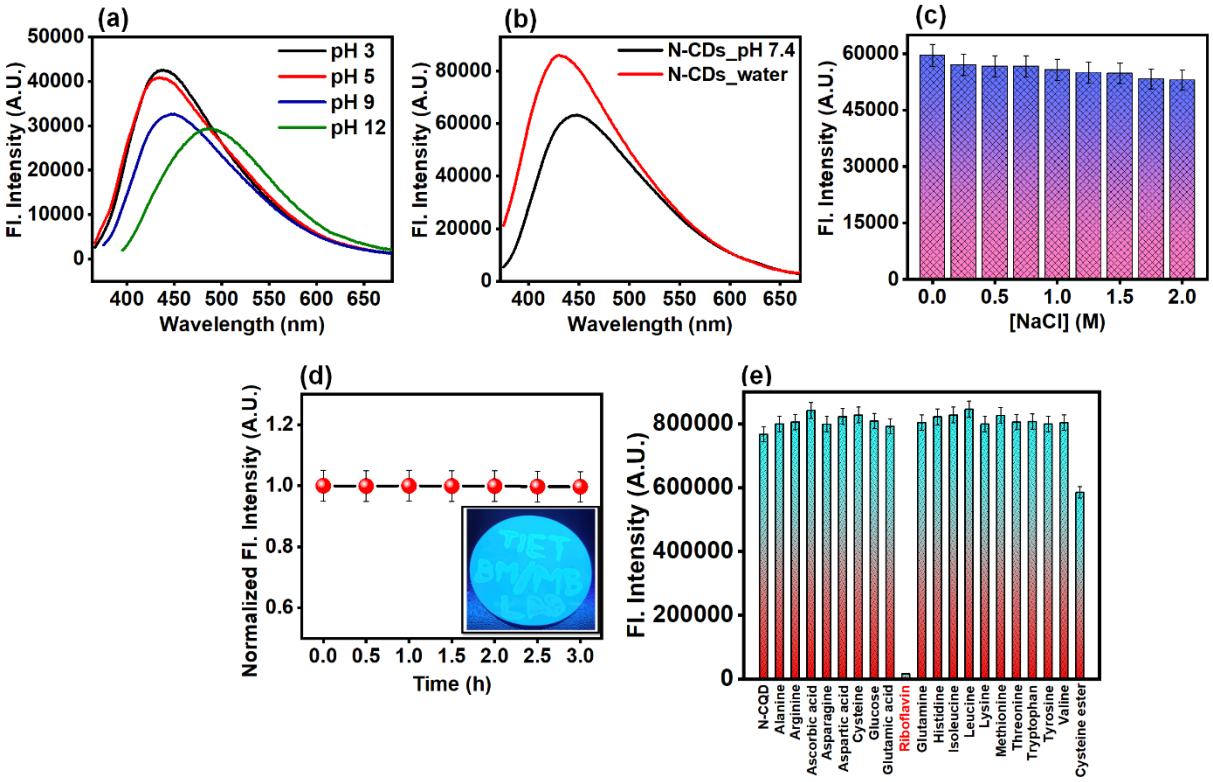

Figure 4.6. (a) Fluorescence emission spectra of N-CDs at variable solution pH (λ_{ex}: 340 nm) (b) FL intensity of N-CDs in aqueous and HEPES buffer at pH 7.4 (λ_{ex}: 360 nm) (c) impact of ionic strength of the medium on N-CDs emission at 430 nm in the presence of variable concentrations of NaCl (0-2 M) (λ_{ex}: 340 nm) and (d) impact of photo-irradiation by a xenon arc lamp on the emission of N-CDs at 430 nm as a function of time(λ_{ex}: 340 nm), (inset) photograph demonstrates practical utility of N-CDs as a fluorescent ink. (e) Selectivity studies of N-CDs with different amino acids and bioactive molecules (λ_{ex}: 340 nm). Error bars represent standard error of measurements obtained from three independent experiments.

4.3.5 Selectivity studies of N-CDs

Selectivity analysis is one of the most important factors for development of a novel nanosensor. In order to verify the selectivity of the analytical sensing platform, the changes in fluorescence intensity of N-CDs was monitored in the presence of several bioactive molecules and amino acids. A particular concentration of different amino acids (1 mM) such as alanine (Ala), arginine (Arg), asparagine (Asn), aspartic acid (Asp), cysteine (Cys), glutamic acid (Glu), glutamine (Gln),

histidine (His), isoleucine (Ile), leucine (Leu), lysine (Lys), methionine (Met), threonine (Thr), tryptophan (Trp), tyrosine (Tyr), valine (Val), in addition to several other bioactive molecules such as N-acetyl-L-cysteine methyl ester, ascorbic acid (AA), glucose, riboflavin (RF i.e. vitamin B_2) (13.25 μM) were prepared. Figure 4.6e reveals that riboflavin (RF) showed maximum fluorescence quenching of the N-CDs, whereas the PL intensity of the N-CDs upon addition of the remaining analytes remained almost unchanged. Thus, our N-CDs as nanosensor was found to be extremely selective towards the detection of RF. Therefore, it can be concluded that N-CDs have excellent practical usability as fluorescent nanosensors for specific detection of RF i.e. vitamin B_2.

4.3.6 Determination of photophysical parameters

As we demonstrated earlier, N-CDs exhibit excellent fluorescence. Therefore, to further decipher their photophysical properties, there is a need to calculate the photoluminescence quantum yield (PLQY). Using equation 2, PLQY of N-CDS was estimated to be ~48%, which reaffirmed that the as-prepared nanoprobe is a bright fluorophore. However, in the presence of RF, the PLQY of N-CDs was significantly reduced to ~19%, confirming a remarkable quenching of its fluorescence (Table 1). The fluorescence quenching phenomenon was also supported by TCSPC analysis. Addition of RF resulted in a decrease in the mean fluorescence lifetime of N-CDs (Table 1).

System	ϕ	τ_m[#] **(ns)**	k_r **(ns^{-1})**	k_{nr} **(ns^{-1})**	k_{ET} **(ns^{-1})**
N-CDs (aqueous medium)	0.48	2.26	0.21	0.23	-
N-CDs (aqueous medium) +RF	0.19	1.55	0.08	0.36	0.20

Error limit = ± 5% [#] $\tau_m = \alpha_1\tau_1+\alpha_2\tau_2+\alpha_3\tau_3$

Table 4.1. Photophysical parameters of N-CDs in the presence of RF.

From the PLQY (ϕ) and mean lifetime (τ_m) data, fluorescence lifetime (τ_f), different radiative (k_r) and non-radiative (k_{nr}) rate constants, were estimated using the following equations[10]:

$$k_r = \frac{\phi_f}{\tau_f} \qquad (5)$$

$$\frac{1}{\tau_f} = k_r + k_{nr} \qquad (6)$$

From Table 1, it is observed that 'k_r' values of N-CDs reduced significantly, while 'k_{nr}' values enhanced in the presence of RF (vitamin B_2). Thus, these results strongly indicated that highly fluorescent N-CDs turned to less fluorescent complex in the presence of RF and presumably, the excited-state electron transfer process was responsible for quenching. In order to gain insights into the quenching mechanism of as-prepared nanosensor in the presence of RF, different concentrations of RF (vitamin B_2) were added into N-CDs and the changes in the fluorescence emission were recorded. We observed that the PL intensity of N-CDs gradually quenched as a function of variable concentrations of RF at shorter emission wavelengths in aqueous and buffer media as well as in the presence of a real sample of vitamin B_2, as shown in Figures 4.7a, 4.10a and 4.10b, respectively.

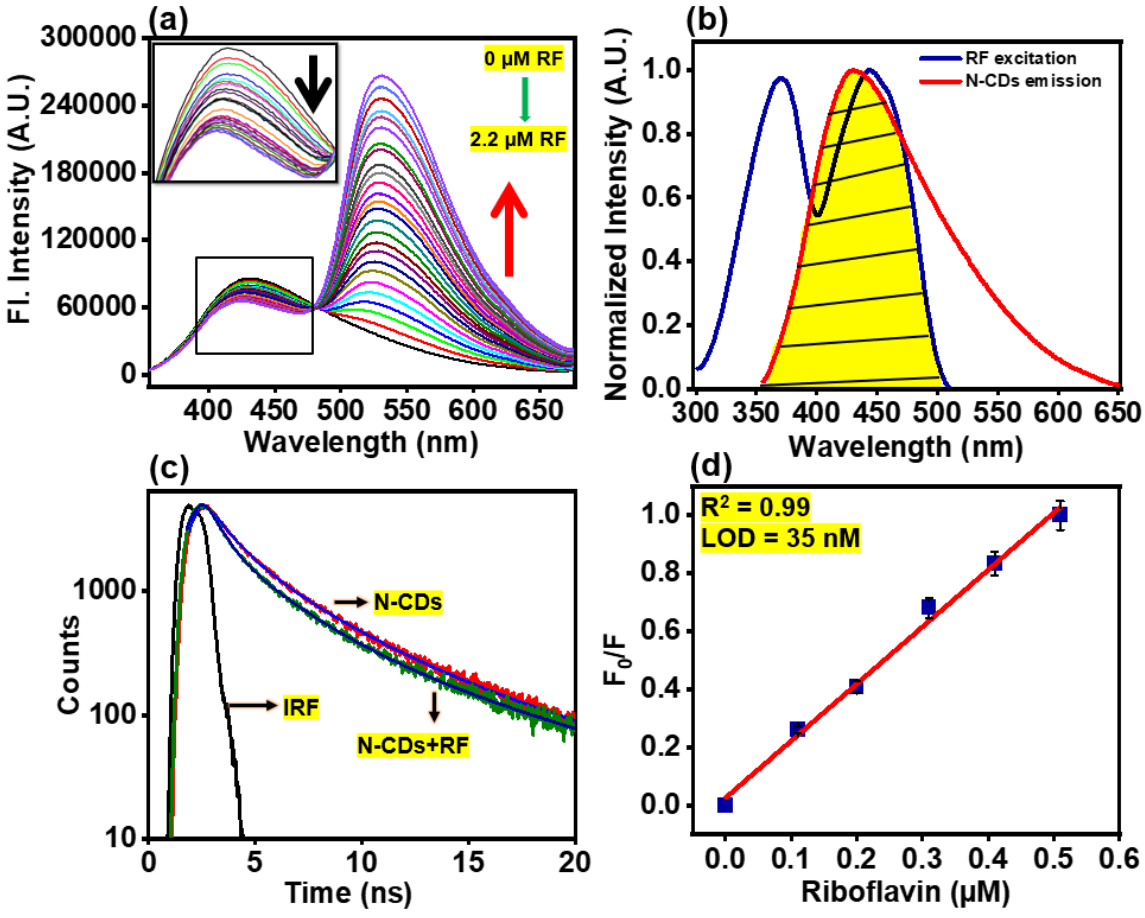

Figure 4.7. (a) Variation in fluorescence spectra of N-CDs (λ_{ex}: 340 nm) in the presence of different concentrations of RF (0-2.2 µM) with inset image showing fluorescence quenching in

aqueous medium. Black arrow depicts the progressive decrease of fl. intensity of N-CDs at shorter emission wavelength, while steady increase at longer emission wavelength is represented by red arrow, (b) spectral overlap between emission spectrum of N-CDs (red) (λ_{ex}: 340 nm) and excitation spectrum of RF (blue) where yellow color demonstrates the overlapped region in aqueous medium, (c) Fluorescence lifetime decays of N-CDs in an aqueous medium where, the sharp, thin black line represents the instrument response function, the red and olive lines represent the actual intensity decays in the absence and presence of RF respectively. The blue and royal blue lines correspond to fits obtained in the absence and presence of RF, respectively, (d) linear relationship of fluorescence response (F_0/F) of N-CDs at $\lambda_{em.}$ = 430 nm with different concentrations of RF (0-2.2 μM; the red line indicates the linear fit of the data). Error bars represent standard error of measurements obtained from three independent experiments.

To comprehend the extent of quenching efficiency of N-CDs, Stern-Volmer quenching constants were evaluated using the following equation[10]:

$$\frac{F_0}{F} = 1 + K_{SV}[Q] \qquad (7)$$

Figures 4.8a, 4.8b and 4.8c depicts a graph between F_0/F and Q i.e. concentration of quencher (RF) in different media. The parameters 'F_0' and 'F' indicate the fluorescence intensity in the absence and presence of RF, respectively. 'K_{sv}' signifies Stern-Volmer quenching constant, which was estimated from the slope of the plots in aqueous as well as in pH 7.4 buffer medium and real sample. The Stern-Volmer quenching constants of N-CDs are tabulated in Table 2 which indicate that the extent of quenching by vitamin B_2 remains the same irrespective of the medium. The values of R^2 were found close to unity, indicating the acceptable linearity of the developed nanosensor.

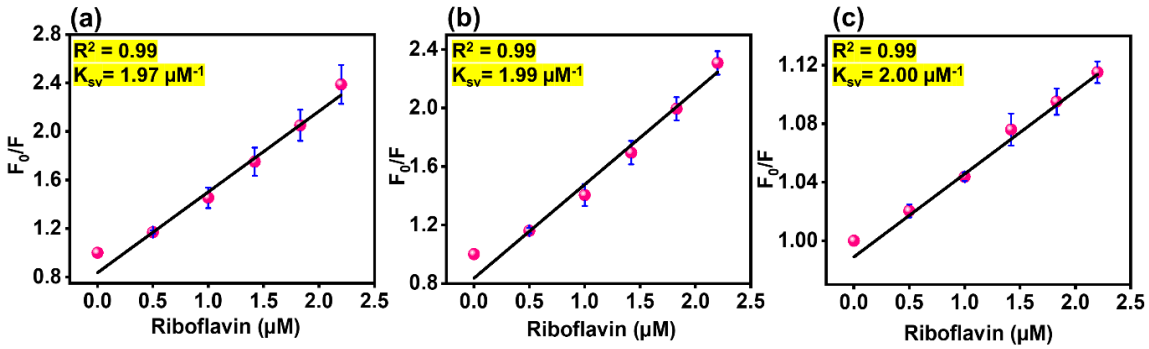

Figure 4.8. Stern-Volmer plots of N-CDs in (a) aqueous medium (λ_{ex}: 340 nm), (b) HEPES buffer at pH 7.4 (λ_{ex}: 360 nm) and (c) real sample of vitamin B_2 (λ_{ex}: 340 nm). The parameters 'F_0' and 'F' indicate the fluorescence intensity in the absence and presence of vitamin B_2, respectively. 'K_{sv}' signifies Stern-Volmer quenching constant, which was estimated from the slope of the plots. The black line indicates the linear fit of the data using OriginPro 2021 and R^2 denotes the goodness of the fits. Error bars represent standard error of measurements obtained from three independent experiments.

Further, to estimate the N-CDS-RF stoichiometry, and to understand the strength of interaction and binding between N-CDs and RF (vitamin B_2), the excited-state binding constant was calculated (Table 2) by taking the corresponding fluorescence intensity into account and using the 1:1 linear Benesi-Hildebrand equation as follows[58]:

$$\frac{1}{F_0 - F} = \frac{1}{F_0 - F_1} + \frac{1}{K_1[RF](F_0 - F)} \qquad (8)$$

'F_1' signifies the fluorescence intensity of N-CDs-RF complex. The plot of ($1/F_0$-F) against 1/[RF] yields a straight line. From the reciprocal of the respective slope values, binding constants (K_1) of N-CDs-RF complex was evaluated in aqueous, physiological buffer medium and real samples of vitamin B_2 supplement, which are shown in Table 2 and in Figures 4.9a, 4.9b and 4.9c. Overall, the binding constant (K_1) of N-CDs and RF (vitamin B_2) appears to be similar irrespective of the source of vitamin B_2 and the dispersant medium. Moreover, the limit of detection of vitamin B_2 at physiological pH (isolated sample) and for real sample (pharmaceutical tablet) appears to be almost similar (Table 2) which, once again, reaffirms the suitability and efficiency of our nanosensor towards detection of vitamin B_2 in real samples.

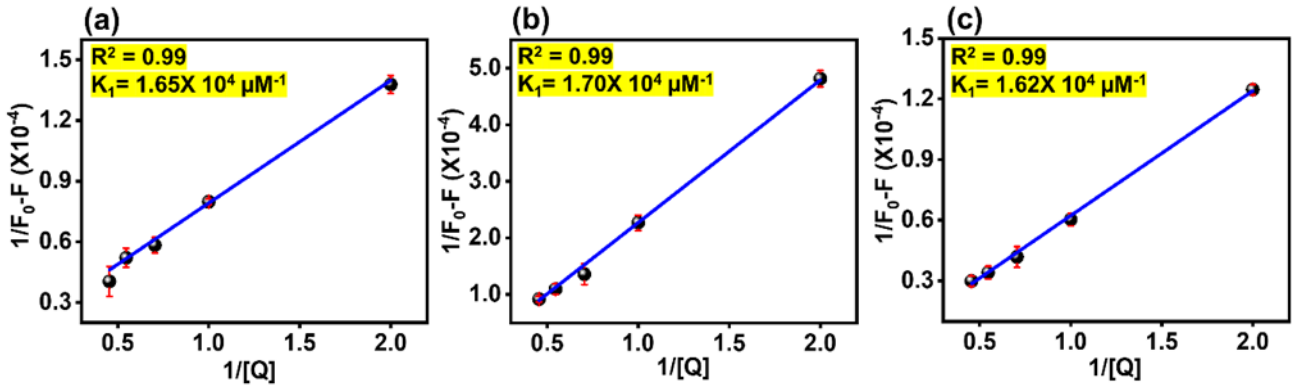

Figure 4.9. Benesi-Hildebrand plot of N-CDs in (a) aqueous medium (λ_{ex}: 340 nm), (b) HEPES buffer medium at pH 7.4 (λ_{ex}: 360 nm) and (c) real sample of vitamin B_2 (λ_{ex}: 340 nm). The parameters 'F_0' and 'F' indicate the fluorescence intensity in the absence and presence of vitamin B_2, respectively. Q indicates the concentration of the quencher (i.e. vitamin B_2) and K_1 depicts the binding constant, which was estimated from the reciprocal of the slope of the plots. The blue line indicates the linear fit of the data using OriginPro 2021 and R^2 denotes the goodness of the fits. Error bars represent standard error of measurements obtained from three independent experiments.

Parameters	**N-CDs+RF in aqueous medium**	**N-CDs+RF in HEPES buffer medium at pH 7.4**	**N-CDs+ real sample of vitamin B_2 tablet**
Linearity range (μM)	0-2.2	0-2.2	0-2.2
Limit of Detection (LOD) (nM)	35	55	61
Limit of Quantification (LOQ) (nM)	118	186	205
Binding constant (K_1) (μM^{-1})	1.65×10^4	1.70×10^4	1.62×10^4
Quenching constant (K_{sv}) (μM^{-1})	1.97	1.99	2.00
Regression coefficient (R^2)	0.99	0.99	0.99

Error limit = ± 5%

Table 4.2. Analytical performance data for RF (vitamin B_2) sensing by N-CDs.

4.3.7 Elucidation of sensing mechanism of RF (vitamin B_2) by N-CDs

It has been documented in the literature that the solution pH affects the structure of RF (vitamin B_2). The anionic species of RF at pH > 9.7 exhibits weak fluorescence; while the neutral and cationic species of RF have considerable fluorescence property with significant quantum yield.[59,60] Therefore, for our studies, sensing of RF was performed in neutral aqueous and buffer media by adjusting the solution pH and thereafter, we directed our efforts to delineate the mechanism of exclusive sensing of RF (vitamin B_2) by the N-CDs. The subsequent titrations of N-CDs were carried out by adding different concentrations of RF (0-2.2 μM) in aqueous solution (Figure 4.7a), HEPES buffer medium at pH 7.4 (Figure 4.10a), and real samples of vitamin B_2 tablet (Figure 4.10b).

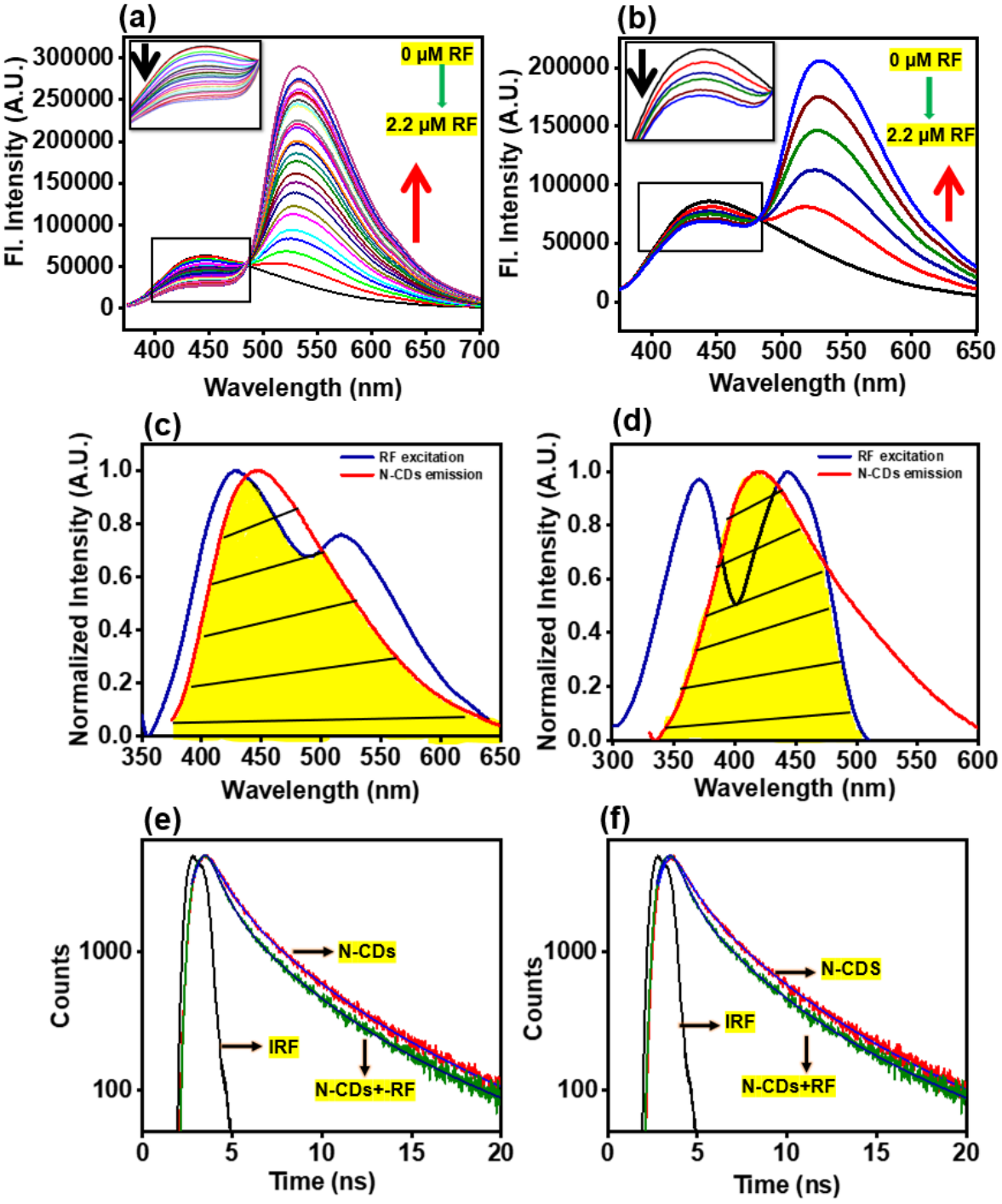

Figure 4.10. Variation in fluorescence emission of N-CDs in the presence of different concentrations of RF (0-2.2 μM) with inset image showing fluorescence quenching (a) in HEPES buffer at pH 7.4 (λ_{ex}: 360 nm), (b) upon addition of a real sample of Vitamin B_2 (λ_{ex}: 340 nm).

Black arrow depicts the progressive decrease of fl. intensity of N-CDs at shorter emission wavelength, while steady increase at longer emission wavelength is represented by red arrow, (c) Spectral overlap between emission spectrum of N-CDs (red) and excitation spectrum of RF (blue) where the yellow color demonstrates the overlapped region in HEPES buffer at pH 7.4, (d) Spectral overlap between emission spectrum of N-CDs (red) and excitation spectrum of RF (blue) where the yellow color demonstrates the overlapped region in real sample of Vitamin B_2, (e) Fluorescence lifetime decays of N-CDs in pH 7.4 HEPES buffer where, the sharp, thin black line represents the instrument response function, the red and olive lines represent the actual intensity decays in the absence and presence of RF respectively. The blue and royal blue lines correspond to fits obtained in the absence and presence of RF, respectively, (f) Fluorescence lifetime decays of N-CDs in the presence of a real sample of Vitamin B_2 where, the sharp, thin black line represents the instrument response function, the red and olive lines represent the actual intensity decays in the absence and presence of RF respectively. The blue and royal blue lines correspond to fits obtained in the absence and presence of RF, respectively.

At physiological pH (i.e. at pH 7.4), both N-CDs (Figure 4.6d) and RF are negatively charged since the pI of the latter is 6[5] and hence, electrostatic interactions between these moieties are unlikely. However, as aforementioned, we observed that only the N-CDs-RF signal produced a noteworthy output, while the other compounds did not show any appreciable changes in N-CDs fluorescence intensity. The N-CDs' selectivity for RF is based on the energy transfer that occurs only between these two moieties.[5] FRET mechanism is operative between N-CDs and RF (vitamin B_2) as clearly demonstrated due to a substantial overlap (Figure 4.7b) between the emission of donor (N-CDs) and excitation of acceptor (RF) probes. Energy transfer occurs as a result of long-range dipole-dipole interactions between donor and acceptor. Table 4 further clearly depicts that the separation distance between donor and acceptor is between 1-2 nm so FRET is highly effective during sensing.[10] In all the cases, the findings demonstrated that the PL intensity of N-CDs progressively decreased at shorter emission wavelength, while steadily increased at longer emission wavelength. The quenching and enhancement of PL intensity at shorter and longer wavelengths were attributed to the donor fluorescence of N-CDs and acceptor fluorescence of RF, respectively. The appearance of isoemissive point in the PL spectra signified the formation of a

complex between N-CDs and RF (vitamin B_2). The outcome clearly demonstrated that FRET mechanism is operative between N-CDs and RF (vitamin B_2) due to a substantial overlap (Figure 4.7b) between the emission of donor (N-CDs) and excitation of acceptor (RF) probes. Similar characteristic FRET mechanism also occurs in pH 7.4 buffer (Figure 4.10c) and also upon addition of the real sample of vitamin B_2 supplement (Figure 4.10d). Additionally, time-resolved fluorescence emission studies were carried out by exciting the respective samples at λ_{ex} = 340 nm. The lifetime components (τ_i), relative amplitudes (α_i) and the mean lifetime values (τ_m) are tabulated in Table 3.

System	**τ_1 (ns) (α_1)**	**τ_2 (ns) (α_2)**	**τ_3 (ns) (α_3)**	**τ_m[#](ns)**	**χ^2**
N-CDs (aqueous medium)	0.95 (0.57)	3.06 (0.36)	8.76 (0.07)	2.26	1.13
N-CDs (aqueous medium) +RF	0.99 (0.72)	1.79 (0.23)	7.90 (0.05)	1.55	1.13
N-CDs + real sample of vitamin B_2 tablet	0.68 (0.69)	2.68 (0.26)	8.49 (0.05)	1.60	1.12
N-CDs (HEPES buffer pH 7.4)	1.00 (0.60)	3.27 (0.33)	9.30 (0.06)	2.24	1.08
N-CDs (HEPES buffer pH 7.4) + RF	0.68 (0.72)	2.78 (0.23)	8.80 (0.05)	1.57	1.13

[#] $\tau_m = \alpha_1\tau_1+\alpha_2\tau_2+\alpha_3\tau_3$

Table 4.3. Fluorescence lifetime components of N-CDs and their respective coefficients along with the mean fluorescence lifetimes in aqueous and pH 7.4 medium. The lifetimes were extracted by fitting the time-resolved emission decays using a tri-exponential function. χ^2 represents the goodness of the fits.

The mean lifetime values of N-CDs were considerably reduced in the presence of RF in aqueous and buffer environments as well as real sample of vitamin B_2 supplements (Tables 1 and 3), confirming that FRET indeed occurs between electron rich donor N-CDs and electron deficient RF (vitamin B_2) (Figures 4.7c, 4.10c, 4.10d, and Figure 4.11). In light of this, the proposed nanosensor provided a simple method for developing a ratiometric FRET mechanism for the determination of RF (vitamin B_2) in aqueous and buffer environments.

To gain more insights into the NCDS-RF FRET process, overlap integral [J(λ)] values were calculated between emission of N-CDs and excitation of RF using the equation 3 (chapter 1)[10].

Moreover, the Förster distance (R_0) for N-CDs-RF pair was also calculated with the help of the equation 4 (chapter 1).[10] The calculated 'R_0' values for the specific N-CDs-RF pair in aqueous medium, HEPES buffer medium at pH 7.4 and real sample of vitamin B_2 supplement were found to be <10 nm (tabulated in Table 4), which obeys classical FRET theory and confirmed efficient energy transfer between N-CDs and RF.[10,61]

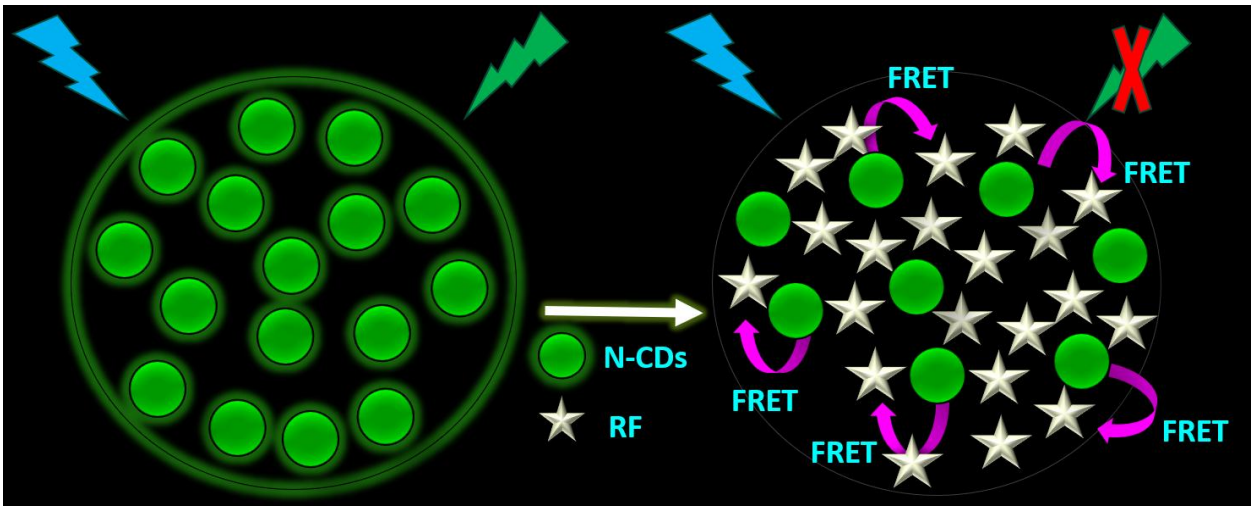

Figure 4.11. Schematic representation of FRET mechanism between N-CDs and RF leading to quenching of fluorescence emission from N-CDs.

Moreover, to estimate the rate of electron transfer (k_{ET}), equation 2 as mentioned in (chapter 1) was employed.[6] The calculated value of 'k_{ET}' is tabulated in Table 1, indicating electron transfer process is favoured between N-CDs and RF. Furthermore, to decipher the nature of electron transfer mechanism, FRET efficiency (E) of N-CDs-RF nanosensor was calculated using the equation 5 (chapter 1).[10] Table 4 clearly confirms that the FRET efficiency of N-CDs with RF (vitamin B_2) corroborated well with real sample analysis. Moreover, the separation distance (r) between the N-CDs-RF was also determined from the respective FRET efficiency values by using the equation 6 (chapter 1).[10] The calculated separation distance (r) values (Table 4) are found within the range of 1.57-2.04 nm (<10 nm), directly supporting the FRET process between N-CDs and RF (vitamin B_2).

N-CDs+RF	**R_0 (nm)**	**r (nm)**	**E (%)**
N-CDs+RF in aqueous medium	1.64	1.80	0.31
N-CDs+RF in HEPES buffer at pH 7.4	1.77	2.04	0.30
N-CDs+ real sample of vitamin B_2 tablet	1.35	1.57	0.29

Table 4.4. FRET parameters of N-CDs@RF nanosensor in different systems.

4.3.8 Estimation of limit of detection

An effective nanosensor for practical applications must have high selectivity and sensitivity for detection of analyte. Limit of detection (LOD) and limit of quantification (LOQ) includes the parameters for sensitivity of an ideal nanosensor. The LOD and LOQ values of N-CDs@RF nanosensor in aqueous physiological buffer medium and real sample of vitamin B_2 tablet (Table 2) were calculated from a linear plot between PL responses (F_0/F) and different concentrations of RF (0-2.2 μM) using the values of ($3\sigma/K$) and ($10\sigma/K$), respectively[23]. The parameters 'σ' denoted the standard deviation of the intercept and 'K' is the slope of the respective graphs. The LOD values of RF (vitamin B_2) in presence of aqueous and buffer medium was found to be ~35 nM (Figure 4.7d) and ~56 nM (Figure 4.12a), respectively with a linear concentration range of 0-2.2 μM along with excellent regression coefficient value of R^2 = 0.99. In comparison to other nanosensors reported in the literature, Table 5 demonstrates that the developed nanosensor has a high sensitivity towards RF (vitamin B_2) and a comparatively lower detection limit. The findings clearly suggest that the developed nanoprobe sensitively detects RF in nanomolar range both in aqueous and physiological buffer environments.

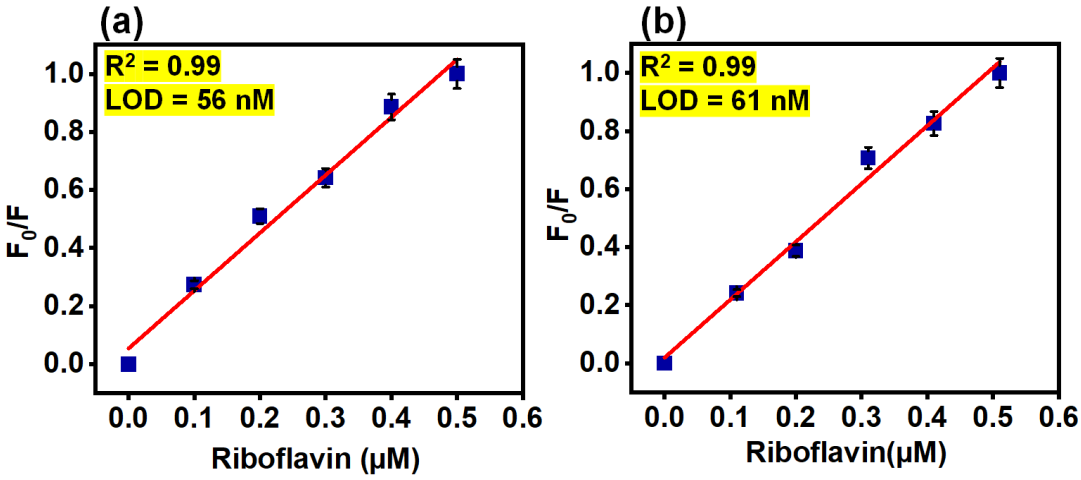

Figure 4.12. Linear relationship of fluorescence response (F_0/F) of N-CDs with different concentrations of RF (0-2.2 μM) in (a) HEPES buffer at pH 7.4 (λ_{ex}: 360 nm), (b) real sample of Vitamin B_2 (λ_{ex}: 340 nm). The parameters 'F_0' and 'F' indicate the fluorescence intensity in the absence and presence of vitamin B_2, respectively. LOD signifies limit of detection. The red line indicates the linear fit of the data using OriginPro 2021 and R^2 denotes the goodness of the fits. Error bars represent standard error of measurements obtained from three independent experiments.

Nanosensor	Method employed	Linear range (μM)	Limit of detection (nM)	Reference
NPCDs/riboflavin /FRET system	Hydrothermal method, 180˚C, 2h	0.5-50	170	4
Graphitic carbon nitride/Fluorimetry (FRET)	Microwave oven at 800 W for 50 s	0.4-1.0	170	55
Graphene-PEG/Fluorescence Quenching	Magnetic stirring, 45 min	0-6.3	90	56
AHNPs/riboflavin/FRET system	Pyrolysis method, 500˚C for 3 hours	0-0.7	71	57
This work	Microwave irradiation 150˚C, 10 min	0-2.2	35	-

Table 4.5. A comparative analysis of LOD for the detection of RF by different nanosensors

4.3.9 Method validation with real sample of vitamin B_2

The proposed nanosensor model was validated in accordance with ICHQ2(R1) recommendations.[65] To validate the efficacy of the designed nanosensor, the study was also performed for commercially available vitamin B_2 tablets using the standard addition method. In the real sample, the LOD value was found to be ~61 nM (Figure 4.12b). The synthesized nanoprobe detected excellent amount of RF with LOD in nanomolar range in real sample of vitamin B_2 tablets (Table 6), with good recovery percentages and a relative standard deviation (RSD) lower than 4%, indicating the reliability and standard precision and accuracy of ratiometric fluorescent nanosensor based detection of RF (vitamin B_2) in real samples.

Conc. added (µM)	**Conc. detected (µM)**	**Recovery rate**	**Recovery error**	**Relative standard deviation (RSD)**
0.5	0.48	93%	4%	2.3
1.42	1.39	97%	2%	2.3
2.2	2.19	99%	0.4%	0.3

Table 4.6. Application of the developed nanosensor for detection of real sample of RF in Tablet

4.4 Conclusions

In summary, using microwave-assisted pyrolysis technique, a rapid, cost-effective, and sustainable strategy was employed to synthesize N-CDs from Indian Gooseberry (*Phyllanthus emblica*). Presence of amino acids, polyphenols, alkaloids, cholesterol in biomass precursor of Indian Gooseberry resulted in intrinsic functionalized N-CDs with high fluorescence property (PLQY 48%). The synthetic methodology was maintained in green environment without the use of any harsh chemicals. The presence of nitrogen functionalization on N-CDs was confirmed by EDS, XPS, FTIR and Raman spectroscopic analysis. HRTEM imaging revealed spherical shape of the as-prepared nanoprobe with an average diameter of 8.1 nm. N-CDs showed green emissive fluorescence under UV-illumination and excitation dependent emission property. With the aid of UV-Visible, fluorescence, and time-resolved emission spectroscopic analysis, the optical properties of N-CDs were characterized. In addition, N-CDs also showed remarkable solubility in aqueous and physiological pH of buffer media, photostability, and environmental stability (pH, ionic strength) in order to fulfill the requirements of an ideal nanosensor. The as-prepared nanoprobe showed selectivity and sensitivity towards detection of RF through FRET mechanism in nanomolar range under both aqueous and physiological conditions. The proposed model of the nanosensor was also validated in real sample of vitamin B_2 supplements with high precision and accuracy level in nanomolar level detection. Therefore, the development of the synthesized nanosensor from biomass may have potential applications in the biological and food industries.

References

1) Kundu, A.; Nandi, S.; Layek, R. K; Nandi, A. K. Fluorescence Resonance Energy Transfer from Sulfonated Graphene to Riboflavin: A Simple Way to Detect Vitamin B_2. *ACS Appl. Mater. Interfaces* **2013**, *5,* 7392-7399. https://doi:10.1021/am4017208

2) Pramanik, S.; Roy, S.; Bhandari, S. The quantum dot-FRET-based detection of vitamin B_{12} at a picomolar level. *Nanoscale Adv.* **2020**, *2*, 3809-3814. https://doi.org/10.1039/D0NA00540A

3) Monte-Filho, S. S.; Andrade, S. I. E.; Lima, M. B.; Araujo, M. C. U. Synthesis of highly fluorescent carbon dots from lemon and onion juices for determination of riboflavin in multivitamin/mineral supplements. *J. Pharm. Anal.* **2019,** *9*, 209-216. https://doi.org/10.1016/j.jpha.2019.02.003

4) Lin, L.; Wang, Y.; Xiao, Y.; Chen, X. Ratiometric fluorescence detection of riboflavin based on fluorescence resonance energy transfer from nitrogen and phosphorus co-doped carbon dots to riboflavin. *Anal. Chem.* **2019**, *411*, 2803-2808. https://doi.org/10.1007/s00216-019-01725-1

5) Sotolongo-García, R.; Rodríguez-Velázquez, R.; Alatorre-Meda, M.; Oropeza-Guzmán, M. T.; Tirado-Guízar, A.; Pina-Luis, G. Optimizing the Efficiency of a Cytocompatible Carbon-Dots-Based FRET Platform and Its Application as a Riboflavin Sensor in Beverages. *Nanomaterials* **2021**, *11*, 1981-1999. https://doi.org/10.3390/nano11081981

6) Qiang, R.; Yang, S.; Hou, K.; Wang, J. Synthesis of carbon quantum dots with green luminescence from potato starch. *New J. Chem.* **2019**, *43*, 10826-10833. https://doi:10.1039/c9nj02291k.

7) Lim, S. Y.; Shen, W.; Gao, Z. Carbon quantum dots and their applications. *Chem. Soc. Rev.* **2015**, *44*, 362-381. https://doi.org/10.1039/C4CS00269E

8) Hu, L.; Yang, X.; Wang, C.; Yuan, H.; Xiao, D. Determination of riboflavin in urine and beverages by capillary electrophoresis with in-column optical fibre laser-induced fluorescence detection. *J. Chromatogr. B* **2007**, *856*, 245-251. https://doi.org/10.1016/j.jchromb.2007.06.011

9) Zandomeneghi, M.; Carbonaro, L.; Calucci, L.; Pinzino, C.; Galleschi, L.; Ghiringhelli, S. Direct fluorometric determination of fluorescent substances in powders: the case of riboflavin in cereal flours. *J. Agric. Food Chem.* **2003**, *51*, 2888-2895. https://doi.org/10.1021/jf0260287

10) Lakowicz, J. R. Principles of Fluorescence Spectroscopy, 3rd edition; Springer: New York, **2006**, 1-95 and 529-575.

11) Dong, W.; Wang, R.; Gong, X.; Dong, C. An efficient turn-on fluorescence biosensor for the detection of glutathione based on FRET between N, S dual-doped carbon dots and gold nanoparticles. *Anal. Bioanal. Chem*. **2019**, *411*, 6687–6695. https://doi.org/10.1007/s00216-019-02042-3

12) Le, T. H.; Ahn, Y. N.; Park, S. J. An effective method for cysteine determination based on fluorescence resonance energy system between co-doped graphene quantum dots and silver nanoparticles. *Korean J. Chem. Eng.* **2022**, *39*,1065–1071. https://doi.org/10.1007/s11814-021-0956-4

13) Zhao, Q.; Song, W.; Zhao B.; Yang, B. Spectroscopic studies of the optical properties of carbon dots: recent advances and future prospects. *Mater. Chem. Front.* **2020**, *4*, 472-488. https://doi:10.1039/c9qm00592g

14) Yan, F.; Sun, Z.; Zhang, H.; Sun, X.; Jiang, Y.; Bai, Z. The fluorescence mechanism of carbon dots, and methods for tuning their emission color: a review. *Microchim Acta* **2019**, *186*, 583-620. https://doi.org/10.1007/s00604-019-3688-y

15) Kumar, P.; Dua, S.; Kaur, R.; Kumar, M.; Bhatt, G. A review on advancements in carbon quantum dots and their application in photovoltaics. *RSC Adv.* **2022**, *12*, 4714–4759. https://doi.org/10.1039/D1RA08452F

16) Ramírez-Barroso, S.; Jacobo-Martín, A.; Navarro-Baena, I.; Hernández, J. J.; Navio, C.; Rodríguez, I.; Wannemacher, R. On the nature of solvothermally synthesized carbon nanodots. *J. Mater. Chem. C* **2021**, *9*, 16935-16944. https://doi.org/10.1039/D1TC04255F

17) Anwar, S.; Ding, H.; Xu, M.; Hu, X.; Li, Z.; Wang, J.; Liu, L.; Jiang, L.; Wang, D.; Dong, C.; Yan, M.; Wang, Q.; Bi, H. Recent Advances in Synthesis, Optical Properties, and Biomedical Applications of Carbon Dots. *ACS Appl. Bio Mater.* **2019**, *2*, 2317-2338. https://doi.org/10.1021/acsabm.9b00112

18) Li, H.; Kang, Z.; Liu, Y.; Lee, S. T. Carbon nanodots: synthesis, properties and applications. *J. Mater. Chem.* **2012**, *22*, 24230-24253. https://doi.org/10.1039/C2JM34690G

19) Barman, M. K.; Patra, A. Current status and prospects on chemical structure driven photoluminescence behaviour of carbon dots. *J. Photochem. Photobiol. C* **2018**, *37*, 1-22. https://doi.org/10.1016/j.jphotochemrev.2018.08.001

20) Yadav, P. K.; Singh, V. K.; Chandra, S.; Bano, D.; Kumar, V.; Talat, M.; Hasan, S. H. Green Synthesis of Fluorescent Carbon Quantum Dots from Azadirachta indica Leaves and Their Peroxidase-Mimetic Activity for the Detection of H_2O_2 and Ascorbic Acid in Common Fresh Fruits. ACS Biomater. Sci. Eng. **2019**, 5, 623–632. https://doi.org/10.1021/acsbiomaterials.8b01528

21) Park, M.; Sharma, A.; Kang, C.; Han, J.; Tripathi, K. M.; Lee, H. N-Doped Carbon Nanorods from Biomass as a Potential Antidiabetic Nanomedicine. ACS Biomater. Sci. Eng. **2022**, 8, 2131–2141. https://doi.org/10.1021/acsbiomaterials.1c01598

22) Deng, W.; Zang, C.; Li, Q.; Sun, B.; Mei, X.; Bai, L.; Shang, X.; Deng, Y.; Xiao, Y.; Ghiladi, R.; Lorimer, G.; Zhang, X.; Wang, J. Hydrothermally Derived Green Carbon Dots from Broccoli Water Extracts: Decreased Toxicity, Enhanced Free-Radical Scavenging, and Anti-Inflammatory Performance. *ACS Biomater. Sci. Eng.* **2023**, *9*, 1307–1319. https://doi.org/10.1021/acsbiomaterials.2c01537

23) Kundu, A.; Maity, B.; Basu, S. Rice Husk-Derived Carbon Quantum Dots-Based Dual-Mode Nanoprobe for Selective and Sensitive Detection of Fe^{3+} and Fluoroquinolones. ACS Biomater. Sci. Eng. **2022**, 8, 4764-4776, https://doi.org/10.1021/acsbiomaterials.2c00798

24) Atchudan, R.; Kishore, S. C.; Gangadaran, P.; Edison, T. N. J. I.; Perumal, S.; Rajendran, R. L.; Alagan, M.; Al-Rashed, S.; Ahn, B. C.; Lee, Y. R. Tunable fluorescent carbon dots from biowaste as fluorescence ink and imaging human normal and cancer cells *Environ. Res*. **2022**, *204*, 112365. https://doi.org/10.1016/j.envres.2021.112365

25) Atchudan, R.; Edison, T. N. J. I.; Perumal, S.; Muthuchamy, N.; Lee, Y. R. Hydrophilic nitrogen-doped carbon dots from biowaste using dwarf banana peel for environmental and biological applications. *Fuel* **2020**, *275*, 117821-117830. https://doi.org/10.1016/j.fuel.2020.117821

26) Atchudan, R.; Edison, T. N. J. I.; Perumal, S.; Vinodh, R.; Lee, Y. R. Betel-derived nitrogen-doped multicolor carbon dots for environmental and biological applications. *J. Mol. Liq.* **2019,** *296,* 111817-111826. https://doi.org/10.1016/j.molliq.2019.111817

27) Atchudan, R.; Edison, T. N. J. I.; Aseer, K. R.; Perumal, S.; Karthik, N.; Lee, Y. R. Highly fluorescent nitrogen-doped carbon dots derived from Phyllanthus acidus utilized as a fluorescent probe for label-free selective detection of Fe^{3+} ions, live cell imaging and fluorescent ink. *Biosens. Bioelectron.* **2018**, *99*, 303-311. http://dx.doi.org/10.1016/j.bios.2017.07.076

28) Atchudan, R.; Edison, T. N. J. I.; Lee, Y. R. Nitrogen-doped carbon dots originating from unripe peach for fluorescent bioimaging and electrocatalytic oxygen reduction reaction. *J. Colloid Interface Sci.* **2016,** *482*, 8-18. http://dx.doi.org/10.1016/j.jcis.2016.07.058

29) Kulkarni, K. V.; Ghurghure, S. M. Indian gooseberry (Emblica officinalis): Complete pharmacognosy review. *Int. J. Chem. Stud.* **2018**, *2*, 5-11. https://doi:10.1016/j.phrs.2016.06.013

30) Shrivastava, S.; Kaur, J.; Mehraj, M.; Feroz, F.; Chawla, J.; Kumari, S. Emblica officinalis (Amla): A comprehensive review of the miracle berry. *J. Pharm. Innov*. **2022**, *11*, 6-16.

31) Arul, V.; Sethuraman, M. G. Hydrothermally Green Synthesized Nitrogen-Doped Carbon Dots from Phyllanthus emblica and Their Catalytic Ability in the Detoxification of Textile Effluents. *ACS Omega* **2019**, *4*, 3449−3457. https://doi:10.1021/acsomega.8b03674

32) Atchudan, R.; Edison, T. N. J. I.; Perumal, S.; Lee, Y. R. Indian Gooseberry-Derived Tunable Fluorescent Carbon Dots as a Promise for In Vitro/In Vivo Multicolor Bioimaging and Fluorescent Ink. *ACS Omega* **2018**, *3*, 17590−17601. https://doi:10.1021/acsomega.8b02463.

33) Jlassi K.; Eid, K.; Sliem, M. H.; Abdullah, A. M.; Chehimi M. M.; Krupa, I. Rational synthesis, characterization, and application of environmentally friendly (polymer–carbon dot) hybrid composite film for fast and efficient UV-assisted Cd^{2+} removal from water. *Environ. Sci. Eur.* **2020**, *32*, 12-25. https://doi.org/10.1186/s12302-020-0292-z

34) Wang, M.; Wan, Y.; Zhang, K.; Fu, Q.; Wang, L.; Zeng, J.; Xia, Z.; Gao, D. Green synthesis of carbon dots using the flowers of Osmanthus fragrans (Thunb.) Lour. as precursors:

application in Fe^{3+} and ascorbic acid determination and cell imaging. *Anal. Bioanal. Chem.* **2019**, *411*, 2715–2727. https://doi.org/10.1007/s00216-019-01712-6

35) Thirukumaran, P.; Atchudan, R.; Balasubramanian, R.; Shakila Parveen, A.; Kim, S. C. Direct Synthesis of Nitrogen-Rich Carbon Sheets via Polybenzoxazine as Highly Active Electrocatalyst for Water Splitting. *Int. J. Hydrog. Energy* **2018**, *43*, 13266−13275. https://doi.org/10.1016/j.ijhydene.2018.05.108

36) Hu, Y.; Yang, J.; Tian, J.; Jia, L.; Yu, J. S. Waste Frying Oil as a Precursor for One-Step Synthesis of Sulfur-Doped Carbon Dots with pH-Sensitive Photoluminescence. *Carbon* **2014**, *77*, 775−782. https://doi.org/10.1016/j.carbon.2014.05.081

37) Shaikh, A. F.; Tamboli, M. S.; Patil. R. H.; Bhan, A.; Ambekar, J. D.; Kale, B. B. Bioinspired Carbon Quantum Dots: An Antibiofilm Agents. *J. Nanosci. Nanotechnol.* **2019**, *19*, 2339–2345. https://doi:10.1166/jnn.2019.16537

38) Alhaidrai SA, A.; Hadi-FA, A.; Kaf AG, A.; Deen AM, T. A. Phytochemical Screening by FTIR Spectroscopic Analysis in the Methanolic Extracts Coffee (C. Arabica. L) to Seeds and Peels (Unroasted and Roasted) Cultivars Grown in Yemen. *Bioequiv & Bioavailab Int J.* **2022**, *6*, 000179-00187. https://doi:10.23880/beba-16000179

39) Hua, Z.; Jiaob, X. Y.; Xu, L. The N, S co-doped carbon dots with excellent luminescent properties from green tea leaf residue and its sensing of gefitinib. *Microchem. J.* **2020**, *154*, 104588-104596. https://doi.org/10.1016/j.microc.2019.104588

40) Khan, W. U.; Wang, D.; Zhang, W.; Tang, Z.; Ma, X.; Ding, X.; Du, S.; Wang, Y. High Quantum Yield Green-Emitting Carbon Dots for Fe (III) Detection, Biocompatible Fluorescent Ink and Cellular Imaging. *Sci. Rep.* **2017**, *7*, 14866-14875. https://doi:10.1038/s41598-017-15054-9

41) Xie, Y.; Cheng, D.; Liu, X.; Han, A. Green Hydrothermal Synthesis of N-doped Carbon Dots from Biomass Highland Barley for the Detection of Hg^{2+}. *Sensors* **2019**, *19*, 3169-3179. https://doi:10.3390/s19143169

42) Sahu, S.; Behera, B.; Maiti, T. K.; Mohapatra, S. Simple One-Step Synthesis of Highly Luminescent Carbon Dots from Orange Juice: Application as Excellent Bio-Imaging Agents. *Chem. Commun.* **2012**, *48*, 8835−8837. https://doi.org/10.1039/C2CC33796G

43) Akhavan, O. Bacteriorhodopsin as a Superior Substitute for Hydrazine in Chemical Reduction of Single-Layer Graphene Oxide Sheets. *Carbon* **2015**, *81*, 158−166. https://doi.org/10.1016/j.carbon.2014.09.044

44) Atchudan, R.; Edison, T. N. J. I.; Perumal, S.; Karthik, N.; Karthikeyan, D.; Shanmugam, M.; Lee, Y. R. Concurrent synthesis of nitrogen-doped carbon dots for cell imaging and ZnO@nitrogen-doped carbon sheets for photocatalytic degradation of methylene blue *J. Photochem. Photobiol. A.* **2018**, *305*, 75-85. https://doi.org/10.1016/j.jphotochem.2017.09.038

45) Khan, Z. M. S. H.; Rahman, R. S.; Shumaila; Islam, S.; Zulfequar, M. Hydrothermal Treatment of Red Lentils for the Synthesis of Fluorescent Carbon Quantum Dots and Its Application for Sensing Fe^{3+}. *Opt. Mater. (Amst).* **2019**, *91*, 386–395. https://doi.org/10.1016/j.optmat.2019.03.054

46) Atchudan, R.; Jebakumar Immanuel Edison, T. N.; Shanmugam, M.; Perumal, S.; Somanathan, T.; Lee, Y. R. Sustainable Synthesis of Carbon Quantum Dots from Banana Peel Waste Using Hydrothermal Process for in Vivo Bioimaging. Phys. E Low-Dimensional Syst. *Nanostructures* **2021**, *126*, 114417. https://doi.org/10.1016/j.physe.2020.114417

47) Zhao, W.; Zhang, Y.; Cao, B.; Li, Z.; Sun, C.; Cao, X.; Cong, S. Characteristics of Mussels-Derived Carbon Dots and Their Applications in Bio-Imaging and Detection of Riboflavin. *Foods* **2022**, *11*, 2451-2465. https://doi.org/10.3390/ foods11162451

48) Bai, M.; Wu, W.; Liu, L.; Chen, J.; Ma, X.; Meng, Y. NaCl and oxalic acid–assisted solvothermal exfoliation of edge-oxidized graphite to produce organic graphene dispersion for transparent conductive film application. *J. Nanopart. Res.* **2019**, *21*, 145-158. https://doi.org/10.1007/s11051-019-4574-6

49) Kainth, S.; Goel, N.; Basu, S.; Maity, B. Surfactant-Derived Water-Soluble Carbon Dots for Quantitative Determination of Fluoride via a Turn-off–on Strategy. *New J. Chem.* **2022**, *46*, 686–694. https://doi.org/10.1039/D1NJ04838D

50) Ma, X.; Li, S.; Hessel, V.; Lin, L.; Meskers, S.; Gallucci, F. Synthesis of luminescent carbon quantum dots by microplasma process. *Chem. Eng. Process.* **2019**, *140*, 29-35. https://doi.org/10.1016/j.cep.2019.04.017

51) Kamalakannan, K.; Morais, A.; Nongwe, I.; Longo, C.; Nogueira, A. F.; Coville, N. J.; Ranganathan, K. Study of photoelectrochemical water splitting using composite films based on TiO_2 nanoparticles and nitrogen or boron doped hollow carbon spheres as photoanodes. *J. Mol. Catal. A Chem.* **2016**, *422*, 165-174. https://doi.org/10.1016/j.molcata.2015.10.024

52) Prasad, P. S. R.; Prasad, K.S.; Thakur, N. K. FTIR signatures of type-II clathrates of carbon dioxide in natural quartz veins. *Curr. Sci.* **2006**, *90*, 1544-1547.

53) Kumari, A.; Kumar, A; Sahu, A. K.; Kumar, S. Synthesis of green fluorescent carbon quantum dots using waste polyolefins residue for Cu^{2+} ion sensing and live cell imaging. *Sens. Actuators B Chem.* **2018**, *254*, 197-205. http://dx.doi.org/10.1016/j.snb.2017.07.075

54) Deng, Y.; Chen, M.; Chen, G.; Zou, W.; Zhao, Y.; Zhang, H.; Zhao, Q. Visible-Ultraviolet Upconversion Carbon Quantum Dots for Enhancement of the Photocatalytic Activity of Titanium Dioxide. *ACS Omega* **2021**, 6, 4247–4254. https://doi.org/10.1021/acsomega.0c05182

55) Mondal, T. K.; Ghorai, U. K.; Saha, S. K. Dual-Emissive Carbon Quantum Dot-Tb Nanocomposite as a Fluorescent Indicator for a Highly Selective Visual Detection of Hg (II) in Water. *ACS Omega* **2018**, *3*, 11439−11446. https://doi.org/10.1021/acsomega.8b01159

56) Wang, L.; Weng, S.; Su, S.; Wang, W. Progress on the luminescence mechanism and application of carbon quantum dots based on biomass synthesis. *RSC Adv.* **2023**, ***13,*** 19173-19194. https://doi.org/10.1039/D3RA02519E

57) Dager, A.; Uchida, T.; Maekawa, T.; Tachibana, M. Synthesis and characterization of Mono-disperse Carbon Quantum Dots from Fennel Seeds: Photoluminescence analysis using Machine Learning. *Sci. Rep.* **2019**, *9*, 14004-14016. https://doi.org/10.1038/s41598-019-50397-5

58) Sohal, N.; Maity, B.; Bau, S. Morphology Effect of One-Dimensional MnO_2 Nanostructures on heteroatom-Doped Carbon Dot-Based Biosensors for Selective Detection of Glutathione. *ACS Appl. Bio Mater.* **2022**, *5*, 2355-2364. https://doi.org/10.1021/acsabm.2c00189

59) Russell, L. F.; Brooks, L.; McRae K. B. Development of a robotic-HPLC determination of riboflavin vitamers in food. *Food Chem.* **1998**, *63*, 125-131. https://doi.org/10.1016/S0308-8146(97)00216-1

60) Eitenmiller RR, Jr WOL, Ye L. Vitamin analysis for the health and food sciences. 2nd ed. Boca Raton: CRC Press, 2008, https://doi.org/10.1201/9781420009750

61) Monte-Filho, S. S.; Andrade, S. I. E.; Lima, M. B.; Araujo, M. C. U. Synthesis of highly fluorescent carbon dots from lemon and onion juices for determination of riboflavin in multivitamin/mineral supplements. *J. Pharm. Anal.* **2019**, *9*, 209-216. https://doi.org/10.1016/j.jpha.2019.02.003

62) Han, J.; Zou, H.Y.; Gao, M.X.; Huang, C.Z. A graphitic carbon nitride-based fluorescence resonance energy transfer detection of riboflavin. *Talanta* **2016**, *148*, 279–284. https://doi.org/10.1016/j.talanta.2015.10.038

63) Díez-Pascual, A.M.; García-García, D.; San Andrés, M.P.; Vera, S. Determination of riboflavin based on fluorescence quenching by graphene dispersions in polyethylene glycol. *RSC Adv.* **2016**, *6*, 19686–19699. https://doi.org/10.1039/C5RA25547C

64) Mahajan, P. G.; Dige, N. C.; Suryawanshi, S. B.; Dalavi, D.K.; Kamble, A. A.; Bhopate, D. P.; Kadam, A. N.; Kondalkar, V. V.; Kolekar, G. B.; Patil, S. R. FRET Between Riboflavin and 9-Anthraldehyde Based Fluorescent Organic Nanoparticles Possessing Antibacterial Activity. *J Fluoresc.* **2018**, *28*, 207-215. https://doi.org/10.1007/s10895-017-2183-2

65) Guideline, I. C. H. H. T., Validation of Analytical Procedures: Text and Methodology, Q2, **2005**, *1*, 20, 5.

Chapter 5

Deep eutectic solvent-assisted carbon quantum dots for nanomolar detection of 4-nitrophenol

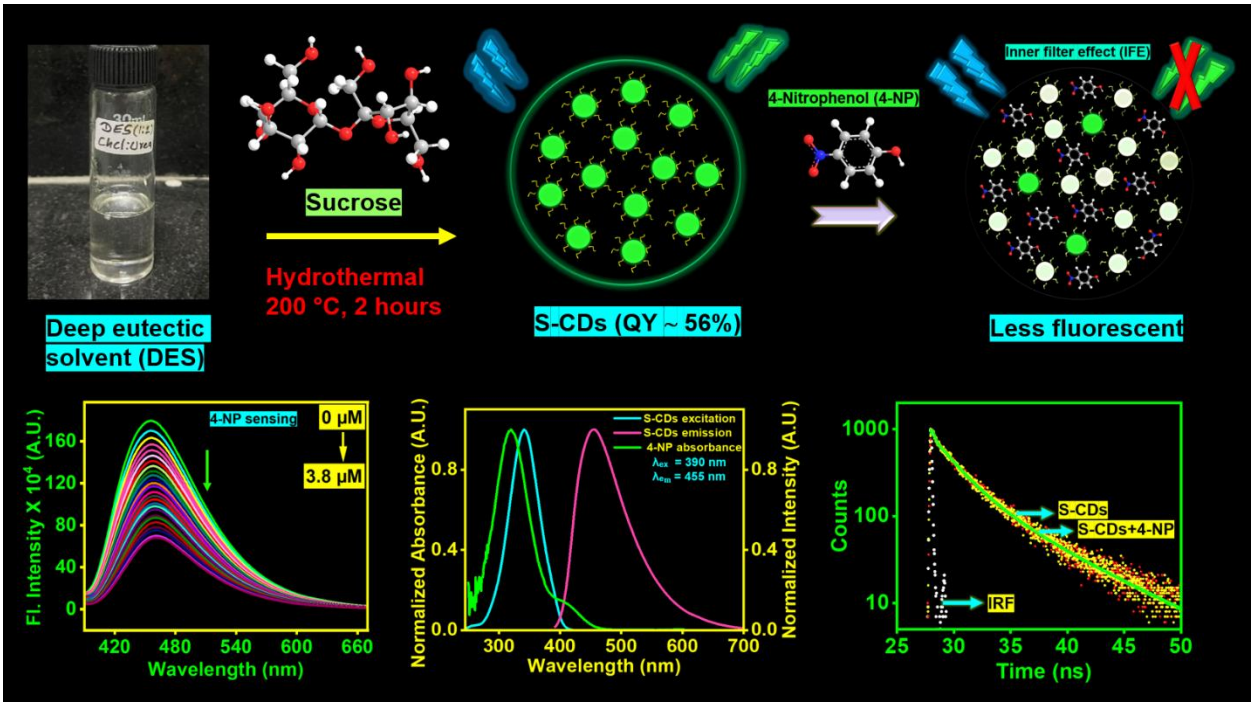

5.1 Introduction

With the advancement of civilization and the expansion of industry, an enormous amount of harmful organic pollutants in industrial wastewater ends up flowing into the environment.[1] 4-NP is a priority contaminant in industrial and agricultural wastewaters and is challenging to quantify owing to its low concentration.[2] 4-NP is often utilized as an intermediary in the manufacturing of synthetic colors, leather processing, pharmaceuticals, and other products. For example, it is used as an intermediary in the manufacture of medicinal chemicals such paracetamphenol and phenacetin, insecticides like parathion and phosphorous salon, and azo dyes.[3] A low concentration of 4-NP has the potential to induce cancer in animals, impede microbial communities, and kill a significant number of aquatic organisms. Additionally, it induces fatal coma and acute poisoning in humans.[1] Owing to its detrimental impacts the U.S. Environmental Protection Agency (USEPA) has established a set a maximum allowable level of 0.43 μM/L in drinking water. 4-NP can persist in the environment for an extended time period, depending on its stability, water solubility, and resistance to degradation.[4] Thus, it is crucial and essential to develop a sensitive and precise technique for 4-NP detection.

In the realm of nanotechnology, carbon quantum dots (CDs) have emerged as versatile contenders, and the scientific community has witnessed immense changes with their introduction. This hottest carbon member has a spherical morphology with a diameter less than 10 nm and are distinguished by a carbon core, crystalline or slightly amorphous, anchored with surface functional groups.[5,6] Among these, carbon quantum dots (CDs) have garnered considerable attention owing to their unique optical, electronic, and chemical properties. Emerging nanomaterials known as carbon quantum dots (CDs) have garnered considerable attention owing to unique optical, electronic, and chemical properties. Unlike conventional dye molecules and semiconductor-based quantum dots, CDs possess excellent light resistance and scintillation light bleaching resistance. Additionally, they exhibit appealing features including low toxicity, biocompatibility, affordability, and great photostability. CDs have thus been proposed as sophisticated materials for use in photocatalysis, sensors, bio-imaging, cell markers, optoelectronic devices, energy conversion and drug delivery. The study of CDs has gained significant popularity recently and is a rapidly expanding research field in both the scientific and industrial worlds.[7]

Bottom-up techniques like carbonization of glucose, glycol, ascorbic acid, citric acids, and other similar substances have garnered considerable interest to synthesize luminescent C-dots. However, the most of these synthesis processes include multiple steps, strong acids and post-treatment with surface passivating chemicals for better water solubility and luminescence. To create self-passivated photoluminescent C-dots, a simple, one-step process with economical approach is essential. Hydrothermal carbonization (is cheaper, environment friendly, and nontoxic method to develop novel carbon quantum dots using a variety of precursors.[8]

Deep eutectic solvents (DES) have emerged recently possessing impressive qualities such as being nontoxic, biodegradable, cheap, recyclable, a wide dissolving range, and high biocompatibility.[9,10] DES are ideal solvents as well as doping agents for synthesizing doped CDs due to their rich elemental composition.[11,12] DES often comprise two or more compounds that may self-associate via hydrogen bonds, resulting in a eutectic mixture which typically has a significant lower melting point as compared to their individual precursor components. DES can be formed by combining hydrogen bond acceptors (HBAs), such as quaternary ammonium compounds, with hydrogen bond donors (HBDs), such as acids, alcohols, amines, and other substances.[13] Interestingly, changing the surface functionalization and starting materials (HBA and HBD) can change the sensing capabilities of CDs and affect their emission characteristics. DES were therefore used in this investigation to make CDs by serving both as doping agents and solvents.[14]

While various methods exist for synthesizing CDs, the utilization of an inexpensive, plentiful, and biocompatible material sucrose as a precursor has offering a sustainable and economically viable route to produce these carbon dots with a lot of functional groups on their surface, which can have a lot of applications.[15] This paper delves into the synthesis, properties, and applications of sucrose-derived carbon quantum dots, shedding light on their promising role in diverse fields. In particular, sucrose in an aqueous solution hydrolyzes into fructose and glucose, which then break down into smaller organic molecules (such as furfurals and weak acids). These organic chemicals are subsequently polymerized into larger molecules, resulting in the synthesis of CDs in the hydrothermal reactor.[16-18]

The most extensively researched DES is choline chloride (ChCl) and urea. Abbott et al. discovered that at a molar ratio of ChCl: urea of 1:2, the mixture has a deep eutectic effect, since it has a lower melting point (12 °C) as compared to that of the individual components (melting point of choline

chloride = 302 °C and urea = 133 °C), therefore, enabling the mixture to be used as an ambient temperature solvent. ChCl-urea has demonstrated outstanding performance in a variety of applications, including catalysis, organic synthesis, electrochemistry, and nanoparticle production.[19,20]

Currently, 4-NP may be detected using a variety of techniques, including spectrophotometry, electrochemistry, chromatography technology, capillary electrophoresis, chemiluminescence, fluorescence, and others. Some of the aforementioned techniques are not feasible owing to the lengthy and costly experimental process, intricate instrument use, and laborious pre- and post-treatment processes and sometimes even the production of toxic substances and secondary pollutants might happen.[21,22] Fluorescence spectrophotometry is widely employed in analysis and detection due to its ease of use, quick, on-site detection, high selectivity and sensitivity, and inexpensive cost of operation.[23,24]

Peng et al. synthesized fluorescent sulphur quantum dots (SQDs) via top down approach using PEG and sublimed sulphur powder by stirring in oil bath for 72 h at 70 °C for detecting 4-NP with LOD 70 nM.[25] Tu et al. used hydrothermal approach in order to develop fluorescent nitrogen and phosphorus-doped carbon dots (Aa N, P-CDs) using Auricularia auricula for detecting 4-nitrophenol (4-NP). The limit of detection was found to be 198 nM ranging linearly 0-37.5 μM.[26] Fang et al. also used hydrothermal approach and interestingly, they discovered metal Cu-doped carbon dots (Cu-CDs) by single-step (180 °C for 10 hours). They also found that these Cu-CDs are effective in detecting *p*-NP with LOD 80 nM ranging linearly 0.5-50 μM.[27] Huang et al. employed cuttlefish ink-based N and S co-doped CDs in order to sensitively detect 4-NP. The detection limit obtained was 0.05 μM.[28] CDS−$Ru(bpy)_3^{2+}$−Ce(IV) chemiluminescence sensor was designed by Amjadi and Hallaj which is derived from a glucose and was further used for determining 4- NP.[29] Tian et al. synthesized N-CDs by following hydrothermal approach (200 °C for 9 hours) using o-phenylenediamine and dicyandiamine for 4-nitrophenol (4-NP). The detection range was f 0.1–39 μM, which corresponded to a detection limit (LOD) of 0.05 μM.[30] Soni et al. synthesized palm shell based carbon quantum dots treated with triflic acid for successful 4-NP detection with limit of detection 0.079 μM with ranging linearly 0.2–0.40 μM.[31]

The S-CDs were created by using a simple, single-step hydrothermal method, where sucrose is used as the carbon precursor, ChCl-urea is des system as a N and Cl-dopant or passivation agent

as well as green solvent medium. The resulting S-CDs have outstanding fluorescence characteristics, were almost spherical shaped, and good aqueous solubility. The generated S-CDs were employed as prospective fluorescent nanoprobes with an aim to detect the important industrial pollutant 4-NP in an extremely selective as well as sensitive was and in the nanomolar range. Dr. A.P.J. Abdul Kalam's statement links a clean environment to the fundamental human rights required for a decent existence. New technologies are critical to satisfying worldwide water treatment demands. This innovative system not only addresses energy and environmental concerns, but it also offers a long-term solution for wastewater treatment and pollutant removal. Implementing a low-cost, high-performance system can ensure water safety for consumption and reuse, opening the path for a healthier, more affluent future for everyone.[32]

5.2 Experimental section

5.2.1 Materials

To prepare fluorescent S-CDs sucrose, ascorbic acid (AA), and glucose were procured from HiMedia and used as obtained. Sodium citrate, sodium phosphate monobasic, trizma base, alanine (Ala), arginine (Arg), asparagine (Asn), aspartic acid (Asp), cysteine (Cys), glutamic acid (Glu), glutamine (Gln), histidine (His), isoleucine (Ile), leucine (Leu), lysine (Lys), methionine (Met), threonine (Thr), tryptophan (Trp), tyrosine (Tyr), valine (Val), were bought from Sigma Aldrich, India, and were employed without any additional purification. 4-Nitrophenol (4-NP), ferric chloride hexahydrate ($FeCl_3.6H_2O$), manganese (II) chloride tetrahydrate ($MnCl_2.3H_2O$), lead nitrate [$Pb(NO_3)_2$], potassium chloride (KCl), cobalt chloride hexahydrate ($CoCl_2.6H_2O$), nickel (II) chloride hexahydrate ($NiCl_2.6H_2O$), sodium chloride (NaCl), magnesium chloride hexahydrate ($MgCl_2.6H_2O$), barium chloride dihydrate ($BaCl_2.2H_2O$), sodium hydroxide pallets (NaOH), 3-NP, 2-NP, ferrous chloride ($FeCl_2$), hydrochloric acid (HCl), mercuric chloride ($HgCl_2$), picric acid, glutathione, quinine sulfate were purchased from Loba Chemie, India and employed without any additional purification. The pH of the buffers was adjusted with a pH meter (EUTECH pH / Ion 510) to a final value of (± 0.02) at ~24-25 ºC. All the investigation has been undertaken using double-distilled water. The 0.22 μM and 0.02 μM membrane filters were bought from Merck Millipore and Whatman (GE Healthcare Life Sciences), respectively. In order to assess the applicability of the current nanosensor, an experiment was carried out using real samples from river water. The water samples were obtained from local river in Patiala, Punjab, India. After

spiking the river water sample with different concentrations 4-NP to the S-CDs aqueous solution and fluorescence measurements were recorded at an excitation wavelength of 390 nm.

5.2.2 Synthesis of DES

DES was synthesized using choline chloride (HBA) and urea (HBD). In a 100 ml beaker, 13.9 g of choline chloride and 12.8 g of urea were combined in a molar ratio of 1:2 (Figure 5.1a). The mixture was then heated at 80 °C while being continuously stirred for 30 minutes until a transparent and homogeneous liquid was formed (Figure 5.1b). The green solvent was stored at room temperature (~24-25 ºC) until further use.

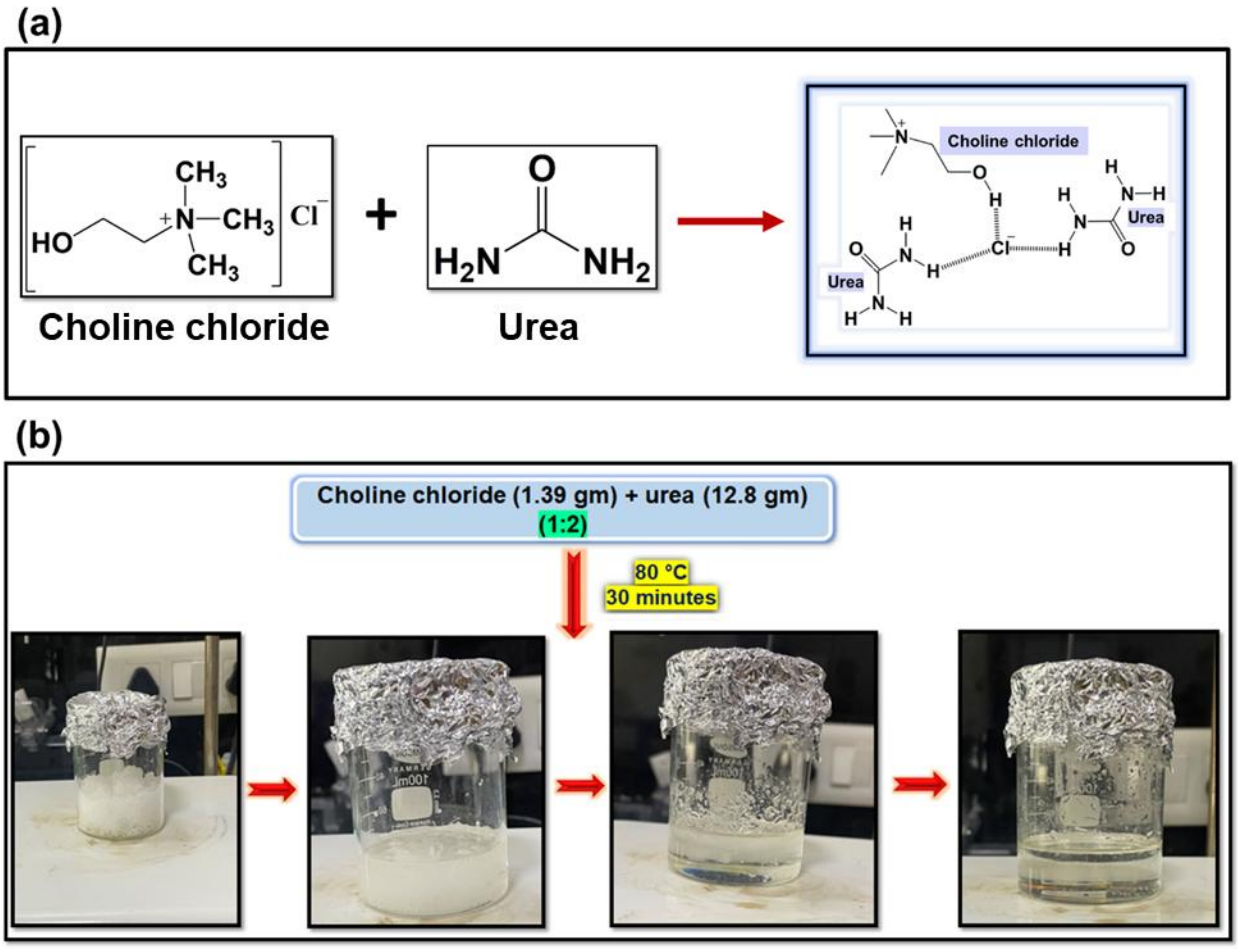

Figure 5.1. (a) Schematic representation of interactions between Choline chloride and urea to form deep eutectic solvent (DES), and (b) Schematic representation of synthetic protocol of DES from choline chloride and urea.

5.2.3 Synthesis of S-CDs

S-CDs were synthesised using a hydrothermal synthesis technique. The sucrose aqueous solution (1 gram in 10 ml double- distilled water) was transferred into an autoclave and the reaction was set up in a hydrothermal reactor at 200 °C for 2 hours. Carbonization changed the color from transparent to dark brown, suggesting the development of S-CDs. After coming to the room temperature, the solution was centrifuged at 8000 rpm for 20 minutes and decanted. In order to further remove larger particles, the decanted solution was filtered via a 0.22 µm syringe filter and a 0.02 µm membrane filter respectively. The methodology for the synthesis of S-CDs is depicted schematically below (Figure 5.2). Finally, the brown-colored S-CDs solution was collected and stored in a refrigerator at 4 °C for future experimental investigations.

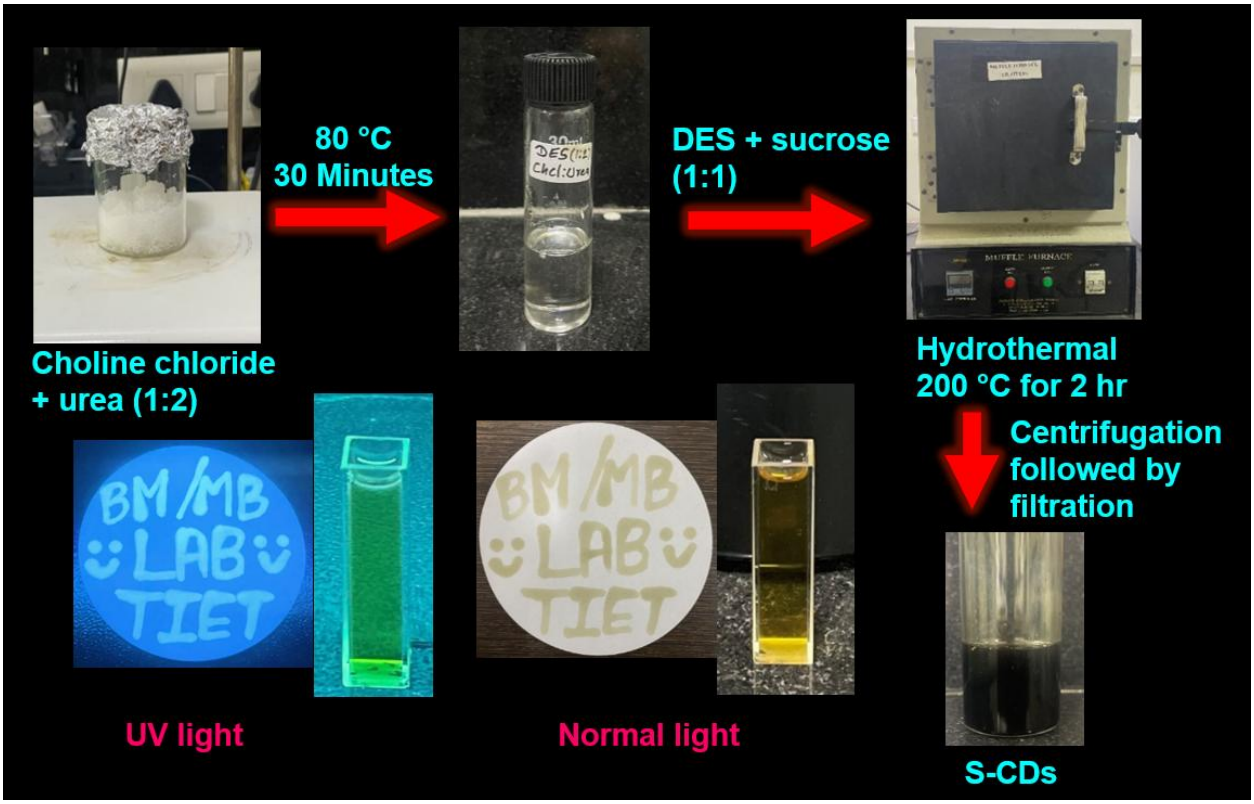

Figure 5.2. Schematic representation of synthetic protocol of S-CDs from sucrose.

5.2.4 Characterization of S-CDs

5.2.4.1 Electron microscopy

High-resolution transmission electron microscopy (HRTEM) via JEM 2100 plus (JEOL) equipped with a charge-coupled device (CCD) camera at an acceleration voltage of 80-200 kV was used to characterize the synthesised S-CDs. The samples were made by spreading a tiny droplet of diluted S-CDs solution (1:1 (v/v) of S-CDs and double distilled water over a copper grid and allowing it to dry overnight ~12-16 hours at room temperature (~24-25 ºC).

5.2.4.2 XPS and EDS analysis

The XPS survey spectra were collected using an Escalab Xi^+ X-ray photoelectron spectrometer from Thermo Fisher Scientific (USA). The spectra were first baseline corrected, and then the peaks were identified using the peak analyzer feature and deconvoluted via multiple peak-fitting employing the Gaussian function, both of which are included in the OriginPro 2021 software. The deconvoluted peaks were best fit using a correlation coefficient (R^2) of 0.99. The energy-dispersive spectroscopy (EDS) of S-CDs was measured using the Bruker QUANTAX 200 from ZEISS Sigma.

5.2.4.3 GIXRD analysis

S-CDs diffraction pattern was captured on the Rigaku SmartLab with a 2θ angular range of 10–90°. The scan pace was 3.02 degrees/minute, and the scan resolution was 0.0001 degrees.

5.2.4.4 ATR FT-IR spectroscopy

The ATR-FTIR spectra of the S-CDs were acquired using an IRTracer-100 spectrophotometer (Shimadzu) equipped with the QATRTM single-reflection integration-type ATR accessory, comprising a diamond crystal, and an air-cooled DLATGS detector. A resolution of 2 cm^{-1} was preserved while capturing all spectra in transmittance mode. The final spectrum was an average of 100 scans. Before putting a sample drop on the crystal, methanol was used to clean the surface and background scan with 100 accumulations was run prior to recording spectrum.10 µL sample drop was utilized to acquire spectra within the range 400-4000 cm^{-1}. Spectral data was replotted using OriginPro 2021.

5.2.4.5 UV-Vis spectroscopy and zeta potential measurements

The UV-Vis absorption spectra of S-CDS aqueous solutions were obtained using a quartz cuvette having a path length of 1 cm using a UV-Vis spectrophotometer (Shimadzu, RF-2600). To record the absorbance, 100 μL of the S-CDs solution was added in double-distilled water to a total volume of 3 mL. The S-CDs zeta potential was measured using a Brookhaven 90 Plus zeta potential analyzer.

5.2.4.6 Preparation of S-CDs sample for fluorescence studies

30 μL of the synthesised S-CDs was added to 2.47 mL of double-distilled water to achieve a total amount of 2.5 mL. During the fluorescence emission measurements, the volume of S-CDs was held constant while the concentration of 4-nitrophenol (4-NP) varied (0-3.8 μM) with an excitation wavelength of 390 nm**.**

5.2.4.7 Steady state fluorescence spectroscopy

The Shimadzu RF-6000 spectrofluorometer was used to acquire the fluorescence spectra of S-CDs. S-CDS fluorescence spectra was collected at λ_{ex} = 390 nm with a scan range of 392-680 nm. Emission and excitation bandwidths were set at 5 and 10 nm respectively. Further to determine the limit of detection, binding constant, and Stern-Volmer quenching constant (K_{sv}), the emission intensities were fitted using a linear equation as used in equation 1 in chapter 4. Every steady-state fluorescence experiment was repeated at least three times.

5.2.4.8 Photoluminescence quantum yield (PLQY) measurements

The photoluminescence quantum yield (PLQY) of S-CDs was determined using quinine sulphate in 0.1 M H_2SO_4 as a standard reference solution (quantum yield ~0.546).[33] The equation 2 in chapter 4 was used to determine PLQY values.[34]

5.2.4.9 Time-resolved emission spectroscopy

Time-resolved fluorescence emission decays were measured using a time correlated single photon counting (TCSPC) fluorometer equipment using the modular fluorescence lifetime system (DeltaFlex, HORIBA Scientific). The excitation source used was a 340 nm nano-LED pulse diode.

The instrument response function (IRF) was measured utilizing a LUDOX®TMA colloidal silica, 34 wt.% suspension in distilled water (Sigma-Aldrich), and the full-width at half-maximum (FWHM) was approximated to be about 200 ps. An emission monochromator was set at a fixed wavelength of 430 nm, with a bandpass of 16 nm.

For fluorescence lifetime measurements, the emission polarizer was set at the magic angle (54.7°) with respect to the excitation polarization. The time-resolved lifetime was measured over a 100-ns decay range, and the time per channel is 0.055 ns. To prevent any sample scattering, a long-pass filter was placed immediately after the sample. All decays were recorded at 25 °C and replotted with OriginPro 2021. The fluorescence emission decays were deconvoluted based on the instrument response function and then analysed and fitted using the equation 3 in chapter 4.[33]

5.3 Results and Discussion

5.3.1 Morphological characterization and compositional analyses of S-CDs

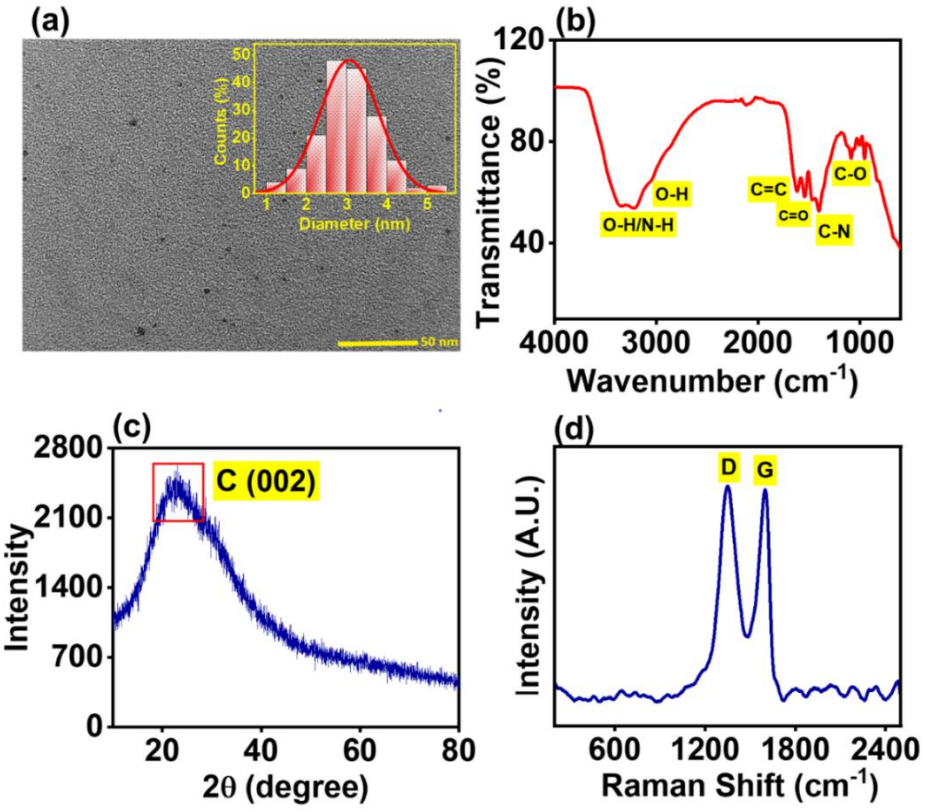

Figure 5.3. (a) HR-TEM image of S-CDs, inset shows particle size distribution histogram plot, (b) XRD spectrum, (c) FTIR spectrum and (d) Energy dispersive spectroscopy (EDS) spectrum of S-

CDs representing various elements presence on the S-CDs surface. The table (inset) displays the percentage composition of each element present in the S-CDs.

The morphological characterization and size distribution of as-prepared S-CDs was performed using high-resolution transmission electron microscopy (HR-TEM). Figure 5.3a displays homogeneous distribution of S-CDs (nearly spherical). The histogram demonstrates a narrow size distribution of S-CDs in the range of 1-5.4 nm, with an average diameter of 3.06 nm (Figure 5.3a inset) displaying a strong resemblance to the Gaussian distribution. Figure 5.3b depicts the FTIR spectra of SCDs. The peak at 3355-3222 cm^{-1} is owing to the stretching vibrations of O-H and N-H functional groups, of S-CDs wherein the broadening is attributed to hydrogen bonding.[52]The S-CDs hydrophilicity and subsequent water dispersibility may be attributed to the presence of these bonds. The bands at 3,034, is obtained because of stretching of -C-H. The absorption band at 2,112 cm^{-1}, obtained only in S-CDs, is known to occur due to the triple bond stretching in groups -C≡C, and -C≡N.[53] The peak obtained at 1624 cm^{-1} occurs due to N–H bending of the amine group coupled with the C–O. A strong feature at 1398 cm^{-1} corresponds to the symmetric stretching of carboxylate group.[54] Band at 1,080 cm^{-1} were assigned to -C-O stretching.[42] Furthermore, Energy dispersive X-Ray spectroscopy (EDS) is shown in Figure 5.4 showing the presence of various elements like carbon, nitrogen, oxygen and chlorine in the synthesized S-CDS. The X-ray diffraction pattern of synthesized S-CDs is shown in Figure 5.3c. Strong wide diffraction peak was identified around $2\theta = 23°$ was credited to the as-prepared CDs (002) graphitic carbon lattice spacing, exhibiting an amorphous carbon phase on the S-CDs surface which is in excellent line with previous literature descriptions.[35-37]

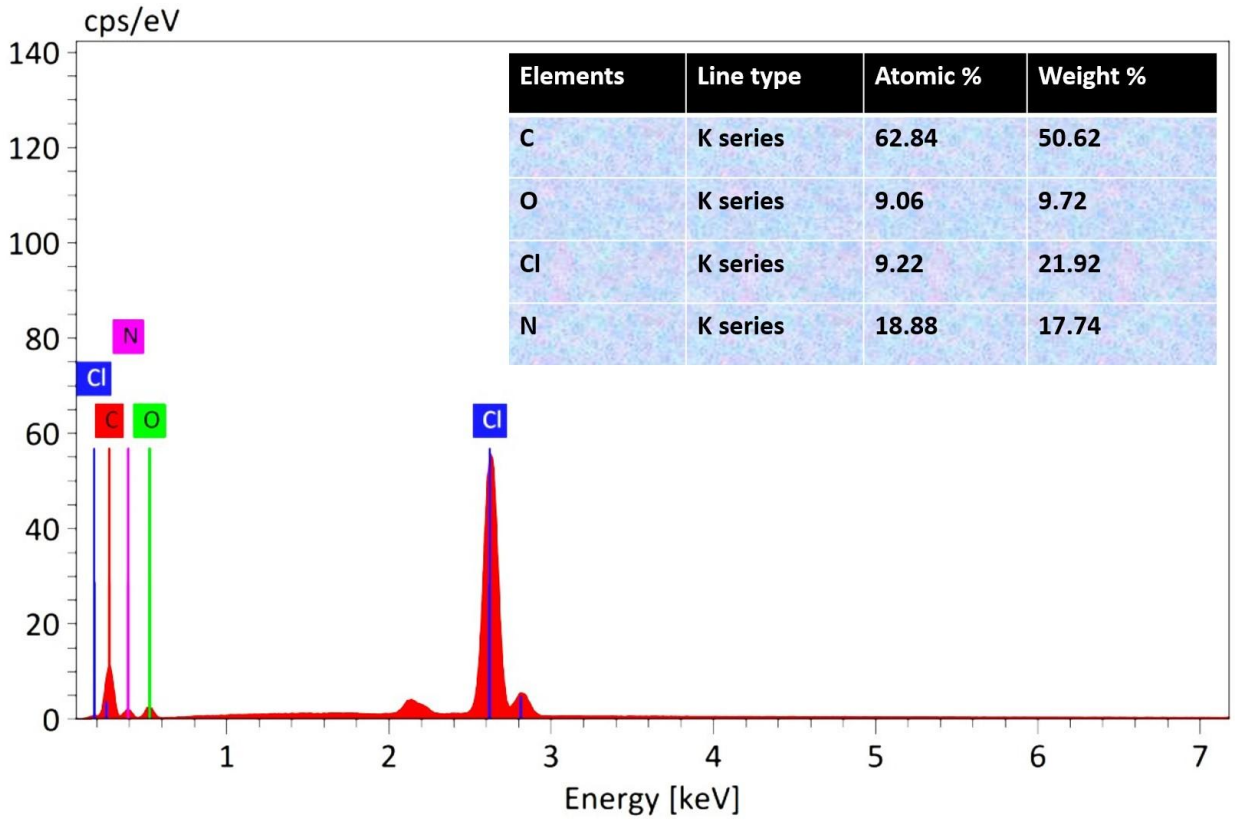

Elements	Line type	Atomic %	Weight %
C	K series	62.84	50.62
O	K series	9.06	9.72
Cl	K series	9.22	21.92
N	K series	18.88	17.74

Figure 5.4. Energy dispersive spectroscopy (EDS) spectrum of S-CDs demonstrating the presence of numerous elements on S-CDs surface. The table (inset) shows the percentage composition of every component found in the S-CDs.

The interlayer distance (d-spacing) was calculated with the help of Bragg's equation:

$$n\lambda = 2d\sin\theta \qquad (1)$$

Where 'n' is a positive integer representing "order" of reflection, 'λ' signifies the incident X-ray wavelength (λ = 1.5406 Å), and the variable 'd' that represents the spacing between the diffracting planes. The S-CDs estimated d-spacing value was 0.39, corresponding to the (002) lattice plane.[38,39] The dissimilarity in the interlayer spacing between S-CDs and bulk graphite (0.34 nm) indicates that the surface of S-CDs is highly adorned with functional groups. Interlayer distance is powerfully influenced by the existence of the attached hydroxyl, carbonyl, and carboxylic acid groups. These functional groups can enhance interlayer distance.[40,41] The Raman spectrum is displayed in Figure 5.3d. It shows two broad features, corresponding to the D (disorder) and G (graphite) bands, respectively, at 1350 cm^{-1} and 1605 cm^{-1}. In glassy carbon or disordered graphite, D band is generated by the vibrations of carbon atoms with dangling bonds in the termination plane

(A_{1g} vibrational mode), whereas the G band is associated with the graphite's E_{2g} mode and the vibration of sp^2-bonded carbon atoms in a two-dimensional hexagonal lattice. Overall, Raman findings demonstrated the presence of hybridized carbon defects in S-CDs, specifically sp^3 (D band) and sp^2 (G band).[43,44] The ratio of intensities of the D:G band (I_D/I_G) is 0.84, suggesting moderate level of graphitization in S-CDs.[45]

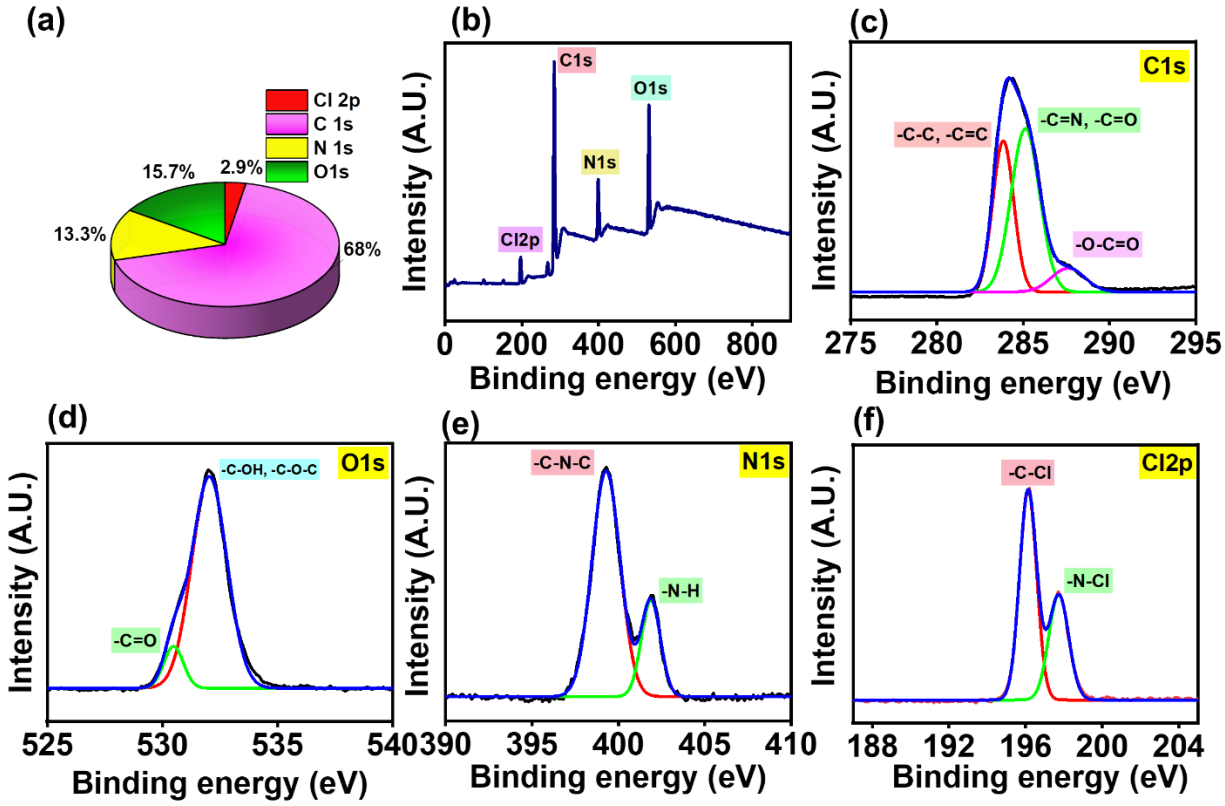

Figure 5.5. (a) Pie chart represents exact elemental composition of S-CDs from XPS analysis, (b) XPS survey spectrum of S-CDs, (c-f) S-CDs deconvoluted XPS spectra shown in an element-specific way i.e (c) C1s, (d) O1s, (e) N1s, and (f) Cl2p.

X-ray photoelectron spectroscopy (XPS) is a highly valuable method for identifying elements, determining the oxidation state of a surface, and quantifying precisely the quantity (percentage) of each element. Figure 5.5 displays the deconvoluted XPS spectra for the C1s, O1s, N1s, and Cl2p elements, together with the pie chart distribution and survey spectrum of the S-CDs. The elemental carbon (68%), oxygen (15.7%), nitrogen (13.3%) and chlorine (2.9%) peaks emerged at 283.3, 530.8, 399.5, and 196.9 eV, respectively (Figures 5.5a, b)[12,45-46]. The C1s deconvolution

spectrum displays distinct peaks at 283.8, 285.1 and 287.5 which corresponds to the transitions involving the -C=C/-C-C, -C=N/-C=O, -O-C=O, respectively (Figure 5.5c). [12] The deconvolution spectrum of O1s displayed two binding energy peaks at 530.5, and 532 eV, owing to the -C=O and -C-OH / -C-O-C groups, respectively (Figure 5.5d).[12,47] The deconvolution spectra of N1s revealed two peaks at 399.3 and 401.8 eV, attributed to the presence of -C-N-C (Pyridine N) and -N-H (Pyrrolic N) groups on the S-CDs surface, respectively (Figure 5.5e).[12]The deconvolution spectrum of Cl2p showed two binding energy peaks at 196, and 197.7 eV, corresponding to the -C-Cl and -N-Cl groups, respectively (Figure 5.5f).[12,47] The XPS results strongly correlates the conclusions drawn from the FTIR analysis. Furthermore, the existence of C, O, N, and Cl elements in the S-CDs was also verified using energy dispersive X-Ray spectroscopy (EDS), shown in Figure 5.4.

5.3.2 Optimization of S-CDs

To produce a high-performing optical nanosensor with powerful photoluminescent (PL) capabilities, it is crucial to fine-tune the response time, volume, and storage duration of the synthesized S-CDs.

5.3.2.1 Reaction time and volume optimization

It is well-established that the reaction time influences the photoluminescence properties of S-CDs. S-CDs were synthesized with reaction periods ranging from 0.5 hour to 2.5 hours to determine the best reaction conditions. Our studies revealed that employing our hydrothermal technique, that entails a reaction spanning 2 hours at 200 °C, produces the desired S-CDs with the most elevated photoluminescence intensity (Figure 5.6a).

In addition, volume adjustment is necessary for sensing efficiency as well as achieving the maximal fluorescence intensity of the produced nanoprobe. In order to optimize the volume, we observed the variations in the emission intensity of S-CDs by gradually adding different quantities of aliquots (ranging from 10 to 60 µL) from the corresponding stock solution of S-CDs into double-distilled water. The greatest photoluminescence (PL) intensity was observed when 30 µL of S-CDs were added into 2.47 mL of double-distilled water, as shown in Figure 5.6b.

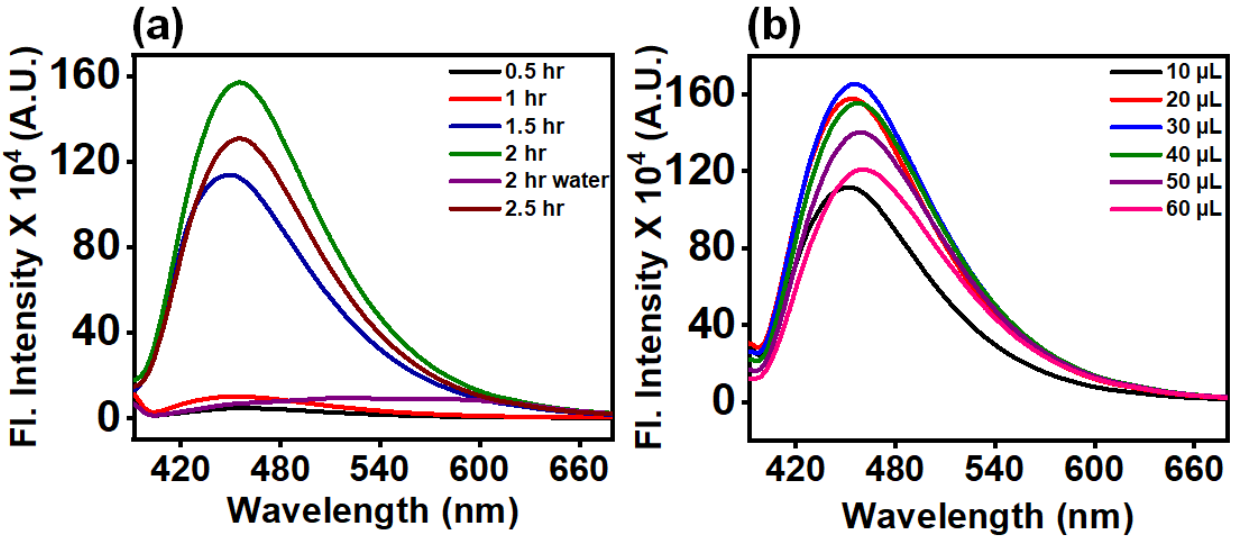

Figure 5.6. S-CDs fluorescence emission spectra (λ_{ex}: 390 nm) for optimization of the (a) reaction time, and (b) volume ratio.

5.3.3 Optical properties of S-CDs

Furthermore, the as-prepared S-CDs demonstrate two discernible absorption bands at approximately 235 nm (π to π* transition, which corresponds to the C=C group of the potentially localized sp^2 clusters in carbon quantum dot's) and 347 nm (n to π*) of the nitrogen and oxygen heteroatoms (C=N/C=O/N=O) present on S-CDs surface as illustrated in UV-visible spectrum in Figure 5.7a.[48-50] S-CDs display a light brown to the unaided eye and green fluorescence emission upon exposure to UV light at 365 nm (Figure 5.7a inset). Furthermore, Figure 5.7b displays the S-CDs excitation and emission spectra, having a λ_{em} at 341 nm and 455 nm, respectively.

S-CDs demonstrated excitation wavelength-dependent emission spectra in aqueous media, with maximum emission intensity at 455 nm following excitation at 390 nm (Figure 5.7c). The fluorescence emission of S-CDs arises from process involving photoinduced charge separation and subsequent entrapment at the surface, leading to radiative recombination between hole and electron pairs.[51] The normalized fluorescence emission of S-CDs is depicted in Figure 5.7d. The fluorescence emission of S-CDs exhibited a notable bathochromic shift of about 64 nm as excitation wavelength was adjusted from 310 to 440 nm. This excitation-dependent emission characteristic of S-CDs is due to various factors, including the quantum confinement effect, zigzag

sites, surface defects, aromatic structure formation on the surface, and non-uniform particle distribution.[52-54]

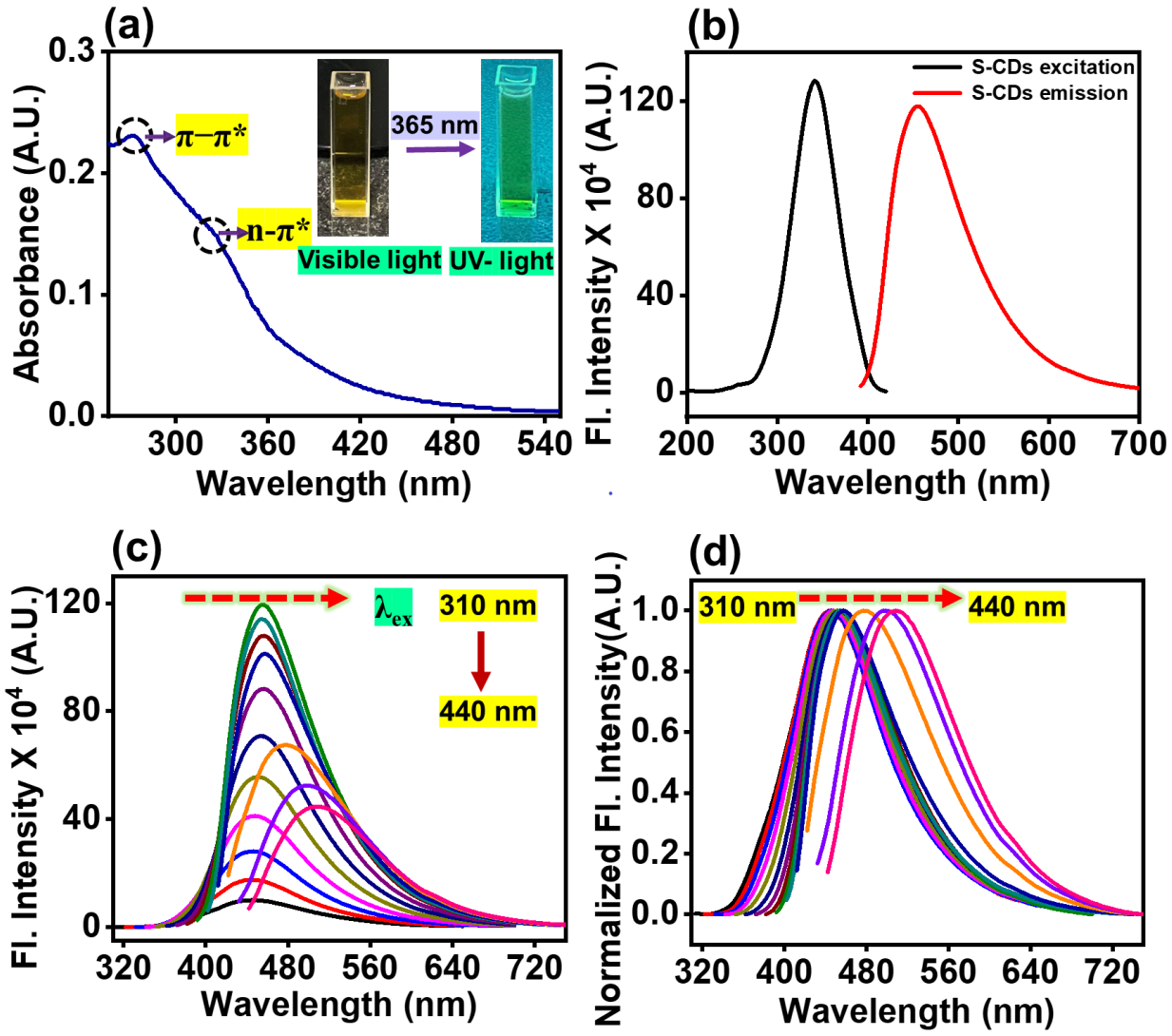

Figure 5.7. (a) S-CDs UV-visible absorption spectrum, with an inset image showing the S-CDs under visible and UV light illumination, (b) excitation and emission spectrum of S-CDs, (c) variations in fluorescence emission spectra of S-CDs and (d) peak position-normalized fluorescence emission of S-CDs plainly depicting the spectral shift, indicated by a dashed red arrow, from 443 nm to 508 nm (λ_{ex}: 310 nm to 440 nm).

5.3.4 Stability of S-CDs

Further we looked into S-CDs stability by examining the influence of photo-irradiation, ionic strengths, as well as pH given its significance in real-world applications for a good and robust nanosensor.

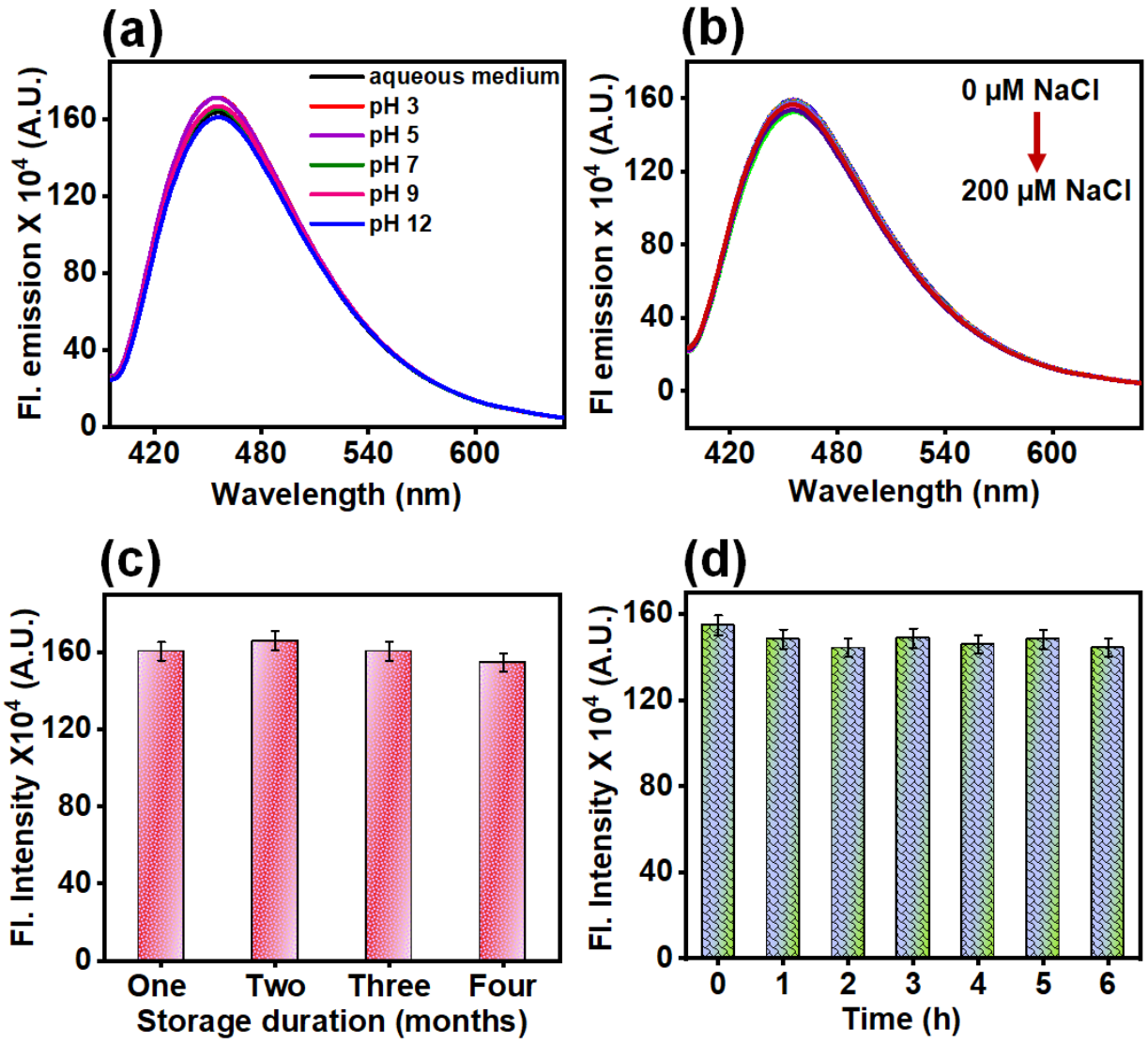

Figure 5.8. Fluorescence emission spectra of S-CDs (λ_{ex}: 390 nm) (a) in aqueous medium and at different solution pH (3, 5, 7, 9 12), (b) effect of medium's ionic strength on S-CDs in the presence of variable concentrations of NaCl (0-200 µM), (c) at differen t storage time interval, and (f) effect of photo-irradiation by a xenon arc lamp on the emission of S-CDs at as a function of time. The error bars show the standard error of measurements taken from three different experiments.

S-CDs exhibited exceptional stability within a pH range of 3 to 12, with minimal fluctuations in fluorescence emission intensity and no alteration in their emission maxima (Figure 5.8a). Therefore, the synthesized S-CDs has been effectively used as a versatile and durable pH sensor. The presence of numerous functional groups on S-CDs surface in an acidic environment result in a greater net surface charge (negative), that causes electrostatic repulsion and amplifies the slight increase in PL emission.

Additionally, S-CDs were tested with a 0-1 M NaCl solution to determine effect of ionic strength. Varying the ionic strength of medium did not significantly alter PL intensity or the emission maxima of S-CDs, indicating that nanoprobe is quite stable (Figure 5.8b). The S-CDs exhibit an intrinsic pH value of approximately 3.2, indicating their acidic character, likely attributed to the existence of carboxylates. In addition, the zeta potential of S-CDs (-9.37 mV) confirmed the presence of plenty of negatively charged components on S-CDs surface (Figure 5.9a).

The emission spectra of S-CDs were obtained at different time intervals over a period of 122 days, equivalent to 4 months. Figure 5.8c displays the emission spectra of S-CDs during different storage periods, revealing no noticeable alterations in the fluorescence intensity. Hence, the results unambiguously demonstrated that the synthesized nanoprobe exhibited exceptional stability in an aqueous solution over an extended period of time. Indeed, it might be beneficial in numerous analytical applications.

The photostability of the S-CDs was also assessed by subjecting them to a 150 W xenon-arc lamp for six hours; however, no notable change in the fluorescence intensity of S-CDs was noted confirming its photostability and resistance to photobleaching (Figure 5.9d).

The fluorescence response of the CDs was examined for the temperature in the range of 10 to 90 °C (Figure 5.9b), revealing a reduction in fluorescence with increasing temperature. The results reveal that S-CDs have outstanding reversibility and recoverability across a temperature range of 10 to 90 °C. In other words, the temperature-dependent fluorescence of S-CDs does not permanently degrade the surface fluorescent structures of the produced nanoprobe. A strong linear correlation ($R^2 = 0.99$) was obtained between the temperature and fluorescence intensity of the S-CDs (Figure 5.9c). Moreover, the peak position of S-CDS emission at 445 nm remained constant across various temperatures. This discernible fall in fluorescence emission on temperature rise,

could be due to CD aggregation or a synergistic interaction between the numerous oxygen-containing functional groups and hydrogen bonds. The phenomena can be attributed to the relaxation of photoexcited electrons, which can occur through radiative relaxation, non-radiative relaxation, and thermally activated traps on surfaces and impurity states throughout the heating process, as per earlier publications.[55-57]

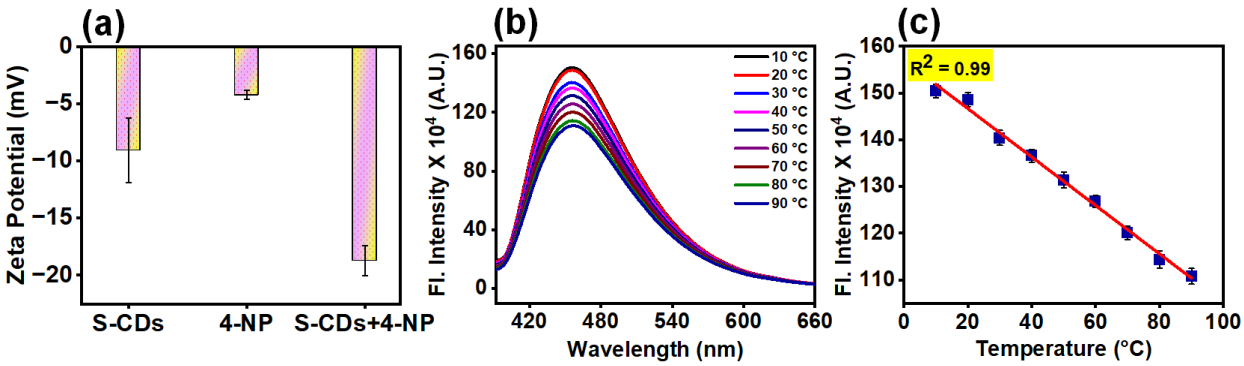

Figure 5.9. (a) Zeta potential of S-CDs, (b) impact of temperature variation on S-CDs (λ_{ex}: 390 nm) from 10-90 °C, (c) Fl. intensity plot as function of temperature (10-90 °C). The red line shows linear fit of data using OriginPro 2023 and R^2 denotes the goodness of these fits. The error bars show standard error of measurements taken from three different experiments.

5.3.5 Selectivity studies of S-CDs

The evaluation of selectivity is an essential factor for development of an innovative nanosensor. To validate the selectivity of the analytical sensing platform, we observed the variations in fluorescence intensity of S-CDs when exposed to various bioactive compounds (Figure 5.10a), metal ions and pollutants (Figure 5.10b). A specific concentration of various biomolecules stock solution (1 mM) was added to the aqueous solution of S-CDs. Bioactive molecules include arginine (Arg), asparagine (Asn), aspartic acid (Asp), cysteine (Cys), glutamic acid (Glu), glutamine (Gln), histidine (His), isoleucine (Ile), leucine (Leu), lysine (Lys), methionine (Met), threonine (Thr), tyrosine (Tyr), and valine (Val), glutathione (gsh). Furthermore, metal ions and pollutants includes 4-nitrophenol (4-NP), 3-nitrophenol (3-NP), 2-nitrophenol (2-NP), ferric chloride hexahydrate ($FeCl_3.6H_2O$), manganese (II) chloride tetrahydrate ($MnCl_2.3H_2O$), lead nitrate [$Pb(NO_3)_2$], cobalt chloride hexahydrate ($CoCl_2.6H_2O$), nickel (II) chloride hexahydrate ($NiCl_2.6H_2O$), magnesium

chloride hexahydrate ($MgCl_2.6H_2O$), barium chloride dihydrate ($BaCl_2.2H_2O$), ferrous chloride ($FeCl_2$), mercuric chloride ($HgCl_2$), picric acid (PA), ammonium chloride (NH_4Cl), copper chloride ($CuCl_2$), chromium (III) nitrate $Cr(NO_3)_3$, sodium arsenate (Na_3AsO_4) and thiourea (CH_4N_2S). Figure 5.10b shows that 4-NP had the strongest fluorescence quenching of S-CDs, although the PL intensity of these S-CDs remained practically unaltered upon addition of the remaining analytes. Therefore, it is inferred that our synthesized S-CDs demonstrated exceptional selectivity as fluorescent nanosensor for 4-NP detection.

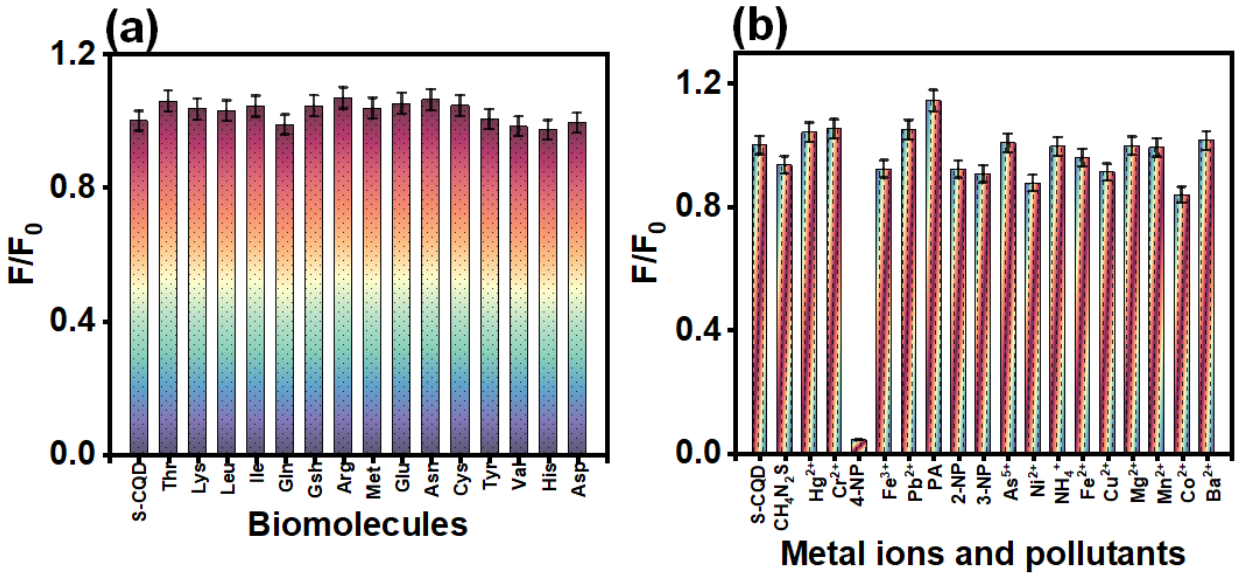

Figure 5.10. Selectivity studies of S-CDs (λ_{ex}: 390 nm) with different (a) biomolecules, and (b) metal ions and pollutants.

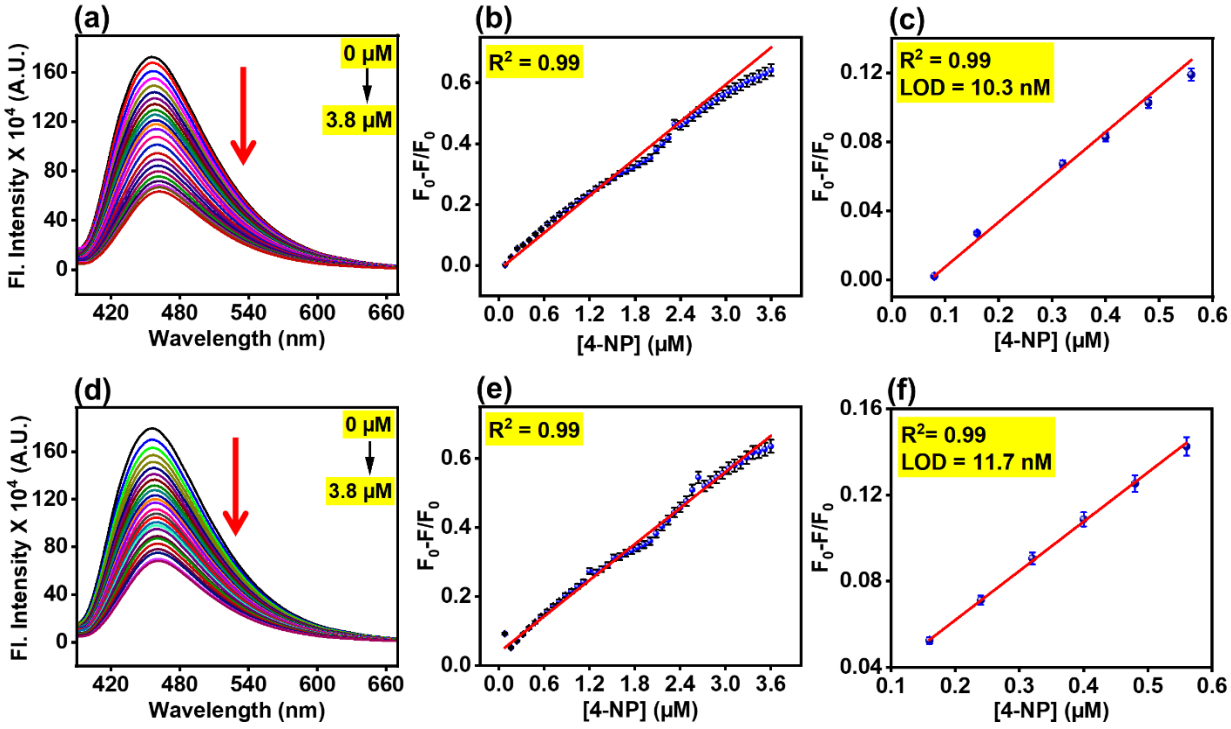

Figure 5.11. (a, d) Variation in fluorescence emission of S-CDs (λ_{ex}: 390 nm) in the presence of different concentrations of 4-NP (0-3.8 µM) in standard and real samples respectively. Red arrow depicts the progressive decrease of fl. intensity of S-CDs, (b, e) The spectra depict linear correlation between F_0- F/F_0 and different concentrations of 4-NP (0 to 3.8µM), (c, f) Linear correlation between F_0- F/F_0 and some specific concentrations of 4-NP (0 to 0.56 µM). Error bars represent standard error of measurements obtained from three independent experiments.

5.3.6 Plausible sensing mechanism for 4-NP detection

The subsequent titrations of S-CDs were carried out by adding variable concentrations of 4-NP (0-3.8 µM) in aqueous solution (Figure 5.11a), and real samples of 4-NP (Figure 5.11d). The PL intensity of S-CDs dropped progressively on gradual addition of 4-NP. Subsequently, a calibration curve was constructed by the plotting of fluorescence quenching efficiency (F_0-F/F_0) against 4-NP concentration and a good linear fit was achieved with the good fit of adjusted R^2 value of 0.99 as shown in figures 5.11b, e. Limit of detection was estimated to be 10.3 nM in aqueous solution (Figure 5.11c), and 11.7 nM in real samples of 4-NP (Figure 5.11f), respectively. It is to be highlighted that previously described fluorescent probes for 4-NP were produced using complicated, time-consuming, and energy-intensive methodologies. Moreover, S-CDs exceptional

fluorescence stability improves the analysis method's reliability and reproducibility. As a result, this work presents an easy, quick, sensitive, and a cheaper technique for 4-NP sensing. There is multiple PL quenching mechanism which include Forster resonant energy transfer (FRET), inner filter effect (IFE), and static or dynamic quenching.[33] The precise PL quenching process used by the as-prepared S-CDs sensing system was thoroughly investigated. In order to investigate the potential fluorescence quenching mechanism of S-CDs by 4-NP, the spectral overlap between the absorption spectrum of 4-NP and the fluorescence emission spectrum of S-CDs was first considered. The absorption spectrum of 4-NP and fluorescence emission spectrum of S-CDs clearly overlapped indicating that Inner filter effect (IFE) or Fluorescence resonance energy transfer (FRET) might have led to the fluorescence quenching (Figure 5.12a).[59] In case of FRET, the probes' excited state energy transfer was responsible for the drop in fluorescence lifetime.[60] Fluorescence quenching may occur with IFE, however the lifetime remains essentially unaltered.[59-62] To further confirm the quenching mechanism, the fluorescence lifetime of S-CDs in the presence and absence of 4-NP was measured. As illustrated in figure 5.12b, the fluorescence lifetime of S-CDs (τ= 2.24 ns) is nearly identical to that of the S-CDs-4-NP (τ= 2.07 ns) sensing system illustrating absence of FRET, similar trend in lifetime values was observed in case of real sample of 4-NP (Figure 5.12c) confirming that the interaction happens solely via the IFE (Table 1). These findings are consistent with previously published results based on IFE theory.[60]

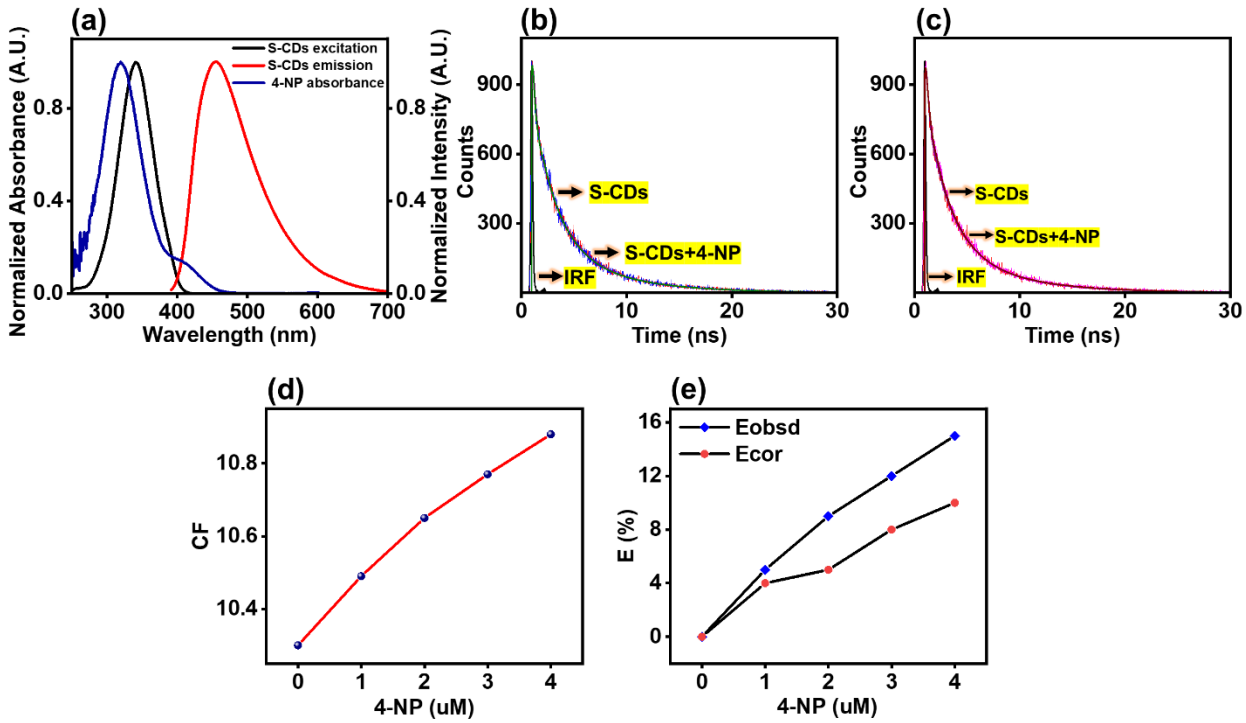

Figure 5.12. (a) Absorption spectrum of 4-NP with S-CDs excitation and emission spectrum, (b) Fluorescence lifetime decays of S-CDs, where the sharp, thin black line represents the instrument response function, the red and magenta lines represent the actual intensity decays in the absence and presence of RF respectively. The wine and purple lines correspond to fits obtained in the absence and presence of RF, respectively using tri-exponential function, (c) Fluorescence lifetime decays of S-CDs, where the sharp, thin black line represents the instrument response function, the red and magenta lines represent the actual intensity decays in the absence and presence of RF respectively. The wine and purple lines correspond to fits obtained in the absence and presence of RF, respectively using tri-exponential function, (d) Plot demonstrates the correction factor (CF) with various concentrations of 4-NP, (e) Suppressed efficiency (E%) of the corrected (redline, E_{cor}) and observed (blackline, E_{obsd}) fluorescence intensities.

System	τ_1 (ns) (α_1)	τ_2 (ns) (α_2)	τ_3 (ns) (α_3)	τ_m[#](ns)	χ^2
S-CDs	2.34 (0.44)	0.32 (0.39)	6.48 (0.17)	2.24	1.17
S-CDs + 3.8 μM 4-NP	2.16 (0.44)	0.22 (0.4)	6.42 (0.16)	2.07	1.17
S-CDs + 3.8 μM 4-NP (real sample)	2.26 (0.5)	0.36 (0.32)	6.71 (0.17)	2.42	1.01

[#] $\tau_m = \alpha_1\tau_1+\alpha_2\tau_2+\alpha_3\tau_3$

Table 1: Fluorescence lifetime components of S-CDs and their respective coefficients along with the mean fluorescence lifetimes. The lifetimes were extracted by fitting the time-resolved emission decays using a tri-exponential function. χ^2 represents the goodness of the fits.

To establish the appropriate mechanism between the IFE and FRET, we tracked the zeta potential values, which are −9.06 mV and −4.21 mV for S-CDs and 4-NP, respectively (Figure 5.9a). Given the fact that they are both negatively charged, it is unlikely that 4-NP will adsorb on S-CDs surface via electrostatic interactions which clearly rules out the existence of FRET quenching mechanism.[63] Furthermore, the energy transfer created by the charge localization might lead to substantial fluorescence quenching of CDs upon addition of 4- NP (contact quenching). As here, the nitro group and the cyclohexadiene ring contain the negative charge, and the iminium group comprises the positive charge. the negative charge might delocalize across the nitro group and the cyclohexadiene ring while the positive charge spreads over the iminium group leading to the formation of zwitterionic spirocyclic Meisenheimer complex (Scheme 3).[61]

To further verify the hypothesis (IFE), corrections were made by taking into consideration the cell geometry and absorption properties of the 4-NP and S-CDs aqueous solution with equation 1 in chapter 1 i.e. Parker equation.[64] Removing IFE from F_{obsd} via equation 1 yields the corrected fluorescence, or F_{cor}. The correction factor (CF) is represented as the ratio of Fcor/Fobsd. $E_{cor} = 1 - F_{cor}/F_{cor,0}$ where $F_{cor,0}$ and F_{cor} represents the corrected fluorescence intensities of S-CDs in the absence and in the presence of 4-NP, respectively (Table 2). The study of various parameters by using Parker equation for the validation of the IFE was examined and is tabulated in Table 2.

4-NP (μM)	**A_{ex}**	**A_{em}**	**CF**	**F_{obsd}**	**F_{cor}**	**E_{obsd}**	**E_{cor}**	**$F_{cor}/F_{cor,0}$**
0	0.034	0.009	10.30	454260.8	4678241.3	0.00	0.00	1.00
1	0.051	0.01	10.40	430039.3	4511106.4	0.05	0.04	0.96
2	0.065	0.011	10.65	415299.7	4421695.1	0.09	0.05	0.95
3	0.077	0.013	10.77	400323.1	733677.2	0.12	0.08	0.92
4	0.086	0.014	10.88	388196	4221768.9	0.15	0.10	0.90

Table 2: The different parameters employed to estimate IFE on the fluorescence quenching of S-CDs by 4-NP.

The CF values were assessed at different 4-NP concentrations. The CF value was found to increase with an increase in the concentration of 4-NP (Figure 5.12d), which agrees to the Parker equation (equation 1 in chapter 1). The drop in photoluminescence (PL) emission of S-CDs due to the addition of 4-NP was measured using a PL spectrophotometer. The corresponding corrected values were investigated as well (Figure 5.12e). The value of E was determined using the equation $E = 1 - F/F_0$, where F_0 and F represents the PL intensity of S-CDs without and with addition of 4-NP, respectively. Hence, suppression of the PL intensity of S-CDs is significantly influenced by the IFE.[63-65]

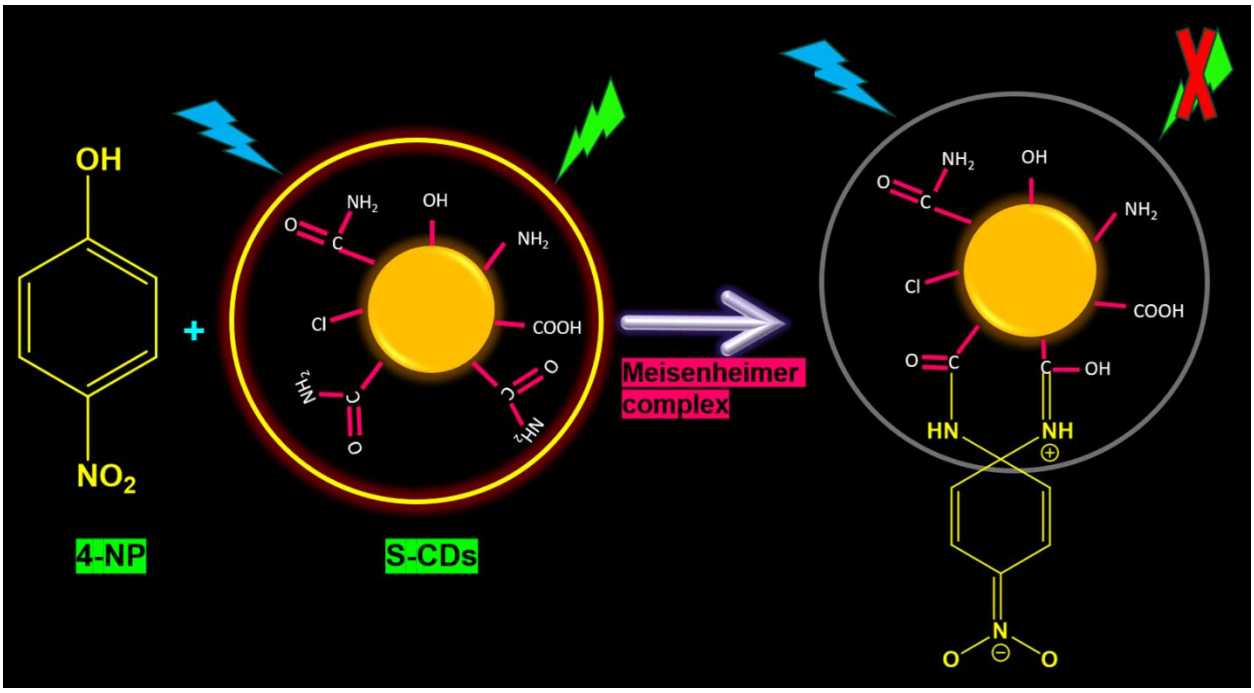

Figure 5.13. Potential quenching mechanism of S-CDs in the presence of 4-NP through formation of the zwitterionic spirocyclic Meisenheimer complex.

5.3.7 Determination of limit of detection

The characteristics for the ideal nanosensor' s sensitivity are included in the limit of detection (LOD) and limit of quantification (LOQ). A linear plot between PL responses (F_0-F/F) and various concentrations of 4-NP was used to compute the LOD and LOQ values of the S-CDs@4-NP nanosensor in aqueous medium and real sample of 4-NP (Table 3) using the values of ($3\sigma/K$) and ($10\sigma/K$), respectively.[60] The variable 'σ' represents the standard deviation of the intercept and 'K' is the slope of the respective graphs. The LOD values of 4-NP in presence of aqueous and real samples was found to be ~10.3 nM (Figure 5.11c) and ~11.7 nM (Figure 5.11f), respectively with a linear concentration range of 0-3.8 µM along with excellent regression coefficient value of R^2 = 0.99. Table 4 shows that the developed nanosensor has a relatively lower detection limit and a high sensitivity when compared to other nanosensors described in the literature.

Parameters	**S-CDs+4-NP in aqueous medium**	**S-CDs+4-NP real sample**
Linearity range (μM)	0-3.8	0-3.8
Limit of Detection (LOD) (nM)	10.3	11.7
Limit of Quantification (LOQ) (nM)	19.6	178.7
Binding constant (K_1) (μM^{-1})	4.93 X 10^5	3.33 X 10^5
Quenching constant (K_{sv}) (μM^{-1})	0.26	0.26
Regression coefficient (R^2)	0.99	0.99

Error limit = ± 5%

Table 3: Analytical performance statistics for S-CDS-based 4-NP sensing.

5.3.8 Determination of photophysical characteristics

As already shown, S-CDs have outstanding fluorescence. Equation 2 was used to estimate the PLQY of NS-CDS, and the result was ~56%, confirming that the nanoprobe in its prepared state is a bright fluorophore. The Stern-Volmer quenching constants were calculated (Table 3) using the equation 7 (chapter 4) in order to understand the degree of quenching efficiency of S-CDs.[33] Figures 5.14a, b illustrates a graph between F_0/F and Q. The variables 'F_0' and 'F' represents the fluorescence intensity in the absence and presence of 4-NP, respectively and [Q] is concentration of the quencher i.e. 4-NP. 'K_{sv}' indicates Stern-Volmer quenching constant, which was computed from the slope of the plots in aqueous (Figure 5.14a) as well as in real sample (Figure 5.14b). K_{sv} values reveals that the degree of S-CDS quenching is consistent regardless of 4-NP source.

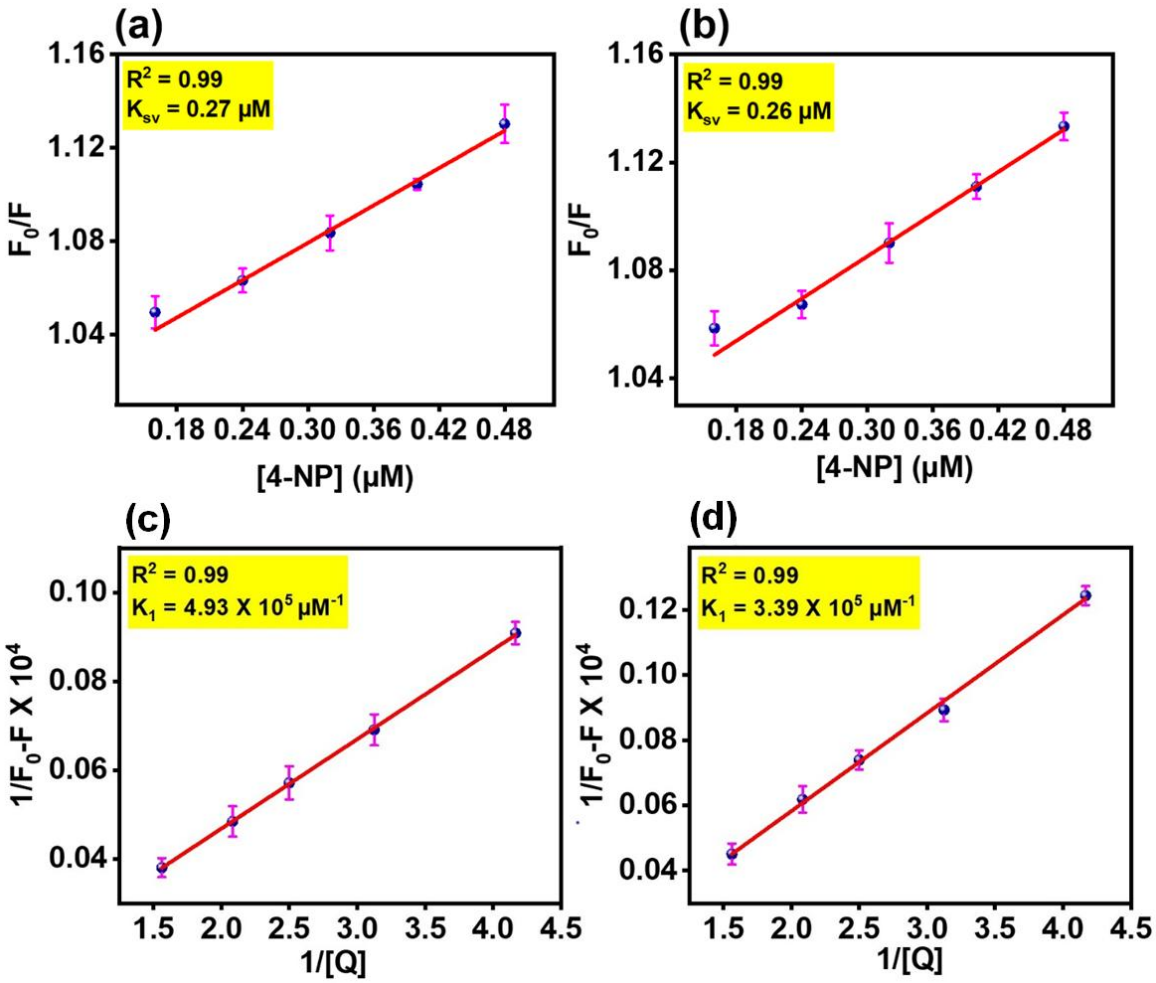

Figure 5.14. Stern-Volmer plot of S-CDs (λ_{ex}: 390 nm) in (a) aqueous medium, and (b) real sample of 4-NP. The variables 'F_0' and 'F' indicate the fluorescence intensity in the absence and presence of 4-NP, respectively. 'K_{sv}' signifies Stern-Volmer quenching constant, calculated from the slope of the plots. Benesi-Hildebrand plot of S-CDs in (c) aqueous medium, and (d) real sample of 4-NP. The variables 'F_0' and 'F' indicate the fluorescence intensity in the absence and presence of 4-NP, respectively. Q indicates the concentration of the quencher (i.e.4-NP) and K_1 depicts the binding constant, calculated using reciprocal of the slope of the plots. The red line represents the linear fit of the data using OriginPro 2023 and R^2 denotes the goodness of the fits. The error bars show the standard error of measurements taken from three different experiments.

Furthermore, by applying the 1:1 linear Benesi-Hildebrand equation (equation 8, chapter 4), the excited-state binding constant was determined (Table 3) to estimate the S-CDS-4-NP stoichiometry and comprehend the extent of interaction and binding in S-CDs and 4-NP.[63] The plot

of ($1/F_0$-F) against 1/[4-NP] gives a straight line. The binding constants (K_1) of the S-CDs-4-NP complex were assessed in aqueous (Figure 5.14c) and real samples of 4-NP (Figure 5.14d) from the reciprocal of the corresponding slope values, as shown in Table 3. Overall, the binding constant (K_1) as well as LOD of S-CDs and 4-NP appears to be similar irrespective of the source of 4-NP (Table 3) confirming our nanoprobe suitability and efficacy for 4-NP detection in real samples.

Fluorescent Probe	**Linear range**	**Detection limit**	**References**
DTD/Ag NP based carbon paste electrode	1.0-100 µM	0.6 µM	66
Nitrogen-doped oxidized carbon dots (NOCDs)	2-100 µM	2 µM	67
Boron and nitrogen co-doped carbon dots (B, N-CDs)	0.5 - 60 µM	0.2 µM	68
Sulphur quantum dots	0.2–30 µM 30–90 µM	70 nM	25
Nitrogen and phosphorus-doped carbon dots (Aa N, P-CDs)	0-37.5 µM	198 nM	26
Cu-doped carbon dots (Cu-CDs)	0.5–50 µM	80 nM	27
Nitrogen-doped carbon dots (NCDs)	1-250 µM	0.4 µM	69
Nitrogen-doped carbon dots (N-CDs)	0.1–39 µM	50 nM	30
Nitrogen and Sulphur co-doped CDs	0.2-0.40 µM	79 nM	31
This work	0-0.56 µM	10.3 nM	-

Table 4: Comparative evaluation of LOD for 4-NP detection using different nanosensors

5.3.9 Method reliability with real sample of 4-NP

It remains a challenging task to analyze the real samples for a presented fluorescent sensor, owing to the presence of potentially unknown interferents in real samples. The proposed nanosensor model was validated in accordance with ICHQ2(R1) recommendations.[70] We used the synthesized S-CDs to identify 4 -NP in the river water samples in order to monitor the sensor's viability. The samples were spiked with varying doses of 4-NP. In the real sample, the LOD value was found to be ~11.7 nM (Figure 5.11f) with good recovery percentages and a relative standard deviation (RSD) as shown in table 5. Findings clearly suggest that our method is accurate, repeatable, and has good recovery rates. According to the aforementioned findings, the sensor offers a great potential for 4-NP detection in real world samples.

Conc. added (µM)	**Conc. detected (µM)**	**Recovery error**	**Recovery rate**	**RSD**
0.56	0.56	0.6 %	100.3 %	0.58
1.04	1.06	1.6 %	101.6 %	0.54
1.52	1.58	3.7 %	103.7 %	1.90
1.84	1.97	6.9 %	106.8 %	1.51
2	2.09	4.7 %	104.7%	0.58

Table 5: Implementation of the synthesized nanosensor for detection of real sample of 4-NP in river water

5.4 Conclusions

To summarise, A rapid, economical, and sustainable strategy was employed to synthesis S-CDs from sucrose (table sugar) adopting a single-step hydrothermal method. DES facilitates the synthesis of S-CDs, leading to the development of intrinsic functionalized S-CDs with a strong fluorescence property (PLQY 56 %). The synthetic procedure was carried out in an environmentally friendly manner, without making use of any abrasive chemicals. The nitrogen and chlorine functionalization on S-CDs was verified by EDS, XPS, and FTIR spectroscopy. HRTEM

imaging indicated that the as-prepared nanoprobe was spherical in a relatively limited range, having a mean diameter of 3.06 nm. S-CDs optical characteristics were described using UV-Visible, steady state fluorescence, and time-resolved emission spectroscopy investigation. S-CDs displayed green emission under UV-illumination as well as possess excitation dependent emission properties. Additionally, S-CDs demonstrated exceptional photostability and environmental stability (pH, ionic strength, temperature), as well as aqueous solubility fulfilling all the criteria for an ideal nanosensor that can be used in various fields. The nanosensor developed showed sensitivity and selectivity for 4-NP detection in the nanomolar range via an inner filter effect mechanism. In addition, the proposed nanosensor model was validated on real sample of 4-NP at a nanomolar level with excellent accuracy and precision. In summary, this study creates a new avenue for the advancement of a selective, sensitive and green fluorescent nanosensor for quick and on the spot screening for 4-NP, which could potentially have an impact on environmental preservation.

References

1) Wang, K.; Tan, L.; Zhang, Y.; Zhang, D.; Wang, N.; Wang, J. A molecular imprinted fluorescence sensor based on carbon quantum dots for selective detection of 4-nitrophenol in aqueous environments. *Mar. Pollut. Bull.* **2023**, *187*, 114587-114595. https://doi.org/10.1016/j.marpolbul.2023.114587

2) Tang, Y.; Huang, R.; Liu, C.; Yang, S.; Lu, Z.; Luo, S. Electrochemical detection of 4-nitrophenol based on a glassy carbon electrode modified with a reduced graphene oxide/Au nanoparticle composite. *Anal. Methods* **2013**, *5*, 5508-5514. https://doi.org/10.1039/C3AY40742J

3) Huang, S.W.; Lin, Y. F.; Li, Y. X.; Hu, C. C.; Chiu, T. C. Synthesis of Fluorescent Carbon Dots as Selective and Sensitive Probes for Cupric Ions and Cell Imaging. *Molecules* **2019**, *24*, 1785- 1796. https://doi.org/10.3390/molecules24091785

4) Narayanan, K. B.; Sakthivel, N. Synthesis and characterization of nano-gold composite using Cylindrocladium floridanum and its heterogeneous catalysis in the degradation of 4-

nitrophenol. *J. Hazard. Mater.* **2011**, *189*, 519-525. https://doi.org/10.1016/j.jhazmat.2011.02.069

5) Ansi, V. A.; Renuka, N. K. Sucrose Derived Luminescent Carbon Dots as a Promising Bio-Medical Agent. *Mater. Today: Proc.* **2019**, *18*, 1724-1728. https://doi.org/10.1016/j.matpr.2019.05.269
6) Ansi, V. A.; Sreelakshmi, P.; Raveendran, P.; Renuka, N. K. Table sugar derived carbon dot-A promising green reducing agent. *Mater. Res. Bull.* **2021**, *129*, 111284-111288. https://doi.org/10.1016/j.materresbull.2021.111284
7) Tang, J.; Zhang, J.; Zhang, Y.; Xiao, Y.; Shi, Y.; Chen, Y.; Ding, L.; Xu, W. Influence of Group Modification at the Edges of Carbon Quantum Dots on Fluorescent Emission *Nanoscale Res. Lett.* **2019**, *14*, 241-250. https://doi.org/10.1186/s11671-019-3079-7
8) Wang, F.; Kreiter, M.; He, B.; Pang, S.; Liu, C. Y. Synthesis of direct white-light emitting carbogenic quantum dots. *Chem. Commun.* **2010**, *46*, 3309-3311. https://doi.org/10.1039/C002206C
9) Liu, S.; Quan, T.; Yang, L.; Deng, L.; Kang, X.; Gao, M.; Xia, Z.; Li, X.; Gao, D. N,Cl-Codoped Carbon Dots from Impatiens balsamina L. Stems and a Deep Eutectic Solvent and Their Applications for Gram-Positive Bacteria Identification, Antibacterial Activity, Cell Imaging, and ClO^- Sensing. *ACS Omega* **2021**, *6*, 29022-29036. https://doi.org/10.1021/acsomega.1c04078
10) Zhang, Q.; Vigier, K. D. O.; Royer, S.; Jérôme, F. Deep eutectic solvents: syntheses, properties and applications. *Chem. Soc. Rev.* **2012**, *41*, 7108−7146. https://doi.org/10.1039/C2CS35178A
11) Wang, X.; Cheng, Z.; Zhou, Y.; Tammina, S. K.; Yang, Y. A double carbon dot system composed of N, Cl-doped carbon dots and N, Cu-doped carbon dots as peroxidase mimics and as fluorescent probes for the determination of hydroquinone by fluorescence *Microchim. Acta* **2020**, *187*, 350-357. https://doi.org/10.1007/s00604-020-04322-7
12) Wang, N.; Zheng, A. Q.; Liu, X.; Chen, J. J.; Yang, T.; Chen, M.; Wang, J. H. Deep Eutectic Solvent-Assisted Preparation of Nitrogen/Chloride-Doped Carbon Dots for Intracellular Biological Sensing and Live Cell Imaging. *ACS Appl. Mater. Interfaces* **2018**, *10*, 7901−7909. https://doi.org/10.1021/acsami.8b00947

13) Jiang, X.; Shi, Y.; Liu, X.; Wang, M.; Song, P.; Xu, F.; Zhang, X. Synthesis of Nitrogen-Doped Lignin/DES Carbon Quantum Dots as a Fluorescent Probe for the Detection of Fe^{3+} Ions. *Polymers* **2018**, *10*, 1282. https://doi.org/10.3390/polym10111282

14) Song, J.; Zhao, N.; Qu, Y.; Zhao, L. Natural deep eutectic solvent-assisted preparation of nitrogen-doped carbon dots for ratiometric determination of pirimicarb and pH. *Dyes Pigm.* **2021**, *193*, 109564. https://doi.org/10.1016/j.dyepig.2021.109564

15) Cailotto, S.; Amadio, E.; Facchin, M.; Selve, M.; Pontoglio, E.; Rizzolio, F.; Riello, P.; Toffoli, G.; Benedetti, A.; Perosa, A. *ACS Med. Chem. Lett.* **2018**, *9*, 832–837. https://doi.org/10.1021/acsmedchemlett.8b00240

16) Nammahachak, N.; Aup-Ngoen, K. K.; Asanithi, P.; Horpratum, M.; Chuangchote, S.; Ratanaphan, S.; Surareungchai, W. Hydrothermal synthesis of carbon quantum dots with size tunability via heterogeneous nucleation. *RSC Adv.* **2022**, *12*, 31729-31733. https://doi.org/10.1039/D2RA05989D

17) Tang, L.; Ji, R.; Li, X.; Teng, K. S.; Lau, S. P. Size-Dependent Structural and Optical Characteristics of Glucose-Derived Graphene Quantum Dots. *Part. Syst. Charact.* **2013**, *30*, 523–531. https://doi.org/10.1002/ppsc.201200131

18) Sadhanala, H. K.; Khatei, J.; Nanda, K. K. Facile hydrothermal synthesis of carbon nanoparticles and possible application as white light phosphors and catalysts for the reduction of nitrophenol. *RSC Adv.* **2014**, *4*, 11481–11485. https://doi.org/10.1039/C3RA47527A

19) Wang, S.; Peng, X.; Zhong, L.; Jing, S.; Cao, X. F.; Lu, F.; Sun, R. Choline chloride/urea as an effective plasticizer for production of cellulose films. *Carbohydr. Polym.* **2015**, *117*, 133-139. https://doi.org/10.1016/j.carbpol.2014.08.113

20) Jablonsky, M.; Sima, J. Is it correct to name DES deep eutectic solvents? *Bio Resources*. **2022**, *17*, 3880-3882. https://doi.org/10.15376/biores.17.3.3880-3882

21) Pinghua, C.; Yangming, S.; Pingping, N.; Tao, W.; Xueqin, L.; Hualin, J.; Weiqiang, Z.; Hongying, S.; Jiezeng, C.; Enzhu, T. Highly sensitive detection of 4-NP in real water with long stability and high anti-inteference ability based on GO–Ag_2CrO_4/GCE *J. Taiwan Inst. Chem. Eng.* **2019**, *97*, 128-136. https://doi.org/10.1016/j.jtice.2018.12.023

22) Wang, Y.; Wu, R.; Zhang, Y.; Cheng, S.; Wang, B.; Zhang, Y.; Zhang, Y. One-step synthesis of N, S-doped carbon dots with green emission and their application in 4-NP detection, pH sensing, and cell imaging. *Spectrochim. Acta A: Mol. Biomol. Spectrosc.* **2024**, *308*, 123709-123719. https://doi.org/10.1016/j.saa.2023.123709

23) Guo, G.; Li, T.; Liu, Z.; Luo, X.; Zhang, T.; Tang, S.; Wang, X.; Chen, D. Bell pepper derived nitrogen-doped carbon dots as a pH-modulated fluorescence switching sensor with high sensitivity for visual sensing of 4-nitrophenol. *Food Chem.* **2024**, *432*, 137232-137241. https://doi.org/10.1016/j.foodchem.2023.137232

24) Yang, L.; Cui, Y.; Hu, B.; Xu, X. Highly Luminescent and Water-Stable $CsPbCl_3/Mn^{2+}$/PEG Nanocrystals for Ultrasensitive Detection of 4-Nitrophenol. *ACS Appl. Nano Mater.* **2024**, *7*, 5146–5155. https://doi.org/10.1021/acsanm.3c05916

25) Peng, X.; Wang, Y.; Luo, Z.; Zhang, B.; Mei, X.; Yang, X. Facile synthesis of fluorescent sulfur quantum dots for selective detection of p-nitrophenol in water samples. *Microchem. J.* **2021**, *170*, 06735-106742. https://doi.org/10.1016/j.microc.2021.106735

26) Tu, Y.; Wang, S.; Yuan, X.; Song, P.; Wei, Y.; Qin, K.; Zhang, Q.; Ji, X. Hydrothermal synthesis of Auricularia auricula derived nitrogen, phosphorus-doped carbon dots and application in Ag(I) and 4-nitrophenol detection and bioimaging. *Anal. Methods* **2020**, *12*, 2237-2243. https://doi.org/10.1039/D0AY00316F

27) Fang, J.; Zhuo, S.; Zhu, C. Fluorescent sensing platform for the detection of p-nitrophenol based on Cu-doped carbon dots. *Opt. Mater.* **2019**, *97*, 109396-109402. https://doi.org/10.1016/j.optmat.2019.109396

28) Huang, X.; Yang, C.; Chen, Y.; Zhu, Z.; Zhou, L. Cuttlefish ink-based N and S co-doped carbon quantum dots as a fluorescent sensor for highly sensitive and selective para-nitrophenol detection. *Anal. Methods* **2021**, *13*, 5351−5359. https://doi.org/ 10.1039/D1AY01496J

29) Amjadi, M.; Hallaj, T. Dramatic enhancement effect of carbon quantum dots on the chemiluminescence of $Ru(bpy)_3^{2+}$-Ce(IV) reaction and application to the determination of 4-nitrophenol. *J. Lumin.* **2016**, *171*, 202−207. http://dx.doi.org/10.1016/j.jlumin.2015.11.019

30) Tian, M.; Liu, Y.; Wang, Y.; Zhang, Y. Yellow-emitting carbon dots for selective detecting 4-NP in aqueous media and living biological imaging. *Spectrochim. Acta A Mol. Biomol. Spectrosc.* **2019**, *220*, 117117-117124. https://doi.org/10.1016/j.saa.2019.05.022

31) Soni, H.; Pamidimukkala, P. S. Green synthesis of N, S co-doped carbon quantum dots from triflic acid treated palm shell waste and their application in nitrophenol sensing. *Mater. Res. Bull.* **2018**, *108*, 250-254. https://doi.org/10.1016/j.materresbull.2018.08.033

32) Roopan, S. M.; Prakash, S. H.; Manjupriya, R.; Hasan, M. S.; Afridha, F.; Rajesh, A.; Sneha, R.; Kumar, P. V.; Shobika, M. Biomass-derived carbon quantum dots-supported metal oxide composite for the photocatalytic degradation of toxic pollutants. *Biomass Convers. Biorefin.* **2024**. https://doi.org/10.1007/s13399-024-05422-7

33) Lakowicz, J. R. Principles of Fluorescence Spectroscopy, 3rd edition; Springer: New York, 2006, 1-95 and 529-575.

34) Williams, A. T. R.; Winfield, S. A.; Miller, J. N. Relative fluorescence quantum yields using a computer-controlled luminescence spectrometer. *Analyst.* **1983**, *108*, 1067– 1071. https://doi.org/10.1039/an9830801067

35) TaDESe, A.; RamaDevi, D.; Hagos, M.; Battu, G.; Basavaiah, K. Synthesis of nitrogen doped carbon quantum dots/magnetite nanocomposites for efficient removal of methyl blue dye pollutant from contaminated water. *RSC Adv.* **2018**, *8*, 8528-8536. https://doi.org/10.1039/C8RA00158H

36) Rooj, B.; Mandal, U. A review on characterization of carbon quantum dots. *Vietnam J. Chem.* **2023**, *61*, 693-718. https://doi.org/10.1002/vjch.202300022

37) Pal, A.; M. P. Sk, M. P.; Chattopadhyay, A. Recent advances in crystalline carbon dots for superior application potential. *Mater. Adv.* **2020**, *1*, 525. https://doi.org/10.1039/d0ma00108b

38) Kazemifard, N.; Ensafi, A. A.; Rezaei, B. Green synthesized carbon dots embedded in silica molecularly imprinted polymers, characterization and application as a rapid and selective fluorimetric sensor for determination of thiabendazole in juices. *Food chem.* **2020**, *310*, 125812-125820. https://doi.org/10.1016/j.foodchem.2019.125812

39) Li, L.; Wu, G.; Yang, G.; Peng, J.; Zhao, J.; Zhu, J. J. Focusing on luminescent graphene quantum dots: current status and future perspectives. *Nanoscale* **2013**, *5*, 4015-4039. https://doi.org/10.1039/C3NR33849E

40) Selvakumar, T.; Rajaram, M.; Natarajan, A.; Harikrishnan, L.; Alwar, K.; Rajaram, A. Highly Efficient Sulfur and Nitrogen Codoped Graphene Quantum Dots as a Metal-Free Green Photocatalyst for Photocatalysis and Fluorescent Ink Applications. *ACS Omega* **2022**, *7*, 12825−12834. https://doi.org/10.1021/acsomega.2c00092

41) Raveendran, V.; Babu, A. R. S.; Renuka, N. K. Mint leaf derived carbon dots for dual analyte detection of Fe(iii) and ascorbic acid. *RSC Adv.* 2**019***, 9*, 12070-12077. https://doi.org/10.1039/C9RA02120E

42) Rossi, B. L.; Andrade, C. M. B.; Therézio, E. M.; Ramos, R. J.; Vasconcelos, L. G.; Terezo, A. J.; Siqueira, A. B. D. Carbon quantum dots: An environmentally friendly and valued approach to sludge disposable. *Front. Chem.* **2022**, *10*, 858323- 858337. https://doi.org/10.3389/fchem.2022.858323

43) Maa, X.; Lia, S.; Hesselb, V.; Linc, L.; Meskersc, S.; Gallucci, F. Synthesis of luminescent carbon quantum dots by microplasma process. *Chem. Eng. Process* **2019**, *140*, 29–35. https://doi.org/10.1016/j.cep.2019.04.017

44) Palaniselvam, T.; Aiyappa, H. B.; Kurungot, S. An efficient oxygen reduction electrocatalyst from graphene by simultaneously generating pores and nitrogen doped active sites. *J. Mater. Chem.* **2012**, *2*, 23799-23805. https://doi.org/10.1039/C2JM35128E

45) Krishnaiah, P.; Atchudan, R.; Perumal, S.; Gangadaran, P.; Manoj, D.; Ahn, B. C.; Kumar, R. S.; Almansour, A. I.; Lee, Y. R.; Jeon, B. H. *Spectrochim. Acta A: Mol. Biomol. Spectrosc.* **2024**, *304*, 123422-123431. https://doi.org/10.1016/j.saa.2023.123422

46) Wang, M.; Li, C.; Zhou, M.; Xia, Z.; Huang, Y. Natural deep eutectic solvent assisted synthesis and applications of chiral carbon dots. *Green Chem.* **2022**, *24*, 6696-6706. https://doi.org/10.1039/D2GC01949C

47) Xie, Y.; Cheng, D.; Liu, X.; Han, A. Green Hydrothermal Synthesis of N-doped Carbon Dots from Biomass Highland Barley for the Detection of Hg^{2+}. *Sensors* **2019**, *19*, 3169 3179. https://doi.org/10.3390/s19143169.

48) Chiua, S. H.; Geddaa, G.; Girmaa, W. M.; Chenb, J.; Lingc, Y. C.; Ghuled, A.; Oue, K.; Chang, J. Rapid fabrication of carbon quantum dots as multifunctional nanovehicles for dual-modal targeted imaging and chemotherapy. *Acta Biomater.* **2016**, *46*, 151–164. http://dx.doi.org/10.1016/j.actbio.2016.09.027

49) Das, A.; Kundelev, E. V.; Vedernikova, A. A.; Cherevkov, S. A.; Danilov, D. V.; Koroleva, A. V.; Zhizhin, E. V.; Tsypkin, A. N.; Litvin, A. P.; Fedorov, A. V. B. A. V.; Ushakova, E. V. Revealing the nature of optical activity in carbon dots produced from different chiral precursor molecules. *Light Sci. Appl.* **2022**, *11*, 1-13. https://doi.org/10.1038/s41377-022-00778-9

50) Singh, S. K.; Srinivasan, A.; Mitra, S.; Pattader, P. S. G. Carbon dots and Methylene blue facilitated photometric quantification of Hemoglobin. *Spectrochim. Acta A Mol. Biomol. Spectrosc.* **2022**, *271*, 120906-120919. https://doi.org/10.1016/j.saa.2022.120906

51) You, W.; Zou, W.; Jiang, S.; Zhang, J.; Ge, Y.; Lu, G.; Bahnemann, D. W.; Pan, J. H. Fluorescent carbon quantum dots with controllable physicochemical properties fantastic for emerging applications: A review. *Carbon neutraliz.* **2023**, *3*, 245-284. https://doi.org/10.1002/cnl2.120

52) Yang, H. L.; Bai, L. F.; Geng, Z. R.; Chen, H.; Xu, L. T.; Xie, Y. C.; Wang, D. J.; Gu, H. W.; Wang, X. M. Carbon quantum dots: Preparation, optical properties, and biomedical applications. *Mater. Today Adv.* **2023**, *18*, 100376-100400. https://doi.org/10.1016/j.mtadv.2023.100376

53) Elugoke, S. E.; Uwaya, G. E.; Quadri, T. W.; Ebenso, E. E. Carbon Dots: Recent Developments and Future Perspectives. Chapter 1, pp 3-42, *ACS Symposium Series* Vol. 1465. https://doi.org/10.1021/bk-2024-1465.ch001

54) Siddique, A. B.; Hossain, S. M.; Pramanick, A. K.; Ray, M. Excitation dependence and independence of photoluminescence in carbon dots and graphene quantum dots: insights into the mechanism of emission. *Nanoscale* **2021**, *13*, 16662-16671. https://doi.org/10.1039/D1NR04301C

55) Zhang, H.; You, J.; Wang, J.; Dong, X.; Guan, R.; Cao, D. Highly luminescent carbon dots as temperature sensors and "off-on" sensing of Hg^{2+} and biothiols. *Dyes Pigm.* **2020**, *173*, 107950-107980. https://doi.org/10.1016/j.dyepig.2019.107950

56) Cui, X.; Wang, Y.; Liu, J.; Yang, Q.; Zhang, B.; Gao, Y.; Wang, Y.; Lu, G. Dual functional N- and S-co-doped carbon dots as the sensor for temperature and Fe^{3+} ions. *Sens. Actuators,* B*: Chem*. **2017**, *242*, 1272-1280. https://doi.org/10.1016/j.snb.2016.09.032

57) Dua, S.; Kumar, P.; Pani, B.; Kaur, A.; Khanna, M.; Bhatt, G. Stability of carbon quantum dots: a critical review. *RSC Adv.* **2023**, *13*, 13845-13861. https://doi.org/10.1039/D2RA07180K

58) Bocong, L.; Xiang, G.; Huang, X.; Jiang, X.; He, L. Self-exothermic reaction assisted green synthesis of carbon dots for the detection of para-nitrophenol and β-glucosidase activity. *Arab. J. Chem.* **2023**, *16*, 104820-104830. https://doi.org/10.1016/j.arabjc.2023.104820

59) Zhang, J.; Zhou, R.; Tang, D.; Hou, X.; Wu, P. Optically-active nanocrystals for inner filter effect-based fluorescence sensing: Achieving better spectral overlap. *Trends Anal. Chem.* **2019**, *110*, 183–190, 609. https://doi.org/10.1016/j.trac.2018.11.002

60) Kundu, A.; Maity, B.; Basu, S. Orange Pomace-Derived Fluorescent Carbon Quantum Dots: Detection of Dual Analytes in the Nanomolar Range. *ACS Omega* **2023**, *8*, 22178-22189. https://doi.org/10.1021/acsomega.3c02474

61) Bogale, R. F.; Chen, Y.; Ye, J.; Yang, Y.; Rauf, A.; Duan, L.; Tian, P.; Ning, G. Highly selective and sensitive detection of 4-nitrophenol and Fe^{3+} ion based on a luminescent layered terbium (III) coordination polymer. *Sens. Actuators, B: Chem.* **2017**, *245*, 171–178. https://doi.org/10.1016/j.snb.2017.01.177

62) Li, w.; Zhang, h.; Chen, S.; Liu, Y.; Zhuang, J.; Lei, B. Synthesis of molecularly imprinted carbon dot grafted YVO4:Eu^{3+} for the ratiometric fluorescent determination of paranitrophenol. *Biosens. Bioelectron.* **2016**, *86*, 706-713. https://doi.org/10.1016/j.bios.2016.07.034

63) Sohal, N.; Maity, B.; Basu, S. Morphology Effect of One-Dimensional MnO2 Nanostructures on Heteroatom-Doped Carbon Dot-Based Biosensors for Selective Detection of Glutathione. *ACS Appl. Bio Mater.* **2022**, *5*, 2355−2364. https://doi.org/10.1021/acsabm.2c00189

64) Liu, J.; Chen, Y.; Wang, W.; Feng, J.; Liang, M.; Ma, S.; Chen, X. "Switch-On" Fluorescent Sensing of Ascorbic Acid in Food Samples Based on Carbon Quantum Dots–MnO_2 Probe. *J. Agric. Food chem.* **2016**, *64*, 371-380. https://doi.org/10.1021/acs.jafc.5b05726

65) Zu, F.; Yan, F.; Bai, Z.; Xu, J.; Wang, Y.; Huang, Y.; Zhou, X. The quenching of the fluorescence of carbon dots: A review on mechanisms and applications. *Microchim. Acta*. **2017**, *184*, 1899−1914. DOI 10.1007/s00604-017-2318-9

66) Yin, H.; Zhou, Y.; Ai, S.; Liu, X.; Zhu, L.; Lu, L. Electrochemical oxidative determination of 4-nitrophenol based on a glassy carbon electrode modified with a hydroxyapatite nano powder. *Microchim. Acta*. **2010**, *169*, 87-92. https://doi.org/10.1007/s00604-010-0309-1 DOI 10.1007/s00604-010-0309-1

67) Bogireddy, N. K. R.; Silva, R. C.; Valenzuela, M. A.; Agarwal, V. 4-nitrophenol optical sensing with N doped oxidized carbon dots. *J. Hazard Mater.* **2020**, *386*, 121643-121669. https://doi.org/10.1016/j.jhazmat.2019.121643

68) Xiao, N.; Liu, S. G.; Mo, S.; Li, N.; Jun Ju, Y.; Ling, Y.; Li, N. B.; Luo, H. Q. Highly selective detection of p-nitrophenol using fluorescence assay based on boron, nitrogen co-doped carbon dots. *Talanta* **2018**, *184*, 184-192. https://doi.org/10.1016/j.talanta.2018.02.114

69) Das, D.; Dutta, R. K. N-Doped Carbon Dots Synthesized from Ethylene Glycol and β-Alanine for Detection of Cr (VI) and 4-Nitrophenol via Photoluminescence Quenching. *ACS Appl. Nano Mater.* **2021**, *4*, 3444–3454. https://doi.org/10.1021/acsanm.0c03329

70) Guideline, I. C. H. H. T., Validation of Analytical Procedures: Text and Methodology, Q2, **2005**, 1, 20, 5.

Conclusions and Future Perspective

Conclusions

In summary, this thesis uncovers a thorough analysis of the interaction of a series of bile salts, sodium deoxycholate (NaDC), sodium cholate (NaC), and sodium taurocholate (NaTC), with a model transport protein, human serum albumin (HSA). Additionally, it focuses on synthesis, characterization and sensing capabilities for CDs formed using biomass precursors and environment friendly solvents, i.e. deep eutectic solvents, that serve as dynamic fluorescent nanomaterials with tremendous potential for use in sensing applications.

HSA is the most prevalent protein in human serum. It regulates plasma oncotic pressure and transports both endogenous and exogenous ligands. Bile salts are naturally occurring amphiphilic molecules produced in the liver and released into the duodenum upon food intake. They are known to play crucial roles in the solubilization and absorption of fats and other fat-soluble substances in the body. The binding of small molecules to proteins is often the initial step in many biologically important processes. This highlights the importance of studying the nature of such interactions, particularly the binding of hydrophobic anions (such as bile salts) to serum albumin. This interaction plays a crucial role in the transport of bile salts in circulation and their uptake by hepatocytes. As a result, investigation into its ligand binding process is significant in understanding many protein's functions.

Carbon dots are new fluorescent carbon nanomaterials with a wide range of exceptional functional features offering tremendous promise. Nowadays, biomass-based carbon dots are regarded as the most ideal fluorescent nanomaterials produced through green synthesis strategies that reduce resource waste and facilitate sustainable development. In summary, carbon dots were made as an active fluorescent nanomaterial that can be used as nanosensors owing to their qualities like being biocompatible, photostability, aqueous solubility, and tunable photoluminescence. Additionally, the essential interaction mechanisms of carbon dots with various biologically active molecules and pollutants have been established using spectroscopic and microscopic approaches.

Chapter 2 of the thesis provides a brief description of the characterization techniques employed for all the experimental work that were conducted throughout this thesis. The widely used

characterization techniques used includes UV-Visible spectroscopy, steady-state fluorescence spectroscopy, time-resolved fluorescence spectroscopy, high-resolution transmission electron microscopy (HRTEM), X-ray photoelectron spectroscopy (XPS), energy dispersive spectroscopy (EDS), attenuated total reflectance Fourier-transform IR (ATR FT-IR) spectroscopy, Raman spectroscopy, grazing-incidence X-ray diffraction (GIXRD), and zeta potential (ζ) measurements. These are used to understand the binding interactions between protein and bile salts, as well as to investigate the physical, chemical, and optical properties of biomass-derived carbon nanoparticles, coupled with their practical applicability as a nanosensor alongside the underlying mechanism.

In chapter 3, we present an investigation into the mechanisms underlying the interaction and binding of the most abundant plasma protein, human serum albumin (HSA), and bile salts of varying hydrophobicity sodium deoxycholate (NaDC), Sodium taurocholate (NaTC), sodium cholate (NaC) across different solution conditions, employing steady state absorption, fluorescence emission, anisotropy, time-resolved emission, and molecular modeling approaches. Our steady-state spectroscopic investigation indicates that the protein largely undergoes structural changes that are mediated by hydrophobic contacts. Furthermore, time-resolved fluorescence experiments reveal significant structural and dynamical details regarding protein-bile salt complexes. Molecular docking experiments show that bile salts bind spontaneously to HSA subdomain IIA, and that there is fall in binding affinity as the bile salts's hydrophobicity reduces (NaDC > NaC > NaTC). The result provides insight into binding affinities and conformational changes of HSA are modulated by amphiphilic surfaces of bile salts under different physico-chemical circumstances. Additionally, it seems apparent from a variety of theoretical and experimental methods that, while electrostatic and hydrogen bonding interactions play important roles, the interaction between bile salts and HSA appears to be primarily governed by bile salts's hydrophobicity. We anticipate that findings presented here will be useful in the development of pharmacological carriers based on protein-bile salts that may be utilized for drug delivery.

In chapter 4, we present the usefulness of fluorescence-based nanosensor enabling riboflavin (RF) detection in both pharmaceutical tablets and its isolated, pure form. Using a microwave-assisted pyrolysis technique, we demonstrate the synthesis procedure along with characterization, and sensing abilities of intrinsic nitrogen-functionalized N-CDs from Indian gooseberry, a renewable biomass precursor. Without using any harsh chemicals, the synthetic process was maintained in an

environmentally-friendly manner. To meet the specifications of the optimal nanosensor, N-CDs additionally demonstrated exceptional photostability, aqueous solubility, and environmental stability (pH, ionic strength). The as-prepared nanoprobe's average diameter was found to be 8.1 nm by HRTEM imaging. The existence of nitrogen functionalization on N-CDs was verified using EDS, XPS, and FTIR. N-CDs optical characteristics were investigated with UV-Vis, fluorescence, and also time-resolved emission spectroscopy. The as-prepared nanoprobe emits strong green luminescence with PLQY of ~48% and excitation wavelength dependent fluorescence emission property. Mechanistic investigations stated that the as-prepared nanoprobe demonstrated selectivity and sensitivity for detecting RF via FRET mechanism in the nanomolar range under both aqueous and physiological circumstances. The developed nanosensor was also verified in a real sample of vitamin B_2 supplements, demonstrating remarkable precision and accuracy. Overall, the current work gives a fresh perspective for the creation of a unique and sensitive technique of a green fluorescent nanosensor for the detection of RF, which may have significant uses in the pharmaceutical and food industries.

In chapter 5 green-emissive environment-friendly, sustainable, facile, simple and cost-effective nitrogen & chlorine co-doped S-CDs were synthesized enabling on-site screening of major industrial pollutant 4- nitrophenol (4-NP). The synthesis employed sucrose and deep eutectic solvent as precursors without addition of any harmful chemicals. HRTEM revealed 3.06 nm being the mean diameter for S-CDs. FTIR, XPS, and EDS methods were used to confirm the existence of several surface functional groups as well as the intrinsic functionalization of nitrogen and chlorine. S-CDs were also characterized using X-ray diffraction (XRD), UV-Vis, steady state fluorescence, and time- resolved emission experiments. Under UV irradiation, the developed nanoprobe emits a vivid green emission. S-CDs exhibited good water solubility, outstanding photostability, excellent stability in the presence of varying solution ionic strength, and high fluorescence quantum yield of ~56%. The nanosensor developed showed sensitivity and selectivity for 4-NP detection with 10 nM as lowest LOD. Spectroscopic examinations confirmed that 4-NP and S-CDs exhibits an inner filter effect mechanism, evident by significant spectrum overlap and a lack of variations in mean lifetime values. This becomes viable due to the development of a zwitterionic spirocyclic Meisenheimer complex. Furthermore, in an effort to better understand the S-CDs sensing mechanism the quenching efficiency and binding constant were also investigated. We also demonstrated that the sensing device was successful in effectively

detecting 4-NP in real water samples. This work successfully describes a highly selective, sensitive and green nanoprobe designed to conduct a rapid, on-site screening of 4-NP, which could potentially have an impact on environmental preservation.

Future Perspectives

1) Protein-Bile salt interaction will help create and formulate pharmacological carriers based on protein-bile salts that are appropriate for medication delivery.
2) Protein-biosurfactant complexes play an essential role in biochemical processes and can be employed in cosmetics, enzymatic or regulatory action, detergency, targeting specific tissues or organs for medication administration, and protein-based vaccinations
3) Study the effect of modification in carbon dots by surface functionalization for analyte detection.
4) The prepared best sensor for the riboflavin detection can be used in biomedical applications.
5) Implementation of prepared sensor in real-time portable devices.
6) Heteroatom doping can be down to develop all new nanosensor with unique properties and applications.

List of Publications
(Related to PhD work)

1) Kaur, M.; Bhattacharya M.; Maity, B. Deciphering conformational changes in human serum albumin induced by bile salts using spectroscopic and molecular modeling approaches, *J. Mol. Liq.* **2023**, *390*, 123026-123036. https://doi.org/10.1016/j.molliq.2023.123026
2) Kaur M.; Bhattacharya M.; Maity, B. Green transformation of biomass-derived Indian gooseberry into fluorescent intrinsic nitrogen-functionalized carbon quantum dots for real-time detection of vitamin B_2 in the nanomolar range, *RSC Sustain.* **2024**, 1472-1486. https://doi.org/10.1039/D3SU00456B
3) Kaur M.; Bhattacharya M.; Maity, B. Deep Eutectic Solvent-Assisted Nitrogen, Chloride-Functionalized Carbon Quantum Dots for detection of 4-nitrophenol in nanomolar range using spectroscopic tools, *RSC Adv.* ***2025, 15, 19884-19898.*** https://doi.org/10.1039/D5RA00824G

Other Publications

1) S.; Kaur, M.; Sohal, N.; Phull, M.; Maity, B. Bile-salt templated green fluorescent copper nanoclusters: detection of 4-nitrophenol in nanomolar range. *RSC Appl. Interfaces* **2024**, *1*, 1174-1185. https://doi.org/10.1039/D4LF00143E
2) Khare, S.; Sohal, N.; Kaur, M.; Maity, B. Deep Eutectic Solvent-Assisted Carbon Quantum Dots from Biomass *Triticum aestivum*: A Fluorescent Sensor for Nanomolar Detection of Dual Analytes Mercury (II) and Glutathione. *Heliyon* **2024**, *11*, e41853. https://doi.org/10.1016/j.heliyon.2025.e41853
3) Kaur, M.; Sandhu, P. P. K.; Phull, M.; Maity B. Waste to Wealth: Sustainable Synthesis of Green Tea-Derived Quantum Dots for Nanomolar Detection of Fe^{3+} ions and Ascorbic Acid. *ChemNanoMat.* **2025***, 11,* e202500140. https://doi.org/10.1002/cnma.202500140

Conferences and Workshops

1) International conference on Recent advances in chemistry held at Punjabi University, Patiala, Punjab, India (awarded as best poster presentation)
2) International conference on emerging materials for sustainable development (emsd-2022)" held at the CSIR-CSIO, Chandigarh, India (Poster Presentation)
3) International conference on Recent trends in biomolecules and therapeutics, Panjab University, Chandigarh, India (Oral Presentation)
4) National Workshop on Fluorescence and Raman spectroscopy (FCSXIV) held at IISER Mohali, Punjab, India (Poster Presentation)
5) International Conference on Nanotechnology: Opportunities & Challenges held at Jamia Millia Islamia (Central University), New Delhi, India (Participation)
6) International Conference on Chemistry of Carbon-Based Nanocomposites and their Applications, Vancouver, Canada (Oral Presentation)

Appendix

Chapter 3

Deciphering conformational changes in human serum albumin induced by bile salts using spectroscopic and molecular modeling approaches

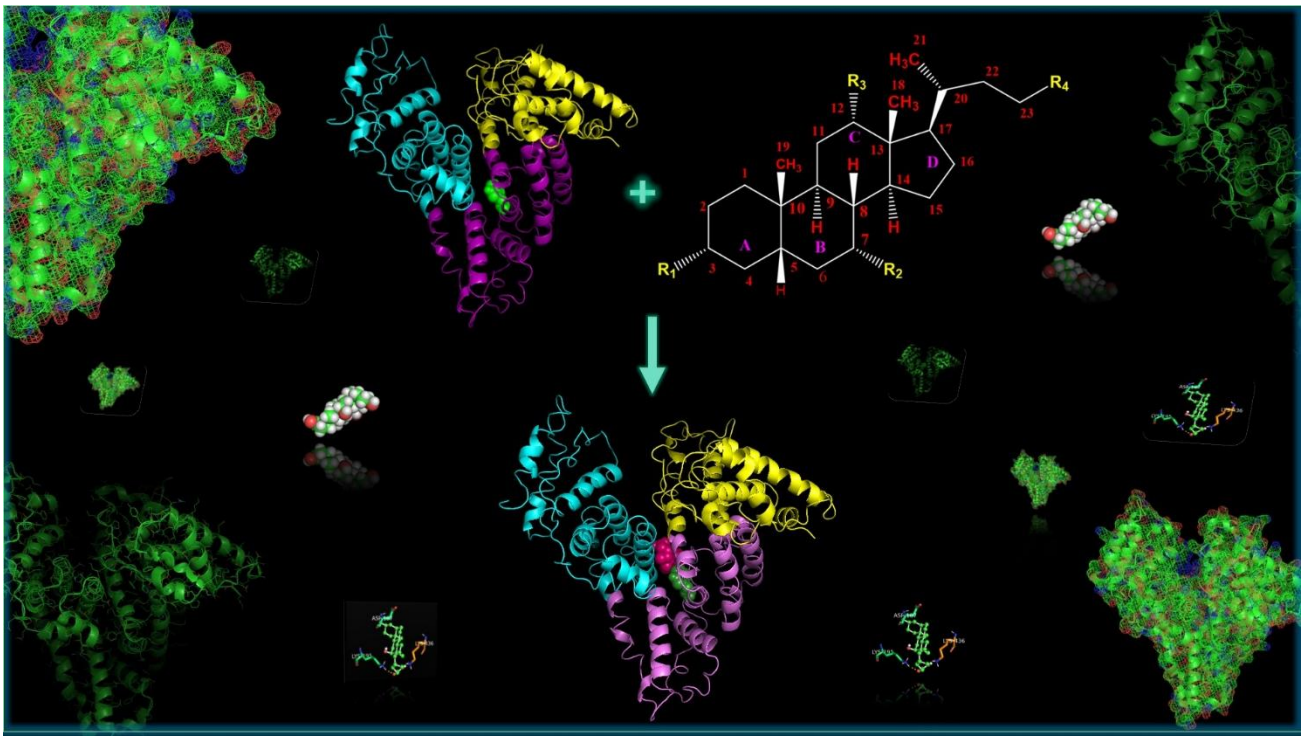

Chapter 4

Green transformation of biomass-derived Indian gooseberry into fluorescent intrinsic nitrogen-functionalized carbon quantum dots for real-time detection of vitamin B_2 in the nanomolar range

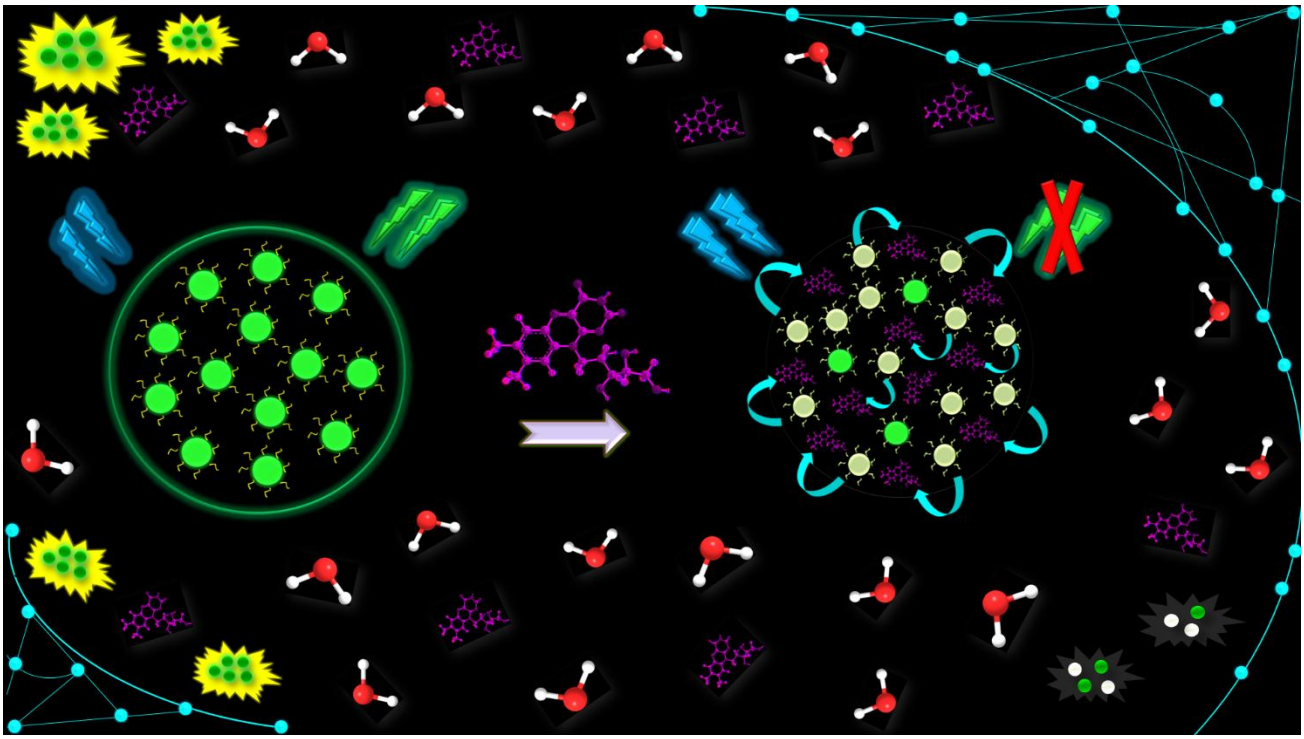

Chapter 5

Deep eutectic solvent-assisted carbon quantum dots for nanomolar detection of 4-nitrophenol

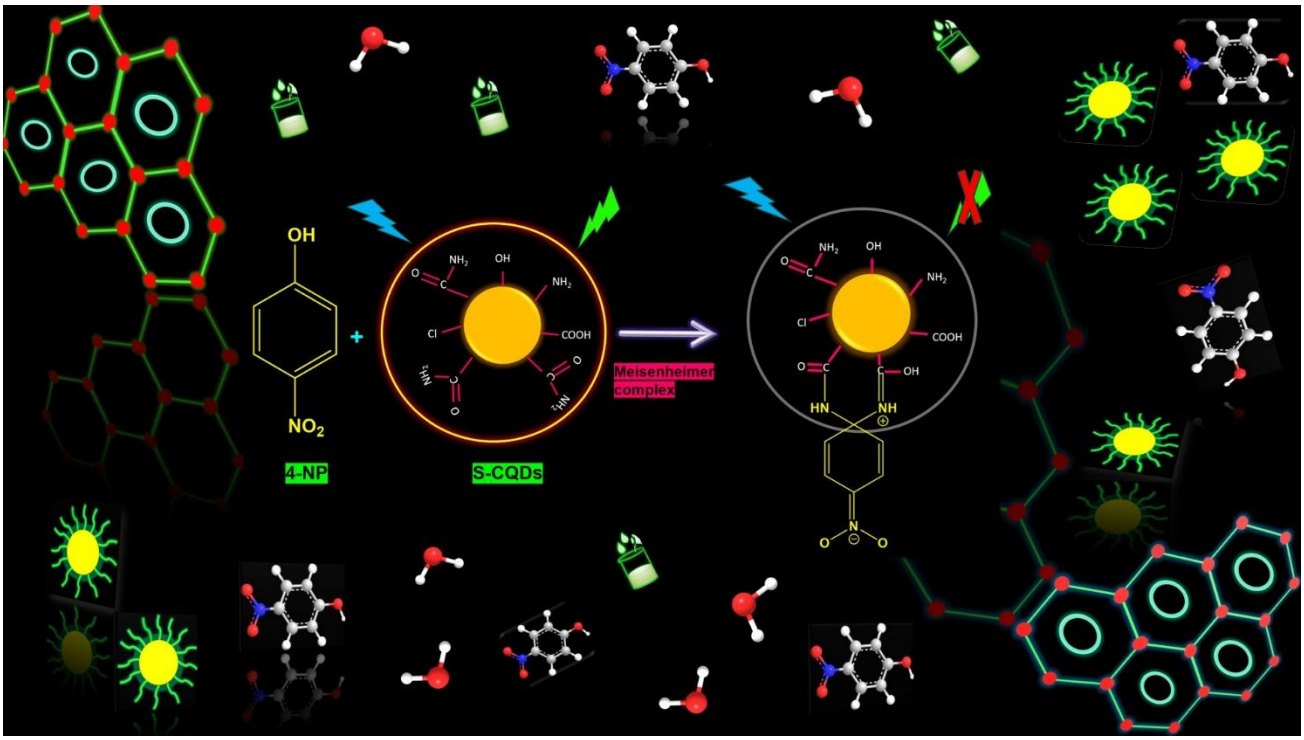

Mandeep Thesis Turnitin Checking_9th February, 2025

ORIGINALITY REPORT

14%	8%	12%	1%
SIMILARITY INDEX	INTERNET SOURCES	PUBLICATIONS	STUDENT PAPERS

PRIMARY SOURCES

1	www.mdpi.com Internet Source	1%
2	link.springer.com Internet Source	1%
3	Mukherjee, Saptarshi. "Hydrophobicity is the Governing Factor in the Interaction of Human Serum Albumin with Bile Salts", Langmuir Publication	1%
4	www.ncbi.nlm.nih.gov Internet Source	<1%
5	www.researchgate.net Internet Source	<1%
6	Junjun Liu, Rui Li, Bai Yang. "Carbon Dots: A New Type of Carbon-Based Nanomaterial with Wide Applications", ACS Central Science, 2020 Publication	<1%
7	www.freepatentsonline.com Internet Source	<1%
8	core.ac.uk Internet Source	<1%
9	Roberto Sotolongo-García, Eustolia Rodríguez-Velázquez, Manuel Alatorre-Meda, Mercedes T. Oropeza-Guzmán et al. "Optimizing the Efficiency of a Cytocompatible Carbon-Dots-Based FRET Platform and Its Application as a Riboflavin Sensor in Beverages", Nanomaterials, 2021	<1%

Mandeep